University of California
Los Angeles

A Precise Measurement of the Top Quark Mass

A dissertation submitted in partial satisfaction
of the requirements for the degree
Doctor of Philosophy in Physics

by

Brian N. Mohr

2007

The dissertation of Brian N. Mohr is approved.

Peter Felker

Zvi Bern

Robert Cousins

Jay Hauser, Committee Chair

University of California, Los Angeles

2007

Table of Contents

List of Figures

List of Tables

Acknowledgments

I would like to thank many members of the UCLA high energy physics group: Jay Hauser, my adviser, for his very kind and generous support and for his understanding in enabling my research at Fermilab; Florencia Canelli, for all the hard work, dedication and effort on this analysis and for passing on her knowledge of the matrix element method; Rainer Wallny, for his work and review of this analysis; Charles Plager, for fruitful discussion of statistics and computer programming; Bob Cousins, for useful discussion of likelihoods and statistics; and An-chi Kao, for her administrative support.

I would also like to thank other people contributing some effort in this analysis: Doug Glenzinski, Mousumi Datta and Sasha Golossanov, for their helping to setup and process events and other contributions; the Fermilab Statistics committee, for useful discussion of statistics; and Adam Gibson, Eva Halkiadakis, Young-Kee Kim, Andrew Kovalev and Daniel Whiteson for discussion and contribution to an earlier version of this analysis.

Many people contributed to reviewing this analysis, especially: Erik Brubaker and Kohei Yorita, for their close internal review; Doug Glenzinski, Takasumi Maruyama, Evelyn Thomson and Un-ki Yang, for their leadership role as conveners of the Top and Top Mass working groups; and Young-Kee Kim, Tom Wright and Erik Brubaker, for their role in reviewing the PRL publication.

I would like to acknowledge the numerous people contributing to, maintaining, and operating the Fermilab accelerator and CDF detector. Many others have contributed to this effort that I have not specifically named.

Additionally, I would like to thank these people for dedicating their support or computer farm processing time so that this analysis could be completed: Alon

Attal, Florencia Canelli, Mousumi Datta, Peter Dong, Robin Erbacher, Doug Glenzinski, Sasha Golossanov, Jay Hauser, Ben Kilminster, Elliot Lipeles, Rob Roser, David Saltzberg, Bernd Stelzer, and Rainer Wallny.

Vita

2001	B.A., Physics Bowdoin College
2003	M.S., Physics University of California, Los Angeles

Abstract of the Dissertation

A Precise Measurement of the Top Quark Mass

by

Brian N. Mohr

Doctor of Philosophy in Physics

University of California, Los Angeles, 2007

Professor Jay Hauser, Chair

We present a measurement of the mass of the top quark using data from proton-antiproton collisions recorded at the CDF experiment in Run II of the Fermilab Tevatron. Events are selected from the single lepton plus jets final state ($t\bar{t} \rightarrow W^+bW^-\bar{b} \rightarrow \ell\nu bq\bar{q}'\bar{b}$). The top quark mass is extracted using a calculation of the probability density for a $t\bar{t}$ final state to resemble a data event. This probability density is a function of both top quark mass and energy scale of calorimeter jets, constrained *in situ* with the hadronic W boson mass. Using 167 events observed in 955 pb^{-1} integrated luminosity, we achieve the single most precise measurement of top quark mass to date of 170.8 $\pm$ 2.2 (stat.) $\pm$ 1.4 (syst.) GeV/c^2, where the quoted statistical uncertainty includes uncertainty from the determination of the jet energy scale.

CHAPTER 1

Introduction

High energy particle physics studies the fundamental constituents of matter and their interactions. A subset of the fundamental particles, quarks, combine to form particles such as the proton and neutron. The recently discovered top quark is the most massive known fundamental particle. Experimental particle physics collides common particles at speeds near that of light. Currently, top quarks have only been directly produced at the highest energy particle accelerator operating in the world to date, the Tevatron, located at the Fermi National Accelerator Laboratory. Specialized detectors and electronic systems, such as the Collider Detector at Fermilab, collect experimental data from these collisions. This analysis applies a sophisticated statistical technique to CDF data, resulting in a precise measurement of the top quark mass.

Chapter 2 briefly outlines the underlying theory of particle physics, known as the Standard Model, and elaborates on the expected properties of the top quark. Particle acceleration and data collection apparatus is discussed in Chapter 3, and event reconstruction, calibration and selection are discussed in Chapter 4. A full description of the data and simulated datasets is the subject of Chapter 5. The analysis method is described in Chapters 6 and 7. Results of the analysis are presented in Chapter 8, and systematic uncertainty is presented in Chapter 9. Conclusions from this analysis are the subject of Chapter 10.

CHAPTER 2

The Top Quark

2.1 The Standard Model

Physicists have discovered four fundamental forces governing the physical world, electromagnetism, gravity, and the weak and strong nuclear forces. All but gravity are described in the Standard Model, a gauge symmetry group described by $\mathrm{SU(3)_C x SU(2)_L x U(1)_Y}$. $\mathrm{SU(3)_C}$ corresponds to Quantum Chromodynamics (QCD) and governs the strong nuclear interactions. $\mathrm{SU(2)_L x U(1)_Y}$ corresponds to the Glashow-Weinberg-Salam (GWS) theory governing unified electroweak interactions [1]. GWS electroweak symmetry is broken into the weak nuclear force and Quantum Electrodynamics (QED).

Fundamental particles can be separated into fermions, which are spin-$\frac{1}{2}$ and obey Fermi-Dirac statistics, and bosons, which are spin-1 and obey Bose-Einstein statistics. The fundamental fermions are divided into six known quarks and six known leptons, each separated into three sets of couplets and each having a corresponding anti-particle. Table 2.1 summarizes the fundamental Fermions.

The fundamental bosons mediate interactions between fermions or other bosons. There are 12 force mediators, known as gauge bosons: 8 gluons in the strong nuclear force, 3 bosons in the weak nuclear force, and the photon in electromagnetism. Gluons couple to color, a quantum property only quarks and gluons contain, so the strong nuclear force does not apply to leptons. Photons couple to

Table 2.1: Fundamental fermions in the Standard Model

	First	Second	Third	Charge
Leptons	electron (e^-)	muon (μ^-)	tau (τ^-)	-1
	e-neutrino (ν_e)	μ-neutrino (ν_μ)	τ-neutrino (ν_τ)	0
Quarks	up (u)	charm (c)	top (t)	$\frac{2}{3}$
	down (d)	strange (s)	bottom (b)	-$\frac{1}{3}$

charge, so electromagnetism does not directly affect neutrinos. All Fermions interact via the weak nuclear force. Table 2.2 summarizes the fundamental bosons.

Table 2.2: Fundamental bosons in the Standard Model

Name	Force	Charge
photon (γ)	EM	0
W, Z boson	weak	$\pm$1, 0
gluon (g)	strong	0

The Standard Model accurately describes all physical measurements, with the exception of non-zero neutrino mass, to date, but one component has yet to be observed. The Higgs boson scalar field is predicted as a mechanism to break GWS electroweak symmetry by which the weak nuclear force gauge bosons acquire mass [2][3]. Fermions also acquire mass via this field. Masses of quarks and leptons vary due to their unique coupling to the field. Table 2.3 lists the experimentally determined masses of the fundamental particles [4]. Note that measured neutrino oscillations mean neutrinos have small masses.

Coupling strength in the strong nuclear force decreases with increasing momentum transfer, Q^2, the amount of momentum given to a particle created in

Table 2.3: Masses of fundamental particles in GeV/c^2

Quarks	Mass	Leptons	Mass	Bosons	Mass
u	0.005	e	0.0005	γ	0
d	0.01	μ	0.1	W	80.4
s	0.15	τ	1.8	Z	91.2
c	1.2	ν_e	< 0.003	g	0
b	5.0	ν_μ	< 0.002		
t	175	ν_τ	< 0.018		

scattering or decay. At high Q^2, quarks behave as essentially free particles, but at low Q^2, quarks are bound into quark/anti-quark pairs (mesons) or quark triplets (baryons). Mesons are bosons and baryons are fermions, and both have integer charge and are color neutral. These particles decay via the weak nuclear force into stable particles, such as protons, electrons, and photons, composing the majority of the visible universe today.

2.2 Top Quark Production and Decay

Top quarks are far too massive and unstable to be observed in the natural world. They are produced via hard scattering processes in particle colliders. Currently, the only collider with enough energy to directly produce top quarks is the Tevatron at FNAL, discussed further in section 3.1. Top quarks were first conclusively observed at FNAL in 1995 [5][6]. Due to its large mass, the top quark decays almost immediately after production, so quickly that it does not hadronize and form bound states as other quarks do.

The largest number of top quarks at the Tevatron are produced via pair

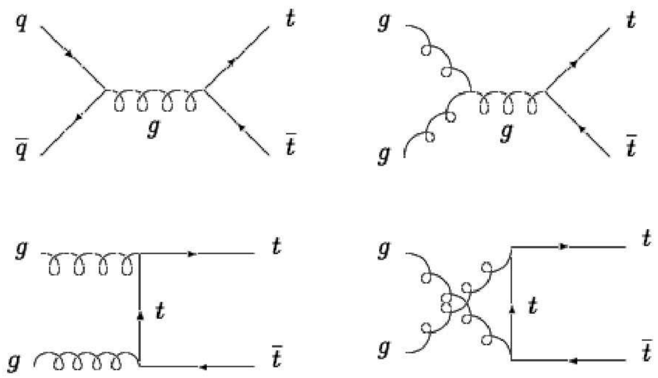

Figure 2.1: Feynman diagrams describing leading-order top quark pair production at hadron colliders.

production with the strong nuclear force. Figure 2.1 shows Feynman diagrams describing leading-order pair production processes. Leading order calculations estimate top quark pairs are produced 95% by quark-quark collisions and 5% by gluon-gluon interactions. Solo top quarks are produced via a charge-current weak interaction, but the predicted cross-section for this process is lower than pair production. There is evidence for single top production at the Tevatron, but it has not yet been confirmed.

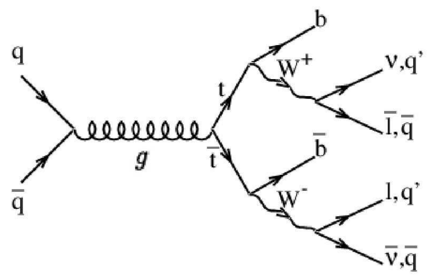

Figure 2.2: A Feynman diagram describing top quark pair production and decay.

Top quarks decay via the weak force almost consistently into a W boson and a b quark. Decays into a W boson and a d or s quark are suppressed by the CKM matrix. Flavor changing neutral current decays are suppressed by even larger amounts. Figure 2.2 gives the prominent Feynman diagram of top quark pair production and decay. The W bosons then decay hadronically into a quark-antiquark pair or leptonically into a lepton-neutrino pair. Electrons and muons from these decays are final state particles observed by the CDF detector. Tau leptons, due to their large mass, are not stable and generally decay within the detector. Quarks produced in these decays interact via QCD. At high energies, these interactions are described by perturbative QCD, but at lower energies, quarks hadronize, creating quark-antiquark pairs from the vacuum to form stable particles. This process is described phenomenologically. The collective perturbative QCD and hadronization is termed fragmentation and results in showers of long-lived hadrons in the detector.

Top quark pair production decays are topologically classified according to the hadronic or leptonic decay of the W bosons. In $t\bar{t}$ pair production the possible configurations are two hadronic decays (all hadronic), two leptonic decays (dilepton), and one hadronic and one leptonic decay (lepton + jets). Taus from W boson decay are inefficiently identified in the CDF detector, see Chapter 4, so τ decay channels are not included. The relative branching ratios for these decays are 44%, 5% and 30%, respectively. This analysis selects events consistent with the lepton + jets decay channel, retaining a relatively large branching ratio but with much smaller background than the all hadronic channel.

Events with the same decay signature as the lepton + jet $t\bar{t}$ signal but produced via a different process are background. The main background is produced by processes such as that shown in Figure 2.3 in which a real W boson is created as well as extra partons. Partons are quarks or gluons created directly from hard scattering processes. Other backgrounds include single top quark produc-

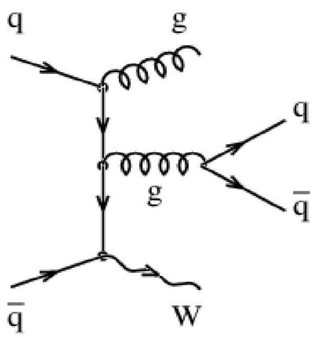

Figure 2.3: A Feynman diagram describing W boson + jets production.

tion, other electroweak interactions producing a real W or Z boson, and QCD interactions mimicking the decay signature of a W boson ("non-W").

2.3 The Significance of Top Quark Mass

The top quark mass is a fundamental parameter in the Standard Model. Due to its relatively large value, it has a more critical influence on Standard Model calculations than the other quarks. It influences non-leading order (radiative) corrections to electroweak processes. It also helps to constrain the mass of the as yet unobserved Higgs boson via the radiative correction to the mass of the W boson. Figure 2.4 shows two differing views of the constraint on the Higgs boson mass [9] using precise electroweak measurements, such as the W boson mass, from LEP [10], and of the top quark mass from FNAL [11]. The uncertainty in the top quark measurement includes the result of this analysis, see Chapter 10.

As indicated in Figure 2.4, the most likely value of the Higgs boson mass is ruled out by lack of direct observation at LEP. Failure of the Standard Model to properly describe these results may indicate new physics yet to be discovered, such as the Minimal Supersymmetric extension to the Standard Model

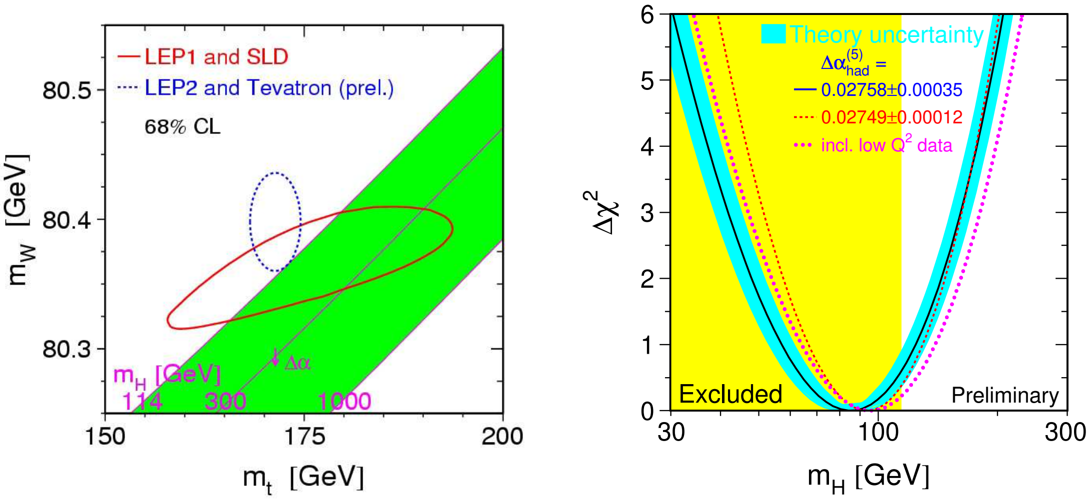

Figure 2.4: Electroweak constraints on the Higgs boson mass using current best measurements of W boson and top quark mass (left). Global fit of Higgs boson mass to several electroweak parameters (right).

(MSSM) [12][13]. Figure 2.5 shows regions of top quark and W boson mass parameter space consistent with the Standard Model and MSSM. The current best measurements and corresponding uncertainty are described by the blue ellipse, which lies predominantly in the MSSM region. The one sigma level hints at possible physics beyond the Standard Model. Note that the measurement made by this analysis decreased the world-average estimate of the top quark mass, thereby increasing the discrepancy with the Standard Model. It is uncertain if the Tevatron will have enough center of mass energy to probe for this physics, but a new collider at CERN (LHC) will be operating in the near future with seven times the center of mass energy. Many expect the discovery of the Higgs boson and supersymmetric particles at LHC.

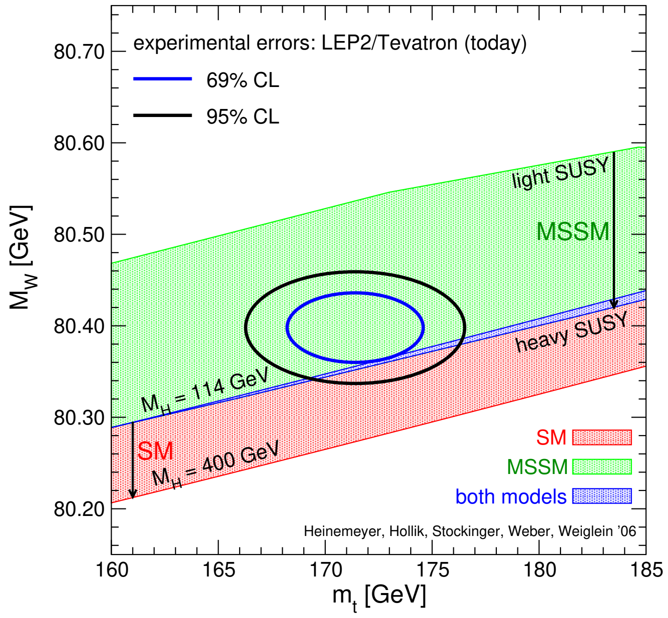

Figure 2.5: Standard Model (SM) and Minimal Supersymmetric extension to the Standard Model (MSSM) parameter space in terms of current best measurements of top quark and W boson mass.

CHAPTER 3

Apparatus

The Fermi National Accelerator Laboratory (FNAL) has been running in its current phase of operation since 2001. Located near Batavia, IL, the $p\bar{p}$ synchrotron accelerator supports several experiments, including two collider detectors, one of which, the Collider Detector at Fermilab (CDF), collected data for this analysis. The accelerator also provides protons to fixed target experiments. CDF is a general purpose hard scattering detector supporting a wide variety of physics analyses. One of the priorities of FNAL is a precise measurement of the top quark mass. Several hundred people support the operation of the accelerator and another several hundred are responsible for the commissioning and operation of the CDF detector. A competing collaboration, DØ, independently measures similar physics quantities. Combined results from these two collaborations have resulted in increasingly precise measurements of the top quark mass and other interesting physical phenomenon. This chapter outlines the basic operation and structure of the accelerator and detector.

3.1 The Tevatron Accelerator

The main accelerator at FNAL, the Tevatron, accelerates protons and anti-protons, colliding them at a center of mass energy of 1.96 TeV. Several stages of acceleration are necessary before protons and anti-protons can be brought to

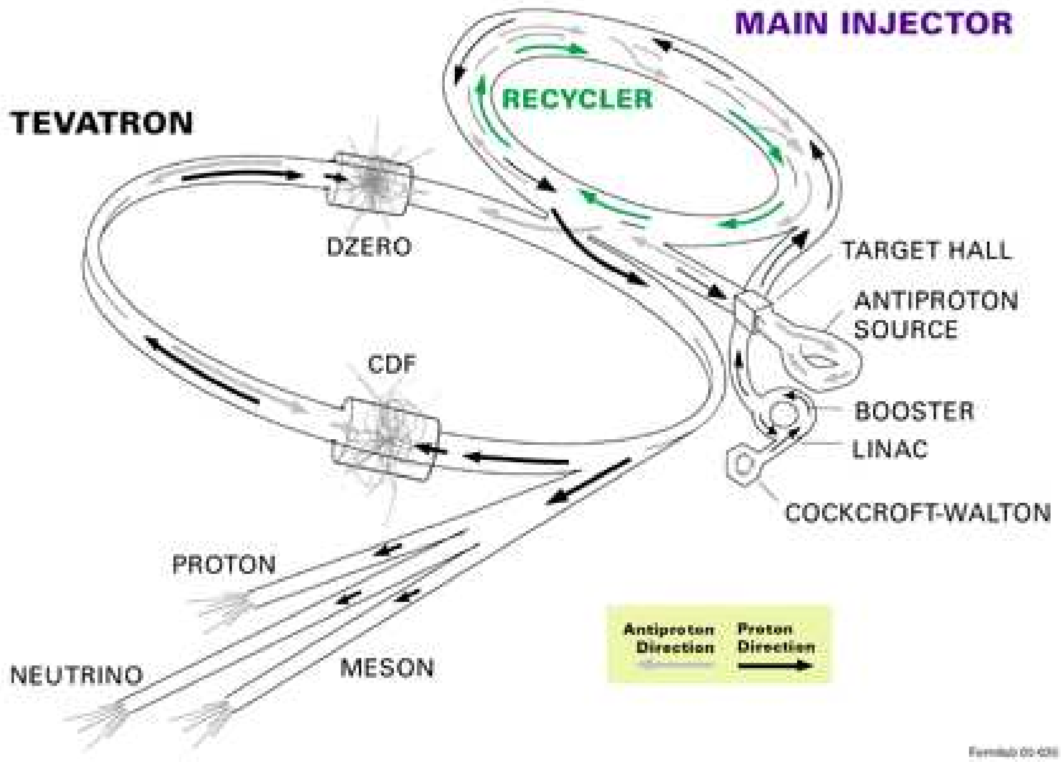

Figure 3.1: Diagram of Tevatron acceleration complex.

this energy. Since no readily available source of anti-protons exists, they must be produced using energetic proton collisions. Figure 3.1 schematically describes the Tevatron acceleration complex.

3.1.1 Acceleration Chain

Protons colliding in the Tevatron start out as hydrogen gas. The hydrogen is ionized by adding an electron and then fed to a Cockcroft-Walton direct current electrostatic accelerator. Exiting the Cockcroft-Walton with 750 keV, the hydrogen ions are fed into a RF linear accelerator, the Linac, and ramped to 400 MeV. The hydrogen ions then strike a stationary target of carbon foil, stripping the two electrons from the ions and leaving bare protons.

Protons are collected and accelerated to 8 GeV in the Booster, a 475 m circumference synchrotron. The Booster then injects them into the Main Injector, a 3 km circumference synchrotron. The Main Injector has several purposes. It accelerates protons and anti-protons from 8 GeV to 150 GeV, preparing them for injection into the Tevatron; and it also accelerates protons to 120 GeV for anti-proton production, as described in section 3.1.2.

The Tevatron is a 6.3 km circumference synchrotron using superconducting magnets with a peak field of 4.2 T. Protons and anti-protons are injected into the Tevatron forming a beam containing 36 discrete packages of particles known as bunches and are accelerated from 150 to 980 GeV. Protons and anti-protons rotate in opposite directions in the ring and are held in separate helical orbits. Focusing quadrupole magnets at two collision points bring the proton and anti-proton beams to intersection. Bunches pass a given collision point every 396 ns. Each bunch collides approximately 2.6x10^{11} p and 3.5 x 10^{10} $\bar{p}$. These numbers contribute to the instantaneous luminosity of the beam [14]

$$\mathcal{L} = \frac{3\gamma f_{\mathrm{o}} N_B N_p N_{\bar{p}} F}{\beta(\epsilon_p + \epsilon_{\bar{p}})}, \tag{3.1}$$

where N_B is the number of bunches in the accelerator; N_p and $N_{\bar{p}}$ are the number of p and $\bar{p}$ per bunch, respectively; f_{o} is the revolution frequency; $\gamma = E/m$ is the relativistic energy factor; β is the beta function at the low beta focus; ϵ_p and $\epsilon_{\bar{p}}$ are the proton and anti-proton beam emittances, respectively; and F is a form factor describing bunch geometry. Integrating instantaneous luminosity over time and taking the product with a scattering cross-section returns the number of events produced.

3.1.2 Anti-proton Production

Anti-protons are produced by colliding accelerated protons from the Main Injector with a stationary nickel target in the Target Station. Magnets focus charged particles from this collision into a beam and strip away everything but the anti-protons. Anti-proton production is not very efficient, requiring a million incident protons to produce 20 anti-protons.

Once collected into a beam, the anti-protons are sent to the Debuncher, a triangular synchrotron with a radius of 90 m, where their spread in energy is reduced using a synchronized oscillating potential in the RF cavities. This potential is designed to accelerate slower particles and decelerate faster particles. Uniform velocity of anti-protons enables more efficient beam manipulation and increases instantaneous luminosity by reducing bunch widths.

Thus prepared, the anti-protons are collected and stored until they are needed for acceleration and collisions. One storage unit, the Accumulator, is a synchrotron in the same tunnel as the Debuncher, labeled "antiproton source" in Figure 3.1. The Accumulator reduces the longitudinal momentum of the anti-protons using a synchronized potential and stochastic cooling [15]. Stochastic cooling was developed at CERN in the 1970s and dampens unwanted momentum phase-space components of the particle beam using a feedback loop. Essentially, the beam orbit is measured with a pickup and corrected with a kicker, schematically described by Figure 3.2.

The other anti-proton storage unit is the Recycler, a synchrotron in the same ring as the Main Injector. The Recycler was originally designed to collect anti-protons from the Tevatron once collisions for a given store were finished, but attempts to use it for this purpose have not been worthwhile. As an additional storage unit, the Recycler has allowed increased instantaneous luminosity since

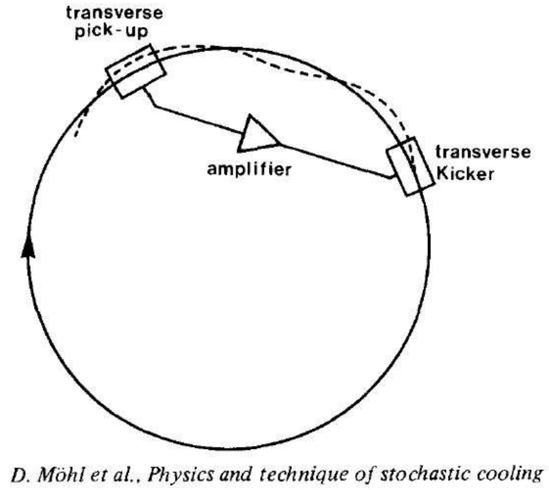

Figure 3.2: Schematic of stochastic cooling in Accumulator. Momentum of anti-proton beam is measured at the pickup and corrected at the kicker.

2004. The Recycler takes advantage of electron cooling, in which a 4.3 MeV beam of electrons over 20 m is used to reduce longitudinal momentum. When a store is ready to begin, anti-protons are transferred from either or both the Accumulator and the Recycler to the Tevatron for final acceleration.

3.2 The CDF Detector

The Collider Detector at FNAL (CDF) is a general purpose charged and neutral particle detector [16][17]. It surrounds one of the beam crossing points described in section 3.1.1. The detector observes particles or their decay remnants via charged tracks bending in a 1.4 T solenoidal field, electromagnetic and hadronic showers in calorimeters, and charged tracks in muon detection chambers. Additionally, Cherenkov counters measure the instantaneous luminosity of the colliding beams. In order from nearest to beamline to the outermost region of

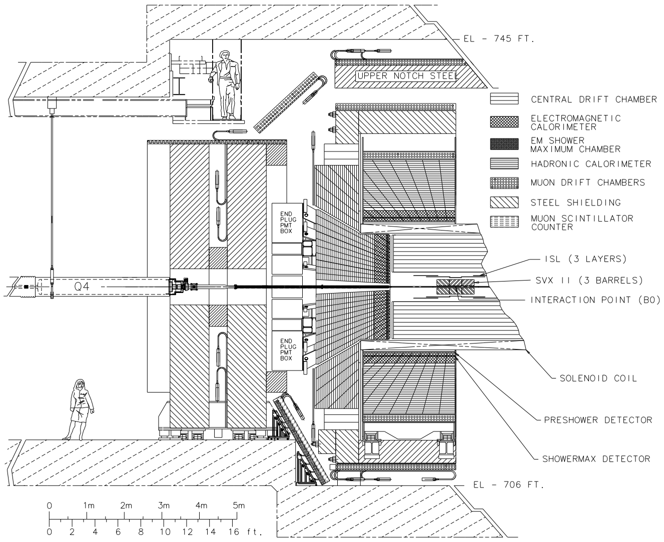

Figure 3.3: Elevation view of the East half of the CDF detector. The West half is nearly mirror symmetric.

the detector, the major components are the silicon tracking system, the central outer tracking system, the solenoid, the calorimeters, and the muon chambers, Figure 3.3.

CDF is cylindrical in construction, with the beam line defining the z-axis oriented with the direction of proton travel, which is also the direction of the solenoid field lines. The x-axis is defined as pointing away from the Tevatron ring, and the y-axis is defined as pointed directly upward, Figure 3.4. Transverse components are defined to be perpendicular to the beamline, in other words the polar r-ϕ dimension. For instance:

$$E_T \equiv E\,\sin\theta. \tag{3.2}$$

Another useful coordinate variable is rapidity

$$y \equiv \frac{1}{2}\ln\frac{E+p_z}{E-p_z}. \tag{3.3}$$

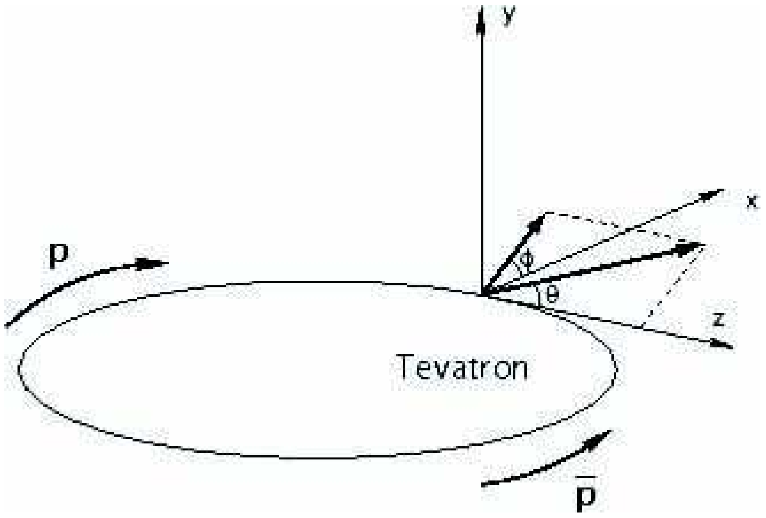

Figure 3.4: Coordinate system of CDF detector relative to Tevatron ring.

Pseudo-rapidity, η, is the massless limit of rapidity and defined as

$$\eta \equiv \frac{1}{2} \ln \frac{p + p_z}{p - p_z} = -\frac{1}{2} \ln(\tan\theta). \tag{3.4}$$

Pseudo-rapidity is always defined with respect to the detector coordinates unless explicitly specified. Many of the components of CDF are segmented in pseudo-rapidity. Figure 3.5 shows the η coordinates relative to the tracking volume and plug calorimeter.

3.2.1 Cherenkov Luminosity Counters

To measure luminosity, Cherenkov Luminosity Counters (CLCs) [18][19] are positioned near the beamline, $3.7 < |\eta| < 4.7$. The counters are long, conical chambers filled with isobutane at atmospheric pressure. Cherenkov light radiated from particles passing through the chambers is collected with Photo-Multiplier Tubes (PMTs) allowing a measurement of the number of inelastic $p\bar{p}$ interactions at each bunch crossing. The momentum threshold for detection of electrons is 9.3 MeV/c

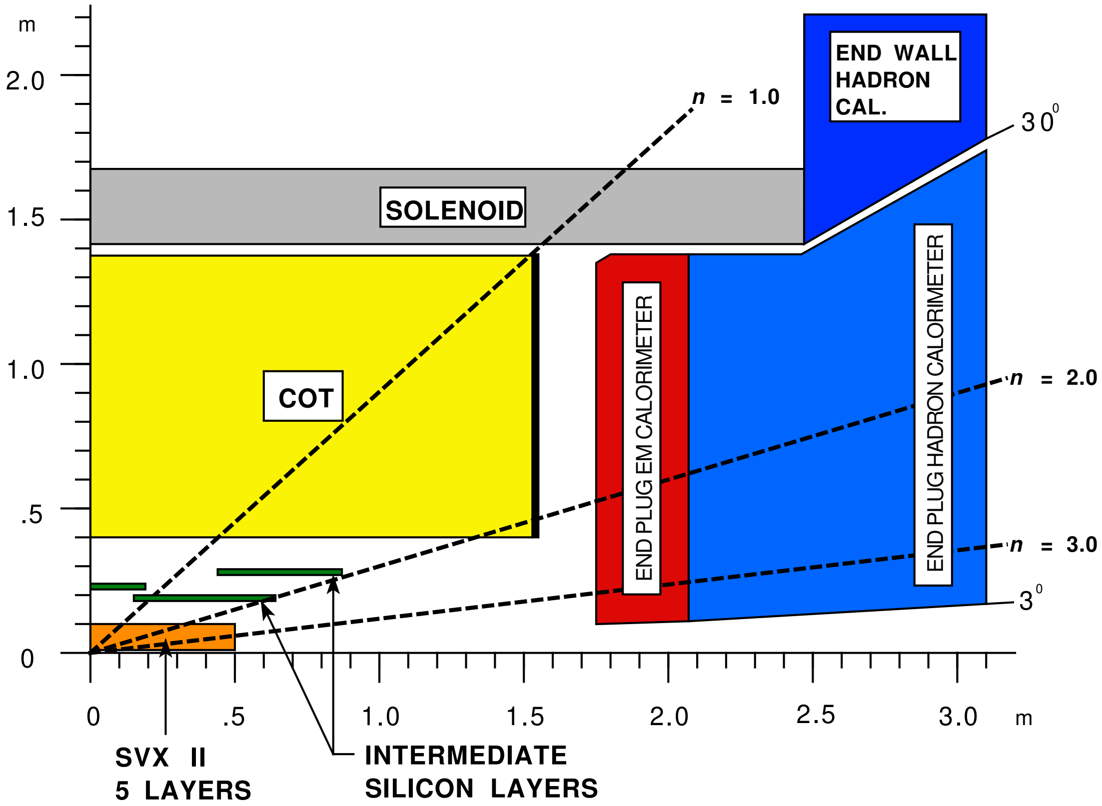

Figure 3.5: Schematic of tracking volume and plug calorimeters of the upper east quadrant of the CDF detector.

and of pions is 2.6 GeV/c. Figure 3.6 shows the initial instantaneous luminosity and total integrated luminosity as a function of year. The initial instantaneous luminosity increased with running time due to improvements such as using the Recycler to store anti-protons. Total integrated luminosity is separated according to that delivered by the Tevatron and that recorded to tape by the CDF detector.

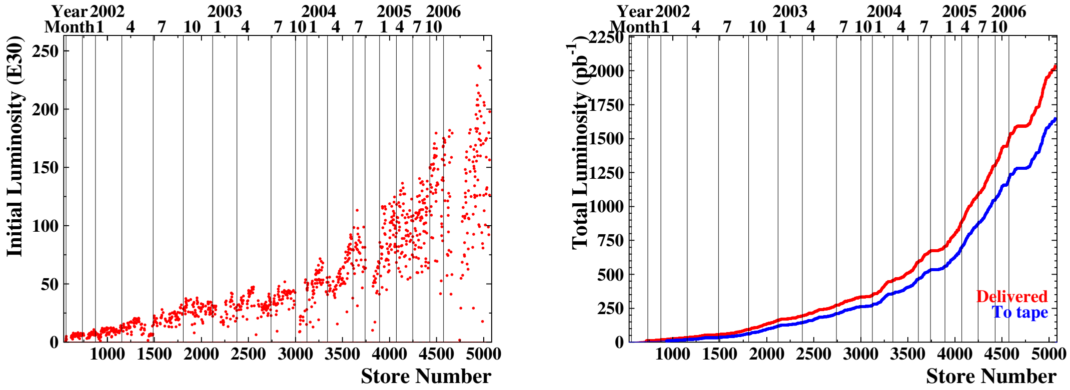

Figure 3.6: Initial instantaneous luminosity (left) and total integrated luminosity (right) as a function of year since the beginning of Run II.

3.2.2 Silicon Tracking

The innermost component of CDF is a tracking system composed of silicon microstrip arrays. Its main function is to provide precise position measurements near collision vertices, and it is essential for identification of secondary vertices, discussed in section 4.4.3.

Constructed in three separate components, L00 [20], SVXII [21] and ISL [22], the silicon tracking system covers detector $|\eta| < 2$. L00 is a single layer mounted directly on the beampipe, $r = 1.6$ cm, and is a single-sided array with a pitch of 50 μm providing solely axial measurements. SVXII is mounted outside of L00, $2.4 < r < 10.7$ cm, and is composed of 5 concentric layers in ϕ and 3 segments,

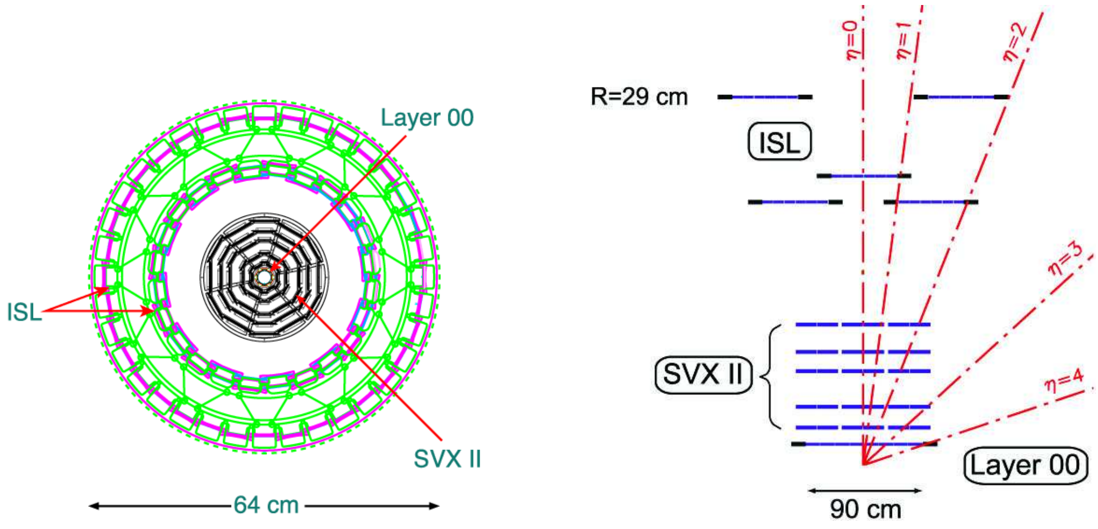

Figure 3.7: Schematic showing r-ϕ and y-z views of the Run II CDF silicon tracking system. Note: vertical and horizontal axes are not to scale.

or barrels, in z. Each layer is further subdivided in to 12 segments in ϕ, or wedges. Double-sided arrays provide axial (r-ϕ) measurements on one side and stereo (z) measurements on the other. The stereo position of layer 0, 1 and 3 is perpendicular to the z-axis, and that of layer 2 and 4 is -1.2^o and +1.2^o, respectively. The SVXII detector spatial resolution for axial measurements is 12 μm. ISL surrounds SVXII, $20 < r < 29$ cm, and is composed of three layers of double-sided arrays. As with SVXII, one side provides axial measurements and the other stereo measurements at 1.2^o relative to the z-axis.The ISL detector resolution for axial measurements is 16 μm.

3.2.3 Central Outer Tracker

The Central Outer Tracker (COT) [23] comprises the bulk of CDF's tracking volume, located between $40 < r < 132$ cm and detector $|\eta| < 1$. The COT provides the best measurements of charged particle momentum, but does not measure position as precisely as the silicon tracking system. It is a 96-layer open-cell drift chamber subdivided into 8 superlayers. Each superlayer is further divided with gold covered Mylar field sheets into cells containing 25 wires alternating between potential and sense wires, see Figure 3.8. In half of the superlayers, the wires are parallel to the beamline and provide axial measurements, while in the other half, the wires are alternately at $\pm 2^{o}$ and provide stereo measurements. The innermost superlayer provides a stereo measurement and subsequent layers alternate between axial and stereo measurements. The gas filling the chamber is comprised of 50% argon and 50% ethane (and lately, some oxygen was added to prevent corrosion). This results in a maximum drift time of 100 ns, far shorter than the time between bunch collisions. The single hit resolution of the COT is 140 μm, and the track momentum resolution using muon cosmic rays is $\sigma_{p_T}/p_T^2 \approx 0.001$ (GeV/c)$^{-1}$.

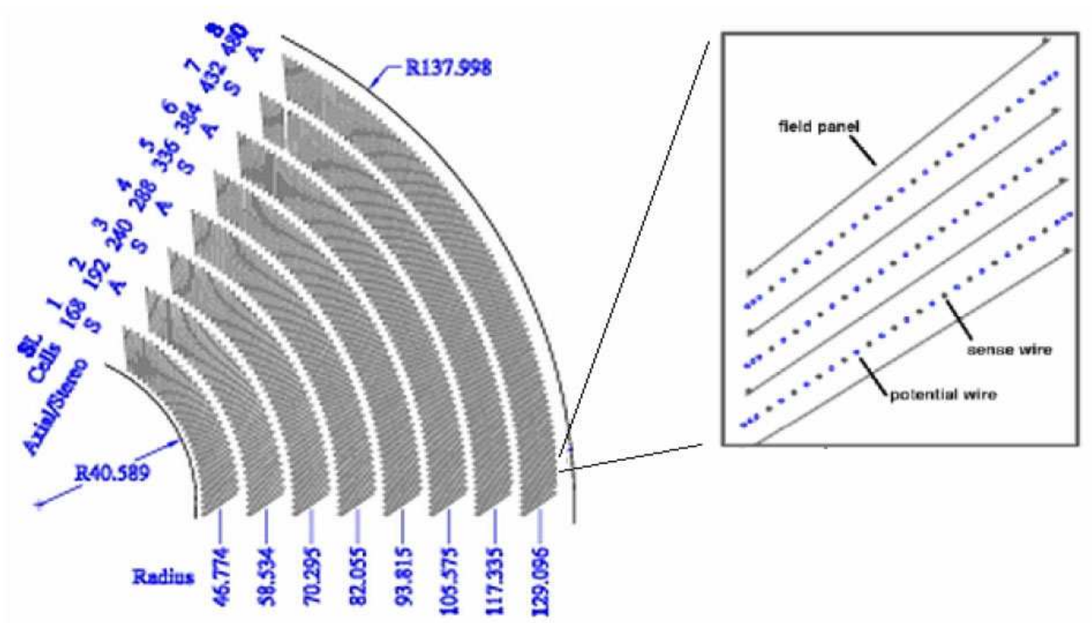

Figure 3.8: COT segment (left). Expanded view showing sense wire configuration (right).

3.2.4 Calorimeters

Calorimeters provide energy and position measurements of electron, photon and hadron showers. They are divided into electromagnetic (EM) and hadronic segments (HA), with EM positioned closer to the interaction region than the HA. Both regions are sampling calorimeters with alternating layers of scintillators and absorbers. Showers generate photons in the scintillators which are collected and carried to Photo-Multiplier Tubes (PMTs) with wavelength shifting optical fibers. Lead is used as the absorber in EM segments and iron in HA segments. The EM segment closest to the interaction region acts as a pre-shower detector useful for photon and π^o discrimination. A shower-maximum detector, placed at about 6 radiation lengths in the EM calorimeter, measures the shower profile and obtains a position measurement with a resolution on the order of a few mm.

Due to detector geometry, calorimeters are divided into a barrel shaped region surrounding the solenoid, the central calorimeters (CPR, CES, CEM and CHA) [24][25]; and calorimeters capping the barrel, the plug calorimeters (PPR, PES, PEM and PHA) [26][27][28]. A wall hadronic calorimeter (WHA) fills the gap between the two. The central region covers detector $|\eta| < 1$, the wall $0.6 < |\eta| < 1.3$, and the plug $1.1 < |\eta| < 3.6$. Each of these regions is further segmented in η and ϕ into towers covering 0.1 x 15^o in the central, 0.1 x 7.5^o in the wall, and 0.16 x 7.5^o or 0.2-0.6 x 15^o in the plug. The energy resolution of the CEM is $\sigma(E)/E = 0.135/\sqrt{E_T\ (GeV)} \pm 0.015$. Figure 3.9 shows a cross-sectional view of the plug calorimeter.

3.2.5 Muon Detectors

Although electrons create showers confined to the calorimeters, the mass of muons makes them nearly minimum ionizing particles (MIPs), and high momentum

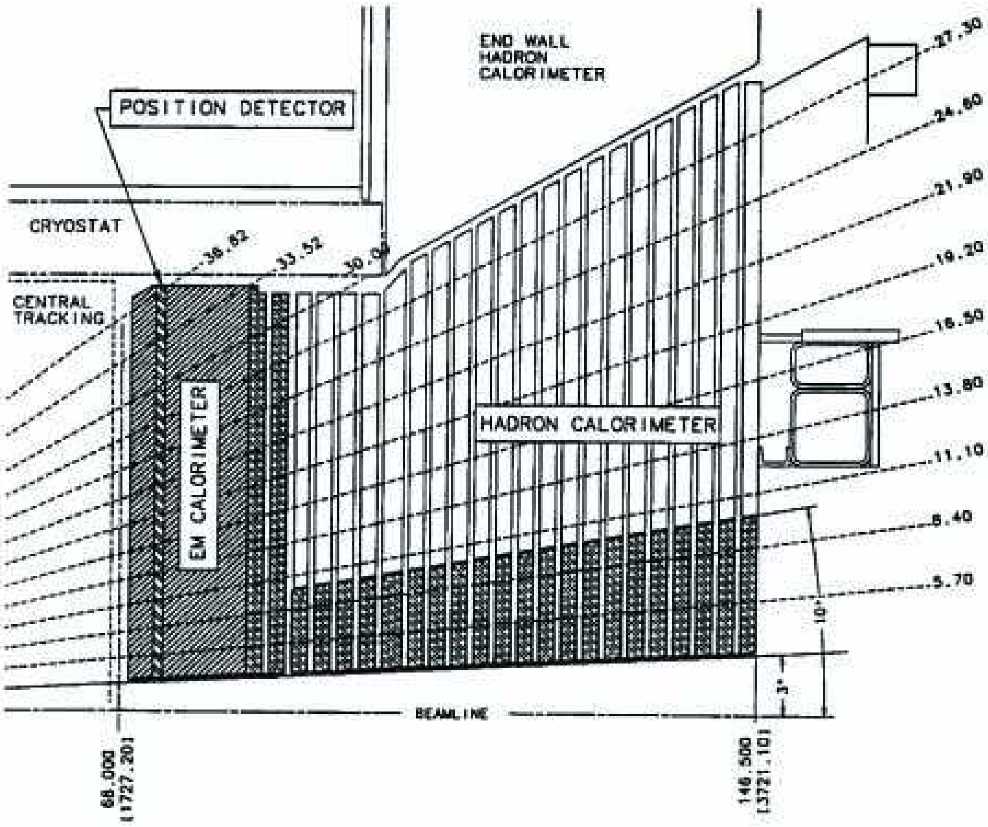

Figure 3.9: Cross-section of upper half of a plug calorimeter.

muons pass though the calorimeters. The calorimeters (and in some cases additional shielding) block the majority of hadronic particles from reaching the outer detector. Drift chambers placed on the outside of the detector identify charged tracks from muons and measure their position. There are three muon detection systems used in this analysis, CMU, CMP and CMX [29]. CMU and CMP cover detector $|\eta| < 0.6$, with CMP located outside CMU, and CMX covers detector $0.6 < |\eta| < 1$.

The CMU chambers surround the central calorimeter in ϕ. They are composed of 4 concentric layers of cells containing argon-ethane gas and high-voltage sense wires parallel to the beam pipe, see Figure 3.10. The CMP chambers are separated from the CMU chambers by 60 cm of steel shielding. They are similar in construction to the CMU chambers, but the layers are successively offset by half of a cell. The CMX chambers are nearly identical to the CMU chambers. They are arranged in four logical layers successively offset by half of a cell. Each logical layer consists of two partially overlapping physical layers of cells. On average, a particle will traverse six cells. Sense wires are independent in the CMP chambers, but are shared between ϕ neighbors in CMU and CMX. The single-hit r-ϕ resolution is 0.25 mm. Measurements in z with a resolution of 1.2 mm are also possible by using differences in arrival times and amplitudes of pulses measured at either end of each wire in neighboring cells.

3.3 CDF Data Acquisition and Triggers

Collisions occur every 396 ns (2.5 MHz), far too quickly even for CDF's custom hardware to process and read out detector information. To reduce the number of collisions for which data is stored, CDF uses information from some detector components to make a decision to save an event, called a trigger. Data is stored

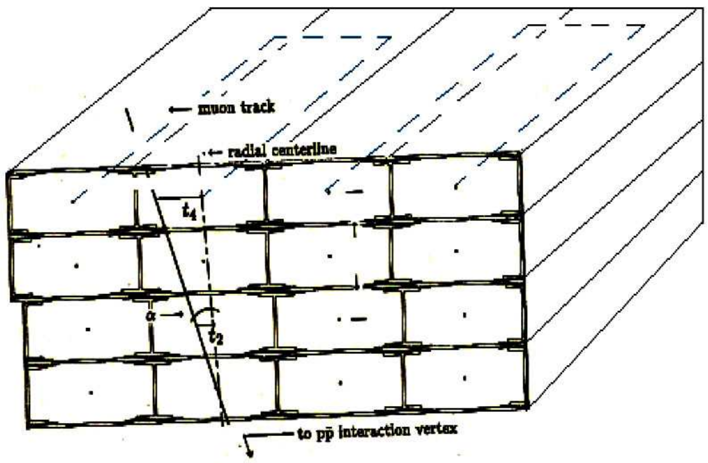

Figure 3.10: Schematic of CMU chamber configuration.

in buffers until trigger decisions cause some of the events to be read out and stored on computer disk or the buffer to be emptied. The trigger is divided into three levels of increasing sophistication in object identification, see Figure 3.11. Chapter 4 describes the specific trigger requirements for this analysis.

Data is stored in synchronous buffers awaiting an initial trigger decision. The first trigger level returns a decision with a latency of 5.5 μs and a maximum accept rate of 50 kHz and will always occur in time to read out the event. Level one uses solely custom hardware operating in three parallel streams. One stream, the eXtremely Fast Tracker (XFT), reconstructs transverse COT tracks and extrapolates them to calorimeters and muon chambers. Another stream detects possible electron, photon or jet candidates, along with total and missing transverse energy. The final stream searches for tracks in muon chambers. These streams are combined in the final level one decision.

After a level one accept, the event information is read out into asynchronous buffers. Since events remain in these buffers until a level two decision is made, it is possible some events passing level one will be lost when these buffers are full. The level two trigger returns a decision with a latency of 25 μs and a maximum accept rate of 300 Hz. Level two uses custom hardware and modified commercial microprocessors to cluster energy in calorimeters and reconstruct tracks in the silicon detector using the Silicon Vertex Tracker (SVT). Calorimeter clusters estimate the total jet energy and help to identify electrons and photons. The SVT measures the impact parameter of tracks, part of locating displaced vertices, see section 4.4.3.

The third trigger level runs on a commercial dual microprocessor farm and returns a decision with a maximum accept rate of 75 Hz. The farm runs a version of CDF offline reconstruction, see Chapter 4, merging information from many detector systems to identify physical objects in the event. Data passing level three trigger requirements is transfered via computer network to a storage facility using a robotic tape library. This data is then processed with offline reconstruction software, see Chapter 4, for use in analysis.

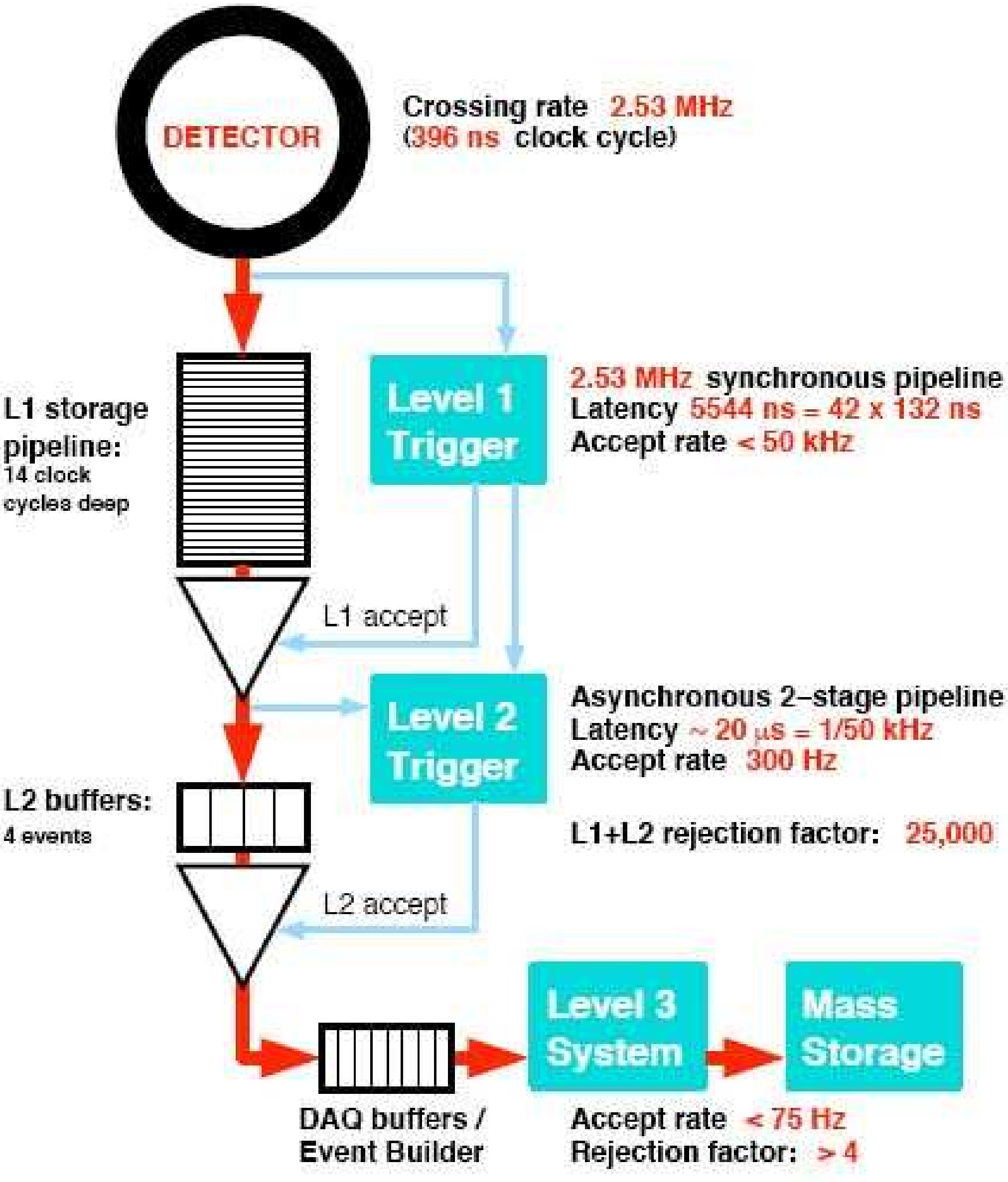

Figure 3.11: Diagram of Run II trigger path at CDF.

CHAPTER 4

Triggers, Reconstruction and Selection

This chapter describes trigger requirements to collect experimental data with the CDF detector, its subsequent offline reconstruction and calibration, and event selection. Simulated data, described in section 5.2, is reconstructed and selected identically to experimental data. Trigger requirements identify potentially interesting hard scattering events in data and cause the detector information to be written to disk. Offline reconstruction software assembles detector information into higher level objects, enabling particle identification and measurement of physical quantities such as momentum. These physical quantities are input to the analysis. Calibrations in offline reconstruction correct for mis-measurement due to instrumentation or physical effects. Final selection requirements are designed to reject possible backgrounds and efficiently retain signal events.

In the lepton + jets decay channel of $t\bar{t}$ pair production, we expect a single energetic charged lepton in the final state from the leptonically decaying W boson, see section 2.2. High momentum electrons and muons are efficiently identified within the detector and are used for this analysis, whereas tau identification is less efficient and not used. Since we expect $t\bar{t}$ pairs to be produced nearly at rest, their decay products are concentrated in central regions of the detector. Central refers to low pseudo-rapidity regions, $|\eta| < 1$. The trigger selects events with energetic central electrons and muons. Electrons and muons follow separate trigger paths and have different identification requirements. Final selection requires an energetic central electron or muon, multiple energetic jets and a neutrino as inferred from large missing transverse energy.

4.1 Tracking

The solenoidal magnetic field bends charged particles in a helical trajectory as they traverse the detector. Hits in the silicon detectors and COT mark the path of these particles, and the reconstruction of this path is known as tracking. Several algorithms using silicon and/or COT information isolate hits from a specific particle and measure its position and momentum by fitting a helical shape to the hits. Tracking information is used to help identify electrons and muons as well as to identify primary and secondary event vertices. This section describes the offline software reconstruction used to identify tracks and their selection for use with this analysis.

4.1.1 Track Reconstruction

Tracks used in this analysis are determined from several possible algorithms. They are generally grouped into categories of similar methodology: OI, OIZ, OIS, IO, COT only and silicon only. Requirements for the silicon detector vary, but those for COT detector are standard: at least 5 hits in at least two axial and two stereo superlayers (unless the track exits the COT in z before the last wire layer, which requires at least 5 hits in at least one stereo superlayer). If both silicon and COT detector information is present, tracks initially formed in the COT and then projected into and compared with hits in the silicon detector are known as “outside-in”, or OI. The OI algorithm requires at least 3 silicon r-ϕ hits. The OI algorithm does not require stereo (z-coordinate) information in the silicon detector. Stereo information is used in the OIZ and OIS algorithms. Tracks initially formed in the silicon detector and projected and compared with COT hits are known as "inside-out" or IO. The IO algorithm places the standard requirement on the COT detector, but does not have requirements on the number of silicon hits. Tracks are also formed using solely silicon (silicon only) or COT detector information (COT only). The COT only algorithm additionally requires the track fit χ^2 to be less than 10. The silicon only algorithm requires at least 5 forward axial hits or 4 central hits and that the track cannot traverse the entire COT volume. Tracks passing algorithms with more stringent requirements are removed from algorithms with less stringent requirements. More information on the algorithms and merging strategy can be found in [30][31].

4.1.2 Primary Vertices

Track vertices are points from which a significant number of tracks originate. Primary vertices are those near the beam line. An algorithm computes the z-position of the vertex using a weighted average of the beam line z-coordinate of tracks passing within 1.0 cm of the beam line. It calculates a χ^2 for all tracks relative to the vertex, removing tracks with $\chi^2 > 10$. The processes iterates until no tracks over the χ^2 threshold are found or no tracks are left. Tracks are required to have silicon and COT detector information and have $p_T \geq 0.5$ GeV/c. The COT must have ≥ 6 hits in at least two axial and two stereo segments. There must be at least three hits in the silicon detector, or more depending on the tracking algorithm. Note that it is possible for the algorithm to return more than one primary vertex per event or to find none. The preferred physics vertex (PPV) is defined as the best vertex for physics use. In the case of this analysis, it is the vertex in closest proximity to the beam line z-coordinate of the track associated with the charged lepton and describes what is expected to be the point of the hard scattering collision between the proton and antiproton.

4.1.3 Lepton Track Selection

Tracks corresponding to energetic electrons or muons in this analysis come from COT tracking based algorithms including silicon information when available. The helical fit to particle trajectory is constrained such that it must originate from the beam line (in the x-y plane). Selection requirements apply only to COT information. Segments having at least 5/12 hits must be formed in at least 3 axial and 3 stereo superlayers. Also, the fitted z coordinate of the track along the beam line must be within 60 cm from the center of the detector. This insures the track is in a region of high tracking efficiency in the COT. Additionally, to remove pions and kaons from muon candidates only, the χ^2 per degree of freedom from the beam constrained fit must be less than 2, and the radius at which the track exits the COT is required to be greater than 140 cm. We require the track associated with the electron or muon to pass within 5.0 cm of a primary vertex at the beam line in the z dimension.

4.2 Electrons

Energetic electrons are identified as electromagnetic showers within the central EM calorimeter corresponding to a high-p_T track. The energy of an electron is measured with the calorimeter, and initial momentum direction is determined from the track.

4.2.1 Electron Trigger

Electron events are collected using a central high-E_T electron trigger. Level 1 requires at least 8 GeV in a calorimeter trigger tower with the ratio of hadronic to electromagnetic energy deposited ($E_{\mathrm{had}}/E_{\mathrm{em}}$) less than 0.125. It also requires an XFT track pointing to this tower with a p_T of at least 8 GeV/c. Level 2 forms a calorimeter cluster by adding adjacent towers to the seed tower found with the level 1 trigger. The adjacent towers must have E_T of at least 7.5 GeV to be included, and the whole cluster must have E_T of at least 16 GeV with $E_{\mathrm{had}}/E_{\mathrm{em}}$ less than 0.125. At this level, the XFT track is confirmed to be pointing to the seed tower. At level 3, an EM cluster is formed and required to have E_T of at least 18 GeV and $E_{\mathrm{had}}/E_{\mathrm{em}}$ less than 0.125. A fully reconstructed COT track with p_T greater than 9 GeV/c must point to the cluster within 8 cm in z.

Trigger accept rates (bandwidth) were approximately 80 Hz, 8 Hz and 1 Hz for levels 1, 2 and 3, respectively. The efficiency of the CEM trigger has be found to be 0.9656 ± 0.0006 [32].

4.2.2 Electron Calorimeter Reconstruction

In the central electromagnetic calorimeter (CEM), electrons are reconstructed as neighboring towers covered by an EM shower. Towers are sorted according to E_T and added to a list of possible seeds if their E_T is greater than 2 GeV. The highest E_T tower is the initial seed. Neighboring towers in η are added to the seed if they have energy greater than 100 MeV (sum of electromagnetic and hadronic calorimeter). All cluster towers are in the same wedge (ϕ-segment). A tower added to a cluster is removed from the possible seed list. Clusters are formed from 1-3 towers. A cluster is also formed in the CES detector by comparing channels with a threshold and attaching neighbors if the threshold is reached. Fitting this cluster with the expected shower profile results in an accurate measurement of the shower position in the calorimeter.

4.2.3 Electron Calibration

Reconstructed electrons are calibrated to remove instrumental effects and to set their absolute energy scale. Instrumental effects include detector edge effects, attenuation, and light loss; and are corrected with test beam data. Some detector effects are time dependent and are corrected by averaging over periods of experimental data. The absolute energy scale is set using $Z \rightarrow e^+e^-$ experimental data: the invariant mass distribution is fit with a Gaussian and tuned to be the precisely known value of 91.18 GeV/c^2 [4].

4.2.4 Electron Identification

An electron is identified as such if it meets the following requirements. An EM cluster is formed with the offline reconstruction software in the CEM region with a maximum of two adjacent towers in detector η. The sum of the cluster E_T must be greater than 20 GeV and the $E_{\mathrm{had}}/E_{\mathrm{em}}$ less than 0.055 + 0.00045 · E, where E is the total energy of the EM cluster. Further, the electron must be isolated, such that after removing the candidate cluster towers, the sum of the E_T within an η-ϕ cone with radius 0.4 around the candidate is less than 10% of the E_T of the candidate. A COT track with p_T more than 10 GeV/c and not consistent with a conversion must point to the most energetic tower. The ratio of the E_T of the cluster (in GeV) over the p_T of the track (in GeV/c) must be less than 2 for clusters with E_T less than 100 GeV. This requirement is not unity to accommodate Bremsstrahlung radiation of the electron. It is removed at high E_T due to imprecision in measuring high p_T tracks. The track is also required to match the position of the EM cluster according to the cluster formed from CES wire hits. The requirements are -3 cm $< q\ \Delta x < 1.5$ cm and $|\Delta z| < 3$ cm, where $\Delta x \equiv r\ \Delta\phi$ and q is the charge in units of e. The $q\ \Delta x$ requirement is asymmetric to account for Bremsstrahlung radiation.

4.3 Muons

Muons have a larger mass than electrons and at high momentum are nearly minimum ionizing particles. They pass though the calorimeters without showering and are detected with drift chambers placed on the outside region of the detector. A muon is identified as a high momentum track corresponding to hits in the drift chambers and energy consistent with a minimum ionizing particle in the calorimeters. The track provides the measurement of muon momenta and energy.

4.3.1 Muon Trigger

Muon events are collected with three triggers CMU, CMP and CMX. The CMU and CMP triggers are merged into a single CMUP trigger. The CMUP trigger covers detector $|\eta| < 0.6$ and the CMX trigger covers $0.6 < |\eta| < 1.0$. At level 1, there must be hits in one or more layers consistent with a charged particle within the CMU or CMX detectors. Additionally, for the CMUP trigger, there must be 3-4 hits in CMP consistent with those in the CMU. Also required is a XFT track matching in the r-ϕ plane of the hits with a p_T of at least 4 GeV/c for CMUP and 8 GeV/c for CMX. Level 2 increases the p_T requirement of the XFT track to 15 GeV/c for both CMUP and CMX triggers. At level 3, muon stubs and COT tracks have been reconstructed, and a COT track with p_T of at least 18 GeV/c is required to match the muon stub in the r-ϕ plane within 10 cm in the CMU and 20 cm in the CMP or within 10 cm of the CMX.

Trigger accept rates (bandwidth) for CMUP were approximately 90 Hz, 9 Hz and 0.4 Hz for levels 1, 2 and 3, respectively. Those for the CMX trigger were approximately 9 Hz, 7 Hz and 0.25 Hz. The efficiency of the CMUP trigger has be found to be 0.887 ± 0.007 and that of CMX to be 0.954 ± 0.006 [32].

4.3.2 Muon Stub Reconstruction

Muons are reconstructed in the CMU, CMP and CMX muon detectors as stubs, or a set of hits consistent with particle trajectory. This requires hits in 3 to 4 out of the 4 layers of the muon chambers. The hits are fit to a straight line, from which a position and direction can be determined.

4.3.3 Muon Calibration

Since particle four momenta is measured from the track associated with the muon, the relevant calibrations are those applied to tracks, specifically curvature corrections affecting the p_T measurement. Calibrations also include the relative alignment within and between the silicon and COT tracking systems. The absolute energy scale is set using $Z \to \mu^+\mu^-$ experimental data: the invariant mass distribution is fit with a Gaussian and tuned to be the precisely known value of 91.18 GeV/c^2 [4].

4.3.4 Muon Identification

A muon is identified as such if it meets the following requirements. Stubs formed from hits in the CMU, CMP and CMX detectors are formed with the offline reconstruction software. The position of these stubs in r-ϕ space must match a COT track with p_T greater than 20 GeV/c extrapolated to the position of the stub within 3 cm for the CMU, 5 cm for the CMP and 6 cm for the CMX. Note that these sizes are mostly determined by the effects of multiple scattering rather than detector position resolution. Further, calorimeter energy in towers corresponding to extrapolated track trajectory must be consistent with with that of minimum ionizing particles – a maximum energy on the order of a few GeV depending on track p_T. Muons also have isolation requirements where the sum of the E_T (in GeV) deposited in the calorimeters within an η-ϕ cone of radius 0.4 must be less than 10% of the p_T (in GeV/c) of the muon candidate.

4.4 Jets

Quark and gluon fragmentation and radiation create showers of particles in the detector known as jets. Jets deposit broad distributions of energy in the electromagnetic and hadronic calorimeters. Reconstructed jets are clustered energy depositions and generally provide less precise measurements of the originating quark or gluon than reconstructed charged leptons. The large multiplicity of possible decays and their non-perturbative nature make it impossible to exactly reconstruct the originating quark or gluon from a jet. Notably, the measured energy of a reconstructed jet maps to the originating parton with a significantly broad resolution. Energy calibrations are determined on average and introduce significant uncertainty in analyses.

4.4.1 Jet Reconstruction

Jets are reconstructed as energy depositions in calorimeter towers. Towers are clustered using the JETCLU algorithm, and are included if they measure $E_T > 1$

GeV, unless the tower corresponds to an electron. The jets used in this analysis have been reconstructed after the final selection of the lepton in the event, and are clustered accordingly. Towers are merged in an η-ϕ cone of radius $R < 0.4$ to form a proto-jet described by

$$\begin{aligned} E_T^{\text{jet}} &= \sum_{i=0}^{N\text{tow}} E_{Ti} \\ \phi^{\text{jet}} &= \sum_{i=0}^{N\text{tow}} \frac{E_{Ti}\phi_i}{E_T^{\text{jet}}} \\ \eta^{\text{jet}} &= \sum_{i=0}^{N\text{tow}} \frac{E_{Ti}\eta_i}{E_T^{\text{jet}}}. \end{aligned} \tag{4.1}$$

Note there is appropriate handling of the 2π boundary in ϕ. This process is run iteratively, dropping and adding towers, and the variables recalculated until the geometrical center of a tower corresponds to the cluster centroid [33]. After reaching this stable point, jets overlapping by more than 50% in η-ϕ space are merged. If overlap is less than this amount, then towers are assigned to the closest jet. Once all the towers have been assigned to jets, the four-momentum and other components of the jet are calculated by summing the information from the towers similarly to Equation 4.1.

4.4.2 Jet Energy Corrections

Compared to electrons and muons, jets are very complicated objects. Various instrumental, algorithm and physics effects combine to make determining the underlying particle energy from a jet uncertain. Calibrating the jet energies and determining their uncertainty is the charge of the Jet Energy and Resolution group at CDF [33]. Corrections to jet energies are derived from studies using both experimental and simulated data.

The hadronic and electromagnetic calorimeters are calibrated before forming

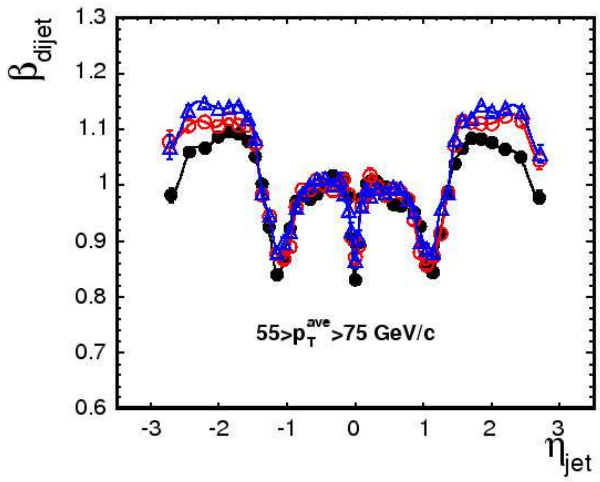

Figure 4.1: Example of dijet balancing in relative jet energy corrections as a function of jet detector η, with $\beta \equiv p_T^{\text{probe}}/p_T^{\text{trigger}}$. Jets have average p_T between 55 and 75 GeV/c.

jets or determining any corrections. Electromagnetic calorimeters are calibrated using electrons as described in section 4.2.3. Hadronic calibrations are initially set using a test beam of 50 GeV/c charged pions. The CHA and WHA calorimeters are further calibrated with a laser system, a Cs^{137} radioactive source system, muons from events containing $J/\psi \rightarrow \mu^+\mu^-$, and minimum bias experimental data. The PEM and PHA calorimeters are calibrated with a laser system and a Co^{60} radioactive source system. The energy loss from muons coming from $W \rightarrow \mu\nu$ events are used to verify the stability of the calibrations over time.

Jet energy corrections are derived and applied in five separate levels: relative, multiple interactions, absolute, underlying event, and out of cone. These corrections are applied in the order listed. After absolute corrections, jets should be independent from instrumental effects.

Relative corrections equilibrate the response of the calorimeter as a function of detector η. This dependence arises because of the physical separation of the two central calorimeter components at $\eta = 0$, the separation of the central and plug calorimeters at $\eta = 1.1$, and the non-uniform response between central and plug calorimeters. Corrections are derived from balancing the p_T between a trigger jet and a probe jet in events with two jets and no additional hard QCD radiation, see Figure 4.1.

Since we are dealing with $p\bar{p}$ collisions, more than one inelastic collision is possible in a given bunch crossing. This is known as multiple interactions. It is unlikely to have two hard scattering processes in a single crossing, but the energy from the second scattering contributes to the energy deposited in the calorimeters and therefore in the jet cone. To keep from biasing the measurement, the average energy from secondary collisions is subtracted from the hard scattering process. This amount depends on the instantaneous luminosity and therefore the number of reconstructed vertices. On average, the correction is 0.36 GeV per jet per additional interaction, or 1% of the energy of the average jet. This correction is derived from minimum bias experimental data by studying the average transverse energy deposited in a jet cone as a function of the number of reconstructed vertices.

The absolute energy correction attempts to map the energy measured in the calorimeter back to that of the particles creating the jet. For this reason, corrections are independent of the CDF detector to first order after this point. Note that this correction does depend on the particle causing the shower: quark showers are different than gluon showers. Since there is no way to *a priori* determine if the shower was caused by a quark or a gluon, the effects are averaged. This correction also averages the effects of particle species and momentum inside of a jet. Electromagnetic particles have a linear calorimeter response, while hadronically

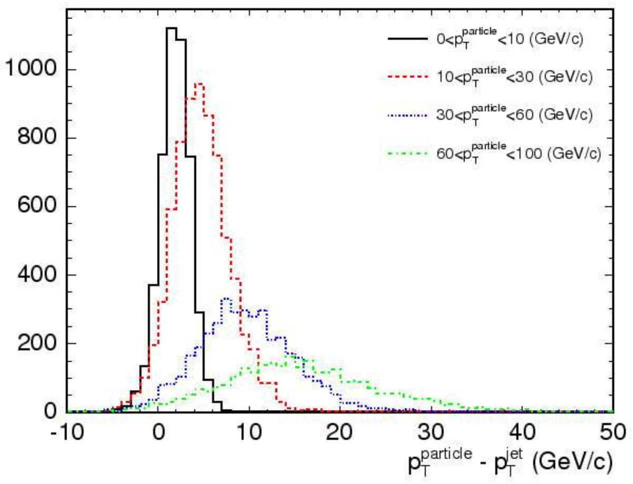

Figure 4.2: Distribution of $\Delta p_T \equiv p_T^{\text{particle}} - p_T^{\text{jet}}$ offsets used in absolute jet energy correction for different bins of p_T^{particle}.

interacting particles have a non-linear response depending on p_T. This correction is derived using simulated data with two jets in an event by comparing the p_T of particle jets and reconstructed jets, see Figure 4.2, and depends on the accuracy of the modeling of the transformation of particle jets into reconstructed jets.

The final two corrections, underlying event and out-of-cone, are not used in this analysis because they depend on the underlying hard scattering process. They are intended to finish mapping jet energy to parton level. Rather than using a generic correction averaging over all possible data, we use a mapping specific to $t\bar{t}$ production, see Chapter 7. Described here for completeness, the underlying event correction averages out effects from initial state radiation and/or spectator partons with color connection to the other partons of the proton. The out-of-cone correction averages the effects of final state radiation at large angles, particles exiting the cone due to fragmentation, and low p_T particles. As with the absolute energy corrections, these corrections are determined using simulated

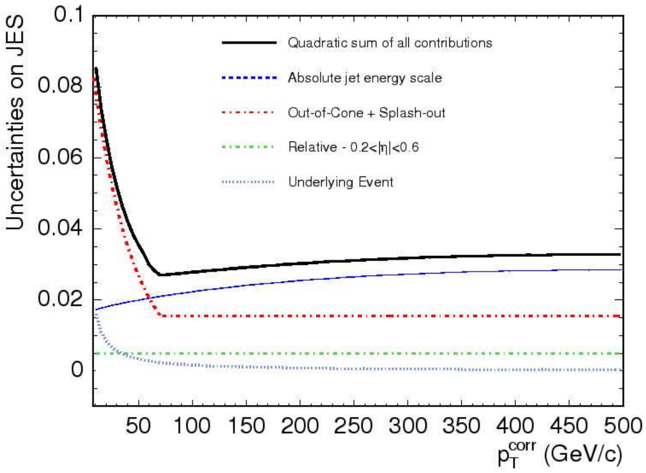

Figure 4.3: Relative contributions to uncertainty of jet energy scale corrections.

data events with two jets. They are solely determined from simulation at particle generator level and not dependent on the CDF detector.

In the process of determining corrections to the jet energy scale, the JER group also estimates the uncertainty for each correction. Figure 4.3 shows these uncertainties as a function of jet p_T. Uncertainty on corrections to the jet energy scale are a source of systematic uncertainty in mass measurements. This analysis measures the jet energy scale, see Section 6.1. The uncertainty from this measurement is a statistical uncertainty, but represents most of the systematic uncertainty due to jet energy scale uncertainty. Additional systematic uncertainty, for effects such as the dependence of the jet energy scale uncertainty on jet p_T and η, is discussed in Section 9.1.

4.4.3 Secondary Vertex Tagging of Jets (b-tags)

Hadrons containing b quarks are unusual in that they have long lifetimes and will travel a significant distance from the interaction point before decaying, creating a secondary vertex. Those from top quark decay are highly boosted and will travel a few millimeters from the interaction point. These secondary vertices are identified in jets with E_T greater than 15 GeV [34]. All SVX tracks with $p_T > 0.5$ GeV/c and within an η-ϕ cone of radius 0.4 of the jet center are considered for vertex determination. A secondary vertex is formed by one of two methods, collectively known as the "SecVtx" algorithm. The first algorithm ranks tracks according to p_T and quality and then determines the two best tracks coming from a single vertex. This vertex is then used as a seed for comparison with other tracks in the jet. A third track must be associated with the vertex. If a third track is not found, the algorithm selects the next two best tracks and continues until no tracks are left. If the first algorithm fails to find a vertex, the second algorithm is run. It identifies secondary vertices similarly to the algorithm identifying primary vertices and requires at least two tracks to pass the χ^2 cut. Vertices consistent with long-lived neutral particles (K_s^o and Λ) are removed. If the the distance in r-ϕ space between primary and secondary vertices (L_{xy}) is greater than 7.5 times its uncertainty (σ_{Lxy}), the secondary vertex is considered tagged. This is considered as positive identification of a jet produced from a b quark, a "b-tag."

4.5 Missing Transverse Energy

Since the CDF detector is essentially in the center of mass frame of the $p\bar{p}$ collisions, we expect the energy deposited in the detector to balance in the transverse dimensions, satisfying energy conservation. Energy in the z-dimension is difficult to measure because of loss of particles down the beam pipe. The extent to which the energy is unbalanced is known as the missing transverse energy ($\not{E}_T$). Neutrinos escape the detector without detection and are often indicated by a significant amount of $\not\!\!E_T$. Missing transverse energy is defined as the magnitude of the vector formed by the negative sum over calorimeter towers with $|\eta| < 3.6$:

$$\vec{\not\!\!E}_T = -\sum_i E_T^i \hat{n}_i, \tag{4.2}$$

where $\hat{n}_i$ is a unit vector perpendicular to the beam axis pointing at tower i. The sum is adjusted for jets with detector $|\eta| < 2.4$ and energy greater than 8 GeV after multiple interaction correction. In muon events, the $\vec{p}_T$ of the track associated with the muon is also included in the sum.

4.6 Event Selection

Event selection mirrors the expected final state particles of $t\bar{t}$ decay into the lepton plus jets channel, see section 2.2. Basic selection requires: a single CEM electron, CMUP muon or CMX muon; exactly four jets with $|\eta| < 2$ and $E_T > 15$ GeV after the multiple interactions correction; at least one of these jets identified with a secondary vertex; missing transverse energy in excess of 20 GeV; and the event to pass a non-W veto. The non-W veto is designed to remove events consistent with the non-W (QCD) background, see section 5.3. Events are removed if they have $\not\!\!E_T < 30$ GeV and the angle, $\Delta\phi$, between transverse charged lepton momentum, $\vec{p}_T$, and $\vec{\not\!\!E}_T$ is $\Delta\phi < 0.5$ or $\Delta\phi > 2.5$. See Table 4.1 for a summary and description of basic event selection.

Further selection removes dilepton decay channel candidates and other backgrounds. Events with two leptons passing dilepton selection requirements [35] are vetoed. Also, to remove Z bosons from the sample, the single charged lepton is required not to form an invariant mass, M, with a second object within a window of $76 < M < 106$ GeV/c^2. In the case of an electron event, the second object is either an isolated electromagnetic object (for instance another electron), a jet

Table 4.1: Summary of Basic Event Selection

lepton	tight CEM, CMUP or CMX
jets	Level 4 $E_T > 15$ GeV, $\eta < 2.0$
secondary vertex	$N_{\text{jets}} \geq 1$
missing transverse energy	$\not{E}_T > 20$ GeV
non-W veto	$0.5 < \Delta\phi < 2.5$ for $\not{E}_T < 30$ GeV

with $E_{\text{had}}/E_{\text{em}} < 0.05$, or an oppositely signed single track. In the case of a muon event, the second object is either another isolated muon or an oppositely signed track. A cosmic ray veto removes virtually all cosmic muons from events by comparing timing information in the COT to the beam crossing and by identifying tracks consistent with particles entering and exiting the detector. Electrons from photon conversions are removed by searching for tracks with opposite curvature that extrapolate to an origin within 0.2 cm in the r-ϕ plane and a difference in angle of less than 0.04 radians at closest approach.

Some additional selection applies to experimental data only. Experimental data taken after the first 333 pb^{-1} integrated luminosity have additional regions of the CMX detector activated: the keystone and miniskirt regions. These regions expand the η and ϕ coverage of the CMX detector, but are not modeled in the simulated data used for this analysis. To keep the experimental data consistent with simulation, events with a muon in either of these regions are removed. Note that events are still vetoed if this muon is part of a dilepton pair to keep our top quark dataset statistically independent from the dataset used to measure the mass in the dilepton decay channel.

CHAPTER 5

Experimental and Simulated Data Collections

This analysis uses 955 pb^{-1} total integrated luminosity collected from the beginning of Run II to February 2006. Before the measurement is made with this data, large amounts of simulated data are used to test the analysis for bias and to model some parameters in the analysis. Simulated events are generated with Monte Carlo event generators and passed though detector simulation and full event reconstruction. Comparisons between simulated data and experimental data show that simulated data is in good agreement with experimental data.

5.1 Experimental Data

Experimental data was collected in three periods with the CDF detector, as described in section 3.2, using triggers and selection as described in Chapter 4. The first period covers February 2002 to August 2004, the second from December 2004 to September 2005, and the third from September 2005 to February 2006. Integrated luminosities for these periods are 333 pb^{-1}, 362 pb^{-1} and 260 pb^{-1}, respectively, for a total of 955 pb^{-1}. They are labeled *0d*, *0h* and *0i* datasets. Data was collected separately for electrons and muons for each of these periods. All of the datasets are combined for the final measurement.

We compare the consistency of kinematic distributions in the three datasets separately for electrons and muons. Events pass nominal selection criteria, except that we accept all events with at least one jet, rather than exactly four jets, to increase the statistics of the samples. Jets are corrected with absolute corrections, see section 4.4.2. The distributions are jet multiplicity, lepton p_T, missing transverse energy (MET), jet E_T, and secondary vertex tagged (b-tagged) jet E_T. The *0d* dataset is used as a reference in comparison with distributions from the *0h* dataset, see Figure 5.1, and the *0i* dataset, see Figure 5.2. Variable bin sizes are used to increase the statistics of bins in the tails of some distributions, and the histograms of the *0h* and *0i* datasets are scaled such that they have an equivalent integral to the *0d* dataset. Figure 5.3 and Figure 5.4 show the ratio of the bin contents of the *0h* and *0i* to the *0d* dataset, respectively. Since the histograms are scaled to have equivalent integral, the expected value for all bin ratios is unity. Good agreement between datasets is observed within statistics in all variables.

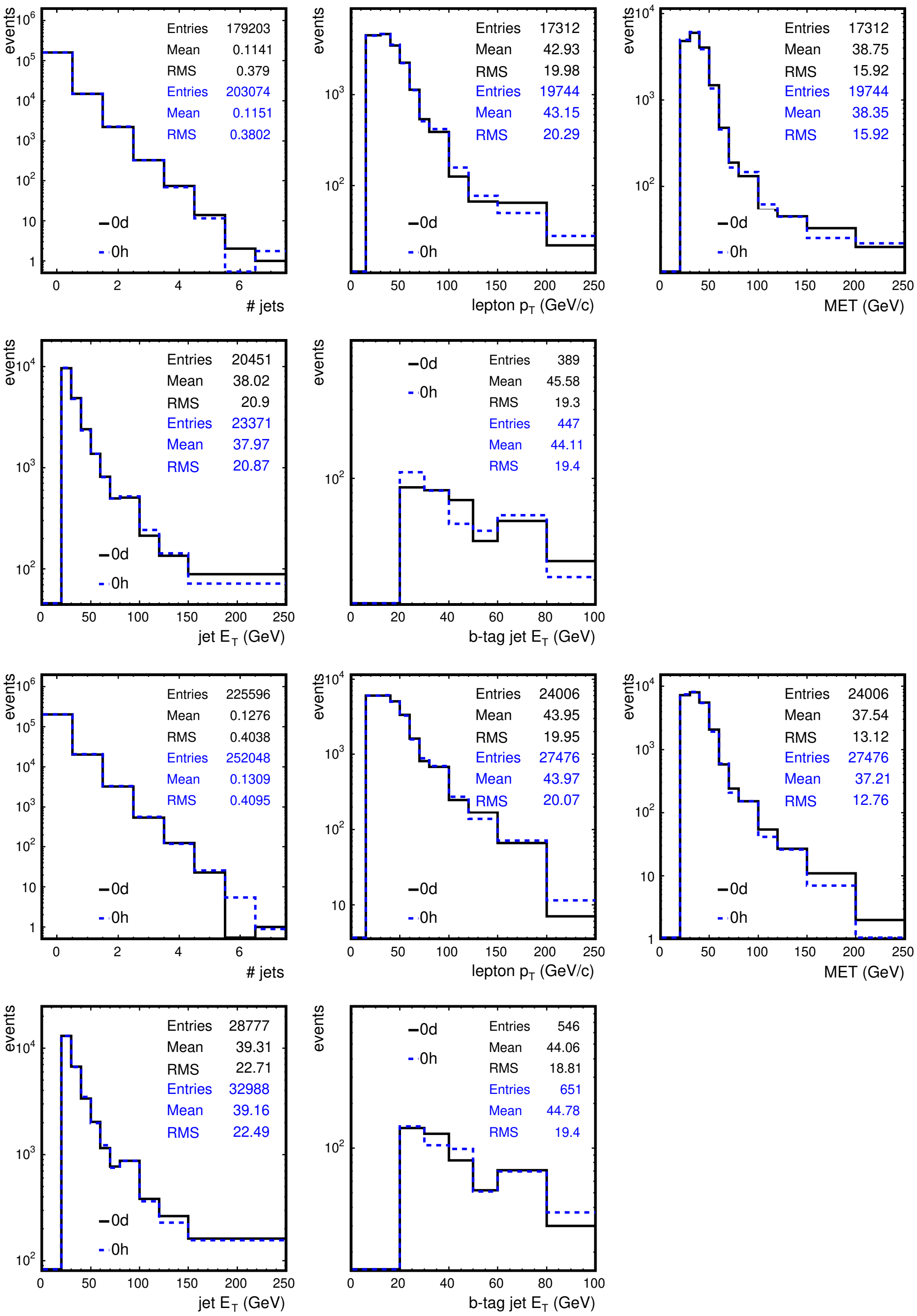

Figure 5.1: Distributions of select kinematic variables in *0d* and *0h* datasets in the muon (top) and electron (bottom) channel.

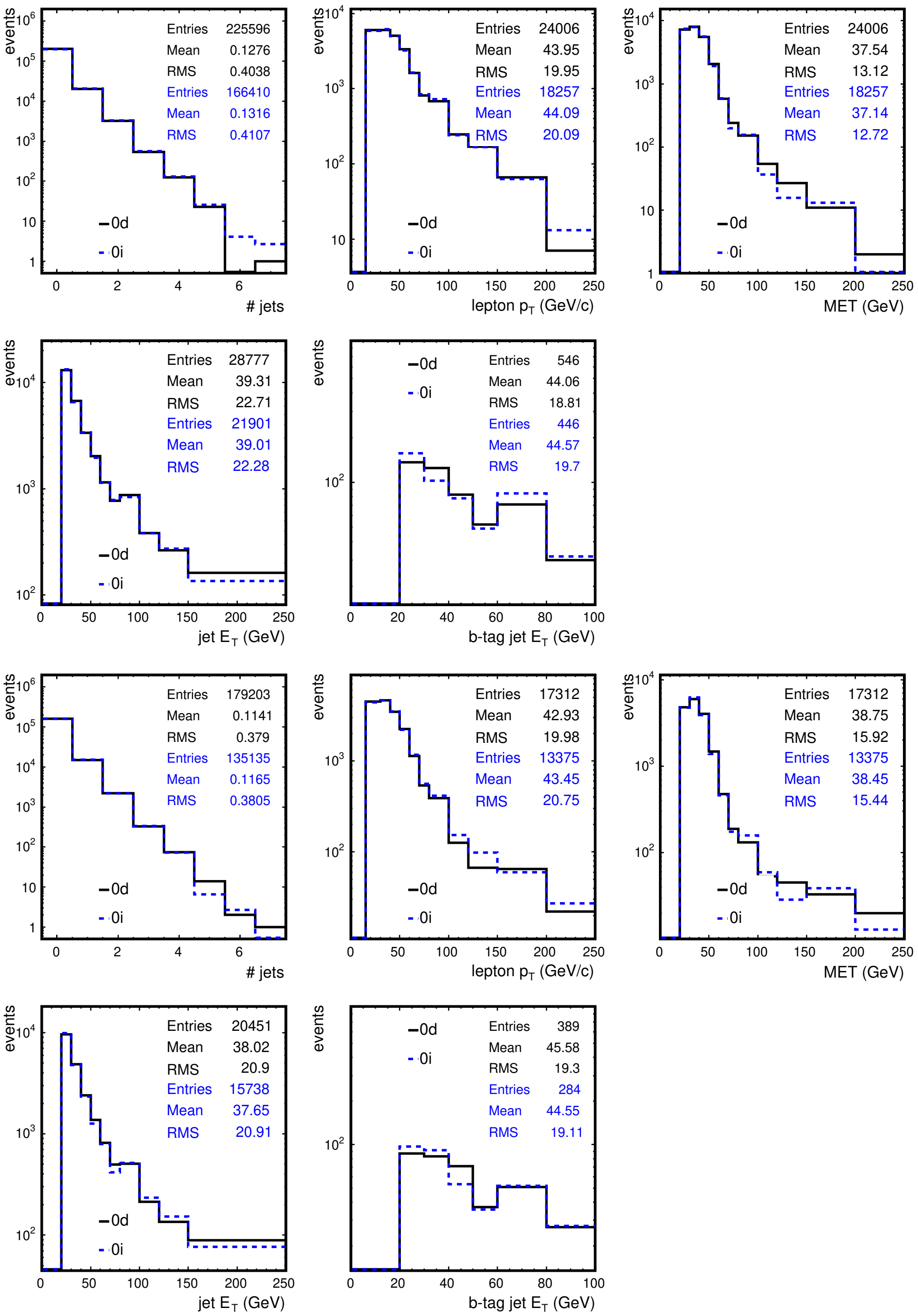

Figure 5.2: Distributions of select kinematic variables in *0d* and *0i* datasets in the muon (top) and electron (bottom) channel.

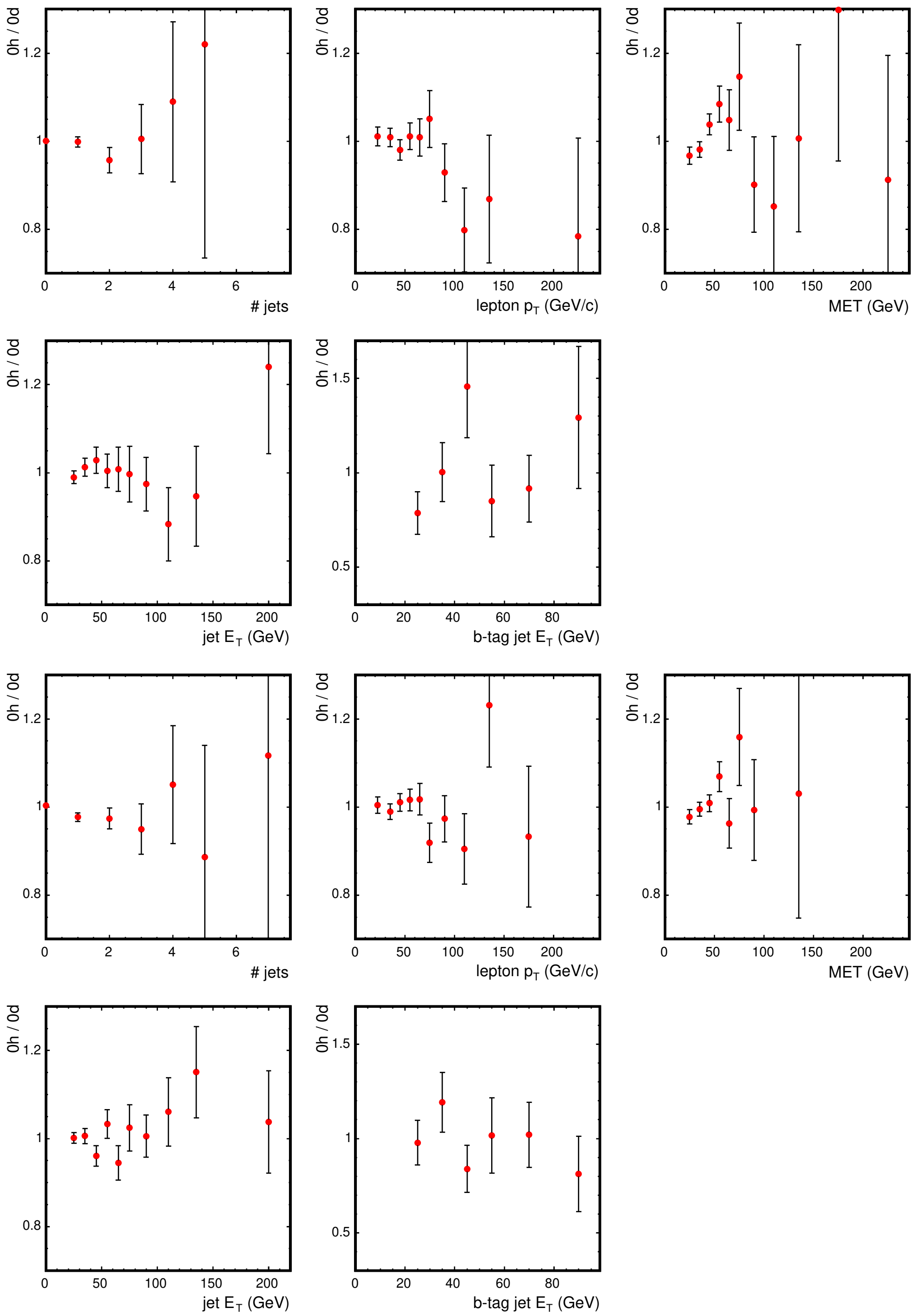

Figure 5.3: Ratios of *0h* to *0d* distributions of select kinematic variables in the muon (top) and electron (bottom) channel.

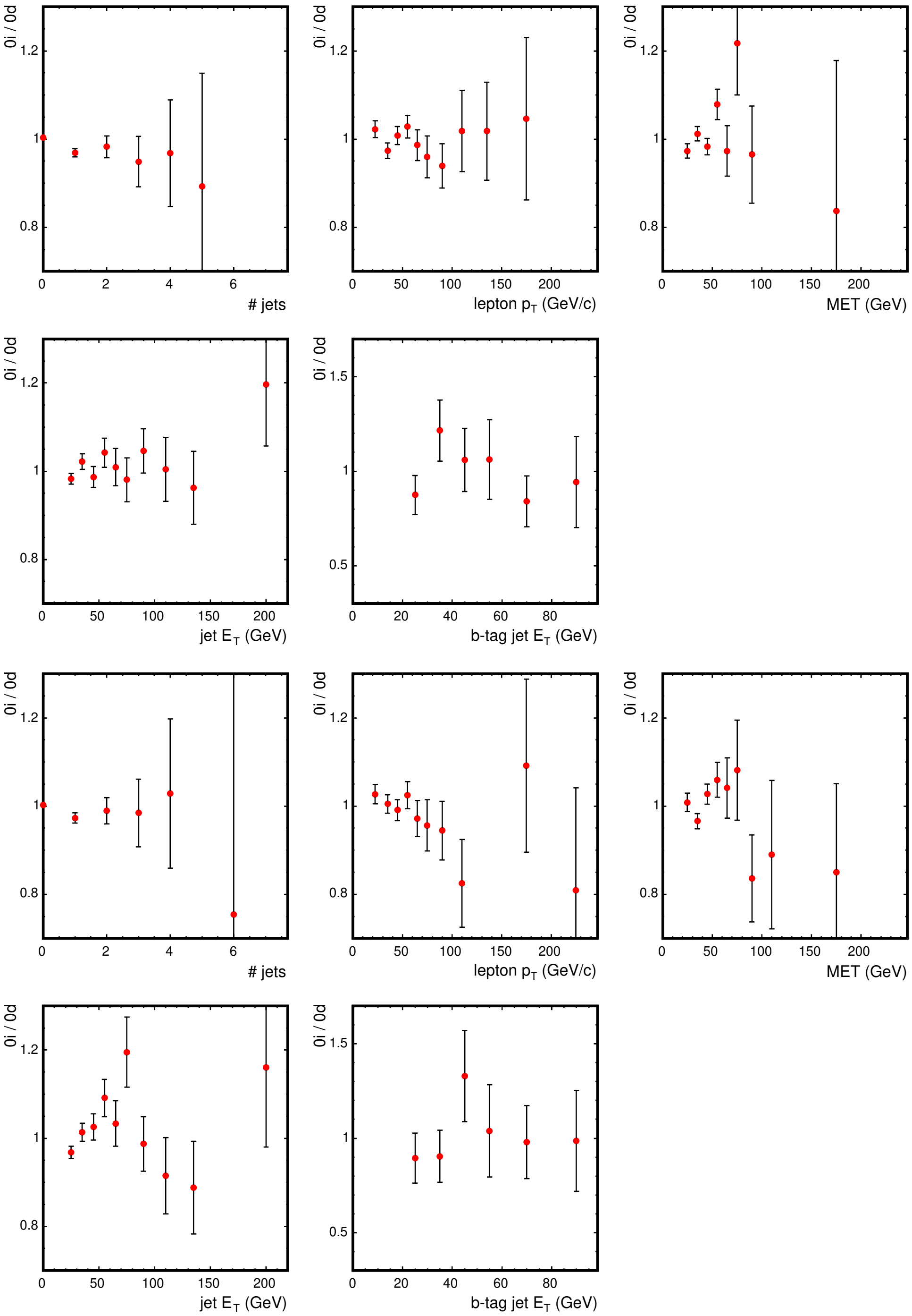

Figure 5.4: Ratios of *0i* to *0d* distributions of select kinematic variables in the muon (top) and electron (bottom) channel.

Because the mass of the hadronically decaying W boson is important to this analysis, we also compare distributions of the invariant mass formed from two jets in events with exactly two jets passing selection. These events do not overlap with the events used in the measurement. The distributions are comparable between the three datasets in electron, muon and combined channels, see Figure 5.5.

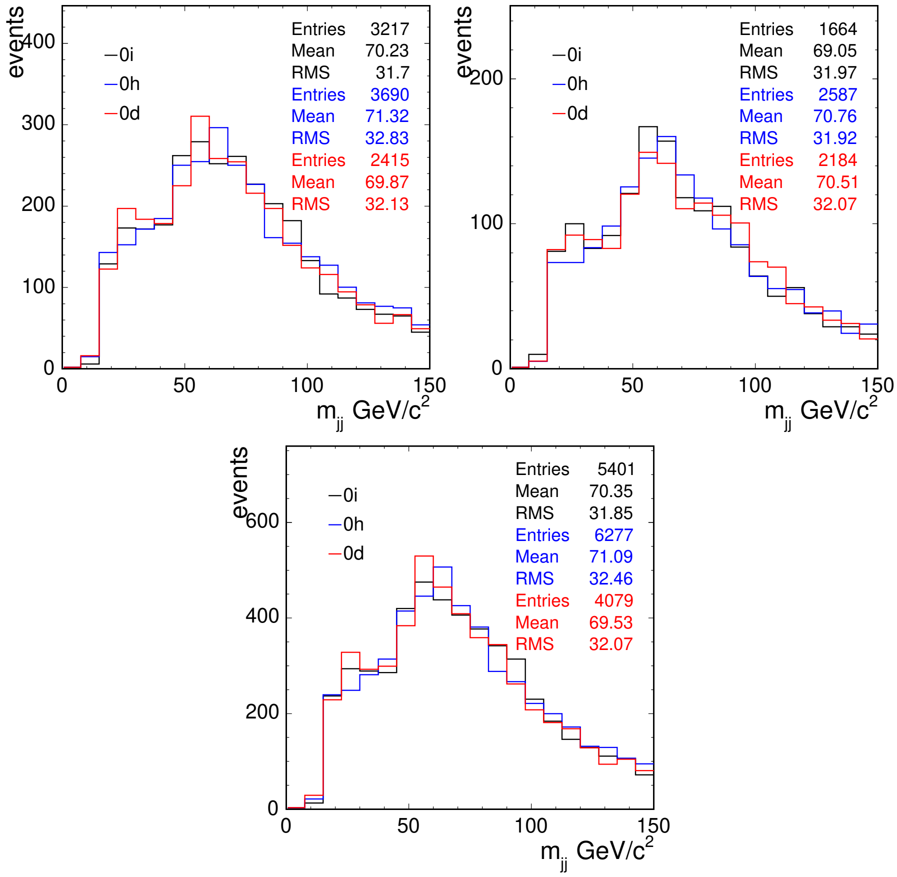

Figure 5.5: Invariant mass of 2 jets in the electron sample (top right), muon sample (top left), and combined sample (bottom).

5.2 Simulated Data

Simulated data is used for many purposes in this analysis: to derive the acceptance as a function of top mass and jet energy scale, section 6.1.2; to model the jet energy resolution, Chapter 7; and to test the method, section 8.1. Simulated events are generated with Monte Carlo event generators. Simulation of $t\bar{t}$ pair production uses `HERWIG` v6.5 [36] and `PYTHIA` v6.2 [37] event generators. They both use leading-order matrix elements to generate the QCD hard scatter interaction. They shower partons, simulating QCD radiation and fragmentation and use `CTEQ5L` parton distribution functions [38]. Note that `PYTHIA` and `HERWIG` independently calculate matrix elements and model hadronization. `PYTHIA` does not include spin-correlations, whereas `HERWIG` does. Heavy flavor jets, those with b and c hadrons, use the decay algorithm `QQ` v9.1 [39]. The dominant background, W + jets events, are generated with `ALPGEN` v1 [40], a leading-order matrix element generator capable of final states with a large number of jets. `HERWIG` and `QQ` shower events after generation with `ALPGEN`.

Detector response is simulated for events generated with Monte Carlo. The geometry and composition of the CDF detector is input to the `GEANT` 3 [41] software package, which provides the framework for detector simulation, including tracking, physical modeling and hits in detector components. Some components have separate software interfaced with `GEANT`. Charge deposition in the silicon detectors is modeled using a calculation based on the path length of the ionizing particle and an unrestricted Landau distribution. Drift times in the COT are simulated with the `GARFIELD` package [42] with parameters tuned to match experimental data. Showers in calorimeters are simulated with `GFLASH` [43], which is tuned with electron and pion test beam data.

Simulated data is generated using some parameters from experimental data.

These include the position of the beamline relative to the detector and the instantaneous luminosity for each run of experimental data taking. At the time of this analysis, simulated events correspond only to the *0d* dataset. Significant differences in these parameters in the *0h* and *0i* datasets include additional η-ϕ coverage in the CMX detector and an increase in average instantaneous luminosity per run.

Since simulated events are used to calibrate and test this analysis, we desire experimental and simulated data to be as similar as possible. As discussed in section 4.6, the effects of increased coverage in CMX muon detectors are removed with additional selection in experimental data. It is not straightforward to adjust for increasing instantaneous luminosity, so we study this effect in simulated events specifically generated for this purpose. Increased instantaneous luminosity results in increased multiple interactions per event. Jets are corrected on average for the relevant effects and the charged lepton is relatively insensitive. Increased multiple interactions also increase the number of tracks in the silicon tracking system, thereby reducing the efficiency of locating secondary vertices and increasing the possibility of improperly reconstructed secondary vertices. Possible effects due to improperly reconstructed vertices on the likelihood are considered in section 8.1.2.2, and systematic effects are discussed in section 9.9 and 9.10.4.

The number of primary vertices reconstructed in an event is directly related to the number of multiple interactions. Figure 5.6 shows the number of vertices in the *0d*, *0h*, and *0i* datasets in the electron, muon and combined channels. Events pass nominal selection, except that we require at least one jet, rather than four, to increase statistics. The dataset with highest average instantaneous luminosity has roughly a 10% increase in the average number of vertices. We also examine the events used in the measurement, with exactly four jets passing selection, in

Figure 5.7. These distributions suffer from low statistics, and we do not attempt to draw any conclusions from them.

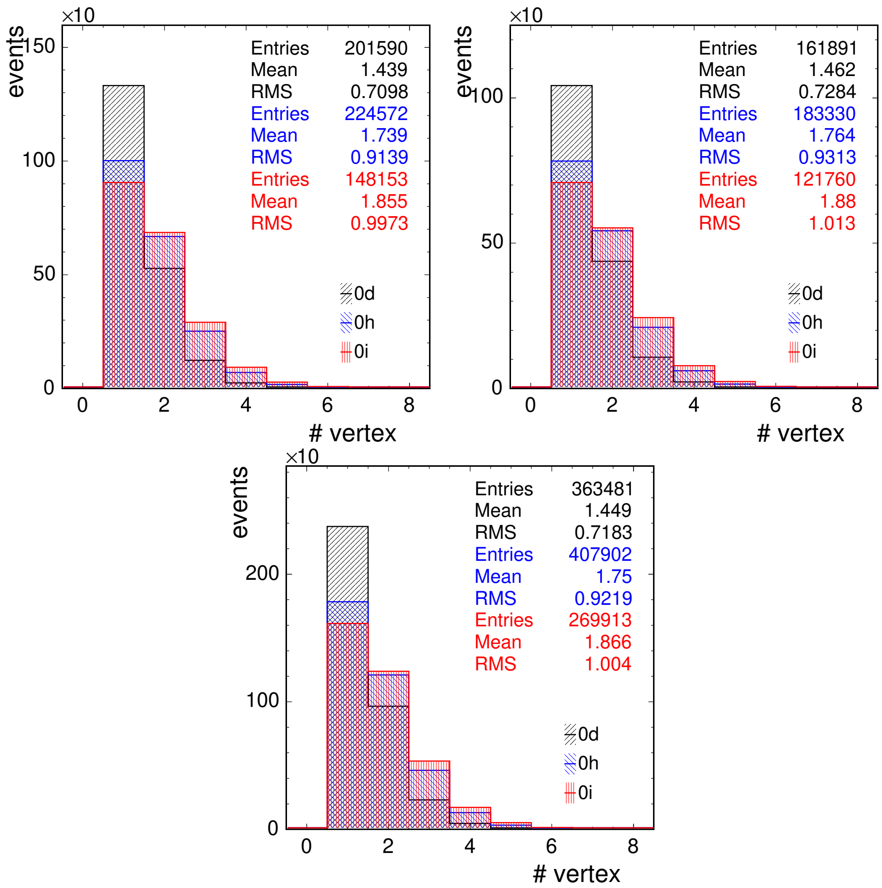

Figure 5.6: Distributions of number of primary event vertices reconstructed in experimental data: electrons (top right), muons (top left), and combined (bottom). We require nominal selection with *one or more* jets in the events.

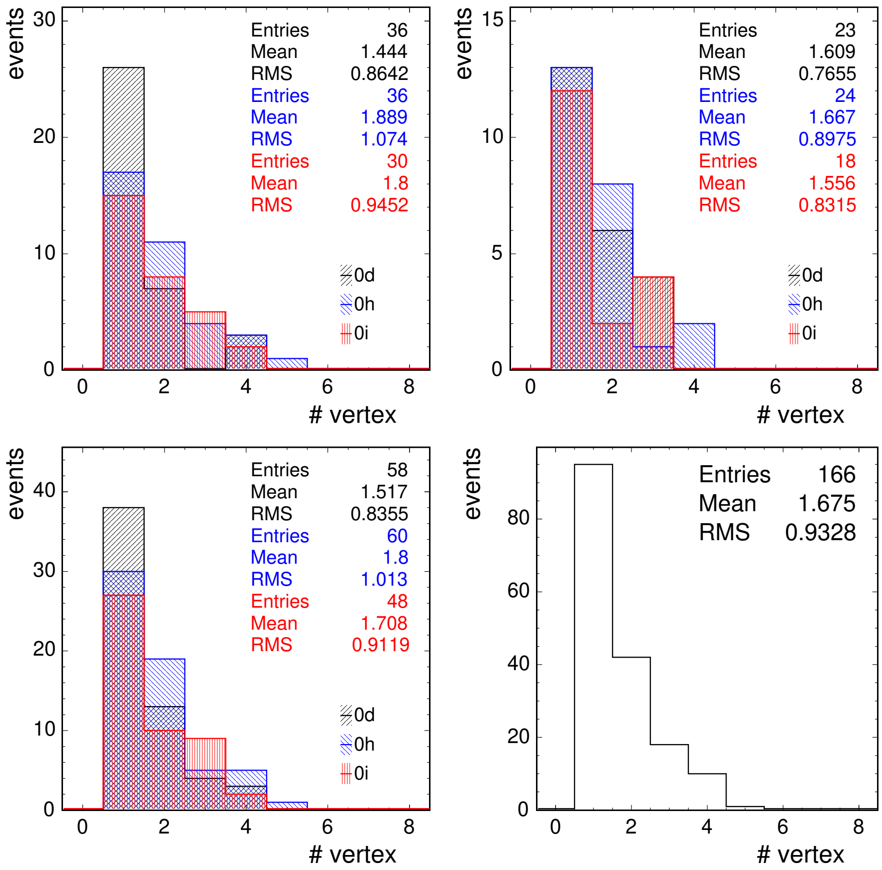

Figure 5.7: Distributions of number of primary event vertices reconstructed in experimental data: electrons (top right), muons (top left), combined electron and muons (bottom left), and all the datasets combined (bottom right). We require nominal selection with *exactly four* jets in the events.

To study the effect of increased number of primary vertices we use simulated $t\bar{t}$ events generated at 50, 100, 150, 200, 250 and 300 x 10^{30} cm^{-2} s^{-1} instantaneous luminosity. Figure 5.8 shows the distribution of the number of vertices in this sample and the average number of vertices as a function of the instantaneous luminosity. A linear fit to the later returns the expected y-intercept (p_0) of one vertex at zero luminosity within uncertainty. The fraction of events passing various selection requirements as a function of number of vertices is shown in Figure 5.9. The stages of selection requirements are progressively inclusive and labeled "tight lepton," requiring a single tight CEM, CMUP or CMX lepton; "lepton + MET," additionally requiring $\not\!\!E_T > 20$ GeV; "pretag," additionally requiring all other selection criteria excluding secondary vertex criteria; "single tag," additionally requiring a secondary vertex tag in at least one jet; and "double tag," requiring a secondary vertex tag in at least two jets. The effects of secondary vertex identification efficiency loss with increasing luminosity are apparent in the decrease in selection efficiency in the single and double tag samples. The loss in efficiency is nearly independent of jet E_T and detector η-position. Although this change varies by up to 20%, the actual variation in the number of reconstructed vertices between simulated data, 1.00, and experimental data, mean of 1.68, does not result in a significant change in acceptance.

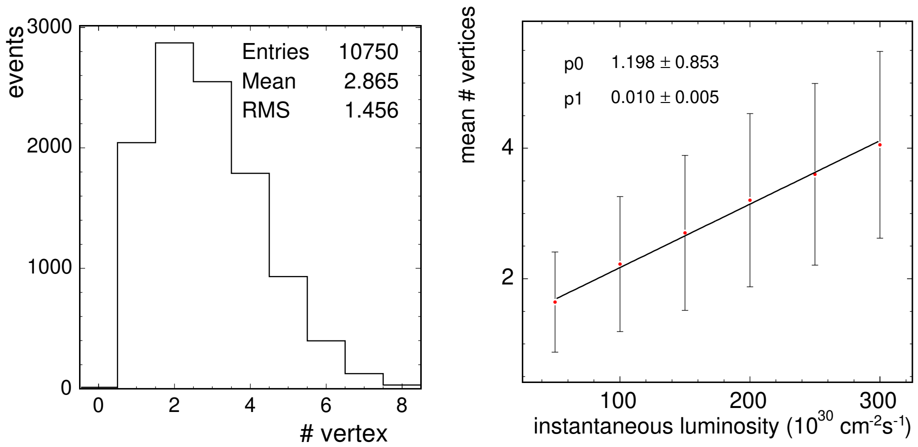

Figure 5.8: Number of primary event vertices reconstructed in simulated data at a range of instantaneous luminosities (left). Mean and RMS of number of vertices in this sample as a function of instantaneous luminosity (right).

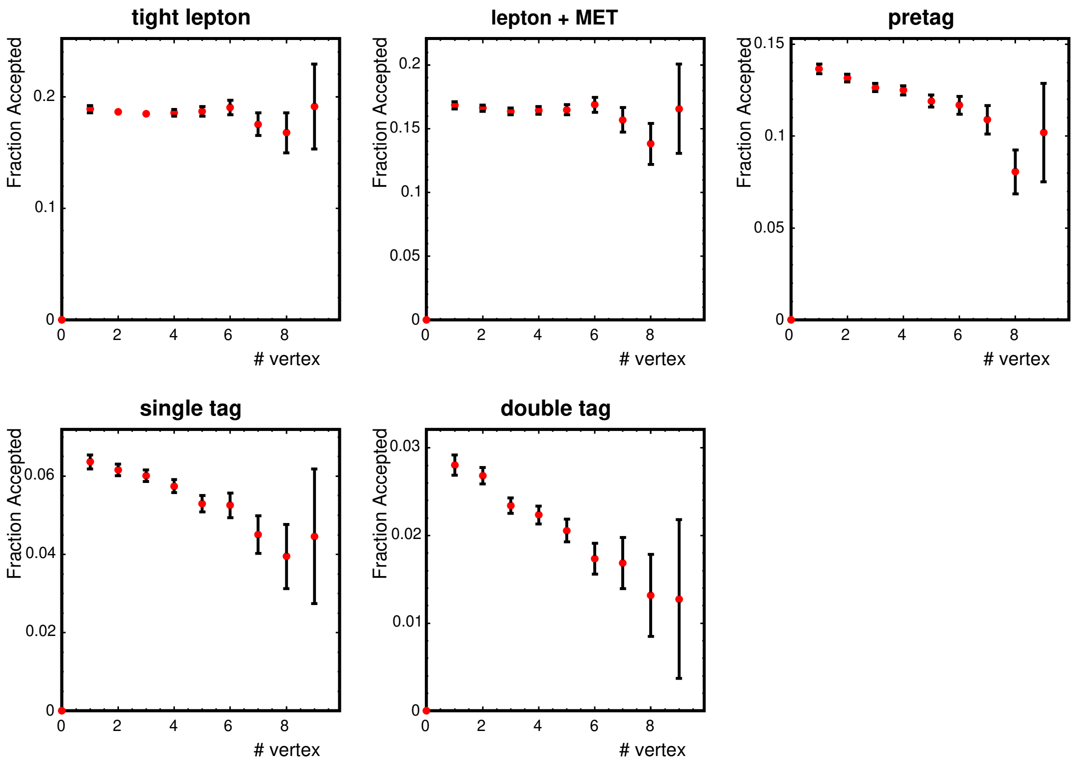

Figure 5.9: Fractions of accepted events in simulated data after various successive selection requirements as functions of the number of primary event vertices reconstructed.

5.3 Estimated Sample Composition

The contributions of various physical processes to the composition of the experimental data sample was estimated for the *0d* dataset by a $t\bar{t}$ cross-section analysis [44]. We do not expect this composition to change significantly in the full dataset used for this measurement, except for the effects of increasing instantaneous luminosity. These effects are covered by systematic error, section 9.5. To estimate the sample composition at 955 pb^{-1}, we scale by luminosity the estimation for the *0d* dataset (the cross-section analysis used 318 pb^{-1}). Table 5.1 summarizes our estimated sample composition.

Sample composition includes signal $t\bar{t}$ events, and the dominant backgrounds: W + jets (including heavy flavor); single top quark; WW, WZ and ZZ diboson; and non-W (QCD) events. Events coming from W + jet production with no heavy flavor contribute because secondary vertex identification incorrectly identifies a tag in about 3% of the four-jet events. These events are termed "mistags" and are the largest single background contribution, followed by non-W. Possible backgrounds with two leptons in the final state, such as $Z \to ll$, are not considered, because the high efficiency of detecting high-p_T electrons and muons means few of these events will be mis-identified.

Most of the background processes are modeled with various simulated samples. Mistags, or W+jet production with no heavy flavor, are modeled with production of a W boson with four light partons (u, d or s quarks or a gluon) and labeled "$W + 4p$." Heavy flavor W+jets samples include: "$Wb\bar{b}$," with a W boson, two b quarks and two light partons; "$Wc\bar{c}$," with a W boson, two c quarks and two light partons; and "Wc," with a W boson, a c quark and three light partons. The other simulated samples are single top production and diboson production, labeled "single top" and "EW," respectively.

Any background process with extra jets in the final state is modeled with events generated with an identical number of extra quark or gluon partons. The mistag sample is modeled with $W + 4p$ simulated events. However, not all final states will have four jets. Also, events generated with other numbers of partons, $W + 2p$, $W + 3p$, etc., will have some events with four jets in the final state. The background is most appropriately treated with a combination of all possible processes ending in four-jet final states. At the time of this analysis, an estimate of the proper combination of these events did not exist. The background was estimated with the largest contributing process.

Simulated events are used to model all backgrounds excluding the the non-W background. This sample is estimated from experimental data with a selection nearly identical to but independent from the data used in the measurement: all requirements are identical except the lepton is required to be non-isolated such that the sum of the E_T within an η-ϕ cone of radius 0.4 around the candidate is greater than 20% of the E_T of the candidate. A non-isolated lepton indicates hadronic activity and therefore a QCD process.

The only significant difference in our event selection from [44] is our additional application of the non-W veto. We include the effects of this selection by determining the change in acceptance in the samples. Using simulated events, we estimate the veto removes 5% of events from $t\bar{t}$, 8% from W + jets and 43% from non-W. We assume an 8% reduction in all backgrounds except non-W. The uncertainty is conservatively inflated for each contributing process, especially diboson and single top. Separate estimations for the diboson and single top samples were not used due to the limited statistics of these samples.

Table 5.1: Estimated sample composition assuming 955 pb^{-1} total integrated luminosity. Assumes $t\bar{t}$ production cross-section of 8.0 pb.

Sample	Expected Events
Background	
W + $4p$ (Mistags)	6.16 ± 1.28
Non-W (QCD)	5.26 ± 2.61
$Wb\bar{b}$	4.70 ± 2.16
$Wc\bar{c}$	2.24 ± 1.07
Wc	1.40 ± 0.63
single top	1.14 ± 0.27
EW (WW,WZ,ZZ)	1.08 ± 0.24
Total Background	21.97 ± 8.25
Signal	
$t\bar{t}$ (8.0 pb)	145.09 ± 16.50
Observed	
Data	167

5.4 Data and Simulated Data Comparisons

We compare distributions of some important kinematic variables between experimental data and simulated data: p_T of the four jets in descending order, $\not\!\!E_T$, lepton p_T, tagged jet p_T, the number of events, angle between leading jet and second jet, angle between leading jet and lepton, and angle between transverse components of the leading jet and $\vec{\not\!\!E}_T$. The leading jet is defined to be the jet with highest p_T. All angular distributions are in the detector frame. The various simulated data processes are weighted by their expected contributions to the event sample. Overall normalization is set by scaling the expected distributions of simulated data to the number of entries in the experimental data distributions.

Figures 5.10 to 5.12 compare distributions for events not requiring a jet to be identified with a secondary vertex. Good agreement within statistics is seen in all distributions except for a 3σ fluctuation in the first bin of lepton p_T. Figures 5.13 to 5.15 compare distributions for events requiring a jet to be identified with a secondary vertex. These are events used in this measurement. Good agreement within statistics is seen in all distributions except for a possible shift toward higher energies in simulated events in the $\not\!\!E_T$ distribution. $\not\!\!E_T$ is not an input variable for this analysis. Figures 5.16 to 5.18 compare distributions for events requiring a jet to be identified with a secondary vertex. In this case, data events are divided according to their dataset. All distributions are normalized by number of entries to that of the *0d* dataset. Behavior is similar to the combined distributions and no significant variations within statistics between datasets are observed.

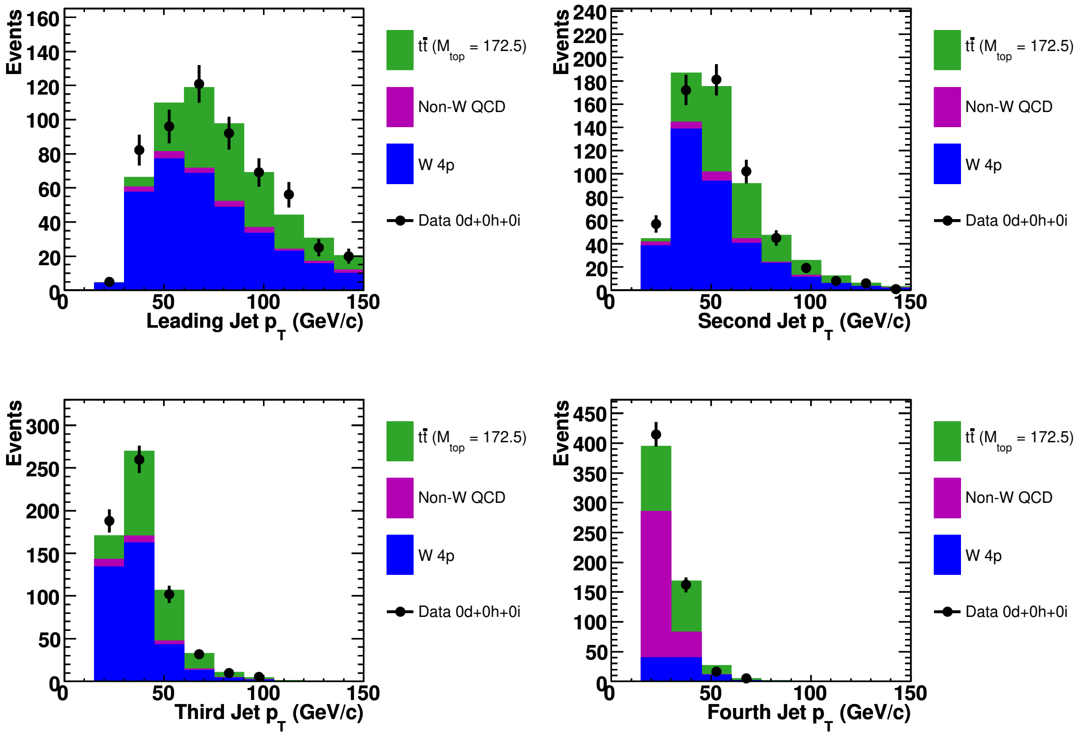

Figure 5.10: Distributions of p_T of the four jets ranked in descending order of p_T. Events pass nominal selection, but are not required to have a jet identified with a secondary vertex.

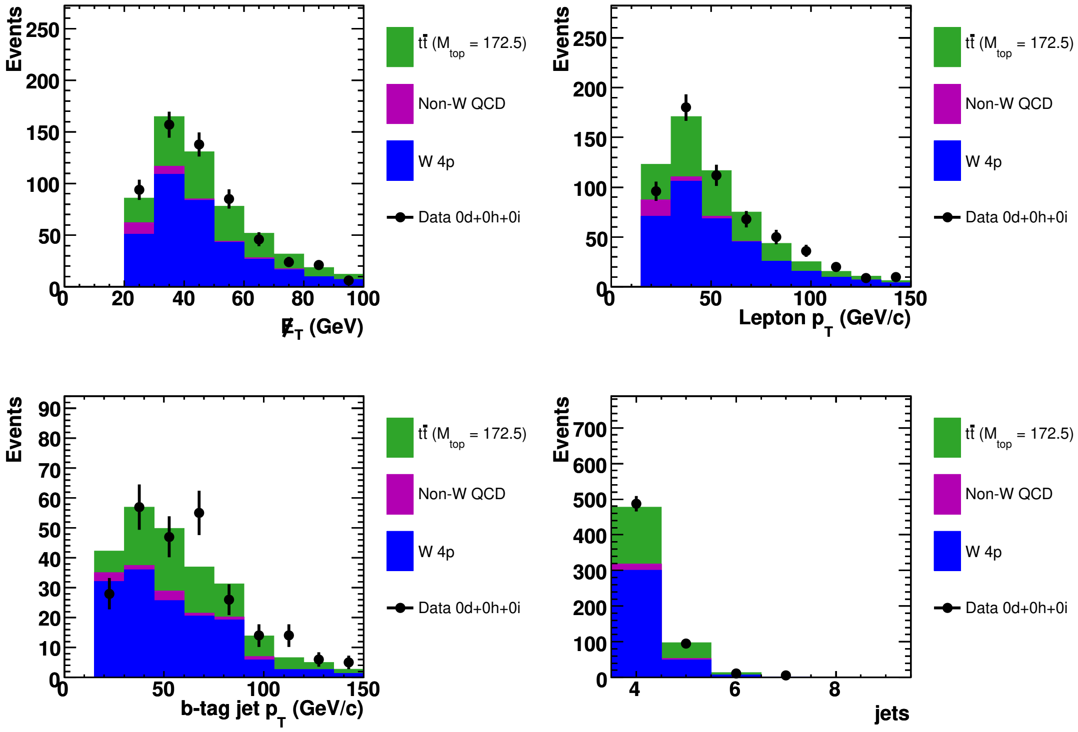

Figure 5.11: Distributions of $\not\!\!E_T$, lepton p_T, b-tagged jet p_T and jet multiplicity. Events pass nominal selection, but are not required to have a jet identified with a secondary vertex.

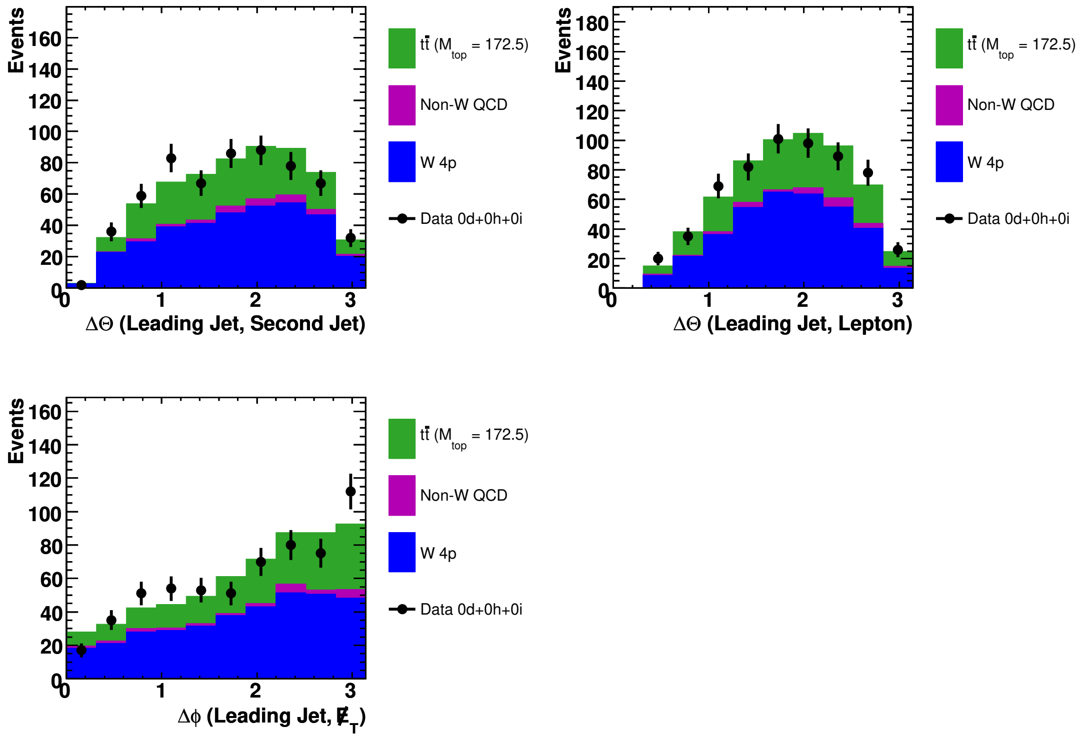

Figure 5.12: Distributions of angular variables. Events pass nominal selection, but are not required to have a jet identified with a secondary vertex.

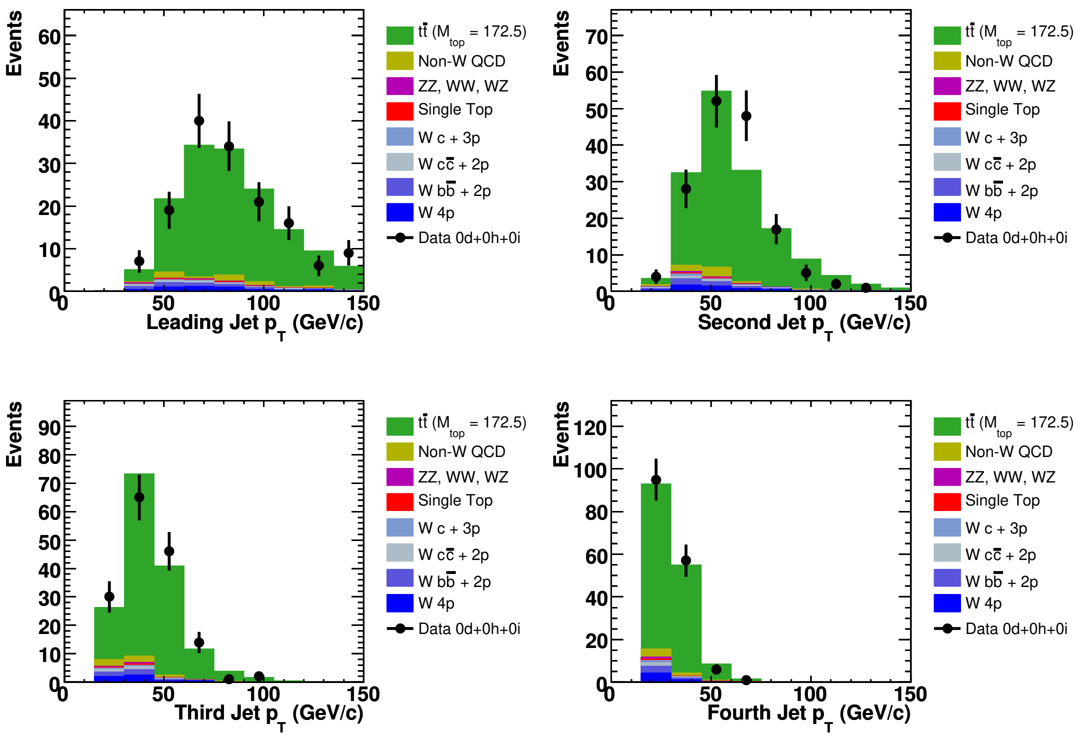

Figure 5.13: Distributions of p_T of the four jets ranked in descending order of p_T. Events pass nominal selection.

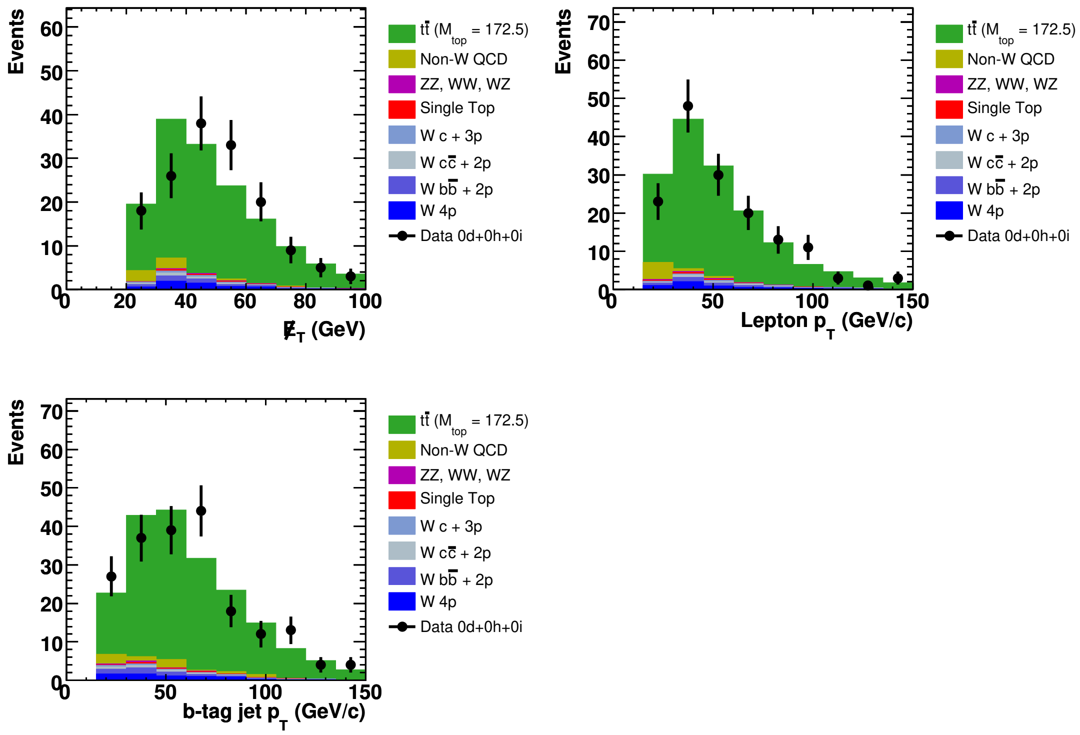

Figure 5.14: Distributions of $\not\!\!E_T$, lepton p_T, and b-tagged jet p_T. Events pass nominal selection.

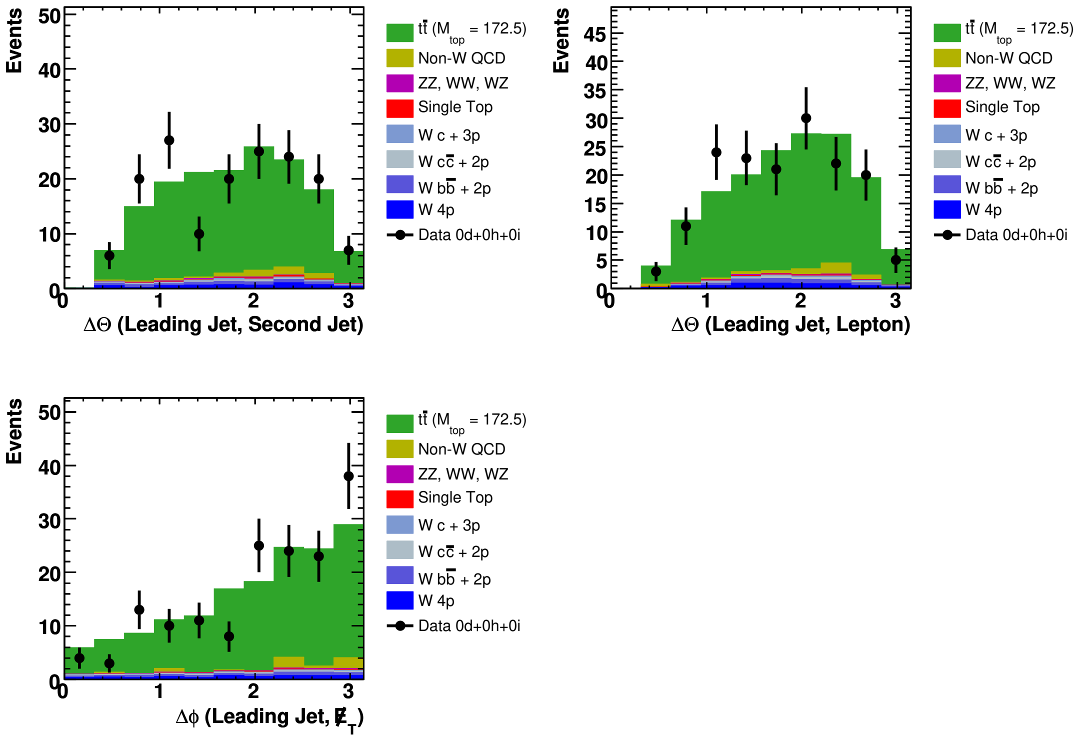

Figure 5.15: Distributions of angular variables. Events pass nominal selection.

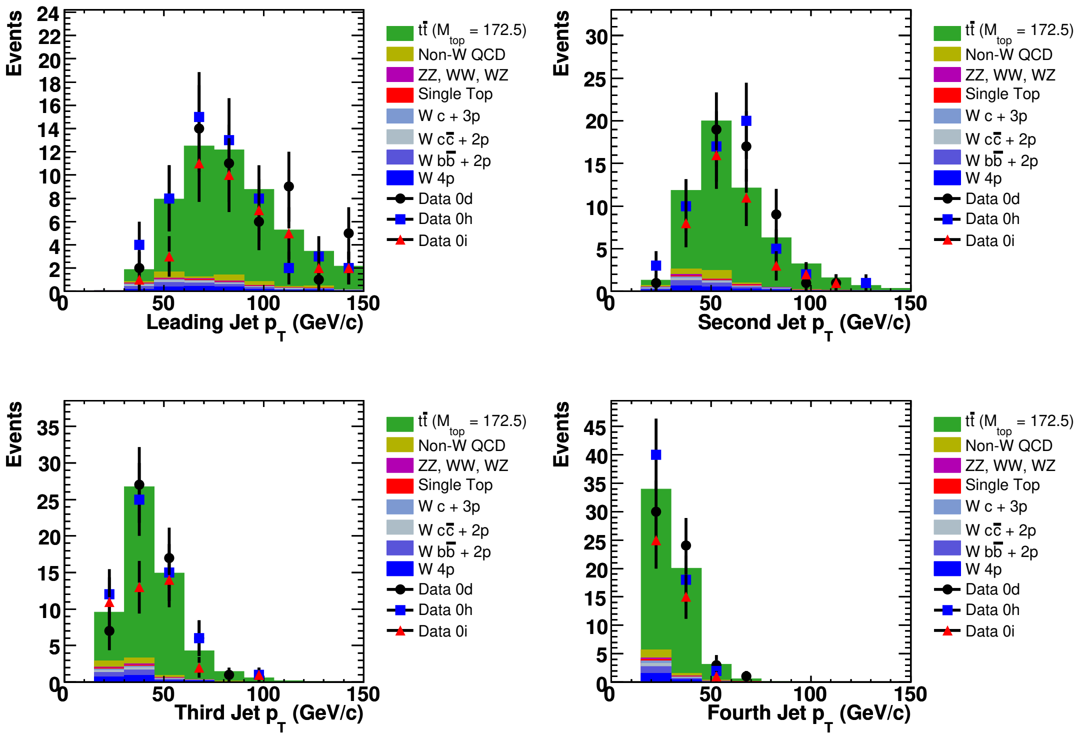

Figure 5.16: Distributions of p_T of the four jets ranked in descending order of p_T. Events pass nominal selection. Data is subdivided into individual datasets.

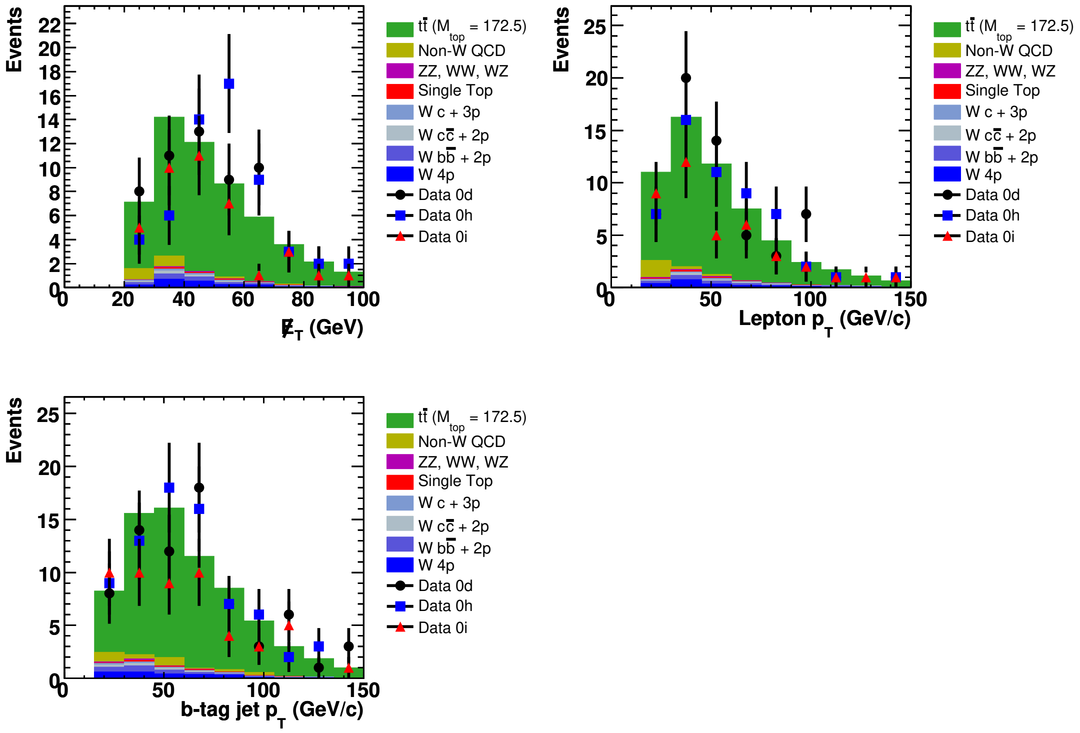

Figure 5.17: Distributions of $\not\!\!E_T$, lepton p_T, and b-tagged jet p_T. Events pass nominal selection. Data is subdivided into individual datasets.

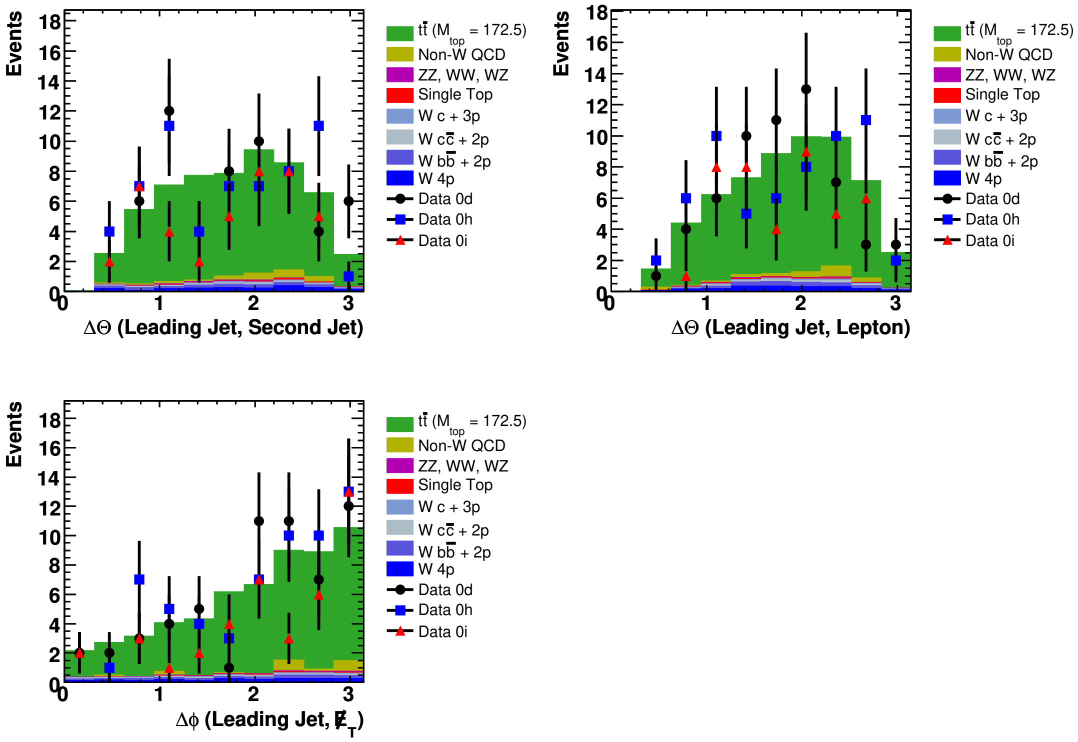

Figure 5.18: Distributions of angular variables. Events pass nominal selection. Data is subdivided into individual datasets.

CHAPTER 6

Top Quark Mass Analysis Method

This chapter describes the method of extracting the mass of the top quark from experimental data. Generally, this is realized using a likelihood to estimate the value of the mass given a set of experimental data. A likelihood [45] is based on a probability density function. The maximum of the likelihood gives the values of the parameters of interest with the smallest RMS variance and the width estimates the uncertainty on these values. Probability densities are formulated in various ways. A simple method, commonly known as the "template" method, creates a probability density by comparing kinematic shapes in experimental data with simulated data. Often, only a single variable is used, an invariant mass. This technique was used in the first measurements of the top quark mass [5][6]. In contrast, the technique used in this analysis formulates a probability density from the theoretical expression for the differential scattering cross-section with explicit dependence on several measured quantities, the final state momenta of the charged lepton and jets. Such methods are commonly known as "matrix element" methods and generally give more precise estimations of the top quark mass compared to template methods given similar numbers of events. One of the reasons matrix element methods reach higher precision is that each event contributes individually to the likelihood rather than the distribution of all the events. Each event shapes the likelihood using the most relevant measured quantities combined with theoretical expectation. The matrix element method was suggested in 1988 [46] and 1992 [47], and was first used to measure the top quark mass by DØ [48]. A full description of the likelihood used for this analysis and its components follows.

6.1 Likelihood

The variable of interest in this analysis is the top quark mass. However, the likelihood scans three free parameters, $\vec{\alpha}$: the top quark mass, m_t; the jet energy scale, JES; and the fraction of events consistent with signal, C_s. Fifteen reconstruction level quantities, $\vec{x}$, as introduced in Chapter 4, are input to the likelihood: three components of charged lepton momentum, and the energy and two angles describing the direction for each of four jets.

The jet energy scale, as used in this analysis, is defined as a the ratio between the energies of reconstructed jets in experimental data (E_{jet}) and simulated data ($E_{\text{jet}}^{\text{MC}}$)

$$E_{\text{jet}} = E_{\text{jet}}^{\text{MC}} / JES. \tag{6.1}$$

Uncertainty in the jet energy scale contributes most significantly to the total systematic uncertainty in many top quark mass measurements at the Tevatron. Measuring JES in the likelihood *in situ* reduces this uncertainty in two ways. First, it acts as a statistical error: decreasing with increasing number of events. Second, many previous analyses treated it as uncorrelated with the top quark mass, measured the effect separately, and over-estimated the uncertainty. In this analysis, the uncertainty on JES does not depend on p_T or η. This dependence is treated as a separate systematic and is described in section 9.1. Section 4.4 further discusses jets and corrections related to their energy scale.

The likelihood is sensitive to the jet energy scale via the mass of the hadronically decaying W boson. The invariant mass of the two jets from the W boson is constrained by a Breit-Wigner resonance with the best known, world-average, pole mass and width measurements, 80.4 GeV/c^2 and 2.124 GeV/c^2, respectively [4]. Varying the energy scale of the two jets corresponding to W boson decay shifts the invariant mass with respect to the resonance, resulting in sensitivity to JES and enabling a measurement.

The fraction of signal events (C_s) is defined as the fraction of the total number of events consistent with the leading order $t\bar{t}$ probability density, see section 6.3. Including C_s in the likelihood makes this analysis relatively insensitive to statistical and systematic variations in the contribution of background events. It also means it is not dependent on an estimate of sample composition. The numbers in Table 5.1 are not an input to the likelihood.

6.1.1 Derivation of Likelihood

This analysis uses a maximum likelihood technique with the Poisson extension [49] constructed as the product of per-event probability densities, P_i, with a Poisson distribution

$$\mathcal{L}(\vec{\alpha}, \mu) = \frac{\mu^N e^{-\mu}}{N!} \prod_{i=1}^{N} P(\vec{\alpha}), \tag{6.2}$$

where $\vec{\alpha}$ are likelihood parameters, μ is the Poisson parameter, $\vec{x}$ are the input measured quantities, and the product is over N events. Maximizing this likelihood for μ determines the normalization of P if it is not *a priori* correctly normalized [50]. Carrying out the maximization of $\mathcal{L}$ with respect to μ analytically reduces the likelihood to

$$\mathcal{L}(\vec{\alpha}) = e^{-N \int P(\vec{\alpha}) d\vec{x}} \prod_{i=1}^{N} P(\vec{\alpha}). \tag{6.3}$$

Equation 6.3 is the basis for the measurement of this analysis. The per-event probability density describes the physical processes contributing to the events in the selected sample. In the case of the lepton plus jets decay channel, these processes are assumed to be $t\bar{t}$ production and $W+$jets production, the dominant background. The approximation is made that these two processes fully describe an event and are statistically independent from one another. In this case, P is the linear combination of two probability densities describing these processes

$$P(\vec{x}; m_t, JES, C_s) = C_s P_{t\bar{t}}(\vec{x}; m_t, JES) + (1 - C_s) P_{W+\text{jets}}(\vec{x}; JES). \quad (6.4)$$

A constraint, $0 \leq C_s \leq 1$, ensures that the sum of the two normalized probability densities is itself normalized. Note that this constraint is naturally satisfied in the final result with experimental data and only affects pseudo-experiments in simulated data at the extremes of all signal or all background.

Thus far, the $t\bar{t}$ and W+jets probability densities are idealized in that they are constructed assuming that the detected events cover the full possible range of kinematic phase-space. However, this phase-space is actually limited by the detector apparatus and data selection criteria, so the experimental probability densities are therefore described taking into account a multiplicative detector *acceptance* term, $A(\vec{x})$, defined as the fraction of fully reconstructed events passing selection out of the total possible for a given set of measurable parameters ($\vec{x}$). The realistic per-event probability density is then defined as the product of acceptance with the ideal per-event probability density

$$P_{\text{real}}(\vec{x}; m_t, JES, C_s) = A(\vec{x}) P_{\text{ideal}}(\vec{x}; m_t, JES, C_s). \quad (6.5)$$

Since acceptance is independent of the underlying process and is solely a property of the detector and data selection criteria, it is also independent of the maximized parameters. Any overall constant factor in the product of Equation 6.3, such as acceptance, has no effect on the outcome of likelihood maximization. Acceptance is therefore dropped from the product and only enters in the exponent of Equation 6.3:

$$\mathcal{L}(\vec{\alpha}) = e^{-N \int A(\vec{x}) P_{\text{ideal}}(\vec{\alpha}) d\vec{x}} \prod_{i=1}^{N} P_{\text{ideal}}(\vec{\alpha}). \tag{6.6}$$

Assuming properly normalized $t\bar{t}$ and W+jets probability densities, the integral in the exponent, performed separately for each term in P, is interpreted as the mean acceptance out of the full range of kinematically-allowed phase-space

$$\langle A_{\,t\bar{t}}\,(m_t, JES)\rangle \;\equiv\; \int A(\vec{x})\; P^{\text{ideal}}_{t\bar{t}}(\vec{x}; m_t, JES)\; d\vec{x} \tag{6.7}$$

$$\langle A_{\,W+\text{jets}}\,(JES)\rangle \;\equiv\; \int A(\vec{x})\; P^{\text{ideal}}_{W+\text{jets}}(\vec{x}; JES)\; d\vec{x} \tag{6.8}$$

It would be prohibitively difficult to parameterize $A(\vec{x})$ for all $\vec{x}$, but the mean acceptance is independent of $\vec{x}$ and extracted from simulated data as the total number of events selected out of the number generated, section 6.1.2.

The final likelihood used for this analysis is

$$\begin{aligned} &\mathcal{L}(m_t, JES, C_s) = \\ &\exp[-NC_s\langle A_{t\bar{t}}(m_t, JES)\rangle]\,\exp[-N(1-C_s)\langle A_{W+\text{jets}}(JES)\rangle] \\ &\prod_{i=1}^{N}[C_s P_{t\bar{t}}(m_t, JES) + (1-C_s)R_{bkg}P_{W+\text{jets}}(JES)]. \end{aligned} \tag{6.9}$$

The $t\bar{t}$ and W + jets probability densities are individually normalized up to undetermined constants independent from the maximized variables. The only important remaining normalization is the relative normalization constant between the two probability densities, R_{bkg}, discussed in section 6.5.

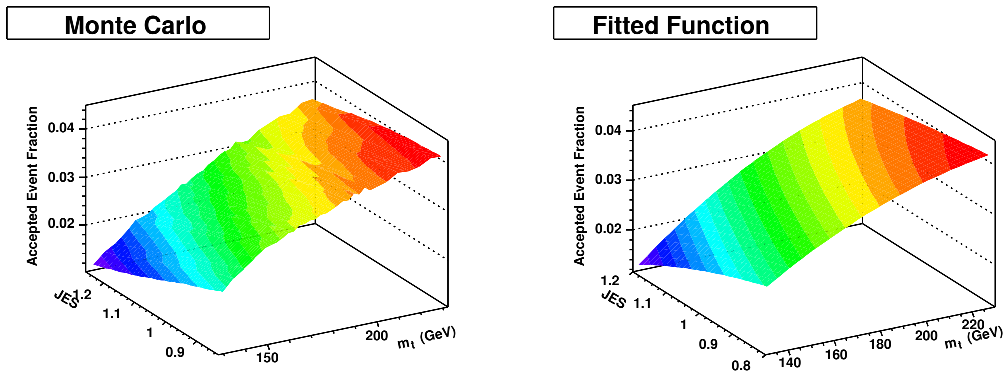

Figure 6.1: Mean acceptance of $t\bar{t}$ events as a function of the input top quark mass and JES (left). Parameterization of this acceptance (right).

6.1.2 Determination of Mean Acceptance

Mean acceptance is defined as the total number of events selected out of the number generated. Event selection at reconstruction level is described in Chapter 4. The mean acceptance is parameterized using simulated **HERWIG** $t\bar{t}$ events generated at several different top quark masses for $\langle A_{t\bar{t}}\rangle$ and **ALPGEN** W + 4p for $\langle A_{W+jets}\rangle$. Mean acceptance as a function of JES was determined by scaling jet energies prior to selection.

Figure 6.1 shows mean acceptance as a function of m_t and JES for $t\bar{t}$ events. The parameterization used to describe $\langle A_{t\bar{t}}\rangle$ is

$$\langle A(m_t, JES)\rangle = a_0 JES^3 + a_1 m_t^2\, JES + a_2 m_t\, JES^2 + a_3 m_t^2 \\ + a_4 m_t\, JES + a_5 JES^2 + a_6 m_t + a_7 JES + a_8 \quad (6.10)$$

where the fitted parameters are listed in Table 6.1. Mean acceptance with overlaying parameterization is shown as a function of top quark mass for various fixed JES points and vice versa in Figure 6.2. The parameterization describes the mean acceptance fairly well over the range of m_t and JES values. Figure 6.3

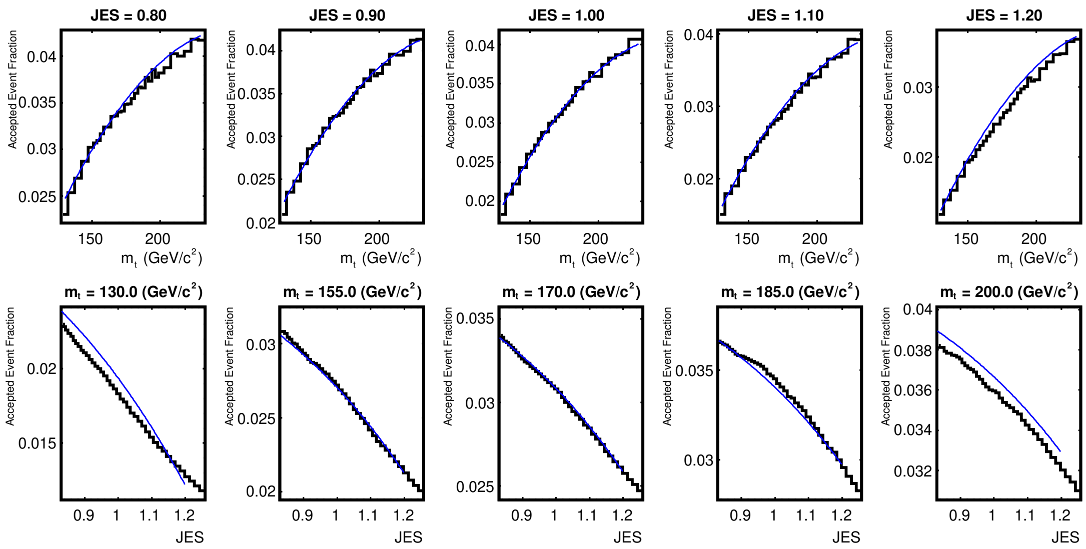

Figure 6.2: Mean acceptances (histograms) and parameterization (curves) in $t\bar{t}$ events as a function of the input top quark mass (top) and JES (bottom) in slices of JES and top quark mass, respectively.

shows the mean acceptance and fitted parameterization as a function of JES for W+4p events. The parameterization used to describe $\langle A_{W+jets} \rangle$ is a second order polynomial in JES with parameters listed in Table 6.2.

6.1.3 Likelihood Application and Maximization

The likelihood is maximized for top quark mass, jet energy scale, and signal fraction. Scanning the likelihood in m_t and JES requires CPU-intensive evaluation of the $t\bar{t}$ and W + jets per-event probability densities. In practice, the integrals described in sections 6.3 and 6.4 are evaluated along a fixed grid in m_t and JES parameter space consisting of 31 m_t steps of 2 GeV/c^2 and 17 JES steps of 0.02 from 142.5 GeV/c^2 to 202.5 GeV/c^2 and 0.8 to 1.12, respectively. The negative log of the maximum likelihood described in Equation 6.10 is calculated for each point in this grid. It is minimized with respect to C_s using `MINUIT` [51] at each

Table 6.1: $\langle A_{t\bar{t}} \rangle$ parameters

param	value	param	value
a_0	-0.00904447	a_5	-0.0195568
a_1	-9.6599e-07	a_6	0.000312924
a_2	0.000164172	a_7	-0.017409
a_3	-3.52343e-07	a_8	-0.000977841
a_4	0.000204782		

Table 6.2: $\langle A_{W+jets} \rangle$ parameters

param	value
a_0	0.03903
a_1	-0.05105
a_2	0.01771

grid point, and then fit with a two dimensional second-order polynomial function, see section C. The fit region covers 40 GeV/c^2 in m_t and 0.24 in JES. Figure 6.4 shows the a likelihood and the resulting fit in a sample of data simulated with `HERWIG` at a top quark mass of 172.5 GeV/c^2 and nominal JES.

The minimum of the fitted polynomial gives the measured m_t and JES parameters, and C_s is taken to be the minimized value at the grid point closest to this minimum. The contours describe $\Delta \ln \mathcal{L}$ of 0.5, 2.0, 4.5, 5 and 8.0; and correspond to uncertainty in the top quark mass of 1σ, 2σ, 3σ, 4σ, and 5σ, respectively, assuming the likelihood is Gaussian. In terms of the top quark mass, the total width of the contour in the m_t dimension represents the uncertainty that the true value of the top quark mass is within this error for any value of

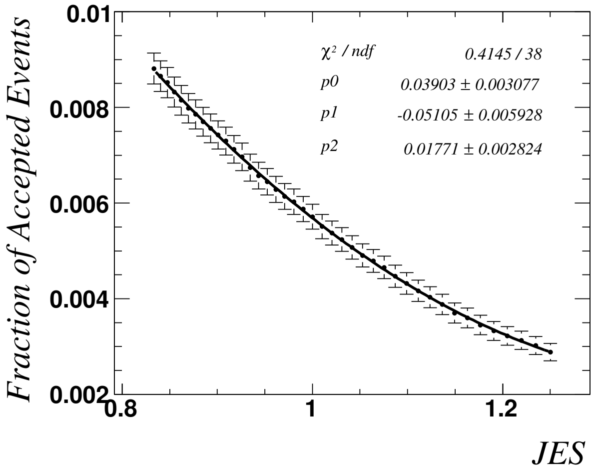

Figure 6.3: Mean acceptance of W+4p events as a function of JES

JES [45]. This width represents the sum of statistical uncertainty and measured jet energy scale systematic uncertainty. A similar uncertainty is quoted as the statistical only uncertainty on the JES measurement. The uncertainty on C_s is estimated by `MINUIT`. Note that the errors from the minimization of C_s are not included with the uncertainty estimated from the fit to the m_t-JES parameter space. This is not a problem, because the likelihood shape weakly varies with C_s and its estimated uncertainty is corrected by a scale factor, see section 8.1.2.2. The likelihood outputs are tested for bias and proper coverage using studies in simulated data, section 8.1.2.

In some cases it is expedient to fix the JES parameter in the likelihood. JES is always fixed to its nominal value, JES = 1. The $t\bar{t}$ probability density is evaluated only in m_t, greatly reducing the necessary CPU time to process an event. After minimization of C_s, the negative log likelihood is fit with a one-dimensional second-order polynomial, see Figure 6.5 for an example in simulated events generated with `HERWIG` at a top quark mass of 172.5 GeV/c^2 and nominal

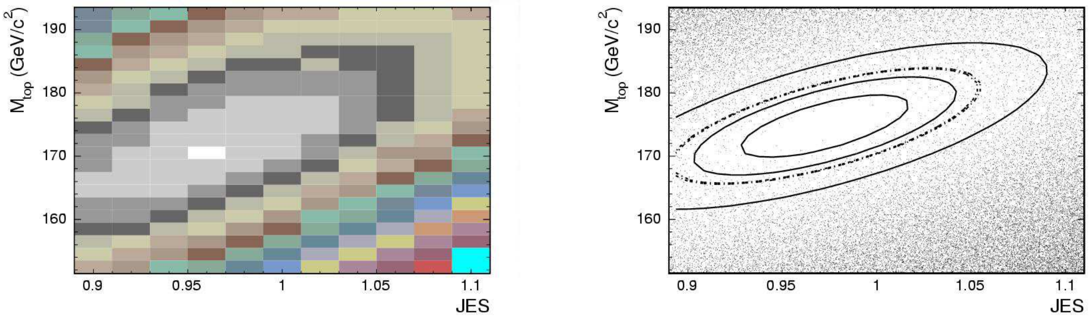

Figure 6.4: Two-dimensional likelihood as a function of m_t and JES (left), and with contours showing Gaussian fit (right) on a pseudo-experiment constructed from simulated events generated with a top quark mass of 172.5 GeV/c^2 and nominal JES.

JES. This figure also shows a one-dimensional fit in JES at 172.5 GeV/c^2, but this type of fit is not commonly used in this analysis. The error on measured m_t is taken as $\Delta\ln\mathcal{L} = 0.5$ and C_s is estimated similarly to the two-dimensional (m_t-JES) case. This one-dimensional likelihood is used in Chapter 9 as a cross-check in simulated data studies and to evaluate some of the contributions to systematic uncertainty.

6.2 Constructing an Event Probability Density

In this analysis, an event probability density for a given physical scattering process is constructed as the ratio of its parton-level differential cross-section to its total cross-section, such that the integral over all phase-space is unity. Parton level quantities ($\vec{y}$) are translated into the input measured quantities ($\vec{x}$) with the appropriate resolution using a *transfer function*. The probability density is written as

$$P(\vec{x}) = \frac{1}{\sigma}\int d\sigma(\vec{y})W(\vec{x},\vec{y}), \tag{6.11}$$

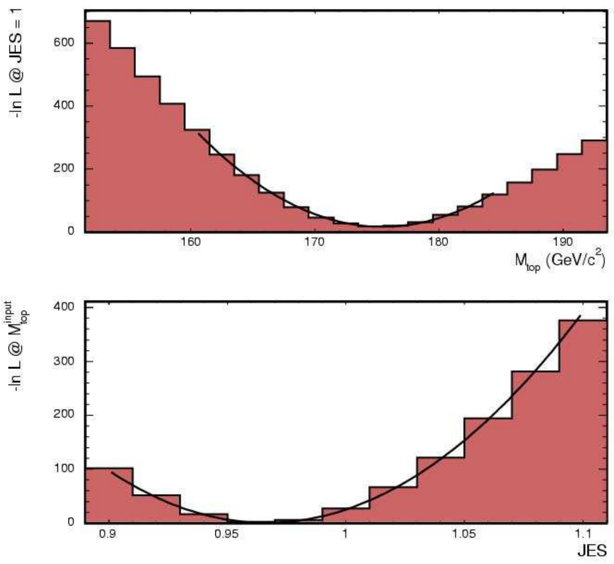

Figure 6.5: One-dimensional likelihood and fit at JES = 1 (top) and $m_t = 172.5$ GeV/c^2 (bottom) on a pseudo-experiment constructed from simulated events generated with a top quark mass of 172.5 GeV/c^2 and nominal JES.

where σ is the total cross-section, $d\sigma(\vec{y})$ is the differential cross-section and $W(\vec{x}, \vec{y})$ is the transfer function. A generic differential cross-section [4] is written as

$$d\sigma = \frac{(2\pi)^4|\mathcal{M}|^2}{4\sqrt{(q_1 \cdot q_2)^2 - m_{q_1}^2 m_{q_2}^2}} d\Phi_n(q_1 + q_2; p_1, ..., p_n), \tag{6.12}$$

where $\mathcal{M}$ is a matrix element, q_1 and q_2 are the four momenta of the incident particles, m_{q_1} and m_{q_2} are the masses of the incident particles, and $d\Phi_n$ is the differential phase space

$$d\Phi_n(q_1 + q_2; p_1, ..., p_n) = \delta^4(q_1 + q_2 - \sum_{i=1}^{n} p_i) \prod_{i=1}^{n} \frac{d^3 p_i}{(2\pi)^3 2E_i}. \tag{6.13}$$

Incident particles come from $p\bar{p}$ collisions, so the differential cross-section is convoluted with parton distribution functions (PDFs) defined in the usual manner as the probability a parton carries longitudinal momentum fraction between $\tilde{q}$

and $\tilde{q} + d\tilde{q}$. It is necessary to integrate over this unknown momentum

$$P(\vec{x}) = \frac{1}{\sigma} \int d\sigma(\vec{y})\; f(\tilde{q}_1) f(\tilde{q}_2)\; W(\vec{x}, \vec{y})\; d\tilde{q}_1 d\tilde{q}_2. \tag{6.14}$$

Included processes contain six final state particles in their decay: 4 quarks, a charged lepton and a neutrino. Thus, Equation 6.14 can be expressed as

$$P(\vec{x}) = \frac{1}{\sigma} \int \frac{(2\pi)^4 |M|^2 f(\tilde{q}_1) f(\tilde{q}_2) W(\vec{x}, \vec{y})}{4\sqrt{(q_1 \cdot q_2)^2 - m_{q_1}^2 m_{q_2}^2}} d\Phi_6 d\tilde{q}_1 d\tilde{q}_2. \tag{6.15}$$

Neglecting the masses and transverse momenta of the initial state particles,

$$\sqrt{(q_1 \cdot q_2)^2 - m_{q_1}^2 m_{q_2}^2} = 4|q_1||q_2|, \tag{6.16}$$

Equation 6.15 transforms into

$$P(\vec{x}) = \frac{1}{\sigma} \frac{(2\pi)^4}{16} \int |M|^2 \frac{f(\tilde{q}_1)}{|q_1|} \frac{f(\tilde{q}_2)}{|q_2|} W(\vec{x}, \vec{y}) d\Phi_6 d\tilde{q}_1 d\tilde{q}_2, \tag{6.17}$$

where the 6-body phase space, $d\Phi_6$, is given by

$$d\Phi_6 = \delta^4(P - \sum_{i=1}^{4q,l,\nu} p_i) \prod_{i=1}^{4q,l,\nu} \frac{d^3 p_i}{(2\pi)^3 2E_i} \tag{6.18}$$

and the sum and product are over 4 quarks ($4q$), a lepton (l), and a neutrino (ν).

The phase space is reduced by energy conservation and assumptions about detector resolution in the transfer functions. This analysis assumes the detector measures electron and muon momenta and angles of jets with good resolution. Therefore, the transfer function models the mapping of these quantities with δ-functions. Significant resolution effects in jet energy are parameterized with a jet energy transfer function, $W_{jet}(E^x, E^y, JES)$. Chapter 7 further discusses the transfer function, $W(\vec{x}, \vec{y}, JES)$, expressed as

$$W(\vec{x}, \vec{y}, JES) = \delta^3(p_l^y - p_l^x) \prod_{i=1}^{4} W_{jet}(E_i^x, E_i^y, JES) \prod_{j=1}^{4} \frac{1}{(p_j^x)^2} \delta^2(\Omega_j^y - \Omega_j^x), \tag{6.19}$$

where Ω is the solid angle. Note that the neutrino is not part of the transfer function as it escapes the detector unmeasured. The momenta of the neutrino is constrained by energy conservation.

Integrating over $\tilde{q}_1$, $\tilde{q}_2$, p_x^ν and p_y^ν in Equation 6.17 removes the four-momentum conservation delta-function and reduces Equation 6.18. Initial energy and z-momentum can be expressed in terms of $|q_1| + |q_2|$ and $|q_1| - |q_2|$, respectively, so integration over the momentum fraction of the colliding protons is converted to

$$d\tilde{q}_1 d\tilde{q}_2 = \frac{1}{2E_p E_{\bar{p}}} d(|q_1| + |q_2|) d(|q_1| - |q_2|), \tag{6.20}$$

assuming $E_p = E_{\bar{p}} = 980$ GeV. Further integration over $d^3 p_l$ and all $d^2\Omega$ in Equation 6.17 eliminates the δ-functions in Equation 6.19, leaving five non-trivial integrations: the momentum magnitude of the non-leptonic final state partons, the hadronic b quark (ρ_{bh}), the leptonic b quark (ρ_{bh}), and the two quarks from hadronic W boson decay (ρ_{j1}, ρ_{j2}); and the z-component of the neutrino momentum (p_ν^z)

$$d\tilde{\Phi} = \frac{1}{(2\pi)^{18} 2^6} \frac{1}{2E_p E_{\bar{p}}} \frac{(\rho_{bh}^y)^2 (\rho_{j1}^y)^2 (\rho_{j2}^y)^2 (\rho_{bl}^y)^2}{(\rho_{bh}^x)^2 (\rho_{j1}^x)^2 (\rho_{j2}^x)^2 (\rho_{bl}^x)^2} \frac{d\rho_{bh} d\rho_{bl} d\rho_{j1} d\rho_{j2} dp_\nu^z}{E_{bh} E_{j1} E_{j2} E_{bl} E_e E_\nu}, \tag{6.21}$$

where the superscripts x and y refer to reconstruction-level and parton-level quantities, respectively.

In general, it is not possible to distinguish between jets in the final state, so the probability density is evaluated summing over all 24 possible permutations of jet-parton identification. The $t\bar{t}$ probability density uses secondary vertex tagging information to reduce the number of necessary permutations, see Section 6.3.2. The final generic probability density for six-particle decay is

$$P(\vec{x}) = \frac{1}{\sigma} \sum_{\text{perm}}^{24} \int |\mathcal{M}|^2 \frac{f(\tilde{q}_1)}{|q_1|} \frac{f(\tilde{q}_2)}{|q_2|} \prod_{i=1}^{4} [W_{jet}(E_i^y, E_i^x, JES)] d\tilde{\Phi}. \tag{6.22}$$

The $t\bar{t}$ and W+jets probability densities are derived from Equation 6.22 using their respective forms of matrix element and specific integration techniques. Details are discussed in sections 6.3 and 6.4, respectively.

6.3 Details Specific to the $t\bar{t}$ Probability Density

The $t\bar{t}$ probability density contains all the sensitivity to the top quark mass. It is a function of m_t and JES parameters and uses a leading-order matrix element. Quarks from the W boson decay are assumed to be massless and b quarks from top quark decay are assumed to have mass of 4.8 GeV/c^2 [4]. Compared to Equation 6.22, we change integration variables to reduce computation time and include integration over the transverse momentum in the $t\bar{t}$ system. It is normalized with a parameterization of the leading order cross-section derived from the `PYTHIA` Monte Carlo generator.

6.3.1 $t\bar{t}$ Matrix Element

The leading order matrix element used in the $t\bar{t}$ probability density describes $t\bar{t}$ production with subsequent decay into a charged lepton, a neutrino and four quarks [52]. It averages over initial spins and colors and sums over final spins and colors. Spin correlations are removed as an approximation, resulting in the amplitude

$$|\mathcal{M}|^2 = \frac{g_s^4}{9} F\bar{F}(2 - \beta^2 \sin^2\theta_{qt}), \tag{6.23}$$

where g_s is the strong coupling constant and θ_{qt} describes the angle between the incoming partons in their rest frame and the top quark. The factors F and $\bar{F}$

describe the leptonic and hadronic decay of the top quark, such that

$$F = \frac{g_W^4}{4}\frac{\pi(m_t^2 - m_{\bar{e}\nu}^2)}{m_t\Gamma_t}\frac{m_t^2(1-c_{\bar{e}b}^2) + m_{\bar{e}\nu}^2(1+c_{\bar{e}b})^2}{(m_{\bar{e}\nu}^2 - m_W^2)^2 + m_W^2\Gamma_W^2} \tag{6.24}$$

$$\bar{F} = \frac{g_W^4}{4}\frac{\pi(m_t^2 - m_{d\bar{u}}^2)}{m_t\Gamma_t}\frac{m_t^2(1-c_{d\bar{b}}^2) + m_{d\bar{u}}^2(1+c_{d\bar{b}}^2)}{(m_{d\bar{u}}^2 - m_W^2)^2 + m_W^2\Gamma_W^2}, \tag{6.25}$$

where g_W is the weak coupling constant and c_{ij} is the cosine of the angle between particle i and particle j in their respective rest frame. The functional forms of the hadronic and leptonic decays are different because the hadronic W boson decay into two jets is made symmetric. Although the flavors of the two quarks are not identical, the detector response is essentially indistinguishable between them. Making the matrix element invariant under the identification of these two jets removes half of the possible 24 permutations of jet-parton assignment.

The decay width of the top quark, approximately 1.5 GeV at 180 GeV/c^2 [53], is small compared to its mass. This relative diminutiveness allows the narrow-width approximation of the top quark Breit-Wigner, replacing it with a delta function:

$$\frac{1}{(m_{event}^2 - m_{pole}^2)^2 + m_{pole}^2\Gamma^2} \approx \frac{\pi}{m_{pole}\Gamma}\delta(m_{event}^2 - m_{pole}^2). \tag{6.26}$$

The narrow-width approximation is used to replace the top quark Breit-Wigners nominally in Equations 6.24 and 6.25. Integrating over the delta functions sets the event masses of the hadronic and leptonic top quarks, see section 6.3.2, to be equivalent to the value of the pole mass parameter, m_t, scanned by the likelihood. This necessarily makes the event mass of the hadronic and leptonic branches equivalent.

An expression for the width of the top decay consistent with all assumptions is derived from the standard expression for the three-body decay of the top quark

$$d\Gamma_t = \frac{1}{2^7(2\pi)^5}\frac{|M|^2}{m_t}(1 - \frac{m_W^2}{m_t^2})dm_W^2 d^2\Omega_W d^2\Omega_e, \tag{6.27}$$

see section A.1. Using Equation 6.23 and the narrow-width approximation, the decay width can be expressed as

$$\begin{aligned}\Gamma_t &= \frac{g_W^4 m_t^3 \Theta}{3\, 2^6 (2\pi)^3} \frac{1 - 3(m_W/m_t)^4 + 2(m_W/m_t)^6}{m_W \Gamma_W} \\ \Theta &\equiv \arctan[\frac{(m_t - m_b)^2 - m_W^2}{m_W \Gamma_W}] - \arctan[\frac{-m_W^2}{m_W \Gamma_W}].\end{aligned} \tag{6.28}$$

6.3.2 $t\bar{t}$ Integration Variables

To expedite integration it is convenient to change variables in Equation 6.22 to the hadronic and leptonic top quark and W boson masses squared (m_{th}^2, m_{tl}^2, m_{Wh}^2, m_{Wl}^2) and the momentum magnitude of one of the quarks from the hadronic W boson decay (ρ_{j1}). The Jacobian for this transformation is

$$J(\frac{m_{th}^2 m_{Wh}^2 m_{tl}^2 m_{Wl}^2}{\rho_{bh}\rho_{j2}\rho_{bl}p_\nu^z}) = a_{11}a_{21}(a_{33}a_{44} - a_{34}a_{43}) \tag{6.29}$$

where

$$a_{11} \equiv \frac{dm_{th}^2}{d\rho_{bh}} = 2(\frac{\rho_{bh}}{E_{bh}}E_{j1} - \rho_{j1}\cos\theta_{b1}) + 2(\frac{\rho_{bh}}{E_{bh}}E_{j2} - \rho_{j2}\cos\theta_{b2}) \tag{6.30}$$

$$a_{21} \equiv \frac{dm_{Wh}^2}{d\rho_{j2}} = 2\rho_{j1}(1 - \cos\theta_{12}) \tag{6.31}$$

$$a_{43} \equiv \frac{dm_{Wl}^2}{d\rho_{bl}} = 2[\frac{dp_\nu^x}{d\rho_{bl}}(\frac{\rho_e}{\rho_\nu}p_\nu^x - p_e^x) + \frac{dp_\nu^y}{d\rho_{bl}}(\frac{\rho_e}{\rho_\nu}p_\nu^y - p_e^y)] \tag{6.32}$$

$$a_{44} \equiv \frac{dm_{Wl}^2}{dp_\nu^z} = 2(\frac{\rho_e}{\rho_\nu}p_\nu^z - p_e^z) \tag{6.33}$$

$$a_{34} \equiv \frac{dm_{tl}^2}{dp_\nu^z} = a_{44} + 2(\frac{E_{bl}}{\rho_\nu}p_\nu^z - \rho_{bl}\cos\theta_{bl}) \tag{6.34}$$

$$\begin{aligned}a_{33} \equiv \frac{dm_{tl}^2}{d\rho_{bl}} &= a_{43} + 2\frac{\rho_{bl}}{E_{bl}}\rho_e - 2p_e\cos\theta_{eb} + 2[\frac{\rho_{bl}}{E_{bl}}\rho_\nu + \frac{E_{bl}}{\rho_\nu}(\frac{d\rho_\nu^x}{d\rho_{bl}}\rho_\nu^x + \frac{d\rho_\nu^y}{d\rho_{bl}}\rho_\nu^x)] \\ &-2[\sin\theta_{bl}\cos\phi_{bl}(p_\nu^x + \rho_{bl}\frac{d\rho_\nu^x}{d\rho_{bl}}) + \sin\theta_{bl}\sin\phi_{bl}(p_\nu^y + \rho_{bl}\frac{d\rho_\nu^y}{d\rho_{bl}}) \\ &+\cos_{bl}p_\nu^z]\end{aligned} \tag{6.35}$$

and

$$\frac{d\rho_\nu^x}{d\rho_{bl}} = -\sin\theta_{bl}\cos\phi_{bl} \quad (6.36)$$

$$\frac{d\rho_\nu^x}{d\rho_{bl}} = -\sin\theta_{bl}\sin\phi_{bl} \quad (6.37)$$

The equation for this variable change is nominally in the form of an eighth-order polynomial. By neglecting the mass of the leptonic b quark, it is reduced to a fourth-order polynomial; the solutions of which can be determined analytically, see section A.2 for details.

Integration over transverse momentum in the $t\bar{t}$ system allows for initial state radiation and non-vanishing p_T in the colliding partons. This is inconsistent with Equation 6.16; any implications are dealt with in tests of the method in simulated data, see section 8.1.2. The integration is performed directly in the x and y components of momentum in flat momentum space and is not weighted with a probability density function. It is normalized by the region of integration in each transverse component: $d\tilde{p}^i_{t\bar{t}} \equiv dp^i_{t\bar{t}}/\int dp^i_{t\bar{t}}$. The region of integration, $\pm$ 30 GeV/c, covers the majority of the distribution of transverse momentum components observed in the $t\bar{t}$ system in HERWIG simulated events. The expression for the probability density becomes

$$P(\vec{x}) = \frac{1}{\sigma_{t\bar{t}}} \int d\sigma(\vec{y})\ f(\tilde{q}_1) f(\tilde{q}_2)\ W(\vec{x},\vec{y})\ d\tilde{q}_1 d\tilde{q}_2\ d\tilde{p}^x_{t\bar{t}} d\tilde{p}^y_{t\bar{t}}. \quad (6.38)$$

After the variable transformation, narrow-width approximation, Equation 6.26, and integration over transverse momentum, the phase space is expressed as

$$d\tilde{\Phi} = \frac{1}{(2\pi)^{18}2^6} \frac{1}{2E_p E_{\bar{p}}} \frac{1}{J} \frac{(\rho^y_{bh})^2(\rho^y_{j1})^2(\rho^y_{j2})^2(\rho^y_{bl})^2}{(\rho^x_{bh})^2(\rho^x_{j1})^2(\rho^x_{j2})^2(\rho^x_{bl})^2} \frac{dm^2_{Wh} dm^2_{Wl} d\rho_{j1} d\tilde{p}^x_{t\bar{t}} d\tilde{p}^y_{t\bar{t}}}{E_{bh}E_{j1}E_{j2}E_{bl}E_e E_\nu}. \quad (6.39)$$

The final form of the probability density includes symmetrization of the hadronic W boson decay in the matrix element, Equation 6.25, reducing the number of jet-parton permutations to 12; and a sum of up to four valid solutions from the change of variables

$$P(\vec{x}; m_t, JES) = \frac{1}{\sigma_{t\bar{t}}} \sum_{\text{perm}}^{12} \int \sum_{\text{soln}}^{4} |\mathcal{M}|^2 \frac{f(\tilde{q}_1)}{|q_1|} \frac{f(\tilde{q}_2)}{|q_2|} \prod_{i=1}^{4} [W_{jet}(E_i^y, E_i^x, JES)] d\tilde{\Phi}. \tag{6.40}$$

The sum over solutions is evaluated inside the integration. The sum over permutations is evaluated outside the integration and further reduced by secondary vertex tagging, section 4.4.3. Displaced vertex jets are assumed to be from b hadrons resulting from the decay of the top quark. Only permutations matching a displaced vertex jet with a b quark are used. This reduces the total number of permutations to 6 in the case of one tag and 2 in the case of two tags. All 12 permutations are evaluated for events with more than 2 tags, although none occur in the dataset used for this analysis. Equation 6.40 is divided by the number of permutations so that events with one tag and two tags contribute to the likelihood sum with equal weight.

Finally, an additional variable change is made to smooth out the W boson Breit-Wigners in the integrand in Equations 6.24 and 6.25

$$\int \frac{dm^2}{(m^2 - M^2)^2 + M^2\Gamma^2} \rightarrow \int \frac{d\mu}{M\Gamma} \tag{6.41}$$

where m is the event mass and M is the pole mass. This implies μ is defined such that

$$m^2 = M\Gamma \tan\mu + M^2. \tag{6.42}$$

Thus, the final form of the $t\bar{t}$ probability density does not contain any Breit-Wigners and is a smoothly varying function. The final integration is over the μ for the hadronic and leptonic W boson mass, the magnitude of momentum of one of the jets from hadronic W boson decay, and the two transverse components of

$t\bar{t}$ momentum. Limits of integration are $-\frac{\pi}{2} < \mu < \frac{\pi}{2}$, $0.5\text{GeV/c} < \rho_{j1} < E^{\max}_{\text{parton}}$, and $-30 < p^i_{t\bar{t}} < 30$ GeV/c, respectively. Details of limits on parton energies $E^{\max}_{\text{parton}}$ are given in section A.4.

6.3.3 $t\bar{t}$ Integration Technique

Integration in Equation 6.40 was performed using the `VEGAS` [55] Monte Carlo integration routine. Available as part of the `GSL` [54] package of computer routines, `VEGAS` is an adaptive algorithm based on importance sampling, which attempts to evaluate the integrand phase-space with a density proportional to its contribution to the integral. Relative contributions are estimated by sampling the phase-space several times, re-evaluating the density each time. In each iteration of phase-space sampling, a grid of phase-space points is thrown and the integral evaluated with a different random seed seven times. The χ^2 per degree of freedom deviation between integration results is computed. If it is between 0.5 and 1.5, the final integration is performed, otherwise, another iteration of phase-space sampling is performed. Grid estimation used 1000 Monte Carlo points and final integration used 10000 points. `VEGAS` typically estimated integration errors to be on the order of 0.1%. This error is not included in the likelihood.

Each of the 12 possible jet-parton permutations for each point scanned in the likelihood requires the evaluation of the integrals in Equation 6.40. This analysis scanned 31 m_t points and 17 JES points, for a total of 6324 integrations. `VEGAS` performed this integration in about 3 seconds per point or 4 hours per event. Using the large resources of distributed computing available, over 20 CPU years on 2 GHz machines were required to complete this analysis.

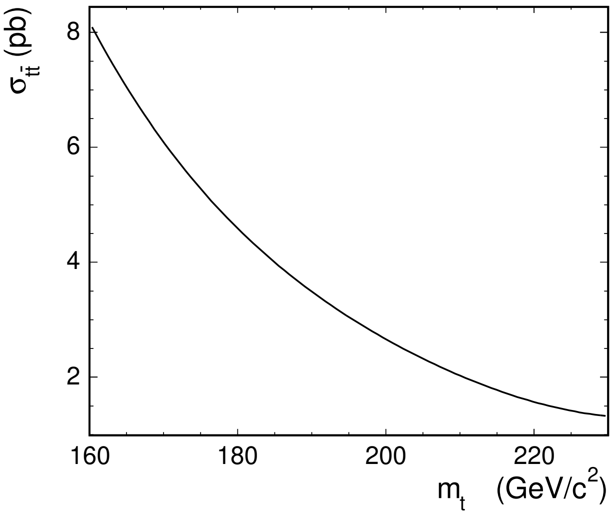

Figure 6.6: $t\bar{t}$ total cross section as function of m_t from `PYTHIA`

6.3.4 $t\bar{t}$ Normalization

The $t\bar{t}$ probability density is normalized with the total cross-section to remove dependence on top quark mass and is independent of JES. Rather than integrating over all the measured quantities in equation 6.40 for each m_t and JES point, the normalization is approximated with a parameterization of the leading-order cross-section given by `PYTHIA`. Figure 6.6 shows this cross-section as a function of top quark mass.

6.4 Details Specific to the W + jets Probability Density

The main purpose of the W + jets probability density is to model the main source of background events. Its matrix element comes from several leading-order diagrams coded in the `VECBOS` Monte Carlo event generator [56]. All jets are assumed to be produced from gluons or u, d, s or c quarks of zero mass. A simple variable change from equation 6.22 is made and custom integration is used. Normalization of the probability density is independent of the top quark mass and JES parameters. The probability density enters the likelihood with a dependence on JES, but is evaluated at a single JES point. JES dependence relative to this point is parameterized with simulated data to reduce the time required to evaluate each event.

6.4.1 W + jets Matrix Element

The W + jets probability density uses an inclusive leading-order matrix element calculated with the `VECBOS` Monte Carlo event generator for W + 4 jets [56]. Version 3.0 of `VECBOS` is tuned with CDF Run II parameters. The amplitude squared includes a sum over quark flavors (u, d, s, c), averages over initial spins and sums over final spins, and includes the sum of several possible diagrams of W + jets production. See Section 5.3 for a discussion of the approximation of modeling W + four jets production from W + four partons.

6.4.2 W + jets Integration Variables

Compared to equation 6.22, integration variables are modified only from the longitudinal component of the neutrino momentum. This variable is transformed to the mass of the W boson squared m_W^2, see section A.3. The phase space becomes

$$\Phi_6 = \frac{1}{2^8(2\pi)^{14}} \frac{1}{E_e|E_e p_{z\nu} - p_{ze}E_\nu|} dm_W^2 \prod_{i=1}^{4} \frac{E_i dp_i}{(p_i^x)^2}, \tag{6.43}$$

where x denotes a reconstruction level quantity and all others are parton level quantities. The final probability density includes a sum over two possible solutions for neutrino longitudinal momentum

$$P_{W+jets}(\vec{x}; JES) = \int \sum_{\text{soln}}^{2} \sum_{\text{perm}}^{24} |\mathcal{M}|^2 \frac{f(\tilde{q}_1)}{|q_1|} \frac{f(\tilde{q}_2)}{|q_2|} \prod_{i=1}^{4} [W_{jet}(E_i^y, E_i^x, JES)] d\Phi_6. \tag{6.44}$$

No total cross-section normalization is used, because it does not depend on the mass of the top quark, see section 6.4.4. Both sums are evaluated inside the integral, so the W + jets probability density is not a function of the permutation as is the $t\bar{t}$ probability density, see Equation 6.40. Note that there are always two possible solutions for the longitudinal neutrino momentum, but either or both of these solutions may not be consistent with the constraint on transverse mass described in section 6.4.3, which also discusses integration limits.

6.4.3 W + jets Integration Techniques

The W + jets probability density described by equation 6.44 includes four integrations over the large intervals of possible parton energies and the relatively narrow interval of the W boson mass. This process requires numerous evaluations of the matrix element and is very CPU intensive. Since the W + jets matrix element is not analytic and more complex in general than the $t\bar{t}$ matrix element, it requires much more time to be evaluated. In this case, `VEGAS` integration would not produce convergent results in a reasonable amount of time. A customized Monte Carlo method of integration was developed with reasonable convergence in relatively minimum CPU time. To reduce the demand on CPU further, the

JES dependence in the W + jets probability density is approximated and only evaluated at a single likelihood point, see section 6.4.4.

The customized method of integration utilizes knowledge of the shape of the parton energy distributions from the transfer function, see section A.4. For a given event, several iterations of parton energies are thrown based on the measured jet energy. The W boson mass is assumed to be 80.4 GeV/c^2, and the transverse mass of the charged lepton and neutrino system is constrained to be less than this value. The reported background probability density for an event is the average probability density obtained from the Monte Carlo iterations.

A convergence test in conjunction with CPU evaluation time was used to select 400 Monte Carlo iterations per event. Figure 6.7 shows the variation in the probability density as a function of the number of iterations using 100 simulated $W \to e\nu + 4p$ events. Average CPU evaluation time scales linearly with the number of iterations as 2 seconds per iteration up to 2000 iterations. The choice of 400 iterations results in a maximum of 20% error on the value of the probability density, requiring about 13 minutes to process one event. These results were tabulated with a Pentium III, 1 GHz processor. This level of convergence is not good enough for the sensitivity required for the top quark mass, but the W + jets probability density functions primarily as a discriminant and does not affect sensitivity to the top quark mass as greatly.

6.4.4 W + jets Normalization

No explicit dependence on top quark mass exists in the W + jets probability density. Any overall constant in its normalization does not affect the outcome of the likelihood, up to the relative $t\bar{t}$ to W + jets normalization discussed in section 6.5. No further normalization is applied to the W + jets probability

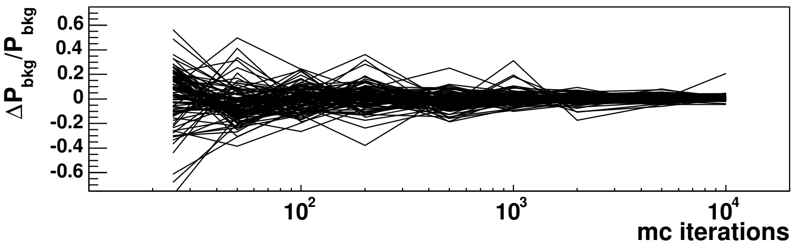

Figure 6.7: Fractional variation in W + jets probability density as a function of Monte Carlo iterations.

density.

The W + jets probability density is not expected to be strongly sensitive to the jet energy scale because it does not contain a hadronic W boson resonance. No measurement per event is possible in this case. In order to reduce CPU time in integration, the probability density is evaluated at a single JES point, the nominal JES = 1. JES dependence is assumed to be factorisable such that

$$P_{W+jets}(\vec{x}; JES) = f(JES)\ P_{W+jets}(\vec{x}; JES = 1). \tag{6.45}$$

The JES dependence, $f(JES)$, is parameterized using simulated data. Figure 6.8 shows the average likelihood response per event of simulated W + $4p$ events relative to the average response at JES = 1. Also shown are the ratio of average likelihood responses of simulated $Wb\bar{b}$ and $t\bar{t}$ events to W + $4p$ events. Within error, no significant deviations are observed between these processes, and the linear dependence of average likelihood response per event as a function of JES is parameterized with

$$f(JES) = 1 - 1.67 \cdot JES \tag{6.46}$$

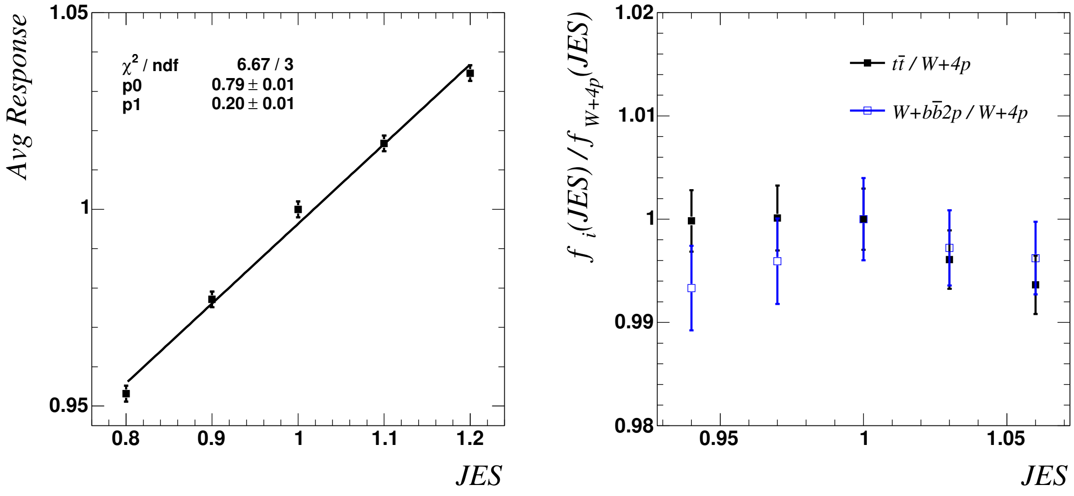

Figure 6.8: Average likelihood response of W + jets probability density as a function of JES in simulated $W + 4p$ events (left). Ratio of average likelihood response in simulated $t\bar{t}$ and $Wb\bar{b}$ events to $W + 4p$ events as a function of JES (right).

6.5 Relative $t\bar{t}$ and W + jets Normalization

As mentioned in section 6.1.1, the $t\bar{t}$ and W + jets probabilities are normalized up to constants in terms of the maximized variables. Since an overall constant factor does not change the output of the likelihood maximization, the only important remaining normalization is the relative constant normalization between the two probabilities. Explicitly, this normalization, R_{bkg}, enters the sum of the probabilities in Equation 6.4 as

$$P(\vec{x}; m_t, JES, C_s) = C_s P_{t\bar{t}}(\vec{x}; m_t, JES) + (1 - C_s) R_{bkg} P_{W+\text{jets}}(\vec{x}; JES), \quad (6.47)$$

and is determined empirically using simulated $t\bar{t}$ events generated with the `HERWIG` Monte Carlo generator at a top quark mass of 175 GeV/c^2. Results are consistent within samples generated at other masses.

Due to radiation, detector geometry, resolution, jet clustering and inefficiencies in event reconstruction, not every jet passing selection is expected to correspond to one of the quarks from $t\bar{t}$ decay. This correspondence is determined by matching jet and parton position in detector η-ϕ space within a cone of radius 0.4, and is identical to the requirement used in fitting jet energy transfer function parameters in Section 7.2. Because the angles of the jets are assumed to correspond exactly to the angles of the partons from tree-level decay, jets which do not match input disinformation to the event probabilities. All four jets matched in 77% of the simulated $t\bar{t}$ data used for this study. Empirically, $t\bar{t}$ events with fewer matched jets tend to have a higher W + jets probability density than events with more matched jets, Figure 6.9. This feature is used to reduce the effects of events with disinformation.

Adjusting the relative normalization constant, R_{bkg}, affects the signal fraction, C_s, output from the likelihood. There is a strong negative correlation between

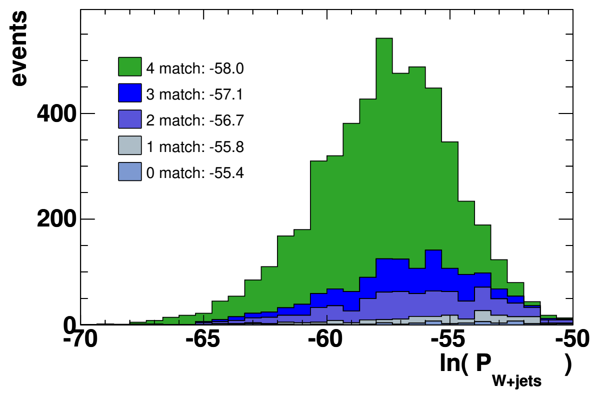

Figure 6.9: W + jets probability density of $t\bar{t}$ events separated by the number of jets matched to partons

R_{bkg} and C_s: as expected, a maximized likelihood with a value of $R_{bkg} = 0$ returns $C_s = 1$ and a very large R_{bkg} returns C_s near 0. Because top quark events with mismatched jets are more likely to have a relatively higher W+jets probability density, the influence of these events on the likelihood shape is reduced compared to fully matched events. In the likelihood, R_{bkg} was adjusted such that the C_s output is equivalent to 0.77, the fraction of events in simulated $t\bar{t}$ events with all four jets matched to partons.

The effects of varying R_{bkg} (and thus C_s) on the output of the maximized likelihood are shown in Figure 6.10. Outputs include the estimated and expected errors, the pull RMS (Equation 8.1), and the top quark mass. At C_s of about 77% the expected and estimated errors coincide, corresponding to a pull RMS of unity. By a barely significant amount, the best sensitivity (smallest expected error) coincides with this point. The small variation with R_{bkg} in the output top quark mass, on the order of 0.13 GeV/c^2, is not considered a source of systematic error because the R_{bkg} factor is applied consistently throughout this analysis.

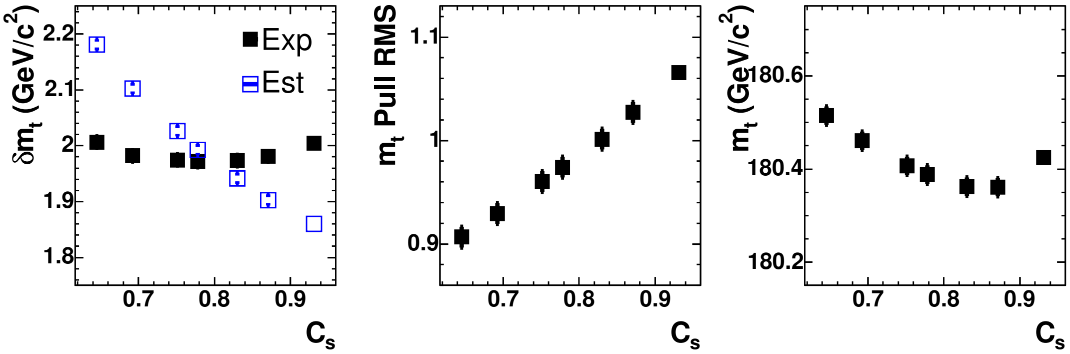

Figure 6.10: Estimated and expected error (left), pull RMS (center), and top quark mass (right), as a function of signal fraction and therefore different normalization constants.

Note that in setting the relative $t\bar{t}$ and W + jets normalization in this manner, C_s does not correctly indicate the true content of $t\bar{t}$ events in the measured sample. The measurement estimates the number of $t\bar{t}$ events consistent with four matched jets and will thus be an underestimate of the true $t\bar{t}$ content. A mapping derived from simulated data is used to estimate the true content and is discussed in section 8.1.2.2.

CHAPTER 7

Parton-Jet Transfer Functions

Transfer functions provide a mapping from reconstruction level quantities measured with the detector to parton level quantities used in the differential cross-section. This analysis assumes everything but jet energies are well measured. They are the only non-trivial parameterization in the transfer function. As discussed in section 4.4.2, jet energies are corrected to remove detector effects using generic corrections, but the final calibration to parton level depends on topology and the underlying hard-scattering process. Simulated $t\bar{t}$ events passing selection are used to determine the final mapping to parton level. One advantage in matrix element analyses is their integration over the jet energy resolution: they correctly incorporate the asymmetric jet-parton energy mapping. Other analyses often use only the most probable value and assume Gaussian resolution.

7.1 Definition

The full transfer function is given in Equation 6.19. Delta-functions map the measured charged lepton momentum and jet angles to parton level because CDF is assumed to have perfect resolution in these quantities. Jet energy mapping is parameterized with the jet energy transfer function, $W_{jet}(E_{jet}, E_{parton}, JES)$. The JES dependence in the transfer function is assumed to apply as

$$W_{\text{jet}}(E_{\text{jet}}, E_{\text{parton}}, JES) = W_{\text{jet}}(JES \cdot E_{\text{jet}}, E_{\text{parton}}) \tag{7.1}$$

where $W_{jet}(E_{jet}, E_{parton})$ is defined to be the jet energy transfer function at the nominal jet energy scale in simulated data (JES = 1). Tests of the assumption in Equation 7.1 are discussed in section 7.3.1. For convenience, the jet energy transfer function at the nominal jet energy scale is referred to as the transfer function throughout this chapter.

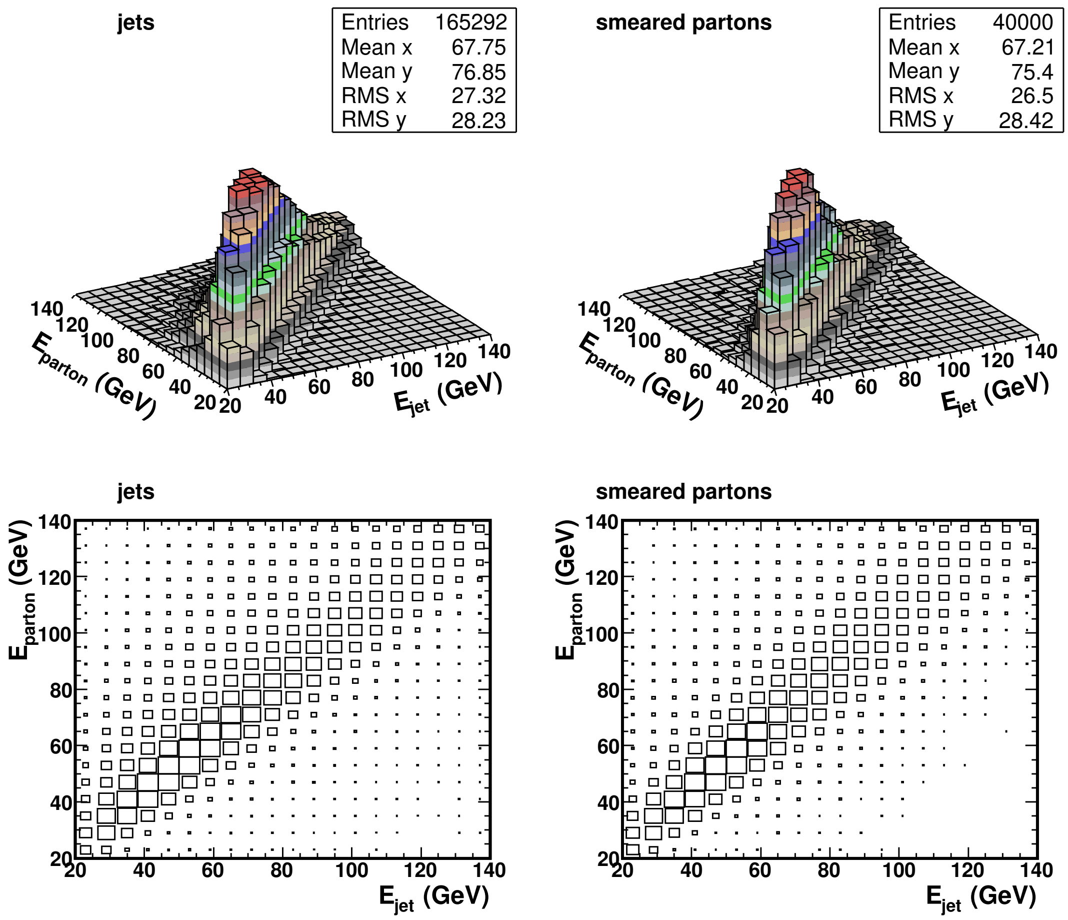

Figure 7.1: Distributions in two-dimensional E_{jet}-E_{parton} space with reconstructed jet energies (left) and jet energies simulated by smearing parton energies with the transfer function (right). Events were generated with a top quark mass of 178 GeV/c^2.

Transfer functions describe the two-dimensional E_{parton}-E_{jet} space. Figure 7.1 shows this two-dimensional space for reconstructed jet energies (left) and simulated jet energies using the transfer function to smear parton energies (right). Since the transfer function is defined as the probability of measuring a jet with energy E_{jet} given a parton with energy E_{parton}, it is normalized by

$$\int W_{\text{jet}}(E_{\text{jet}}, E_{\text{parton}}) dE_{\text{jet}} = 1. \tag{7.2}$$

A few assumptions are made. The first is that jet energies within an event are independent from one another such that all jets can be described with the same transfer function based on their energy. The second is that the transfer function is separable from the parton energy distribution and therefore independent from the mass of the top quark

$$n^2(E_{parton}, E_{jet}) dE_{jet} dE_{parton} = n(E_{parton}) dE_{parton} W_{jet}(E_{jet}, E_{parton}) dE_{jet}, \tag{7.3}$$

where $n^2(i, j)$ or $n(i)$ describes the appropriate two-dimensional or one-dimensional density of jets and/or partons in the event sample between E_i and $E_i + dE_i$ and E_j and $E_j + dE_j$ or E_i and $E_i + dE_i$, respectively.

The transfer function is parameterized using two Gaussian functions

$$W_{\text{jet}}(E_{\text{jet}}, E_{\text{parton}}) = \frac{1}{\sqrt{2\pi}(p_2 + p_3 p_5)} \Big[exp \frac{-(\delta_E - p_1)^2}{2p_2^2} + p_3 \; exp \frac{-(\delta_E - p_4)^2}{2p_5^2} \Big], \tag{7.4}$$

where $\delta_E \equiv E_{\text{parton}} - E_{\text{jet}}$ and p_i are fitted parameters. Figure 7.2 shows the two-dimensional distribution projected onto the δ_E axis. Since the hadronization process depends on quark flavor, the distributions differ for b quarks versus lighter (u, d, s, c) quarks. Parameters are fit separately for b quarks and the collected lighter quarks. Conceptually, the first Gaussian function describes the peak and the second the tails of the distribution in δ_E. The shape of this distribution depends on parton energy, as shown for the lighter quarks in in Figure 7.3 and for b quarks in Figure 7.4. Note that the relative normalization between plots in these figures is consistent, but does not correspond to that of Figure 7.2 or Equation 7.2. This dependence is approximated with a linear dependence on E_{parton} in the p_i parameters of Equation 7.4, $p_i = a_i + b_i E_{\text{parton}}$.

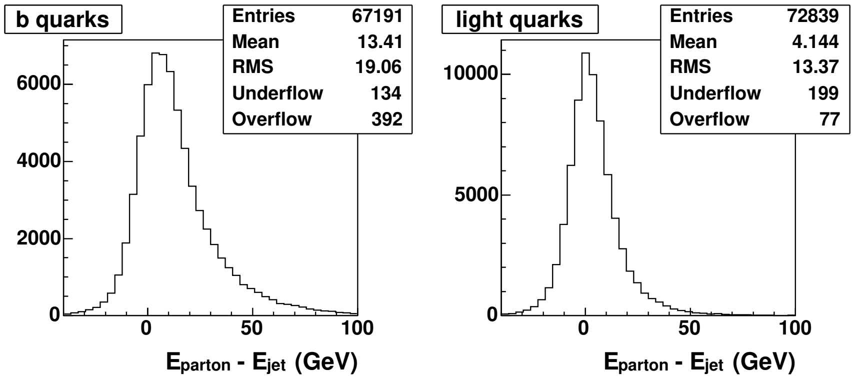

Figure 7.2: Distribution of $\delta_E \equiv E_{\text{parton}} - E_{\text{jet}}$ in simulated b quarks (left) and light (u, d, s, c) quarks (right) from $t\bar{t}$ events generated at a top quark mass of 178 GeV/c^2.

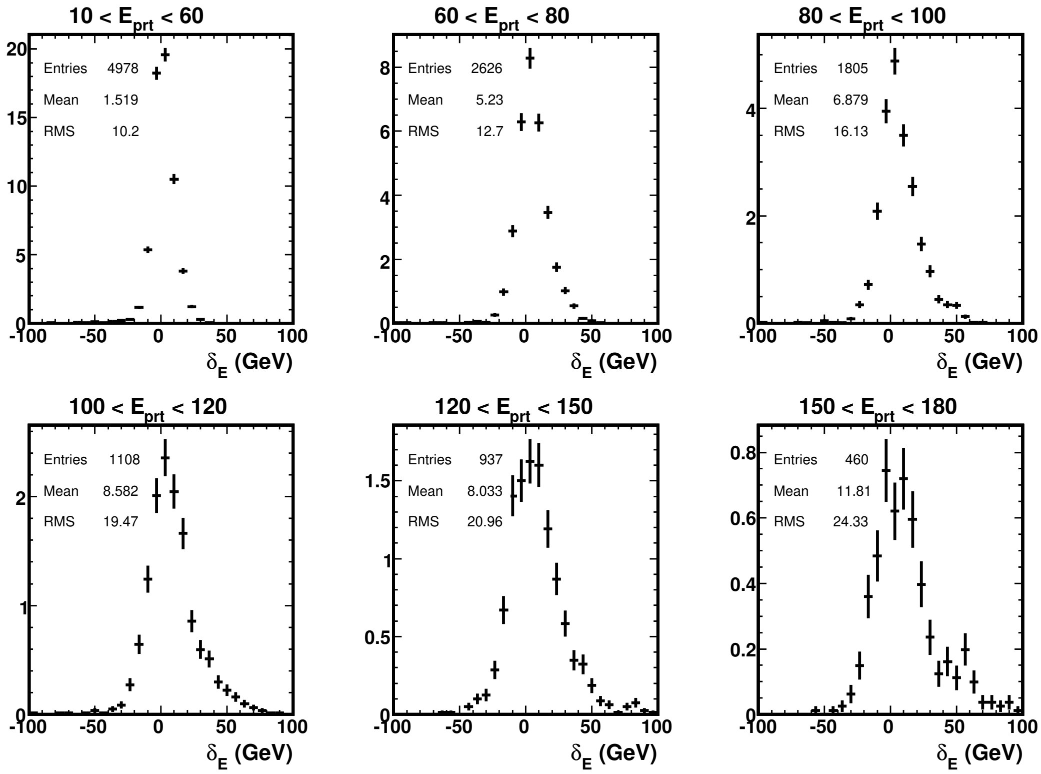

Figure 7.3: Dependence on $E_{\rm parton}$ of $\delta_E \equiv E_{\rm parton} - E_{\rm jet}$ distributions in simulated light (u, d, s, c) quarks from $t\bar{t}$ events generated at a top quark mass of 170 GeV/c^2.

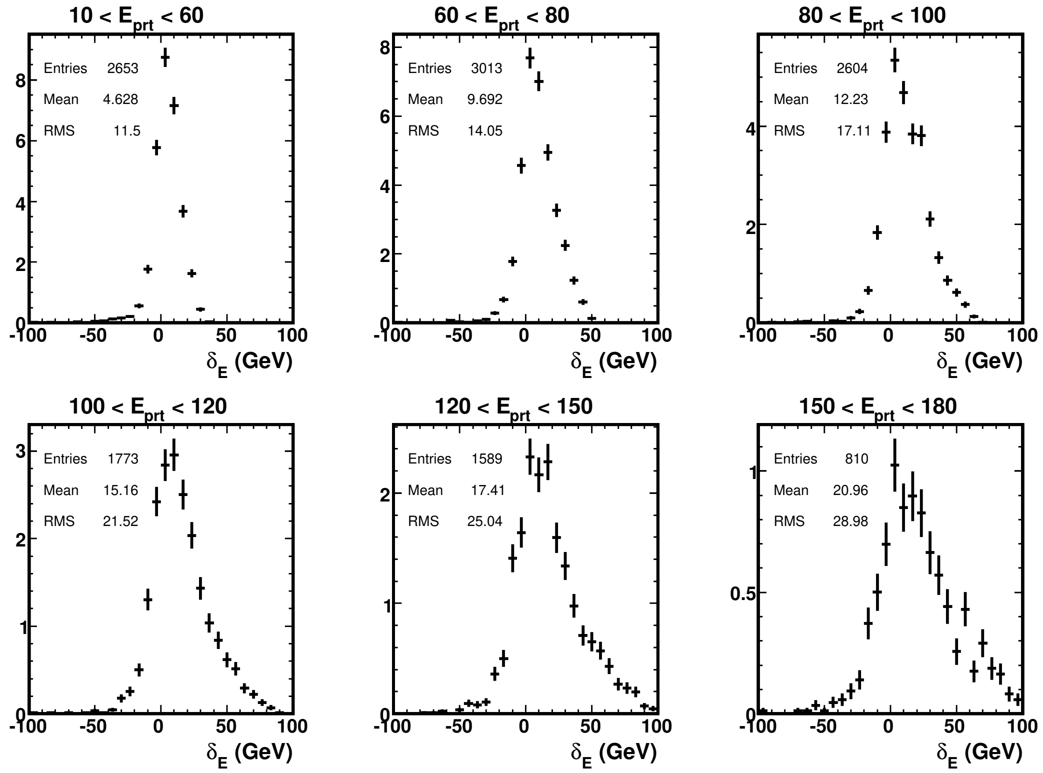

Figure 7.4: Dependence on E_{parton} of $\delta_E \equiv E_{\text{parton}} - E_{\text{jet}}$ distributions in simulated b quarks from $t\bar{t}$ events generated at a top quark mass of 170 GeV/c^2.

7.2 Parameterization with Simulated Data

Transfer function parameters are extracted from simulated $t\bar{t}$ data passing event selection using a likelihood fit. Several sets of parameters are extracted and compared using `HERWIG` and `PYTHIA` event generators. Partons are particles immediately decaying from the top quark or W boson and have not radiated or showered. It is necessary to match reconstructed jets with partons. Simulated data does not contain an exact mapping between jets and partons. Hadronization, radiation and detector simulation complicate the identification of jets with a specific parton from $t\bar{t}$ decay. Jets are often the product of hard radiation or partons closely overlapping in η-ϕ space forming a single jet rather than two individual jets.

Matching is performed by comparing jet and parton direction in η-ϕ detector space. A jet is required to be within a certain conical radius, $\Delta R \equiv \sqrt{\Delta\phi^2 + \Delta\eta^2}$, of the parton. Jet and parton pairs are selected according to the lowest ΔR separation, not allowing a jet or parton to overlap between pairs. An event is selected if all four pairs meet the maximum ΔR requirement. Matching modifies the event sample topology depending on the amount of allowed deviation between jet and parton direction and affects the outcome of parameterization. Figure 7.5 shows ΔR distributions for b quarks and light (u, d, s, c) quarks in simulated data generated with `HERWIG` at a top quark mass of 178 GeV/c^2.

An unbinned likelihood fit determines the transfer function parameters in Equation 7.4. After matching, each event contributes up to two b quarks and two light quarks from W boson decay. The likelihood is derived from Equation 7.3 and is evaluated separately for b quarks and W daughters

$$-ln\mathcal{L} = -\sum_{i=1}^{N} ln\ n(E_{\mathrm{parton}}) - \sum_{i=1}^{N} ln\ W_{\mathrm{jet}}(E_{\mathrm{jet}}, E_{\mathrm{parton}}). \tag{7.5}$$

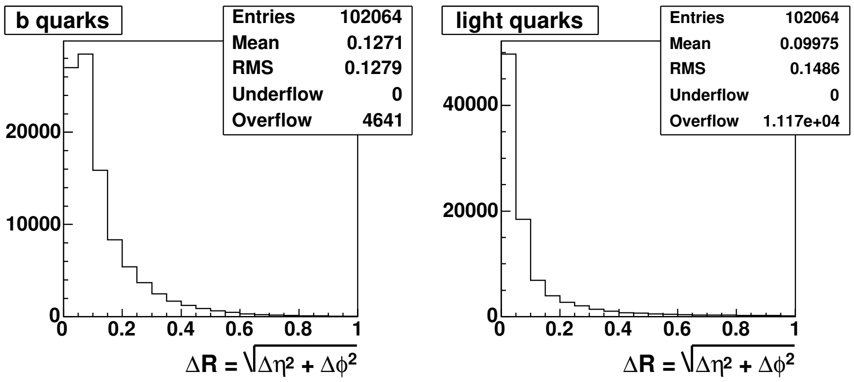

Figure 7.5: Distribution of ΔR matching between jets and partons in simulated data for b quarks (left) and light (u, d, s, c) quarks (right).

The first term has no dependence on the parameters and is ignored. MINUIT fits the parameters and estimates their errors summing over a maximum of 10,000 matched pairs in a given simulated data sample.

Several sets of transfer function parameters were fit with various requirements. The parameters used for the top quark mass measurement were extracted from PYTHIA simulated events generated with a top quark mass of 178 GeV/c^2 using matching of $\Delta R < 0.4$ and the entire η-ϕ region of the detector, Table 7.1. Parameters determined with other generators and/or other matching requirements were used in tests and cross-checks, see Section 7.3, and validation, see Section 7.4. The parameters chosen for the top quark mass measurement were determined in part by the outcome of studies described in these sections.

Four sets of cross-check parameters were fit, all using simulated events generated with a top quark mass of 178 GeV/c^2: three derived from HERWIG and one from PYTHIA. They have an additional isolation requirement such that two jets passing nominal selection or two partons cannot be within $\Delta R < 0.6$ of each other. Two of the HERWIG sets are fit using the entire η-ϕ region of the detector with matching requirements of $\Delta R < 0.15$ and $\Delta R < 0.4$, Table 7.2 and Table 7.3, respectively. The set fit from `PYTHIA` uses the entire η-ϕ region of the detector and a matching requirement of $\Delta R < 0.15$, Table 7.4. The third set from `HERWIG` are fit in binned sections of detector η and use a matching requirement of $\Delta R < 0.15$, Table 7.5 and Table 7.6. The η bin regions, $0 < |\eta| < 0.2$, $0.2 < |\eta| < 0.6$, $0.6 < |\eta| < 0.9$, $0.9 < |\eta| < 1.4$ and $1.4 < |\eta| < 2.0$, were chosen for consistency with variations in jet energy systematic uncertainty estimated by the CDF JER group [33].

Table 7.1: `PYTHIA` non η-dependent, $\Delta R < 0.4$ parameters (used in measurement).

	light quark jets		b quark jets	
$p_i = a_i + b_i E_{parton}$	a_i	b_i	a_i	b_i
p_1 (GeV)	1.779668	-0.076186	-3.537469	-0.036760
p_2 (GeV)	1.887788	0.113952	3.726674	0.075021
p_3	0.000000	0.000294	0.000000	0.001766
p_4 (GeV)	39.243978	-0.619110	16.022991	-0.383466
p_5 (GeV)	31.261185	0.021547	15.205335	0.105315

Table 7.2: `HERWIG` non η-dependent, $\Delta R < 0.15$ parameters

	light quark jets		b quark jets	
$p_i = a_i + b_i E_{parton}$	a_i	b_i	a_i	b_i
p_1 (GeV)	1.09923	-0.0522277	-1.59438	-0.0473066
p_2 (GeV)	2.02192	0.103122	2.77686	0.0737285
p_3	0.0506705	5.69989e-12	0.413792	1.78746e-12
p_4 (GeV)	25.0381	-0.531444	5.57249	-0.261912
p_5 (GeV)	10.9866	0.114647	0.991688	0.197914

Table 7.3: `HERWIG` non η-dependent, $\Delta R < 0.4$ parameters

	light quark jets		b quark jets	
$p_i = a_i + b_i E_{parton}$	a_i	b_i	a_i	b_i
p_1 (GeV)	1.24399	-0.0696011	-3.66376	-0.0338927
p_2 (GeV)	2.46904	0.110541	3.17748	0.0784294
p_3	0.0172778	0.000144707	0.384582	1.21431e-09
p_4 (GeV)	38.1079	-0.67746	9.3725	-0.300313
p_5 (GeV)	22.574	0.0454405	5.21558	0.176317

Table 7.4: PYTHIA non η-dependent, $\Delta R < 0.15$ parameters

	light quark jets		b quark jets	
$p_i = a_i + b_i E_{parton}$	a_i	b_i	a_i	b_i
p_1 (GeV)	1.61338	-0.0661955	-2.5913	-0.0308291
p_2 (GeV)	1.96434	0.105353	2.3282	0.0775365
p_3	3.48876e-11	0.000440751	0.280996	1.4981e-09
p_4 (GeV)	18.574	-0.398868	10.3548	-0.327036
p_5 (GeV)	16.863	0.115175	3.57095	0.168435

Table 7.5: HERWIG η-dependent, $\Delta R < 0.15$ parameters

	light quark jets		b quark jets	
$p_i = a_i + b_i E_{parton}$	a_i	b_i	a_i	b_i
$0.0 < \lvert\eta\rvert < 0.2$				
p_1 (GeV)	0.258781	-0.040627	-2.43418	-0.0470396
p_2 (GeV)	0.790448	0.133943	2.02772	0.0887038
p_3	0.127939	3.44169e-14	0.518893	4.59577e-11
p_4 (GeV)	18.4516	-0.495877	10.6732	-0.364515
p_5 (GeV)	4.54502	0.193371	3.31059	0.168388
$0.2 < \lvert\eta\rvert < 0.6$				
p_1 (GeV)	1.24031	-0.0590222	-1.22801	-0.048967
p_2 (GeV)	1.56601	0.104045	1.322	0.0842175
p_3	0.0285821	5.77316e-13	0.365415	3.49249e-09
p_4 (GeV)	19.6473	-0.44556	7.72854	-0.297383
p_5 (GeV)	3.73394	0.27307	2.19713	0.17331
$0.6 < \lvert\eta\rvert < 0.9$				
p_1 (GeV)	0.65426	-0.0824347	-2.60365	-0.0396823
p_2 (GeV)	0.6616	0.111052	2.68585	0.0819051
p_3	0.00835448	0.000243034	0.375112	4.34532e-09
p_4 (GeV)	8.7735	-0.738859	7.90805	-0.288673
p_5 (GeV)	1.1265	-0.00329004	2.29644	0.184217

Table 7.6: HERWIG η-dependent, $\Delta R < 0.15$ parameters (continued)

	light quark jets		b quark jets	
$p_i = a_i + b_i E_{parton}$	a_i	b_i	a_i	b_i
$0.09 < \lvert\eta\rvert < 1.4$				
p_1 (GeV)	4.78823	-0.0936547	-0.121987	-0.0714796
p_2 (GeV)	1.70108	0.118585	2.99938	0.0836469
p_3	0.0128375	0.000171554	0.323027	0.000190321
p_4 (GeV)	40.5982	-0.620804	12.4818	-0.303603
p_5 (GeV)	19.7934	0.0673071	2.30887	0.185047
$1.4 < \lvert\eta\rvert < 2.0$				
p_1 (GeV)	5.36653	-0.0754567	-0.79356	-0.0417387
p_2 (GeV)	3.72446	0.067595	3.23225	0.0635439
p_3	0.0396169	2.7401e-05	0.299744	6.55187e-11
p_4 (GeV)	38.8061	-0.466476	19.0147	-0.31458
p_5 (GeV)	13.5561	0.116469	4.63328	0.159609

7.3 Tests and Cross-Checks

Quality of the transfer function parameterization is checked by comparing distributions of reconstruction level quantities with predictions obtained using the transfer function and parton level quantities in simulated data. Two types of tests are performed. The first is one-dimensional and compares binned projections of Figure 7.1 along different axes. The second compares invariant masses of the four vector sum of two jets from W boson decay or three jets from top quark decay. Since they are correlated with the JES and m_t variables in the likelihood, the two-jet and three-jet invariant masses are used to estimate possible effects due to transfer function parameterization.

Several plots in this section show a χ^2 deviation in the upper right hand corner. It is calculated as a function of bin offset between histogram and prediction, using bins with at least 10 entries around the peak of the distribution, and fit with a second order polynomial. The minimum of the fit estimates the offset between histogram and prediction with an uncertainty given by the width at a χ^2 deviation of unity. Estimated offset (shift) and width are printed with the plot statistics. The shift is always defined as prediction minus reference. Since matching and event selection modify the topology of events, it is necessary to keep these requirements consistent between histogrammed and predicted quantities.

7.3.1 One-dimensional Checks

One-dimensional checks compare three projections of of Figure 7.1: E_{jet}, E_{parton}, and $\delta_E \equiv E_{\text{parton}} - E_{\text{jet}}$. These projections are binned in E_{parton}, E_{jet} and E_{parton}, respectively, in the ranges $10 < E < 60$, $60 < E < 80$, $80 < E < 100$, $100 < E < 120$, $120 < E < 150$, and $150 < E < 180$ GeV. Reconstruction level quantities are histogrammed. Predicted distributions, H, are analytical and calculated by integrating the transfer function with the parton energy spectrum, $n(E_{parton})$,

$$
\begin{aligned}
H(E_{jet}) &= \int_{E^1_{parton}}^{E^2_{parton}} n(E_{parton})\, W_{jet}(E_{jet}, E_{parton})\, dE_{parton} \\
H(E_{parton}) &= \int_{E^1_{jet}}^{E^2_{jet}} n(E_{parton})\, W_{jet}(E_{jet}, E_{parton})\, dE_{jet} \qquad (7.6)\\
H(\delta_E) &= \int_{E^1_{parton}}^{E^2_{parton}} n(E_{parton})\, W_{jet}(E_{parton} - \delta_E, E_{parton})\, dE_{parton}
\end{aligned}
$$

The integral over dE_i covers the bin range of the histogrammed jet distribution.

The parton energy spectrum, $n(E_{parton})$, is an analytical function parameterized by fitting to the parton energy distribution. The analytical function has different forms for W daughters and b quarks:

$$
\begin{aligned}
n(E^{\text{lightquarks}}_{\text{parton}}) &= c_1\, exp\frac{(c_2 - E_{\text{parton}})^2}{2c_3^2} + c_4\, exp\frac{(c_5 - E_{\text{parton}})^2}{2c_6^2} \\
n(E^{\text{b-quarks}}_{\text{parton}}) &= c_1(E_{\text{parton}} - c_2)^{c_3}\, exp[-c_4(E_{\text{parton}} - c_2)] \qquad (7.7)
\end{aligned}
$$

Table 7.7 lists parameters derived from $t\bar{t}$ events simulated with HERWIG at a top quark mass of 178 GeV/c^2. Figure 7.6 shows good agreement between the parton energy distribution at reconstruction level (histogram in 6 GeV bins) and parameterization (dotted line).

Table 7.7: Parton energy spectrum parameters corresponding to Equation 7.7.

	c_1	c_2	c_3	c_4	c_5	c_6
light quarks	242.08	-676.23	184.77	-0.30182	-3.8753	25.611
b quarks	0.22263	38.792	1.21023	0.032703	0.016693	-

Figure 7.7 to Figure 7.12 compare histogrammed reconstruction level distributions with those calculated from Equation 7.7, using the transfer function parameters listed in Table 7.1. Simulated $t\bar{t}$ data was generated with HERWIG at a top

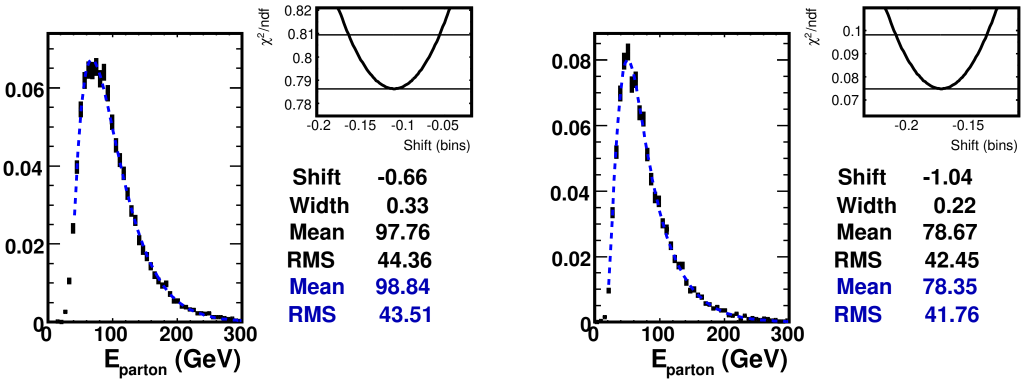

Figure 7.6: Distribution of jet energy compared to fitted functions for b-jets (left) and W-jets (right).

quark mass of 172.5 GeV/c^2. Histogram bins are 10 GeV for $E_{\rm jet}$ and $E_{\rm parton}$ and 6.6 GeV for δ_E. The relative normalization between histogram and prediction is set such that they have equal integrals and not by Equation 7.7. Offsets between histogram and prediction are generally smallest for $60 < E_{parton} < 120$ GeV, where the largest number of statistics are available for fitting transfer function parameters.

The assumption concerning implementation of jet energy scale in the transfer function, Equation 7.1, is tested using the δ_E distribution across the full range of $E_{\rm parton}$. Simulated $t\bar{t}$ data was generated with `HERWIG` at a top quark mass of 178 GeV/c^2 and jet energy scales of 0.95, 1.00 and 1.05. Figure 7.13 compares histogrammed reconstruction distributions with predictions setting JES to the appropriate value in transfer functions using parameters in Table 7.1. No χ^2 test is performed, but good agreement in shape is observed for all JES values.

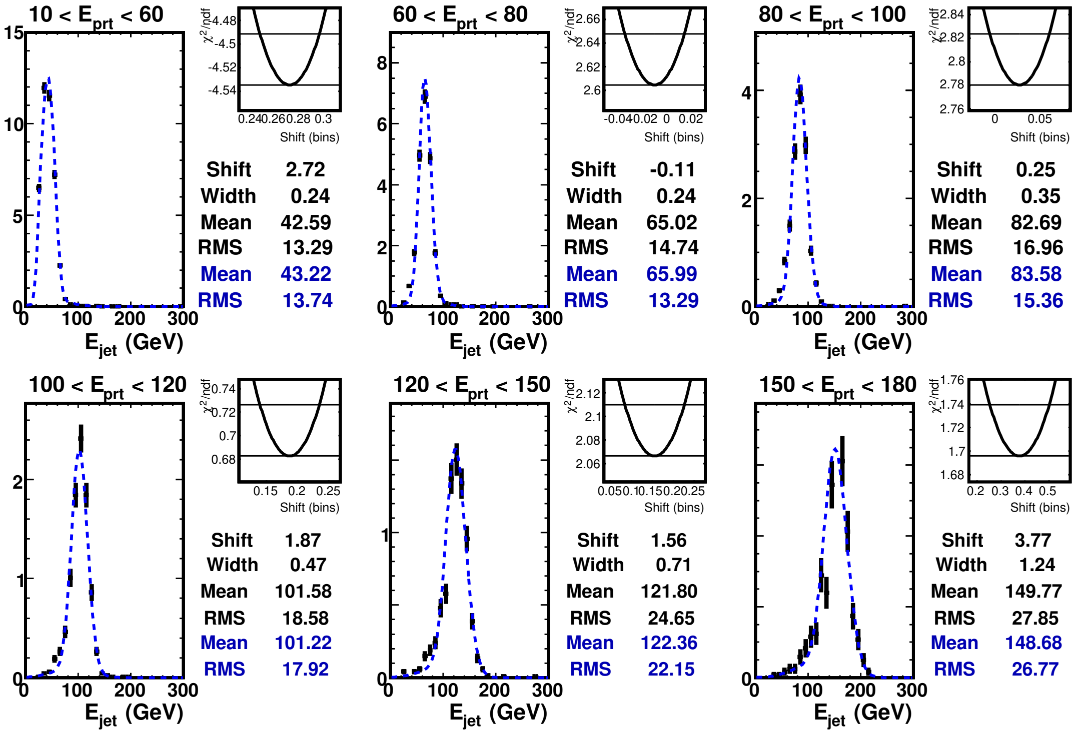

Figure 7.7: E_{jet} distribution in bins of E_{parton} compared to $H(E_{jet})$ prediction in jets from W boson decay.

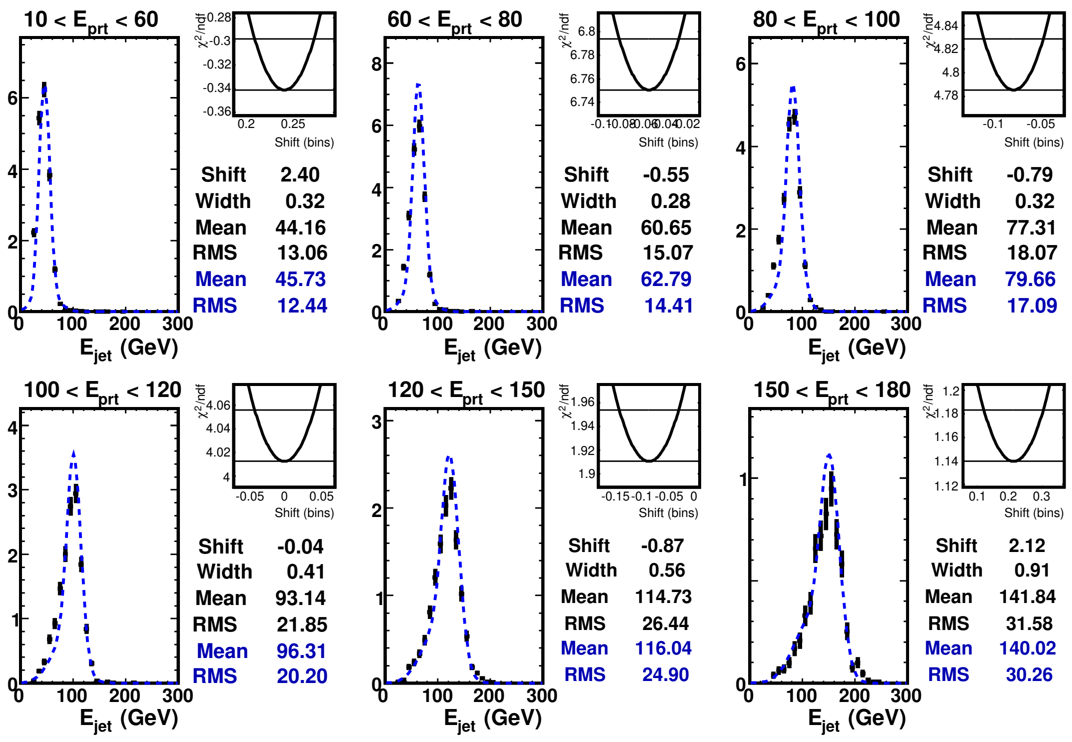

Figure 7.8: E_{jet} distribution in bins of E_{parton} compared to $H(E_{jet})$ prediction in b quark jets.

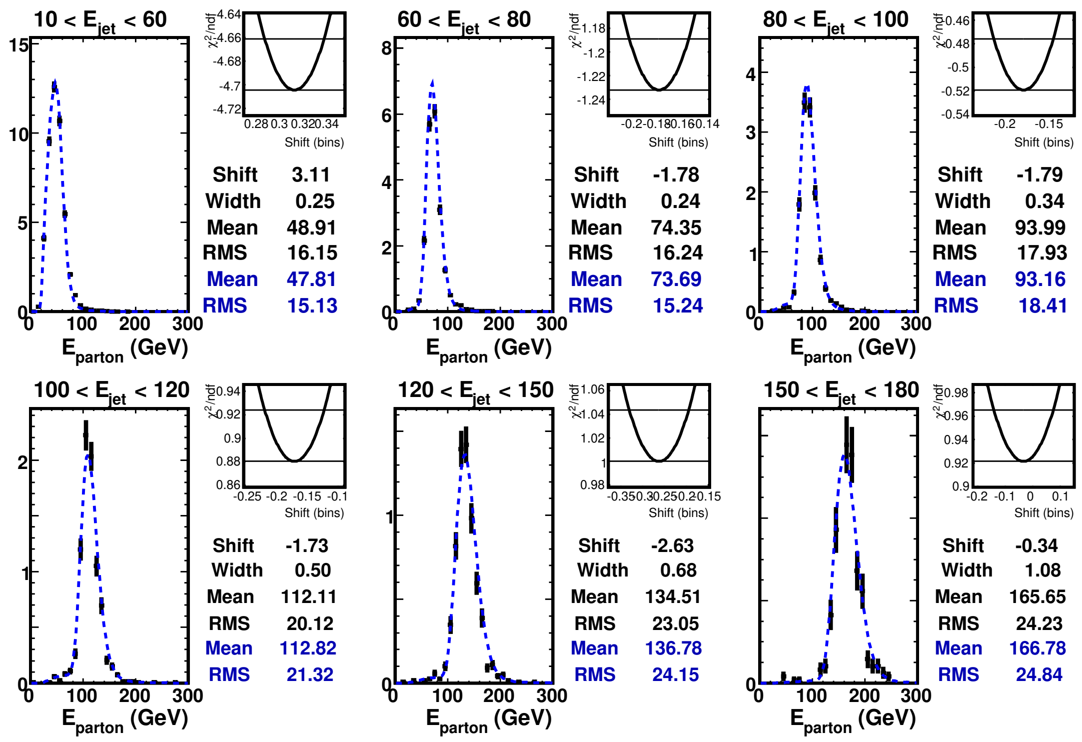

Figure 7.9: E_{parton} distribution in bins of E_{jet} compared to $H(E_{parton})$ prediction in jets from W boson decay.

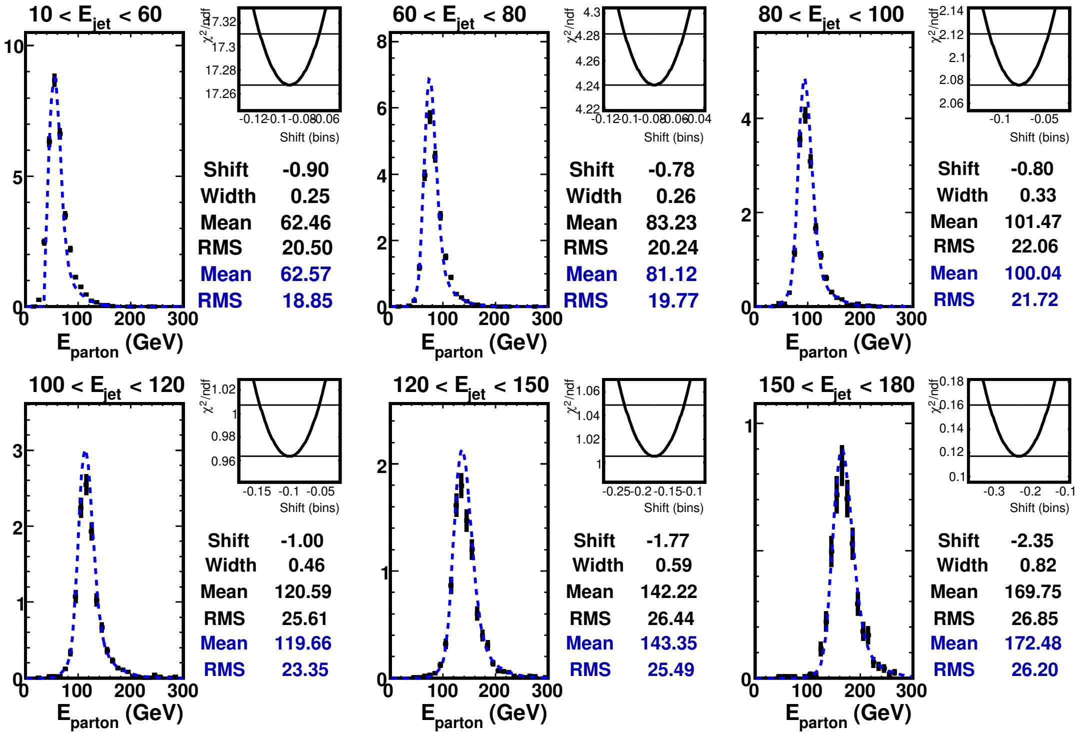

Figure 7.10: E_{parton} distribution in bins of E_{jet} compared to $H(E_{parton})$ prediction in b quark jets.

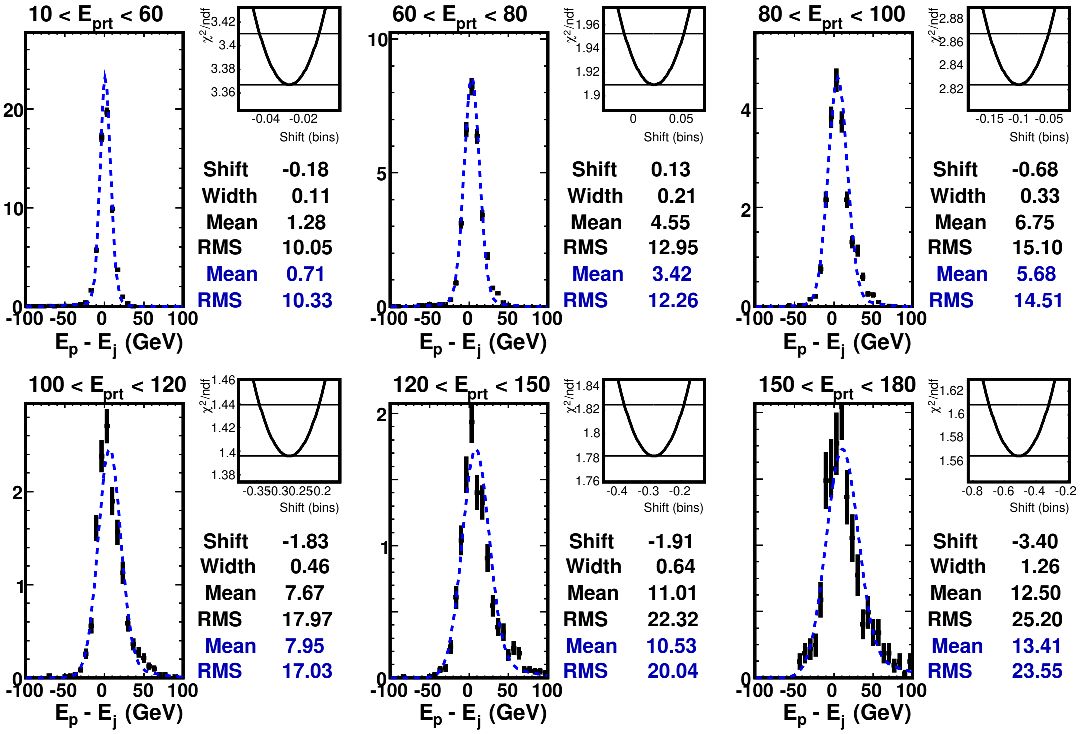

Figure 7.11: δ_E distribution in bins of E_{parton} compared to $H(\delta_E)$ prediction in jets from W boson decay.

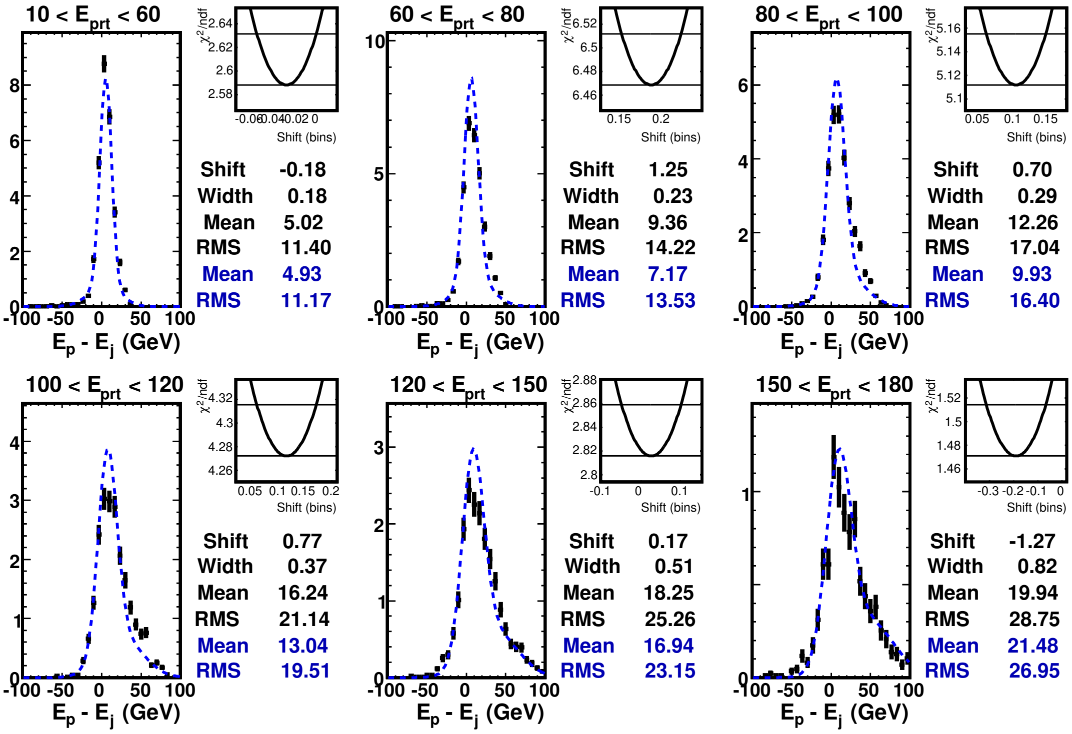

Figure 7.12: δ_E distribution in bins of E_{parton} compared to $H(\delta_E)$ prediction in b quark jets.

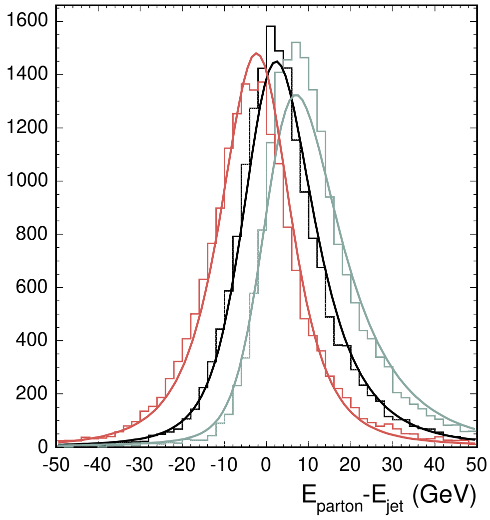

Figure 7.13: δ_E distribution and $H(\delta_E)$ prediction for JES values of 0.95 (red), 1.00 (black) and 1.05 (grey) in jets from W boson decay.

7.3.2 Two-jet and Three-jet invariant masses

A more sophisticated test of transfer function parameterization compares two-jet and three-jet invariant mass distributions. Reconstruction level quantities are calculated from the four-vector sum of jets in a simulated event. The two-jet invariant mass is nominally constructed from the two jets from the hadronic W boson decay, and the three-jet invariant mass is nominally constructed from these two jets and the b quark jet from top quark decay. Assumptions about jet mass are identical to those of partons: jets corresponding to light quarks are assumed to be massless, and jets corresponding to b quarks are assumed to have a mass of 4.8 GeV/c^2 [4]. The prediction from parton level quantities and transfer functions involves integration over jet energies in the transfer function for each parton in the event. This test has been described previously [48], but is discussed in full detail here.

In general, given an acceptance function, $A(\vec{x})$, and a normalized probability density, $P(\vec{x})$, the number of observed events is given by

$$N = \int A(\vec{x})P(\vec{x})d\vec{x} \tag{7.8}$$

To determine the two-jet or three-jet invariant mass distribution, we first change variables from $\vec{x} = (x_1, x_2, ..., x_n)$ to $(m_i, x_2, ..., x_n)$:

$$N = \int A(\vec{x})P(\vec{x})J(\frac{x_1, x_2, ..., x_n}{m_i, x_2, ..., x_n})dm_i dx_2...dx_n \tag{7.9}$$

and then differentiate with respect to m_i, where m_i is the two-jet or three-jet invariant mass. A plot of dN/dm_i is the predicted distribution of the invariant mass

$$\frac{dN}{dm_i} = \int A(\vec{x})P(\vec{x})J(\frac{x_1, x_2, ..., x_n}{m_i, x_2, ..., x_n})dx_2...dx_n. \tag{7.10}$$

In this analysis, the normalized probability density of interest is constructed from the differential cross-section for $t\bar{t}$ events, Equation 6.14. There are 15 measured parameters in this analysis ($\vec{x}$): three components of electron or muon momentum; and the angles (η, ϕ) and energies of four jets. Rather than applying the delta functions of the full transfer function to the parton level integrals, as done in section 6.2, they are applied to the reconstruction level integrals. The 11 delta functions remove all but 4 of the integrations over the jet energies. One of these integrations is removed in differentiation (dN/dm_i). We also apply the sum over possible permutations of jet-parton identification, resulting in

$$\frac{dN}{dm_i} = \int d^n\sigma(\vec{y})d\tilde{q}_1 d\tilde{q}_2 f(\tilde{q}_1)f(\tilde{q}_2)\, Q(\vec{y}) \tag{7.11}$$

where we define the integral over the remaining reconstruction level quantities as

$$Q(\vec{y}) \equiv \sum_{perm.} \int dx_2 dx_3 dx_4 J(\frac{x_1, x_2, ..., x_n}{m_i, x_2, ..., x_n})A(\vec{x}) \prod_{ijet=1}^{4} W_{jet}(E_i^x, E_i^y) \tag{7.12}$$

Monte Carlo integration over the parton level quantities is performed using simulated data. We assume the partons were generated with the same matrix element, phase space and parton distribution functions. Requiring events to pass selection at reconstruction level effectively includes the acceptance, $A(\vec{x})$, in $Q(\vec{y})$. We generally use 5000 such events when performing this integration. In the Monte Carlo integration of the invariant mass distribution, we numerically evaluate $Q(\vec{y})$ (not including acceptance) for each parton event. The invariant masses are

$$\begin{aligned}
m_{jj}^2 &= p_1 p_2(1 - cos\theta_{12}) \\
m_{jjj}^2 &= m_b^2 + 2(E_b p_1 - p_b p_1 \cos\theta_{b1}) + 2(E_b p_2 - p_b p_2 \cos\theta_{b2}) \\
&+ 2p_1 p_2(1 - \cos\theta_{12}),
\end{aligned} \tag{7.13}$$

and the Jacobians given by

$$
\begin{aligned}
J(\frac{E_1E_2}{m_{jj}E_2}) &= \frac{m_{jj}}{E_2(1-cos\theta_{12})} \\
J(\frac{E_1E_2}{m_{jjj}E_2}) &= \frac{m_{jjj}}{E_b - p_b\cos\theta_{b1} + E_2(1-\cos\theta_{12})}
\end{aligned} \tag{7.14}
$$

Inserting Equation 7.13 and Equation 7.14 into Equation 7.11 gives the prediction for the two-jet and three-jet invariant mass distributions. The normalization of the prediction is not determined in this calculation and is set such that the integral of the prediction is equal to that of the histogram.

The requirement of consistent selection and matching requirements is very significant in the invariant mass tests because of the acceptance term and Monte Carlo integration. This includes assumptions about the masses of jets at reconstruction level and in Equation 7.11. When setting the mass of a jet, its energy is held fixed and the magnitude of the momentum is scaled to the appropriate value. Also, the appropriate transfer function is used based on quark flavor.

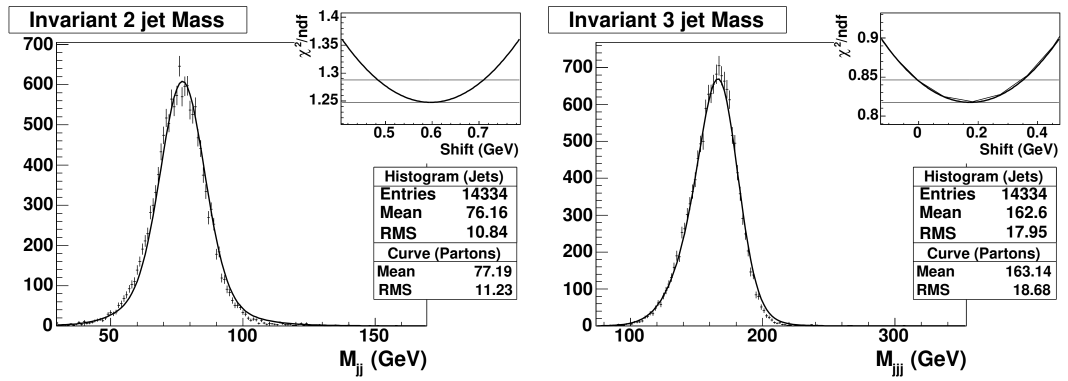

Figure 7.14: Two-jet (left) and three-jet (right) invariant mass comparisons using the jet-parton permutation determined by matching and transfer function parameters from Table 7.2 in HERWIG simulated events.

Figure 7.14 contains the two-jet and three-jet invariant mass comparisons for transfer function parameters from Table 7.2, using only the jet-parton permutation identified by matching. Simulated HERWIG events generated at a top quark mass of 178 GeV/c^2 passing selection and matching were used in integration and in the reference histogram. The χ^2 fit range is 65-90 GeV/c^2 in m_{jj} and 120-190 GeV/c^2 in m_{jjj} in bins of 1 and 2 GeV/c^2, respectively. Relatively good agreement is observed in both invariant masses. Figure 7.15 shows the same comparison except that all 12 possible permutations of jet and parton pairing are used. In this case, the χ^2 fit range is 25-220 GeV in m_{jj} and 80-400 GeV in m_{jjj} in bins of 1 and 2 GeV/c^2, respectively. Note that each event has 12 entries corresponding to the possible permutations. Again relatively good agreement is observed.

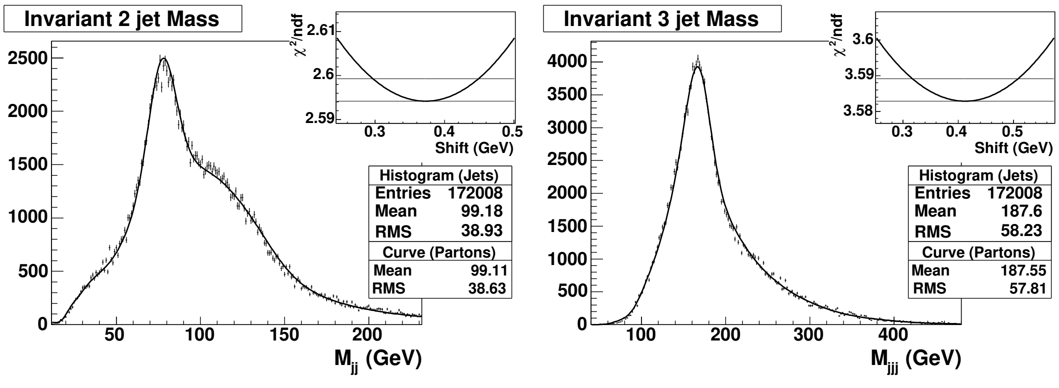

Figure 7.15: Two-jet (left) and three-jet (right) invariant mass comparisons using all 12 possible jet-parton permutations and transfer function parameters from Table 7.2 in HERWIG simulated events.

Figure 7.16 displays the effects of removing matching requirements. Both partons and jets are selected consistently with data, and the reconstruction level histogram realistically models the distribution from $t\bar{t}$ events in data. Note that transfer function parameters were still fit with the matching requirement applied.

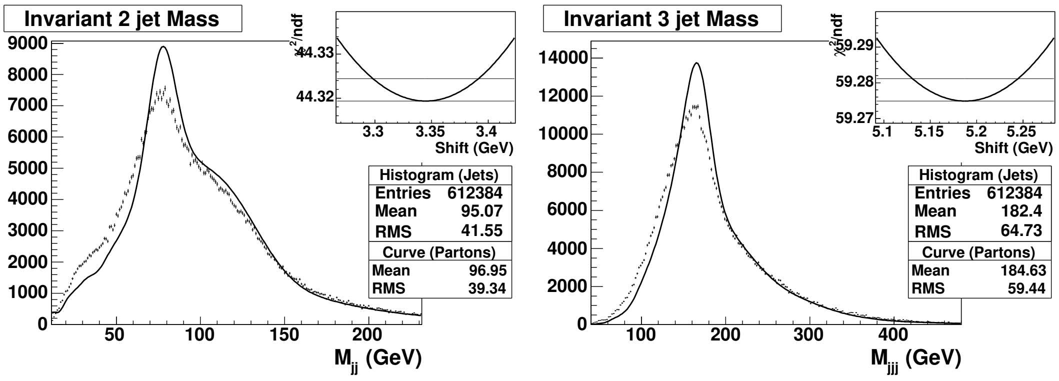

Figure 7.16: Two-jet (left) and three-jet (right) invariant mass comparisons relaxing matching requirements and using all 12 possible jet-parton permutations and transfer function parameters from Table 7.2 in `HERWIG` simulated events.

The χ^2 is calculated in the same range as in Figure 7.15. A clear bias and poor agreement in shape in the prediction is observed, primarily due to events with hard radiation excluded from transfer function parameterization. Radiation softens the invariant mass distributions. Some of this effect is removed in the likelihood with the background probability as discussed in section 6.5. Although it is possible this effect could bias the likelihood, simulated events are used to test for any biases in the measured quantities, see Section 8.1.2, and no shifts are observed in the top quark mass.

Table 7.8 summarizes the results of the invariant mass tests discussed in this section. Shapes of distributions requiring matching are consistent and calculated χ^2 offsets minimal. Removing the matching requirement causes significant differences in the shape of the compared distributions as well as calculated offsets.

Table 7.8: Summary of Shifts in Invariant Mass Comparisons

Sample	Δm_{jj} (GeV/c^2)	Δm_{jjj} (GeV/c^2)
Matching identified permutation	0.60 ± 0.11	0.17 ± 0.18
Matching and all 12 permutations	0.37 ± 0.08	0.41 ± 0.10
Not matched and all 12 permutations	3.3 ± 0.05	5.2 ± 0.06

7.4 Validation

Before transfer function parameters were chosen for the top quark mass analysis, we made various studies to validate and understand parameterization. The two-jet and three-jet invariant mass comparisons described in section 7.3.2 approximate the effects of changing transfer function parameterization on the top quark mass measurement. These tests are performed much more quickly than evaluating the likelihood and allow many different parameterizations to be studied. Transfer function parameters are fixed in this analysis and any related bias or improper modeling is treated with pseudo-experiment tests in simulated data, section 8.1.

Simulated events were generated with `HERWIG` at a top quark mass of 178 GeV/c^2, the matching requirement was $\Delta R < 0.15$, and only the permutation identified by matching was used unless explicitly stated otherwise. Studies include: dependence on top quark mass, dependence on ΔR matching requirement, dependence on amount of radiation, dependence on simulated event generator, and parameterization with η binning.

7.4.1 Top Quark Mass Dependence

Transfer functions are defined as the probability of measuring a jet energy given a parton energy and assumed to be independent from the parton energy spectrum, Equation 7.3. Implicitly, this assumes the transfer functions are independent of the top quark mass. This assumption is tested by plotting the χ^2 shift between reconstructed jet histogram and prediction in the three-jet invariant mass as a function of the top quark mass, Figure 7.17. Indicated uncertainty is the error given by the width of the χ^2 deviation. Simulated events were generated with `HERWIG` and the transfer function parameters used in prediction are given in Table 7.2. Neglecting the highest mass point at 230 GeV/c^2, a flat line fits to the points with a reasonable χ^2. The highest mass scanned with the likelihood was 202.5 GeV/c^2, and transfer functions appear to be independent of top quark mass in the relevant region.

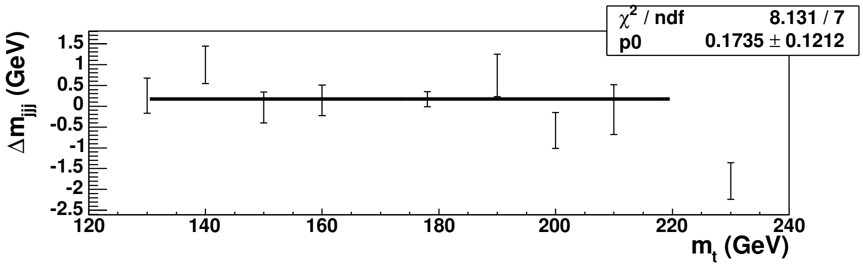

Figure 7.17: Shift (prediction minus reference) in three-jet invariant mass as a function of top quark mass in simulated events.

7.4.2 Matching Requirement

As discussed in Section 7.2, matching modifies the topology of the selected event sample. Ideally, transfer function parameters would be fit using selection consistent with experimental data. Variations in predicted invariant mass distributions are used to understand the effects of the modified topology on transfer function parameterization. Parameters with a matching requirement of $\Delta R < 0.4$ were chosen for the top quark mass measurement because of their consistency with the jet cone size in clustering, see Section 4.4.1.

Matching requirements used when fitting transfer function parameters are denoted R_{wxy}, those used in selecting simulated events for the invariant mass tests are denoted ΔR_{evt}, and the isolation of the jets and partons from other jets or partons is denoted ΔR_{iso}. Transfer function parameters are from Table 7.2 or Table 7.3 corresponding to fits with a matching requirement of $\Delta R_{\mathrm{wxy}} < 0.15$ and $\Delta R_{\mathrm{wxy}} < 0.4$ respectively.

Table 7.9: Summary of shifts (prediction minus reference) in single-permutation invariant mass tests with various matching requirements

ΔR_{wxy}	ΔR_{evt}	ΔR_{iso}	Δm_{jj} (GeV/c^2)	Δm_{jjj} (GeV/c^2)
0.15	0.15	0.6	0.60 ± 0.11	0.17 ± 0.18
0.15	0.15	-	0.60 ± 0.11	0.17 ± 0.18
0.15	0.4	-	1.6 ± 0.1	2.7 ± 0.1
0.4	0.15	-	-0.47 ± 0.12	-1.4 ± 0.2
0.4	0.4	-	0.64 ± 0.09	1.3 ± 0.1

Table 7.9 outlines results from invariant mass tests using a single permutation of jet-parton identification. No effect is seen when removing the isolation requirement. When $\Delta R_{\mathrm{evt}} > \Delta R_{\mathrm{wxy}}$, a more positive shift between prediction and histogram is observed. Similarly, when $\Delta R_{\mathrm{evt}} < \Delta R_{\mathrm{wxy}}$, a more negative shift between prediction and histogram is observed. This trend indicates the effects of

radiation on event topology, matching, and transfer function parameterization.

Table 7.10: Summary of shifts (prediction minus reference) in all-permutation invariant mass tests with various matching requirements

ΔR_{wxy}	ΔR_{evt}	Δm_{jj} (GeV/c^2)	Δm_{jjj} (GeV/c^2)
0.15	0.15	0.37 $\pm$ 0.08	0.41 $\pm$ 0.10
0.15	-	3.3 $\pm$ 0.05	5.2 $\pm$ 0.06
0.4	0.4	1.4 $\pm$ 0.06	2.4 $\pm$ 0.07
0.4	-	2.8 $\pm$ 0.05	4.4 $\pm$ 0.06

Similar tests were performed using all 12 possible jet-parton assignment permutations. No isolation requirement was applied to these events. No requirement on ΔR_{evt} indicates the jet and parton pairs are still matched with the lowest ΔR, but no additional selection requirement is applied to the events. As listed in Table 7.10, smaller shifts in unmatched events are observed with transfer function parameters fit with $\Delta R_{\text{wxy}} < 0.4$, indicating these transfer functions include more radiative effects than those with the tighter matching requirement.

7.4.3 Initial and Final State Radiation

Studies in previous sections indicate radiation as expressed through matching has a strong effect on transfer function parameterization. To understand the size of this effect, we compare the effects of matching with the effect of varying the amount of initial-state and final-state radiation (ISR and FSR) by their respective one sigma uncertainties in simulated event generation. The ISR and FSR samples were generated using `PYTHIA` with less (-1σ) or more ($+1\sigma$) radiation and are described in more detail in Section 9.3.

Table 7.11: Summary of shifts (prediction minus reference) in invariant mass tests with events simulated with less or more ISR or FSR

Sample	Δm_{jj} (GeV/c^2)	Δm_{jjj} (GeV/c^2)
nominal	0.80 $\pm$ 0.10	-0.01 $\pm$ 0.16
less ISR	0.77 $\pm$ 0.10	-0.09 $\pm$ 0.16
more ISR	0.70 $\pm$ 0.10	-0.07 $\pm$ 0.16
less FSR	0.72 $\pm$ 0.10	-0.13 $\pm$ 0.16
more FSR	0.66 $\pm$ 0.10	-0.14 $\pm$ 0.16

Invariant mass shifts for nominal and more or less amounts of radiation are compared in Table 7.11. Within errors, no effect due to the variations in radiation is observed. A much larger difference in shape is observed due to matching, see Figure 7.16, than due to one sigma changes in radiation, see Figure 7.18. The latter figure plots the distributions of invariant masses in reconstruction level jets without matching for all 12 possible permutations of parton-jet assignment.

7.4.4 Generator Comparison

Parameters such as production, radiation and hadronization are independently modeled between the `HERWIG` and `PYTHIA` Monte Carlo event generators. To study the effect on transfer functions, parameters are fit with `PYTHIA` events, Table 7.4. Table 7.12 summarizes the outcome of invariant mass tests. Shifts from `PYTHIA` parameters are approximately 0.4 GeV/c^2 lower in m_{jj} and 0.5 GeV/c^2 higher in m_{jjj} than those from `HERWIG` parameters.

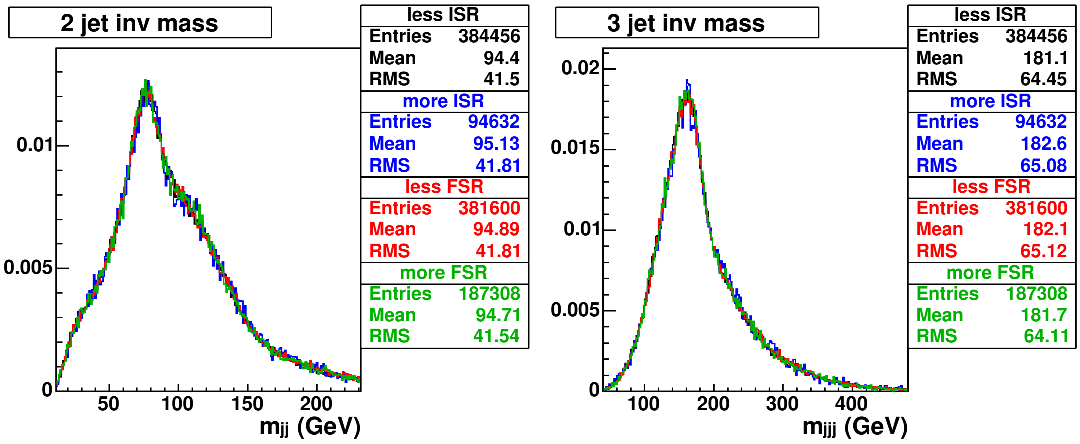

Figure 7.18: Invariant two-jet mass (left) and three-jet mass (right) including all 12 possible permutations from simulated data with less or more amounts of ISR or FSR.

7.4.5 Detector η-dependence

Transfer function parameters are fit using jets corrected with absolute energy corrections intended to remove all detector dependence. Some residual dependence is possible. To test for possible η dependence, independent transfer function parameters were fit in binned η regions, Table 7.5 and Table 7.6. Since events generally do not have all their jets in a single η region, the invariant mass test is not useful for these sets of parameters individually. Table 7.13 summarizes the shifts of the η dependent and non-η dependent transfer functions. A slightly larger shift in both the two and three-jet invariant masses is observed with the η dependent transfer function and no advantage to η-binning is found.

Table 7.12: Summary of shifts (prediction minus reference) in invariant mass tests with events and parameters from `HERWIG` and `PYTHIA`

Parameters	Events	Δm_{jj} (GeV/c^2)	Δm_{jjj} (GeV/c^2)
`HERWIG`	`HERWIG`	0.60 $\pm$ 0.11	0.17 $\pm$ 0.18
`HERWIG`	`PYTHIA`	0.80 $\pm$ 0.10	-0.01 $\pm$ 0.16
`PYTHIA`	`HERWIG`	0.25 $\pm$ 0.11	0.73 $\pm$ 0.17
`PYTHIA`	`PYTHIA`	0.40 $\pm$ 0.10	0.44 $\pm$ 0.15

Table 7.13: Summary of shifts (prediction minus reference) in invariant mass tests with η and non-η dependent transfer function parameters

Sample	Δm_{jj} (GeV/c^2)	Δm_{jjj} (GeV/c^2)
non-η dependent	0.60 $\pm$ 0.11	0.17 $\pm$ 0.18
η dependent	0.78 $\pm$ 0.11	0.48 $\pm$ 0.17

CHAPTER 8

Top Quark Mass Results

The analysis method described in Chapter 6 is evaluated and tested in simulated data in section 8.1. Tests in simulated data study the discrimination of the W+jets probability density and calibrate bias in the likelihood. The measurement in experimental data is given and shown to be consistent within various subdivisions in section 8.2.1. Comparisons between experimental data and simulated data involving information from the likelihood indicate simulated data accurately models experimental data in section 8.3.

8.1 Results in Simulated Data

8.1.1 Evaluation of W+jets Probability Density

The W+jets probability density is shown to similarly describe events with and without heavy flavor. It is also shown to have good discrimination between simulated $t\bar{t}$ and W+jets events. Roughly 1500 W + 4p, 1000 $Wb\bar{b}$, 7000 $t\bar{t}$ and 80 non-W events, see section 5.3, are used in these tests.

The matrix element used in the W+jets probability density, section 6.4, specifically describes W production with jets coming from u, d, s and c quarks or a gluon. Figure 8.1 plots the distribution of its output on a logarithmic scale for $W + 4p$ and $Wb\bar{b}$ events. No significant difference between distributions with b

quarks and lighter quarks or electrons and muons is observed.

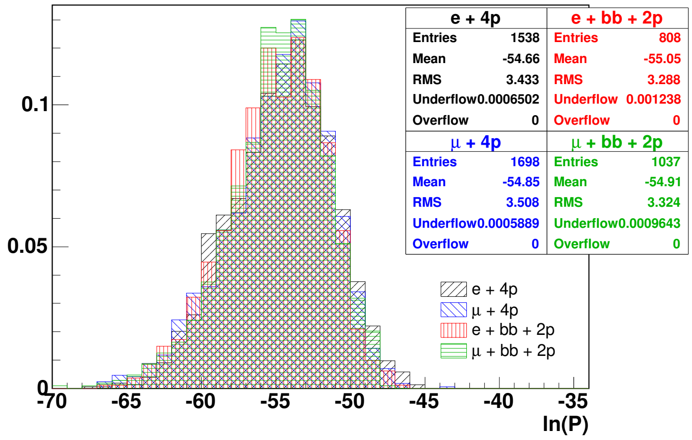

Figure 8.1: Distribution of W+jets probability density in simulated W+jets data with and without b quarks.

Primarily, the W+jets probability density discriminates between $t\bar{t}$ and background events. Figure 8.2 shows the logarithmic distribution of $t\bar{t}$ events generated at a top quark mass of 178 GeV/c^2, and the dominant background samples, $W + 4p$ and non-W. Histograms are normalized by entries and the non-W histogram is scaled by 50% for visibility. Clear distinction between $t\bar{t}$ and $W + 4p$ is evident. Separation between $t\bar{t}$ and non-W events is also observed. Discrimination between $t\bar{t}$ and $W + 4p$ is further illuminated in Figure 8.3, plotting the fraction of $t\bar{t}$ and $W + 4p$ events retained as a function of the logarithm of the probability density. At the point of maximum separation, at $\ln(P) =$ -56.2, 68.3% of $t\bar{t}$, 31.7% of $W + 4p$, and 40.3% of non-W events (not shown) are retained. No selection based on the W+jets probability density is used in the analysis, it is used here to elucidate discrimination capability.

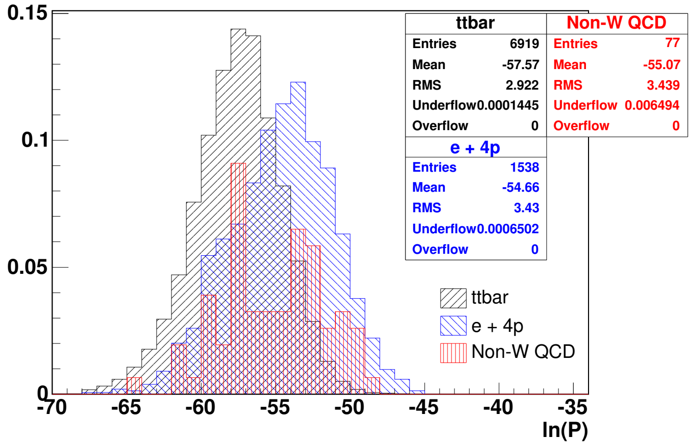

Figure 8.2: Distribution of W+jets probability density in simulated $t\bar{t}$, W+jets and non-W samples.

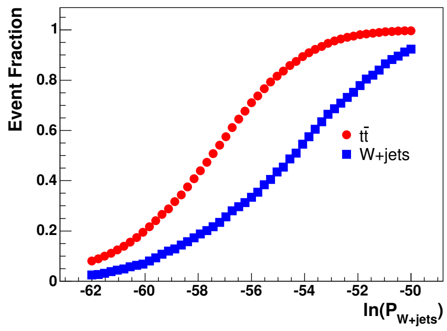

Figure 8.3: Fraction of simulated $t\bar{t}$ and W+jets events retained as a function of selection on logarithm of W+jets probability density.

8.1.2 Evaluation of Likelihood

The performance of the likelihood in simulated data measurements, pseudo-experiments, is evaluated and used to check for bias and linearity in the measured parameters, calibrating them where necessary. Table 8.1 lists the available statistics for all processes in pseudo-experiment construction. Note that statistics are limited by the large amount of CPU time necessary to process the $t\bar{t}$ probability density and are thus fewer than those used in the previous section.

Table 8.1: Statistics of simulated data samples used in likelihood tests

Process	Number of Events	Event Generator
$t\bar{t}$ m_t= 162.5 GeV/c^2	2169	HERWIG
$t\bar{t}$ m_t= 165.0 GeV/c^2	2148	HERWIG
$t\bar{t}$ m_t= 167.5 GeV/c^2	2353	HERWIG
$t\bar{t}$ m_t= 170.0 GeV/c^2	2499	HERWIG
$t\bar{t}$ m_t= 172.5 GeV/c^2	2073	HERWIG
$t\bar{t}$ m_t= 175.0 GeV/c^2	2521	HERWIG
$t\bar{t}$ m_t= 178.0 GeV/c^2	2745	HERWIG
$t\bar{t}$ m_t= 180.0 GeV/c^2	1993	HERWIG
$t\bar{t}$ m_t= 182.5 GeV/c^2	1967	HERWIG
non-W (QCD)	121	experimental data
W+4p (Mistags)	967	ALPGEN
$Wb\bar{b}$	768	ALPGEN
$Wc\bar{c}$	264	ALPGEN
Wc	124	ALPGEN
Single top	184	ALPGEN
EW (WW, WZ, ZZ)	59	ALPGEN

Pseudo-experiments are constructed with the relative contribution of $t\bar{t}$ and various background events according to the expected event yield, section 5.3. In most of the pseudo-experiments, the $t\bar{t}$ cross-section is assumed to be such that the average fraction of $t\bar{t}$ events is 83%. Two different types of event sample construction are used: the first combines as many events as possible into a single large set, and the second constructs samples of 118 events by drawing randomly from event pools. Results from these two types of tests are described in the following two sections. Likelihoods from pseudo-experiments are maximized according to section 6.1.3.

8.1.2.1 Tests using high-statistics pseudo-experiments

Likelihood measurements in large samples of simulated events are reported in this section. The samples for each m_t value use all the available statistics from Table 8.1 in a single pseudo-experiment. In most cases, the number of background events available limits the size of the pseudo-experiments. Comparisons between measured values and generated values test for biases and "linearity" in the method. Resampling only improves the estimation of the RMS of a distribution so is not helpful here. Reported uncertainties are the errors estimated by likelihood maximization. No bias is observed in the measured top quark mass, but a correction is determined for the jet energy scale measurement.

The top quark mass measured by the likelihood as a function of the generated mass is shown in Figure 8.4 using the two-dimensional fit to m_t and JES. Most of the points, the red circles, have events set at JES = 1. We also test events with JES = 0.94, blue squares, and JES = 1.06, green triangles. The plot on the left is fit with a first order polynomial about m_t = 172.5 GeV/c^2. We expect $p0$ = 172.5 GeV/c^2 and $p1$ = 1 for an unbiased measurement of top quark mass, which is what we observe within statistical error of the fit. The plot on the right shows the same information except as a residual and is fit with a zeroth order polynomial. We expect $p0 = 0$ for an unbiased measurement, which is what we observe within statistical error of the fit. We conclude the measurement of the top quark mass is unbiased for all values of jet energy scale.

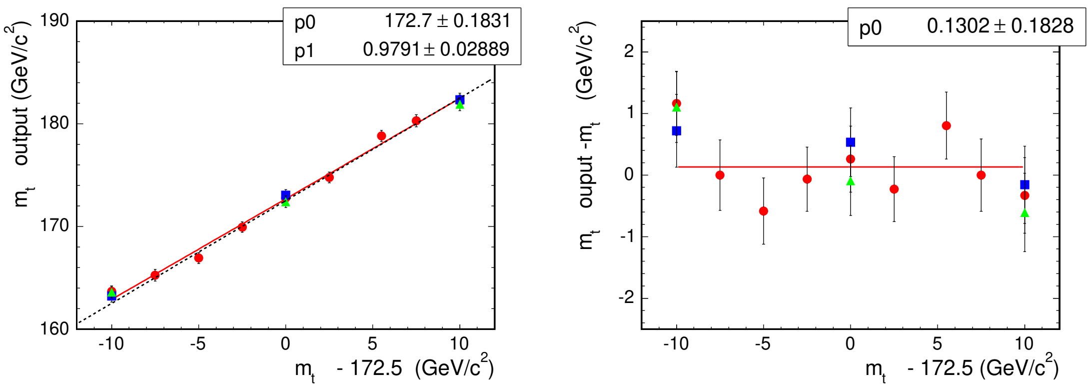

Figure 8.4: Linearity check in m_t using two-dimensional fit. Red dots represent events with JES=1, blue squares JES=0.94, and green triangles JES=1.06.

The jet energy scale measured by the likelihood as a function of the scale set in the events is shown in Figure 8.5. All of these events were generated with a top quark mass of 172.5 GeV/c^2. The points are fit with a first order polynomial about JES = 0. We expect $p0 = 1$ and $p1 = 1$ for an unbiased measurement. In this case, we see significant deviations within statistics, indicating bias. These fit parameters are used to correct the JES dimension in the two dimensional m_t-JES space before likelihood maximization for measurement in data. Note that this bias does not affect measurement of the top quark mass and thus no additional systematic error for this mapping needs to be assessed.

As a cross-check, JES is fixed to unity and the likelihood is maximized as a one-dimensional function in top mass. Figure 8.6 shows measured m_t as a function of generated top quark mass. The results are fit to a first order polynomial

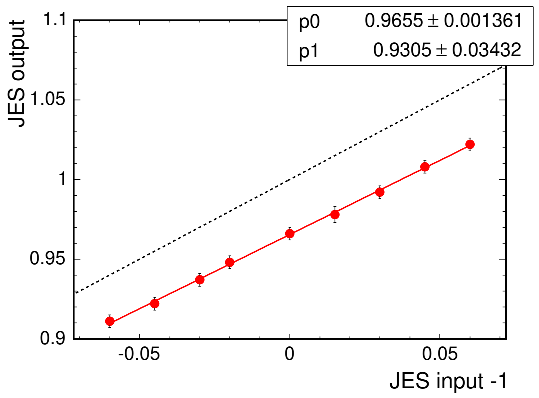

Figure 8.5: Linearity check in JES using two-dimensional fit. Events were all generated at $m_t = 172.5$ GeV/c^2. This curve is used to correct the JES before fitting in the data measurement.

about $m_t = 172.5$ GeV/c^2. We expect $p0 = 172.5$ and $p1 = 1$ for an unbiased measurement of top quark mass. The plot on the left is before correction to JES derived from Figure 8.5 and shows an offset of 3.1 GeV/c^2. This offset is absorbed by the JES parameter in the two-dimensional fit. The plot on the right is after correction to JES and shows values nearly unbiased. This is an indication that the mapping derived for JES is correct.

Returning to the two-dimensional fit, Figure 8.7 shows the measured JES as function of the generated top quark mass residual at three values of jet energy scale: 0.94, 1.00 and 1.06. The plot on the left shows results before correction for JES and the plot on the right after. We find the measurement after correction is consistent with the set jet energy scale in the events at all top quark masses.

The final test with large pseudo-experiments is to determine the dependence of the measured m_t and JES parameters on the amount of background events present in the sample. We keep the relative contribution of the various backgrounds fixed and plot the measured values as a function of the contribution of $t\bar{t}$ events to

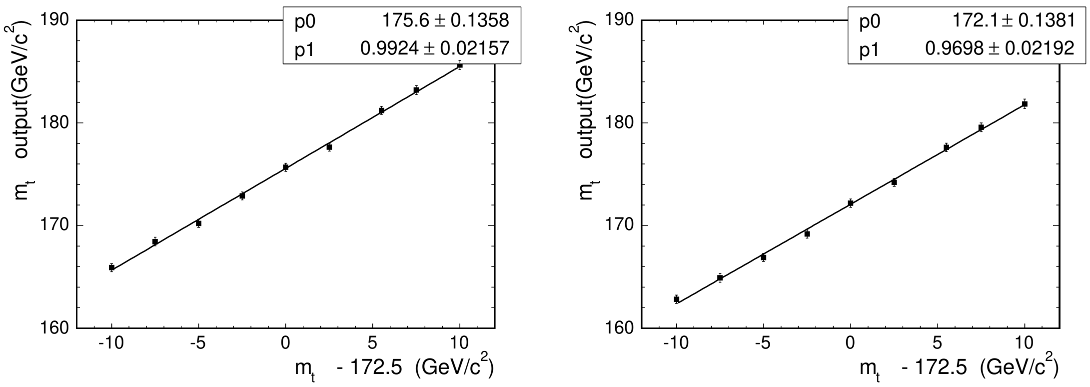

Figure 8.6: Linearity check in m_t with JES fixed to unity before correction (left) and after correction (right).

the sample, Figure 8.8. Events were generated with a top quark mass of 172.5 GeV/c^2 and a jet energy scale of unity. The points are fit with a zeroth order polynomial. We expect $p0 = 172.5$ GeV/c^2 for m_t (top) and $p0 = 1$ for JES (bottom), which is what we observe within fit error. No bias is observed as low as 60% $t\bar{t}$ contribution, far below the expected contribution in data. Systematic error is assigned for variations in sample composition in section 9.5.

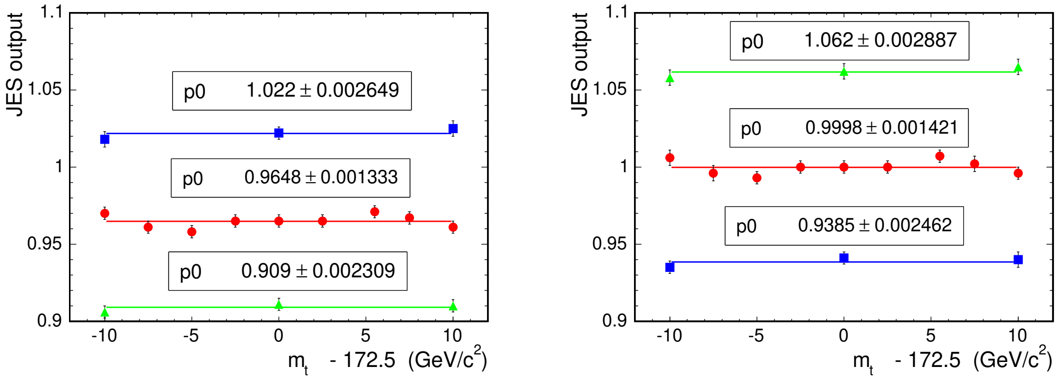

Figure 8.7: Measured JES as a function of the generated m_t before (left) and after (right) JES correction. Red dots represent events with JES=1, blue squares JES=0.94, and green triangles JES=1.06.

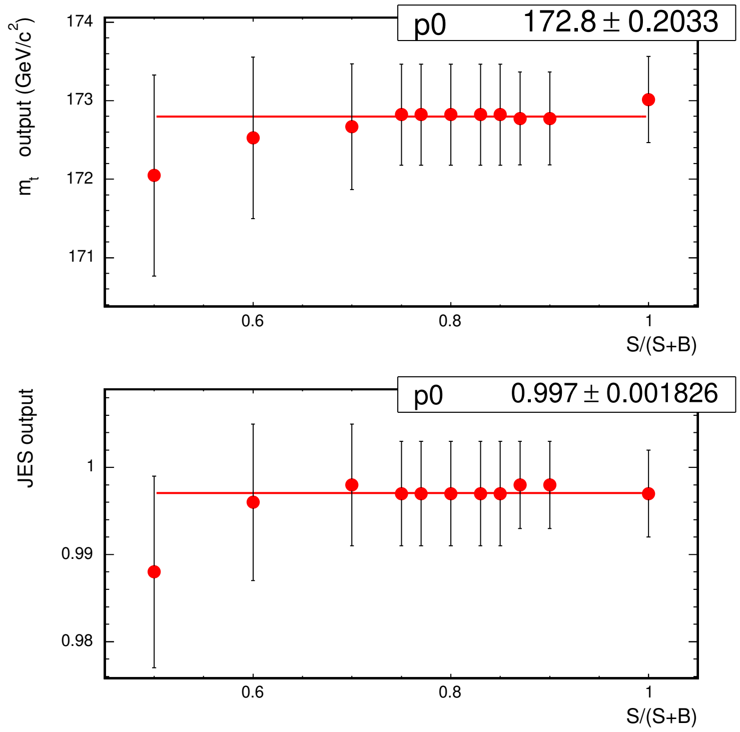

Figure 8.8: Measured m_t (top) and JES after correction (bottom) as a function of $t\bar{t}$ contribution to sample (S/(S+B)). Events were generated with a top quark mass of 172.5 GeV/c^2 and jet energy scale of unity.

8.1.2.2 Tests using resampled events in pseudo-experiments

Resampled pseudo-experiments, as explained below, are conducted to test the behavior of the likelihood with a number of events comparable to data. The data sample used for this measurement contains 167 events. Pseudo-experiment tests were originally done for a smaller dataset with 118 events and updated to the larger dataset in section 8.1.2.3. Not all of the tests with 118 events in this section are updated. The m_t and JES linearity tests are confirmed, including measurements in simulated samples where the generated top quark mass and jet energy scale are not *a priori* known. Pull distributions are made to test and correct the error of likelihood measurements. A correction is determined for the measured signal fraction. We make measurements as a function of number of multiple interactions and in simulated samples entirely composed of background.

Pseudo-experiments constructed with event resampling draw events randomly from the entire available event pool. The same event is allowed to be selected from the event pool multiple times in the construction of a single pseudo-experiment, known as replacement. Events are separately drawn from the respective pool for each production process comprising the total sample. The total number of events and the contribution of background events in a pseudo-experiment are both Poisson fluctuated about their expected values of 118 and 22, respectively. Note that the actual number of selected events in data is 167. Updates to affected pseudo-experiment tests with the correct sample size are described in section 8.1.2.3.

All measurements are done with the two-dimensional likelihood, and JES has been corrected with the mapping function derived from the large pseudo-experiments in the previous section. Pull is calculated as

$$\text{Pull} \equiv \frac{\alpha^{\text{meas}} - \alpha^{\text{true}}}{\sigma_{\text{estimated}}}, \tag{8.1}$$

where α is the measurement of interest and σ is its corresponding estimated error. A pull distribution with mean of zero indicates an unbiased measurement, and one with RMS of unity indicates the errors are correctly estimated. A pull distribution with an RMS larger than unity indicates the errors are underestimated.

Example results from pseudo-experiment tests are shown for measurements in simulated events generated with a top quark mass of 172.5 GeV/c^2 and a jet energy scale of unity. Figure 8.9 contains the distributions of the m_t measurement, estimated error, and pull. The slight offset in the mean of the m_t measurement and difference between the RMS of the m_t measurement, the expected error, and the estimated error are reflected in the mean of 0.05 and sigma of 1.08, respectively. On average, the likelihood measures the mass slightly higher than the true value and under-estimates the error by 8%. Figure 8.10 contains the distributions of the JES measurement, estimated error, and pull. The mean and sigma of the pull distribution are -0.05 and 1.11, reflecting a low measurement of the JES and under-estimate of the error, respectively. Figure 8.11 shows the distribution of measured signal fraction, C_s, corresponding to this set of pseudo-experiments. Pull distributions were not studied for the C_s parameter.

We check for bias and linearity in the likelihood by plotting the mean of pseudo-experiment measurement distributions against generated top quark mass and jet energy scale, Figure 8.12. Reported uncertainty is the RMS corresponding to these distributions. Results are similar to those obtained with the high-statistics experiments. As an additional check, we measure m_t and JES in samples generated with *a priori* unknown top quark mass and jet energy scales. Figure 8.13 shows the residuals from these measurements in ten different samples. Solid points indicate simulated events were generated in the run range of the *0d* dataset, and open points indicate events were generated in the run range

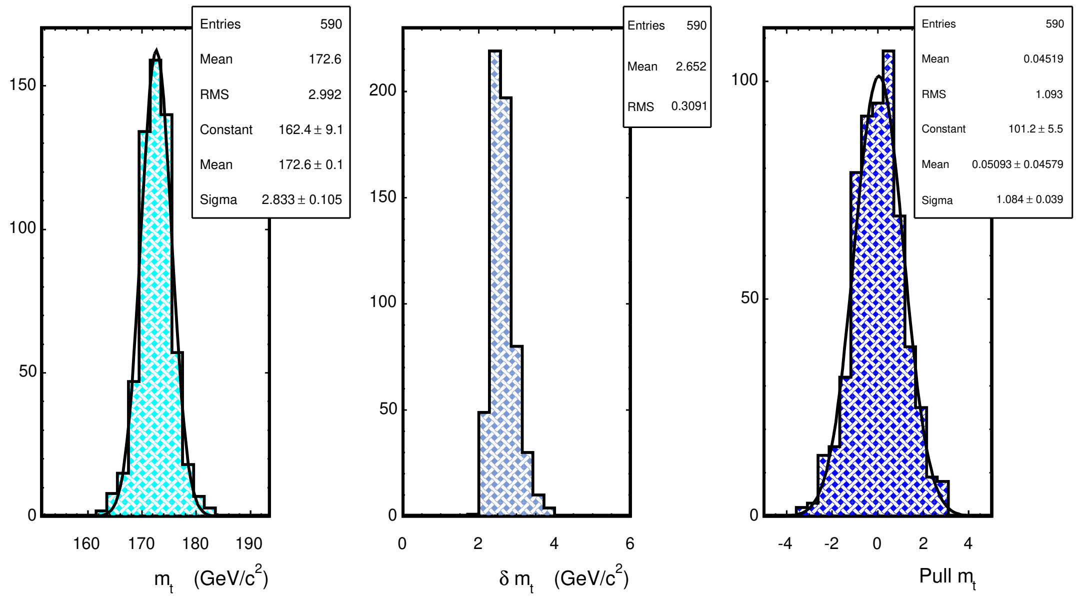

Figure 8.9: Pseudo-experiment results in m_t for simulated events generated with top quark mass of 172.5 GeV/c^2 and jet energy scale of unity.

of the *0h* dataset. The results are plotted against sample number and are randomly ordered in generated top quark mass and jet energy scale. The results are consistent with no bias in either measured m_t or JES.

We next test the expected errors given by the likelihood. Figure 8.14 shows the mean estimated error and pull RMS for measurements in m_t as a function of generated top quark mass. The RMS is estimated as σ in a Gaussian fit with uncertainty returned by `MINUIT`. The expected error increases with increasing top quark mass. Note that the number of $t\bar{t}$ events is constant for each of these points and is not adjusted for the theoretical cross-section at each mass point. This adjustment would increase the error of the lower generated top quark masses and decrease the error of the higher masses. The average expected error is roughly 2.6 GeV/c^2 and includes statistical error on the measured top quark mass with

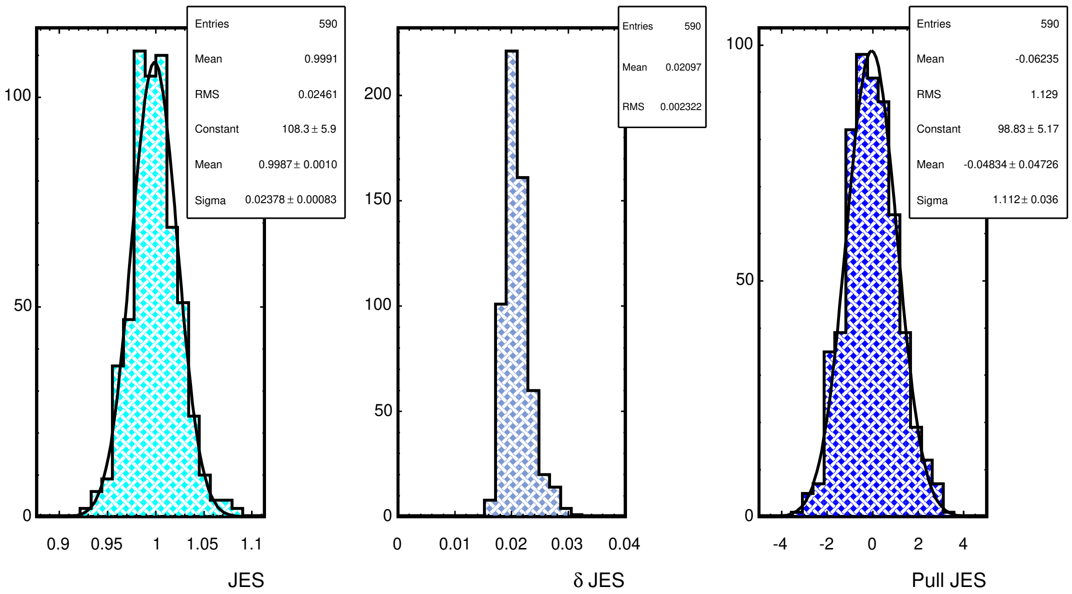

Figure 8.10: Pseudo-experiment results in JES for for simulated events generated with top quark mass of 172.5 GeV/c^2 and jet energy scale of unity.

the measured jet energy scale systematic error. The fit to the RMS of pull distributions results in a 6% correction to this error for 118 events. This correction is estimated for the 167 events observed in the full dataset in the next section. Figure 8.15 shows the fitted σ of pull distributions for measurements in JES. The fit gives a 10% correction for 118 events.

As discussed in section 6.5, the relative normalization of $t\bar{t}$ and W+jets probability densities in the likelihood causes the measured C_s parameter to not correctly indicate the true fraction of $t\bar{t}$ events in the sample. Figure 8.16 plots the mean C_s parameter as a function of mean $t\bar{t}$ contribution (S/(S+B)). A C_s of 0.77 is measured for a pure $t\bar{t}$ sample as expected from the relative normalization. We use this plot to correct our estimate of the amount of $t\bar{t}$ in data.

As discussed in section 5.2, simulated events were generated in a limited range

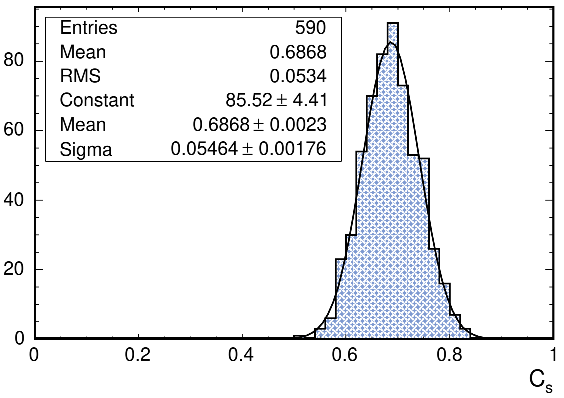

Figure 8.11: Pseudo-experiment results in C_s for for simulated events generated with top quark mass of 172.5 GeV/c^2 and jet energy scale of unity.

of the full dataset and therefore have lower average instantaneous luminosity. The increase in instantaneous luminosity can be measured via the number of reconstructed vertices. The effect on measured m_t and JES is estimated using a simulated $t\bar{t}$ event sample generated with a top quark mass of 175 GeV/c^2 and nominal JES at instantaneous luminosities of 50, 100, 150, 200, 250 and 300 x 10^{30} cm^{-2} s^{-1}, Figure 8.17. We expect $p1 = 0$ for no dependence on the number of reconstructed vertices. With the given statistics, the measured m_t parameter has no dependence, but the measured JES parameter shows some dependence. The mean number of reconstructed vertices in data is 1.68. A systematic error for this difference is assigned in section 9.9.

As a final cross-check, we form pseudo-experiments using only background events. Relative contributions of the individual background samples are held constant, but a total of 88 events are used for each experiment. Figure 8.18 shows the distributions of measured m_t and JES parameters. The results show measurements in pure background are consistent with flat distributions. The lower limit of scanned likelihood range is responsible for the pileup in the lowest

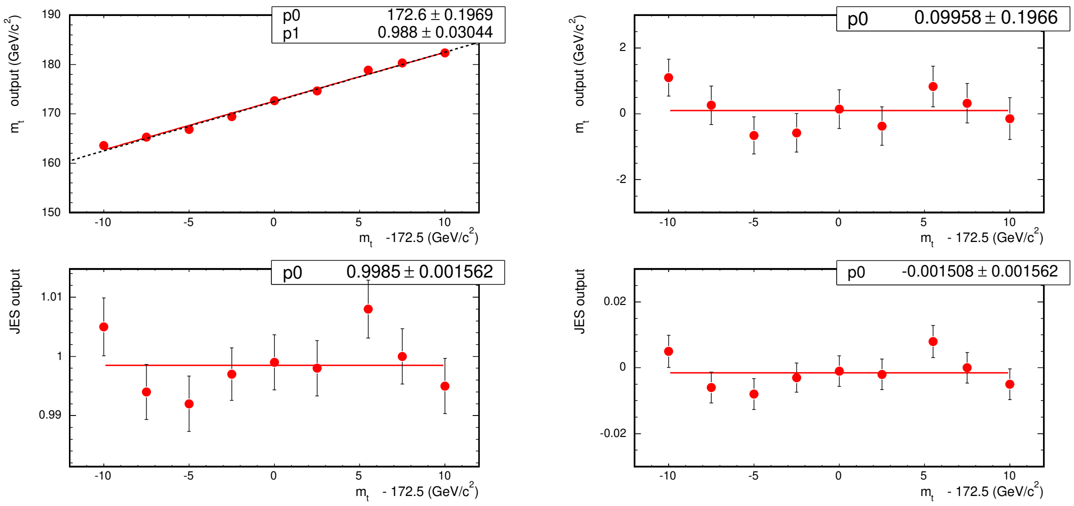

Figure 8.12: Linearity check in m_t (top) and JES as a function of generated top quark mass (bottom), each with nominal output (left) and residual (right). Events all set with nominal jet energy scale.

and highest bins. The measured C_s for these pseudo-experiments is consistent with zero, see Figure 8.19.

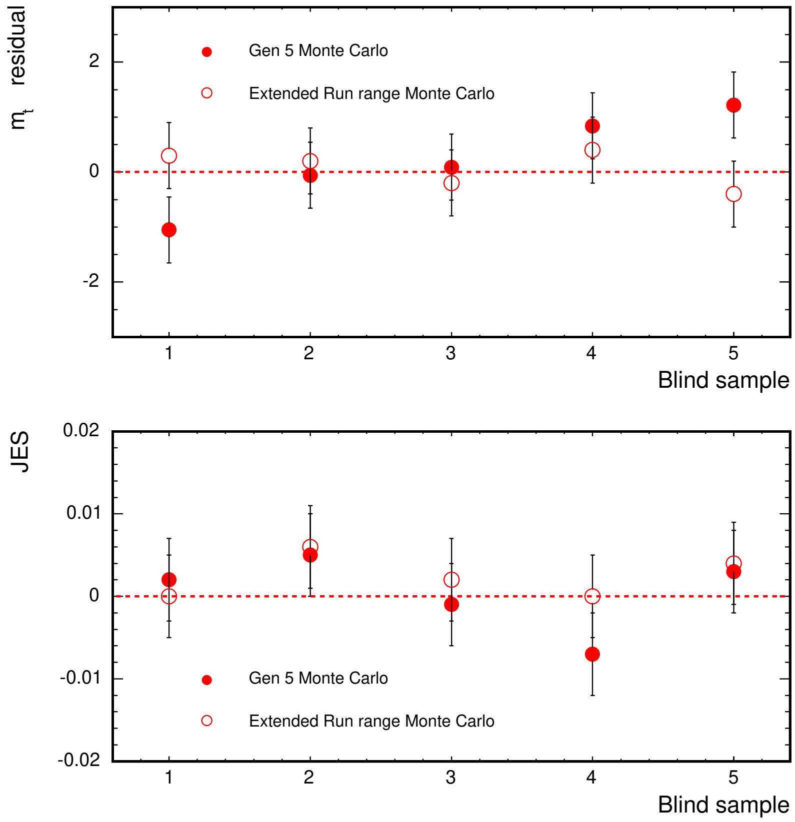

Figure 8.13: Residual measurement in m_t (top) and JES (bottom). Samples 1 and 2 were generated with PYTHIA and the other ones with HERWIG.

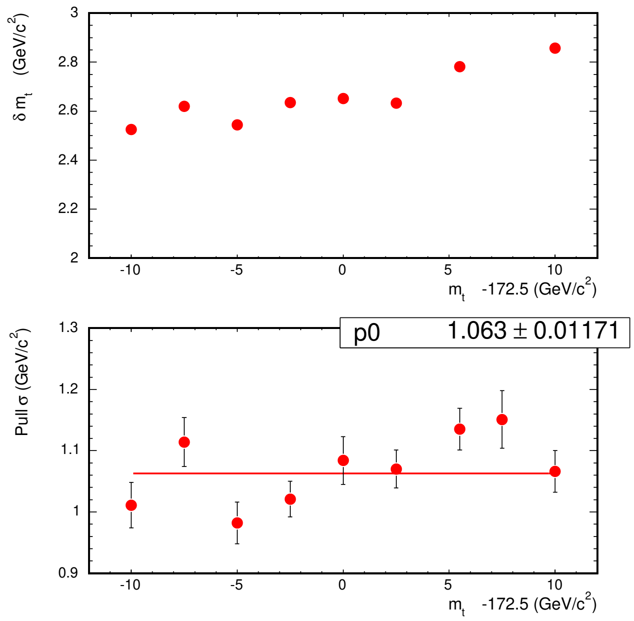

Figure 8.14: Expected error (top) and σ of Gaussian fit to pull distribution (bottom) of m_t parameter using pseudo-experiments as a function of top quark mass. Events all set with nominal jet energy scale.

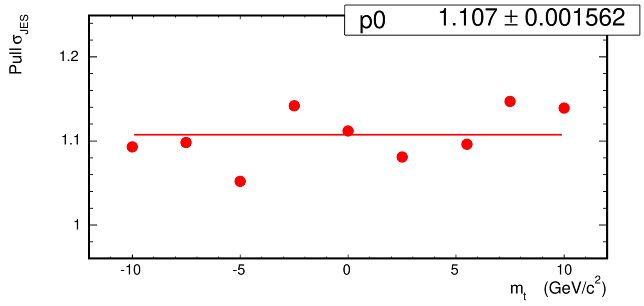

Figure 8.15: σ of Gaussian fit to pull distribution of JES parameter using pseudo-experiments as a function of generated top quark mass. Events all set with nominal jet energy scale.

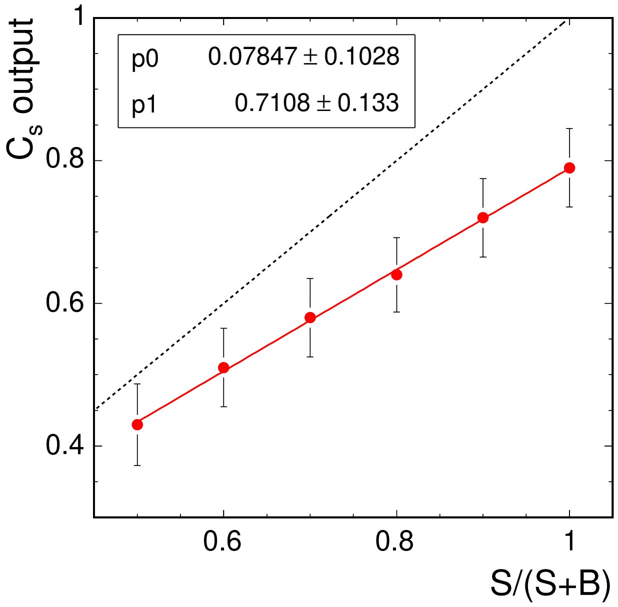

Figure 8.16: Measured C_s as a function of $t\bar{t}$ contribution in sample (S/(S+B)). Events generated with a top quark mass of 172.5 GeV/c^2 and set with nominal jet energy scale.

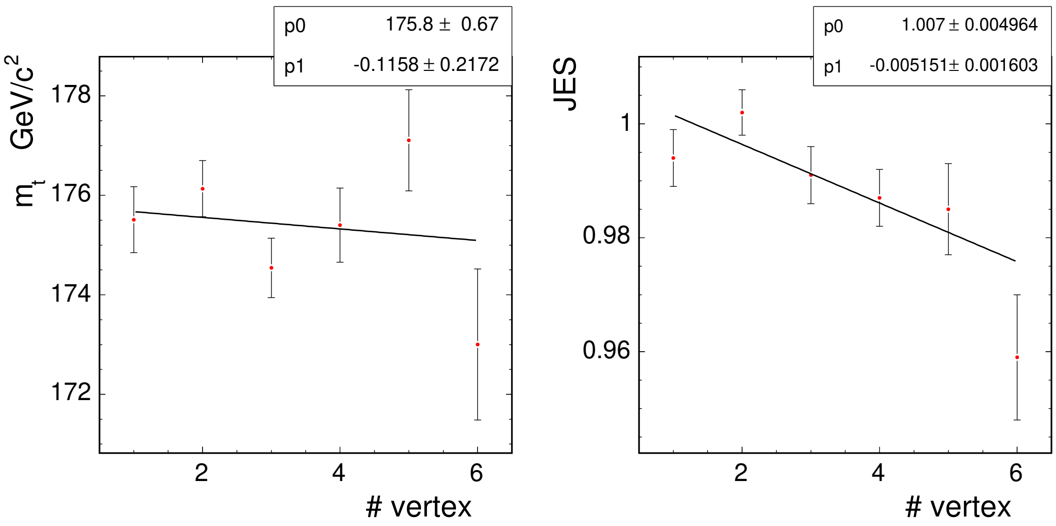

Figure 8.17: Measured m_t and JES in pseudo-experiments as a function of the number of reconstructed vertices. Events generated with a top quark mass of 175 GeV/c^2 and nominal jet energy scale.

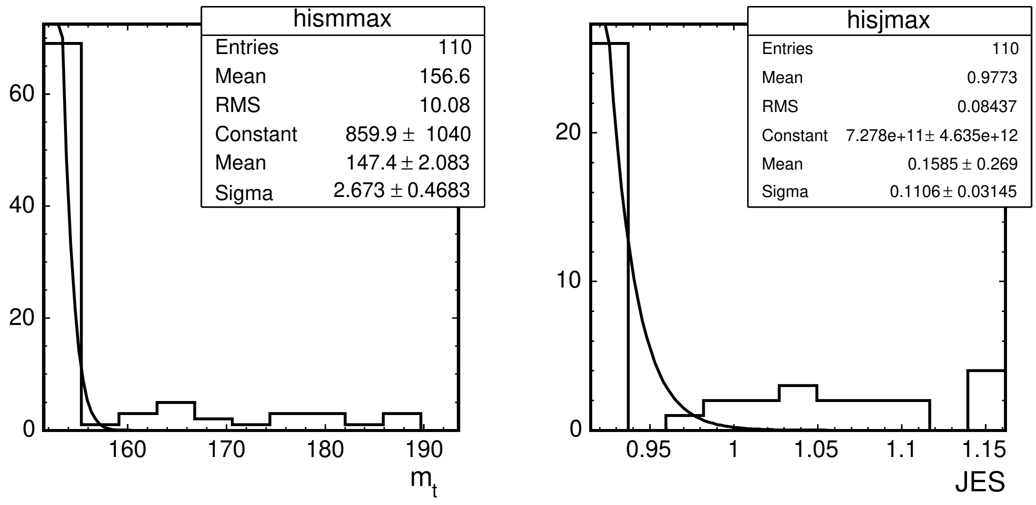

Figure 8.18: Measured m_t and JES using experiments of 88 simulated background events.

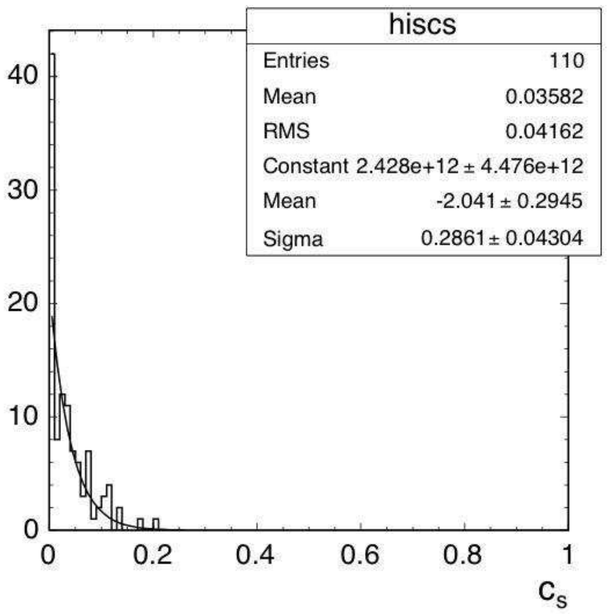

Figure 8.19: Measured C_s using experiments of 88 simulated background events.

8.1.2.3 Updates with Increased Sample Size

The data sample used for this measurement contains 167 events. Since the original pseudo-experiment tests were done with 118 events, pseudo-experiments of 166 events are created to test the expected error with a sample size similar to that of data. It was theorized that the likelihood will become more Gaussian with a larger number of events and thus estimate measurement errors more correctly. Sample size is not expected to affect any of the other results in pseudo-experiment tests. Events were generated with a top quark mass of 175 GeV/c^2 and nominal jet energy scale and resampled such that the total number of pseudo-experiments is about the square of the number of possible exclusive pseudo-experiments.

Figure 8.20 shows the fitted pull σ as a function of mass for pseudo-experiment tests generated with differing random seeds. These points are fit with a zeroth order polynomial. To account for variations due to the random seed, we plot the distribution of the fitted parameters from these tests in Figure 8.21. We take the mean of this distribution, 1.03, as the correction factor to the estimated statistical plus JES systematic error. Figure 8.22 shows a linearity test in the top quark mass using pseudo-experiments of 166 events and a plot of fitted pull σ similar to those in Figure 8.20. The 3% correction to the estimated uncertainty agrees with Figure 8.21, and the offset from zero in the fitted linearity is consistent with Figure 8.4 and Figure 8.12. This offset is added as a systematic uncertainty in section 9.7. Figure 8.23 shows results from a pseudo-experiment test: mean, expected error, and pull distributions. The expected error is corrected by 3% and thus the RMS of the pull distribution is expected to be unity. After correction, the mean expected error is 2.3 GeV/c^2.

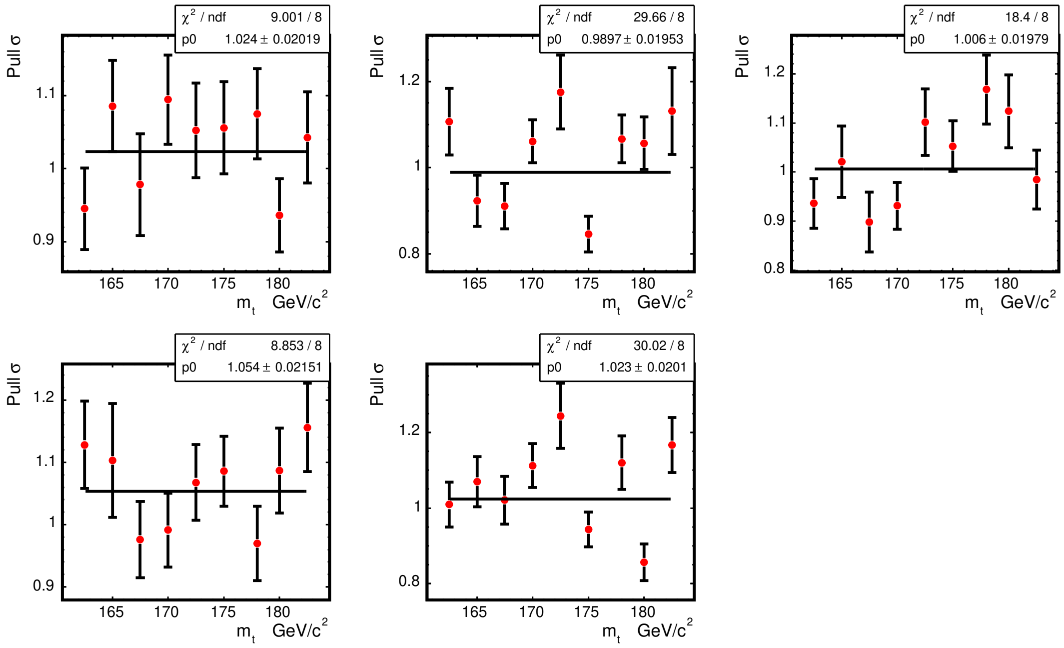

Figure 8.20: Fitted pull sigma as a function of generated top quark mass for pseudo-experiment tests using resampling and drawn with different starting random number seed.

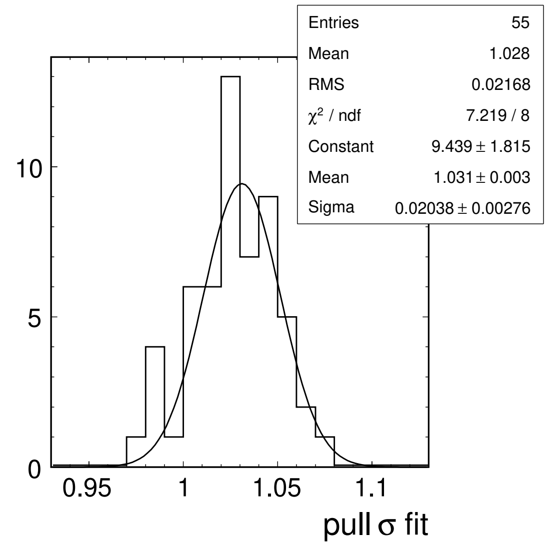

Figure 8.21: Distribution of fitted pull sigma from pseudo-experiments such as those shown in Figure 8.20.

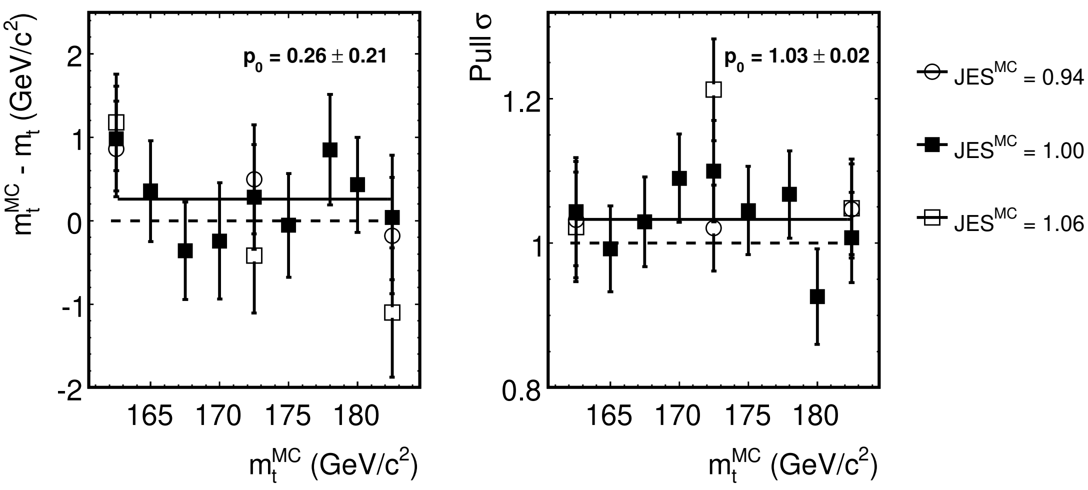

Figure 8.22: Linearity check in m_t as a function of generated top quark mass m_t^{MC} (left). Pull σ as a function of m_t^{MC} (right).

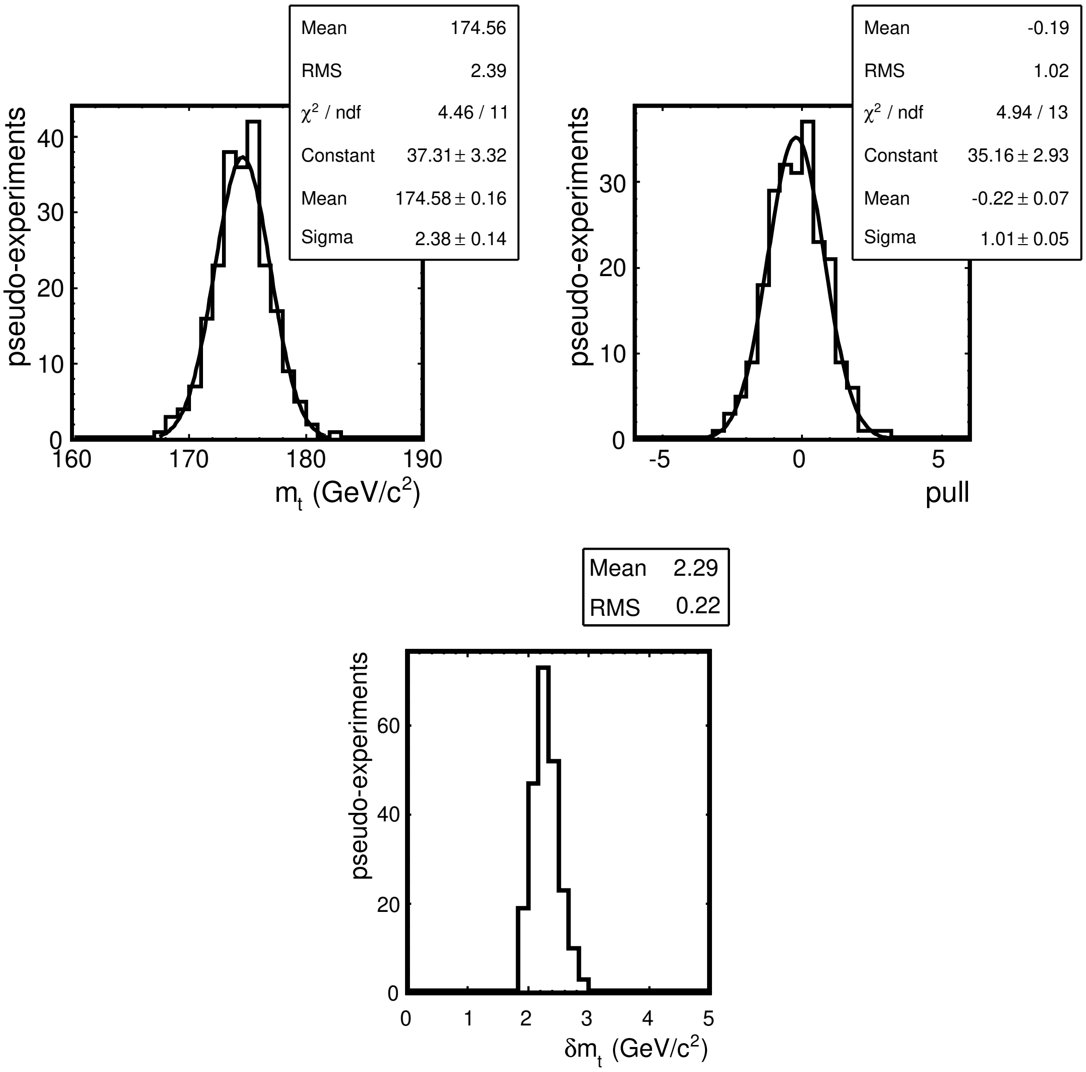

Figure 8.23: Pseudo-experiment results in m_t for simulated events generated with a top quark mass of 175 GeV/c^2 and jet energy scale of unity.

8.2 Measurement in Experimental Data

We use the full 955 pb^{-1} dataset, see section 5.1, to simultaneously measure the top quark mass (m_t), jet energy scale (JES) and signal fraction (C_s) in the 167 events passing selection criteria. No bias correction is applied to the top quark mass, but the JES parameter is mapped according to Figure 8.5. The estimated statistical plus JES systematic error on the top quark mass is corrected by a factor of 1.03 as discussed in section 8.1.2.3. We apply a factor of 1.10 to the estimated JES parameter error. The signal fraction has been corrected by Figure 8.16. Figure 8.24 shows the minus log likelihood after minimization of the C_s parameter and the fit contours corresponding to 1σ, 2σ, 3σ, and 4σ in the top quark mass. We measure a top quark mass, jet energy scale and signal fraction:

$$\begin{aligned} m_t &= 170.8 \pm 2.2\ (\text{stat} + \text{JES})\ \text{GeV/c}^2 \\ JES &= 0.99 \pm 0.02\ (\text{stat}) \\ C_s &= 0.84 \pm 0.10\ (\text{stat}). \end{aligned} \tag{8.2}$$

Selected event likelihoods representative of the full data sample are shown in Appendix D. Figure 8.25 shows the minus log likelihood and fit after minimization of the C_s parameter in the JES dimension at $m_t = 170.5$ GeV/c^2 and in the m_t dimension at JES = 0.99. We observe relatively good agreement between likelihood and fit. Note that the fit shown is the result of the full two-dimensional fit and is not expected to perfectly fit in either of the single bin projections of the likelihood.

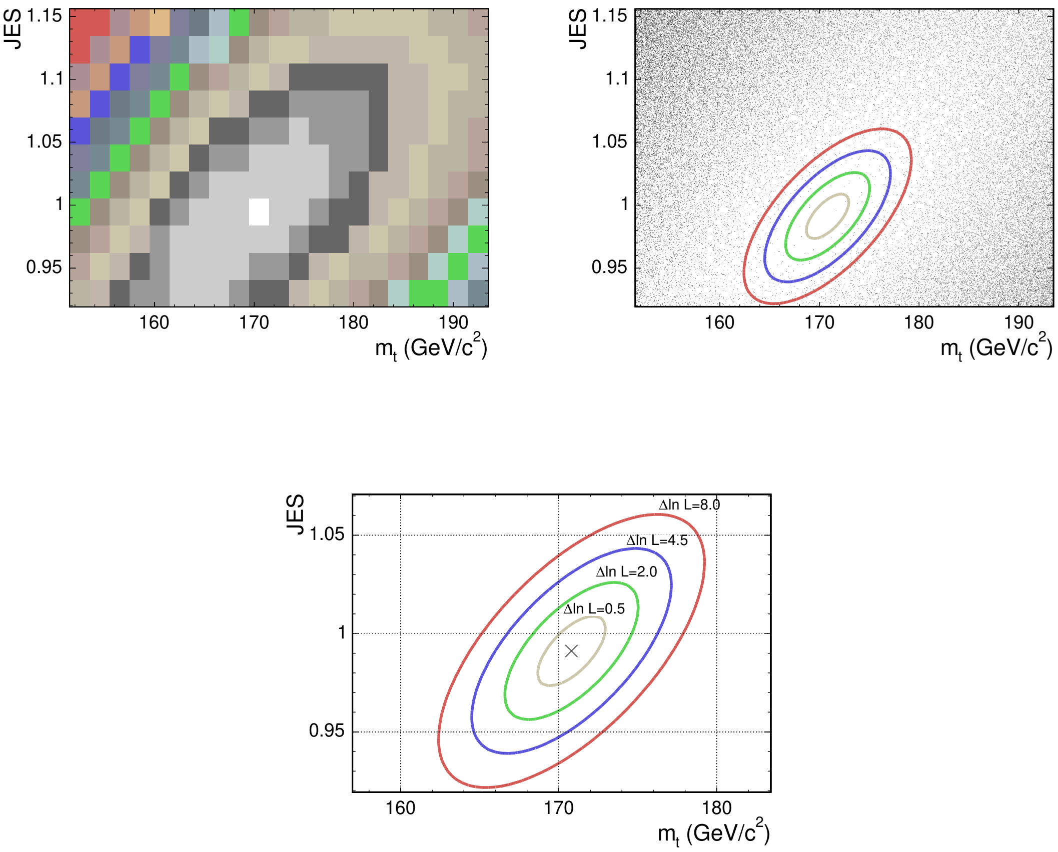

Figure 8.24: Minus log likelihood after minimization of C_s in full experimental dataset (left). Fit contours and minus log likelihood (right). Zoom view of contours (center).

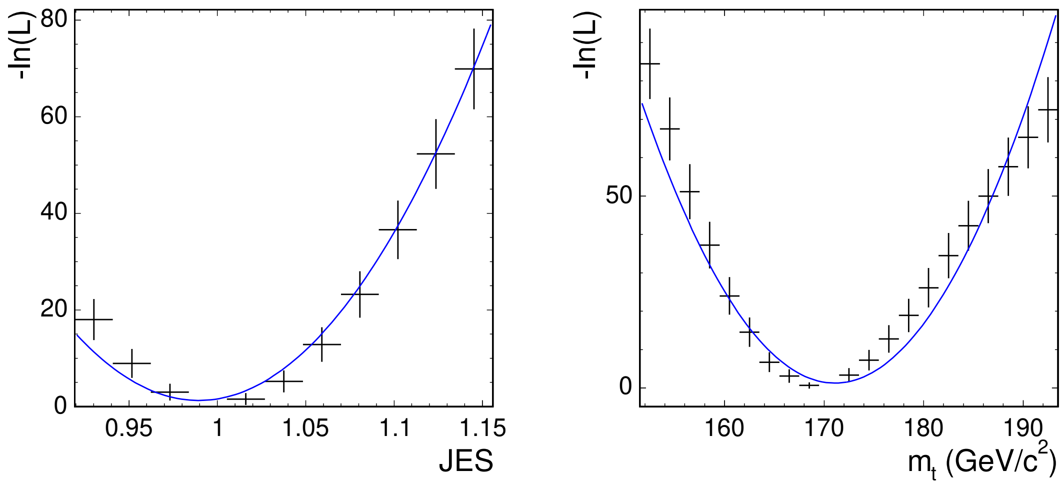

Figure 8.25: Minus log likelihood histogram and fit at m_t = 170.5 GeV/c^2 (left) and at JES = 0.99 (right) after minimization of C_s in full experimental dataset.

8.2.1 Measurement in Data Subsamples

The full dataset is divided to check consistency between various subsamples: individual datasets, charged lepton type, and number of secondary vertex tags. Table 8.2 summarizes the results for measurements in these data subsets. None of the errors shown in these figures or reported in these tables have been adjusted for proper coverage unless explicitly stated otherwise. There are some fluctuations in the measurements in data subsets, the largest being the measurement in the *0i* dataset. Measurements as a function of the number of reconstructed vertices are shown in Figure 8.26. No significant dependence of either m_t or JES is observed within statistics.

Table 8.2: Measurement Results in Data Subsamples

Dataset	m_t (GeV/c^2)	JES	C_s
full	170.8 ± 2.1	0.99 ± 0.02	0.68
0i	162.4 ± 3.6	0.92 ± 0.03	0.74
0h	174.7 ± 3.8	1.03 ± 0.03	0.60
0d	173.8 ± 3.1	1.01 ± 0.03	0.74
electrons	169.2 ± 2.7	0.96 ± 0.02	0.64
muons	174.1 ± 3.2	1.04 ± 0.03	0.75
single-tag	166.9 ± 2.9	0.97 ± 0.02	0.64
double-tag	175.5 ± 3.1	1.01 ± 0.03	0.79

Figure 8.27 shows the likelihood as a function of m_t and JES for the individual datasets (*0d*, *0h* and *0i*). These measurements, with properly adjusted errors, are compared to the measurement in the full dataset in Figure 8.28, which also shows differences in measurements between datasets. Errors were corrected by a factor of about 1.09 in m_t and 1.12 in JES depending on pseudo-experiment

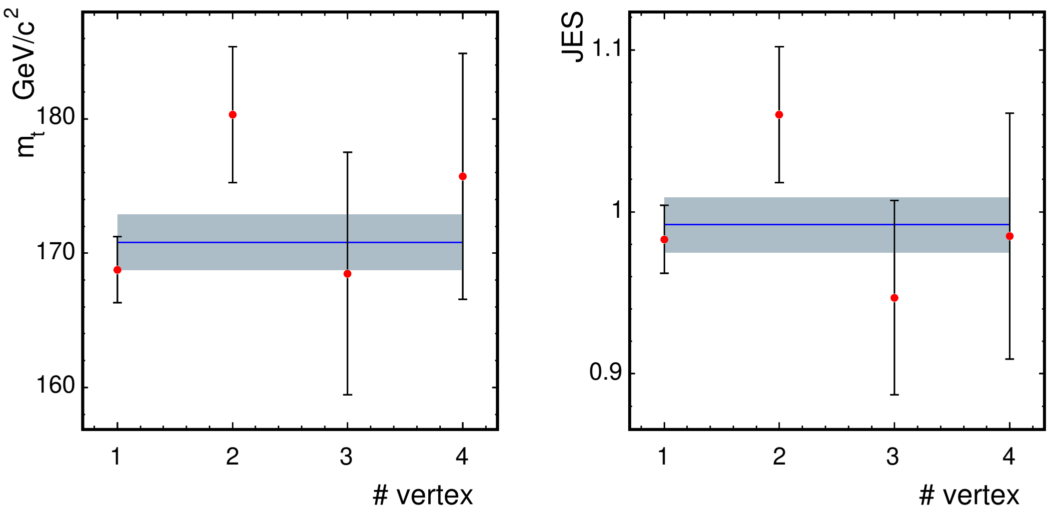

Figure 8.26: Measurement in full dataset of m_t and JES as a function of the number of reconstructed vertices in the sample. The horizontal line and band is the combined measurement and error respectively.

tests with an average number of events equal to that observed in the individual dataset. A simultaneous fit to the correlated m_t and JES parameters in these three datasets results in a χ^2 of 6.94 with 4 degrees of freedom, or a p-value of 14%. Fitting m_t alone results in a 7% probability and JES alone results in a 8% probability [58]. Using pseudo-experiments, we calculate a 5% probability of the *0i* dataset fluctuating to its measured value from that of the combined *0d* and *0h* datasets.

As an additional check of the *0i* dataset fluctuation, this sample is further divided by charged lepton and number of secondary vertex tags. Table 8.3 lists the results of measurements in these subsets of the *0i* dataset. The measurements of all the subsets agree within errors.

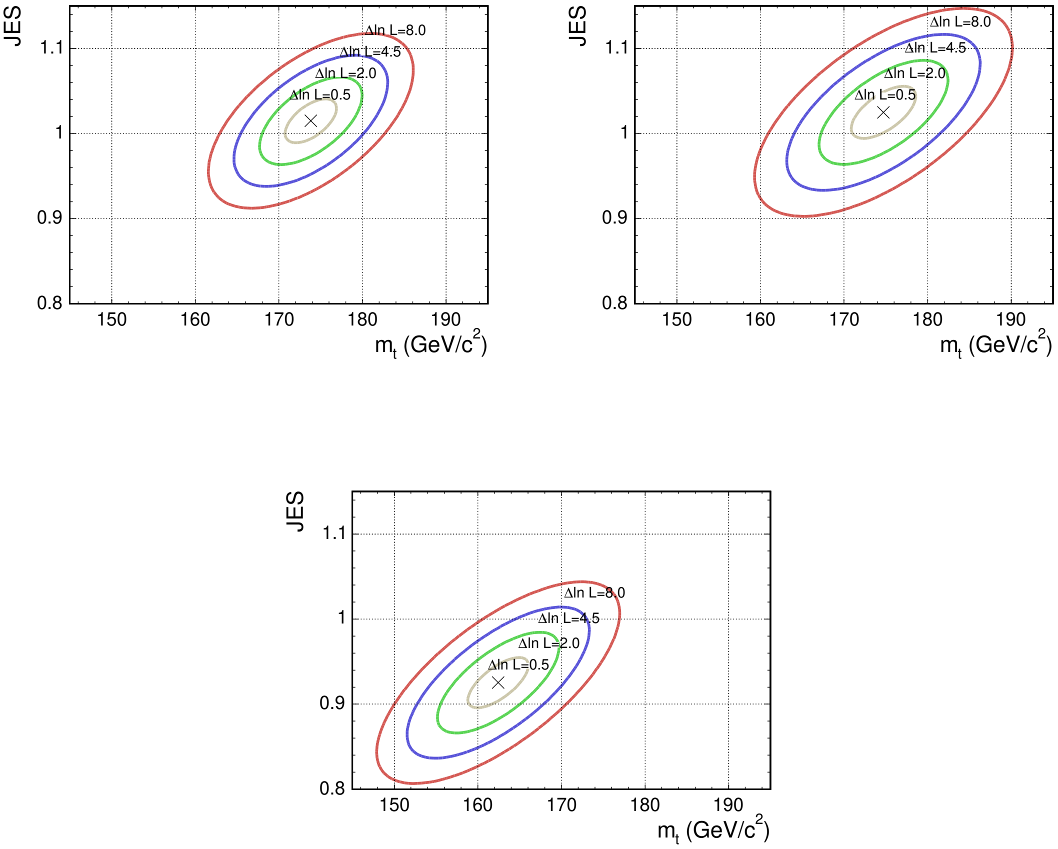

Figure 8.27: Gaussian fit to likelihoods after minimization of C_s for the individual datasets *0d* (left), *0h* (right) and *0i* (center).

Table 8.3: Measurement results in subdivisions of *0i* dataset

Dataset	m_t (GeV/c^2)	JES	C_s
Electrons	160.8 $\pm$ 4.9	0.92 $\pm$ 0.04	0.68
Muons	164.5 $\pm$ 5.3	0.93 $\pm$ 0.05	0.87
Single-tag	157.8 $\pm$ 5.9	0.89 $\pm$ 0.05	0.70
Double-tag	165.3 $\pm$ 4.7	0.94 $\pm$ 0.04	0.84

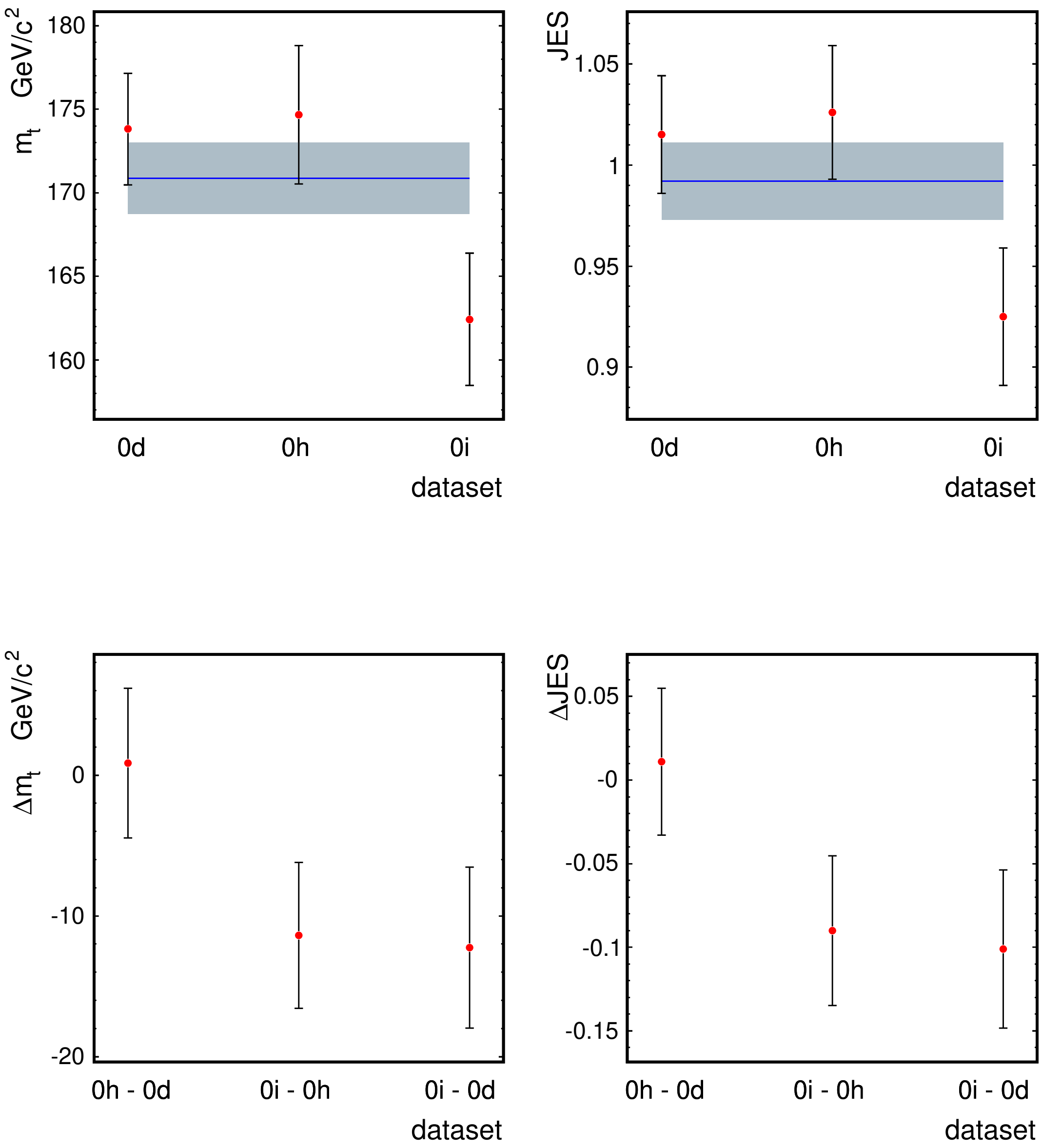

Figure 8.28: Measurements in individual datasets of m_t (upper left) and JES (upper right). The blue line and shaded band represent the combined measurement and error, respectively. Differences in measurements between datasets in m_t (lower left) and JES (lower right).

8.3 Experimental and Simulated Data Comparison

In this section we compare experimental and simulated data distributions that involve information from the likelihood in some way. We use the full dataset, and simulated $t\bar{t}$ events are generated with a top quark mass of 170 GeV/c^2 and jet energy scale of 0.99. The simulated event sample is comprised of events described in section 5.3 with specific contributions weighted according to Table 5.1.

Jets are identified with a specific parton by using the permutation, section 6.3.2, yielding the highest maximum likelihood value for a given event. This method for choosing a permutation is not expected to correctly identify the originating parton 100% accurately. Figure 8.29 shows distributions of jet η and p_T. No significant deviations between data and simulated data are observed. Figure 8.30 shows two-jet and three-jet invariant mass distributions. Again, data and simulated data agree well. Figure 8.31 shows the invariant mass distributions with the chosen permutation as a function of η and p_T, calculated from the sum of the respective four-vectors in the lab frame. Good agreement is observed between data and simulated data. Kolmogorov-Smirnov tests return reasonably distributed probabilities, $0 < \mathrm{KS} < 1$, for these distributions.

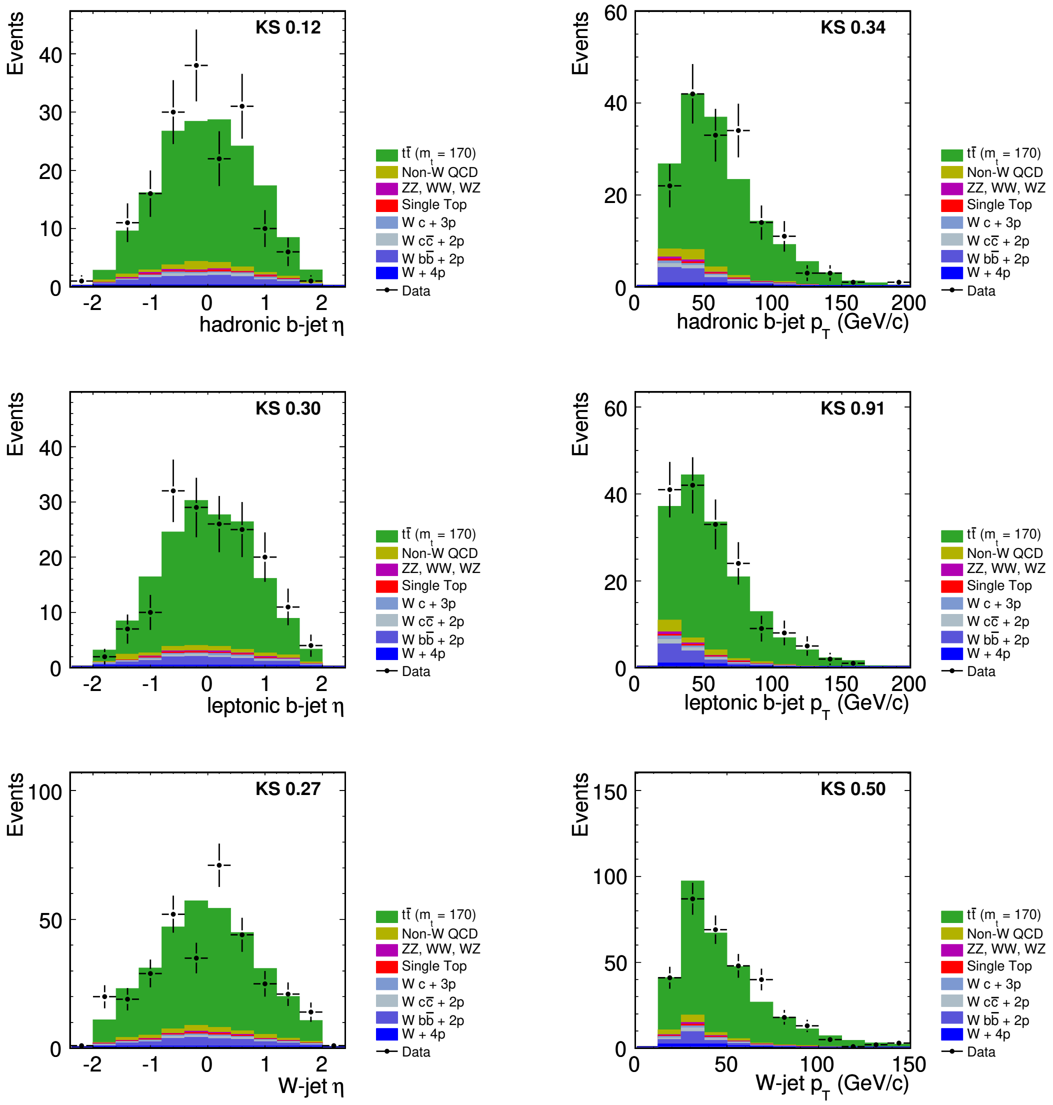

Figure 8.29: Distribution of jet η (left) and p_T (right) in data and simulated for jets identified with hadronic b quarks (upper), leptonic b quarks (center), and quarks from W boson decay (lower).

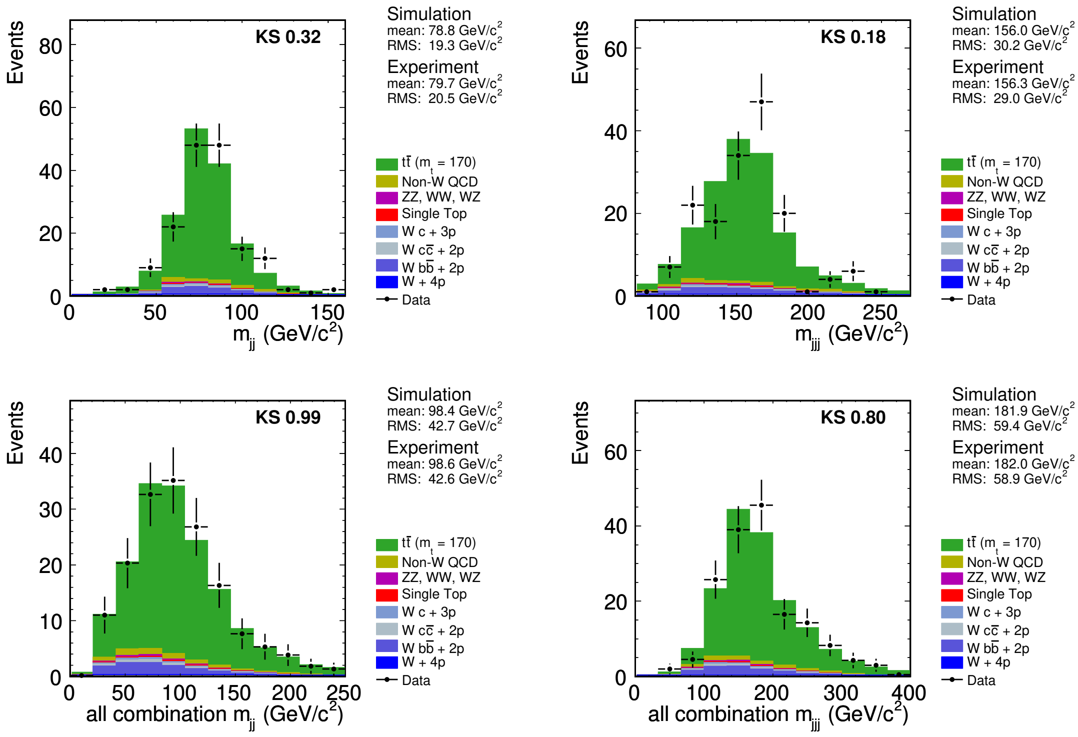

Figure 8.30: Distribution of two-jet (left) and three-jet (right) invariant mass for the chosen permutation (upper) and all possible permutations (lower) in data and simulated data.

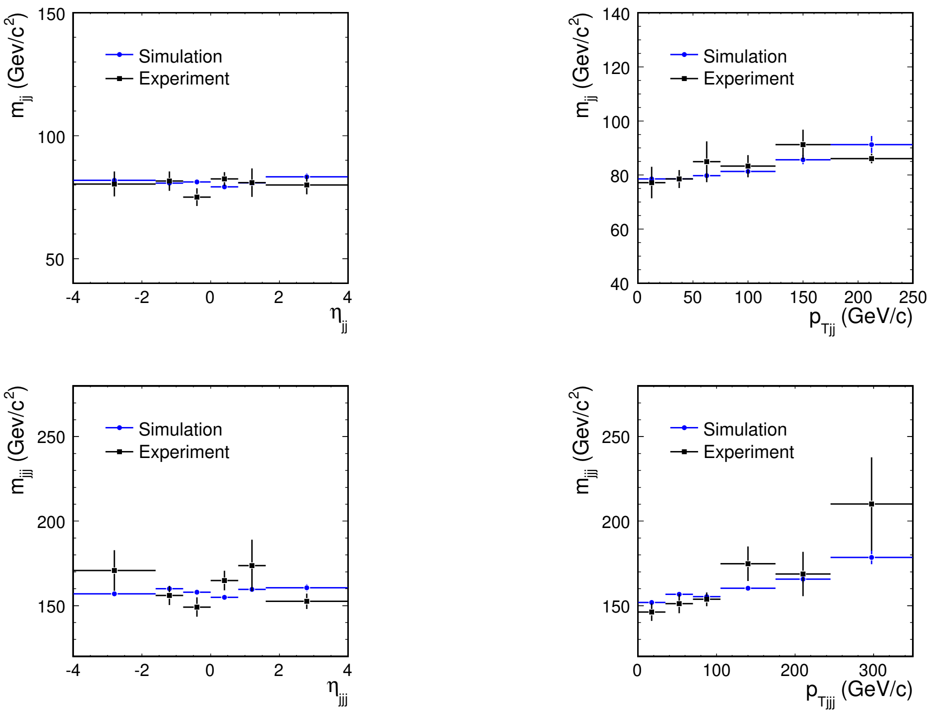

Figure 8.31: Two-jet (upper) and three-jet (lower) invariant mass as a function of η (left) and p_T (right) for the chosen permutation in data and simulated data.

Comparisons of distributions of quantities specific to the likelihood are also made. Figure 8.32 shows the distribution of the log of the $t\bar{t}$ probability density evaluated at m_t = 174.5 GeV/c^2 and JES = 1 and the distribution of the log of the W + jets probability evaluated at JES = 1. Good agreement is observed between data and simulated data. Figure 8.33 shows the distribution of the most probable m_t parameter for each event at specific intervals of JES. Similarly, Figure 8.34 shows the distribution of the most probably JES parameter for each event at specific intervals of m_t. In both cases, good agreement between data and simulated data is observed.

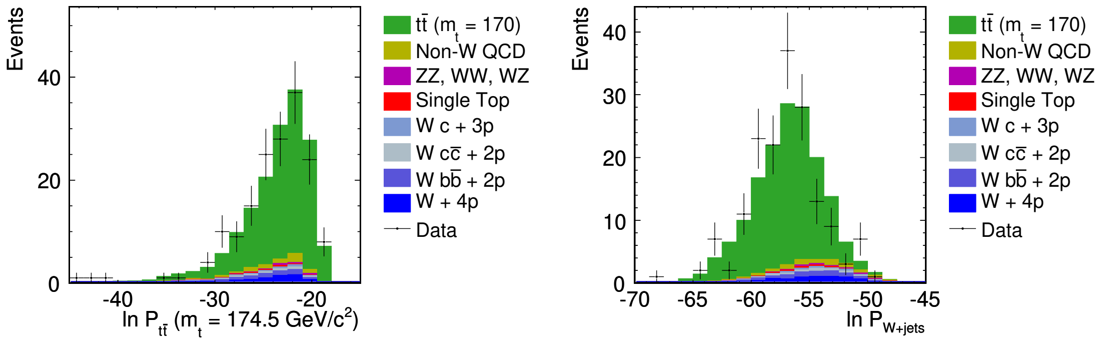

Figure 8.32: Distribution of $t\bar{t}$ probability evaluated at m_t = 174.5 GeV/c^2 and JES = 1 (left) and distribution of W+jets probability evaluated at JES = 1 (right) in data and simulated data.

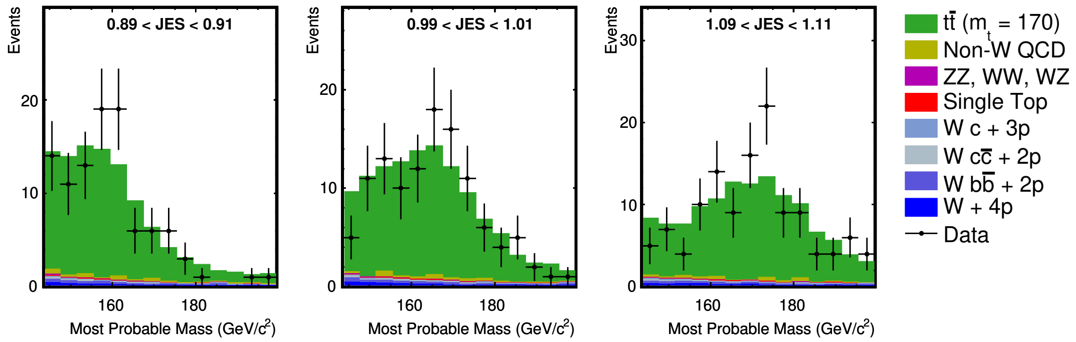

Figure 8.33: Distribution of most probable mass of $t\bar{t}$ probability evaluated at JES = 0.9 (left), 1.0 (center) and 1.1 (right), in data and simulated data.

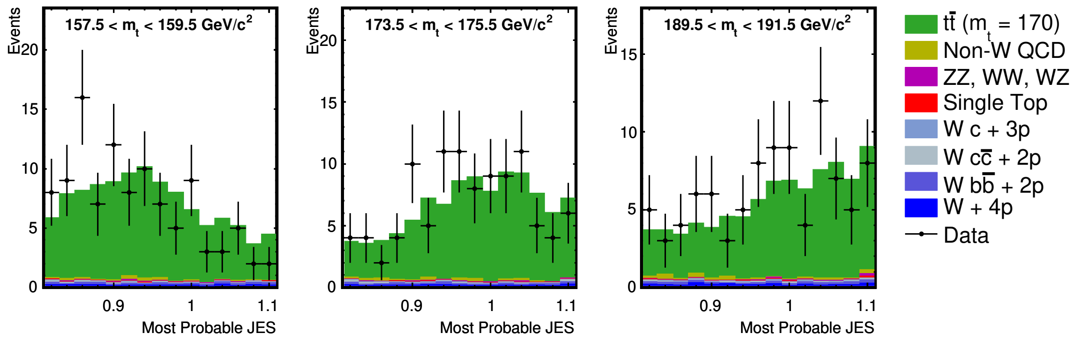

Figure 8.34: Distribution of most probable JES of $t\bar{t}$ probability evaluated at m_t = 158.5 (left), 174.5 (center) and 190.5 (right) GeV/c^2, in data and simulated data.

CHAPTER 9

Top Quark Mass Systematic Uncertainty

This chapter discusses the procedures used to estimate the systematic uncertainty quoted on the measurement of the top quark mass. Systematic uncertainties for some effects, such as limitations in event simulation or reconstruction and calibration, are individually estimated, assumed to be uncorrelated, and combined in quadrature to estimate a total systematic uncertainty. Some systematic effects, such as a full, non-leading order description of simulated events, are difficult if not impossible to model. Non-leading order effects in simulated events are included in part when varying QCD radiation. Other effects are correlated and therefore over-estimate the total uncertainty. Table 9.1 lists the individually assessed systematic uncertainties on the measurement of the top quark mass. The items in this list are described in detail in the following sections. These uncertainties are conservatively estimated and the total systematic uncertainty, 1.38 GeV/c^2, is expected to be a conservative estimate.

Individual systematic uncertainties are generally estimated by constructing pseudo-experiments similarly to those described in section 8.1.2. Pseudo-experiments use 118 Poisson fluctuated events. The estimation of systematic uncertainty is usually made by taking the difference between the measured top quark mass in nominally simulated events with that of events with $\pm 1\sigma$ of the effect in question. Two methods are used to shift events: they are either independently generated or assigned a weight.

Table 9.1: Summary of Systematic Uncertainty

Source of Systematic Uncertainty	Magnitude (GeV/c^2)
Residual Jet Energy Scale	0.42
b quark Jet Energy Scale	0.60
Simulated Event Generator	0.19
Initial State QCD Radiation	0.72
Final State QCD Radiation	0.76
Secondary Vertex Tag Scale Factor	0.31
Background Composition	0.21
Parton Distribution Function	0.12
Statistical Limitations	0.26
Lepton p_T	0.22
Multiple Interactions	0.05
Total	1.39

Events in independently generated samples are not correlated and statistical uncertainty is relevant. These uncertainties are reduced by using the one-dimensional likelihood, which greatly decreases the CPU time required to process an event and increases the total number of events available for pseudo-experiment construction. Section 9.10.1 shows uncertainties estimated using the one-dimensional likelihood are consistent with the two-dimensional likelihood for one of the largest contributions to systematic uncertainty.

Events in weighted samples are correlated, so statistical uncertainties are irrelevant and ignored when taking the difference in the measured top quark mass.

The two-dimensional likelihood is modified to weight each event in the term:

$$\ln\mathcal{L} = \sum_{i=1}^{N} w_i \ln P_i, \tag{9.1}$$

where P_i is the probability associated with event i and w_i is the corresponding systematic weight. Although approximately 118 unique events are used in each pseudo-experiment, the sum of weights is approximately 12000. Studies with pseudo-experiments have shown the best fit parameter from such a likelihood has a reasonable distribution even though the uncertainties are not valid and not used in the study of systematic uncertainty [59].

9.1 Jet Energy Scale

The likelihood fits for the effects of uncertainty in jet energy scale. Additional effects, such as the dependence on jet p_T or η, also contribute to systematic uncertainty. Also, the measured JES is determined for jets from the W boson decay and assumed to be correct for jets from b quark decay. Additional systematic uncertainty is assigned for jets originating from b quarks.

Second order effects are estimated by fluctuating jet energies by $\pm 1\ \sigma$ in simulated $t\bar{t}$ events with a top quark mass of 175 GeV/c^2 and fitting with the two-dimensional likelihood so as not to double count the systematic uncertainty. Uncertainty in jet energy, σ, is estimated by the CDF Jet Energy and Resolution (JER) working group [33], and is a function of η and p_T. The results are shown in Table 9.2, and the largest difference from events generated with nominal jet energy scale is taken as the residual jet energy scale systematic uncertainty, 0.42 GeV/c^2. Note that statistical errors on the measurements are not significant because the majority of events in the samples are correlated.

Also shown in Table 9.2, the JES measurements in these simulated events

Table 9.2: JES Systematic Uncertainty

Sample	-σ	nominal	+σ
2D m_t (GeV/c^2)	174.33 $\pm$ 0.59	174.75 $\pm$ 0.64	174.44 $\pm$ 0.55
2D Δm_t (GeV/c^2)	-0.42	-	-0.31
2D JES	1.031 $\pm$ 0.029	0.999 $\pm$ 0.025	0.966 $\pm$ 0.026
2D ΔJES	0.032	-	-0.033
1D m_t (GeV/c^2)	170.94 $\pm$ 0.39	173.99 $\pm$ 0.40	176.55 $\pm$ 0.40
1D Δm_t (GeV/c^2)	-3.05	-	2.56

return reasonable values given the jet energy scale at which they were generated. Note that we expect to measure JES > 1 in the $-\sigma$ sample and JES < 1 in the $+\sigma$ sample given the definition of the JES parameter. Measurements of m_t in one-dimension also show the expected dependence on jet energy scale uncertainty. Since these effects are removed to first-order in the two-dimensional measurement, it is reasonable that the nominal m_t is not bounded by the $\pm 1\ \sigma$ measurements. This effect is seen in some of the other samples used to estimate systematic uncertainty.

The estimation of jet energy scale uncertainty by the JER group assumes the jets are from quarks with smaller masses than b quarks. Additional uncertainty is associated with jets from b quark decay: fragmentation, energy scale and color flow. Detailed studies [60] find a 0.2 ± 0.4 GeV uncertainty due to fragmentation, a 0.4 GeV/c^2 uncertainty on the b-jet JES and a 0.3 GeV/c^2 uncertainty due to modeling of the color flow. Other analyses have estimated the uncertainty on the top quark mass due to these effects to be 0.6 GeV/c^2 [61]. Their estimation is taken to be the systematic uncertainty for this analysis.

9.2 Simulated Event Generator

Simulated events are used to model transfer function parameters, chapter 7, and to test the likelihood, section 8.1. Dependence of the m_t measurement on the event generator is estimated by comparing measurements in events generated with two different event generators, PYTHIA and HERWIG. These generators are independent and have different hadronization models and tuning of underlying events. Using events generated with a top quark mass of 178 GeV/c^2, we observe a difference of 0.09 ± 0.19 GeV/c^2 in m_t measurement between these two generators using a one-dimensional likelihood fit, Table 9.3. These events are uncorrelated, so the systematic uncertainty is conservatively taken as the statistical error on this difference, or 0.19 GeV/c^2.

Table 9.3: Generator Systematic Uncertainty

PYTHIA (GeV/c^2)	HERWIG (GeV/c^2)	Δm_t (GeV/c^2)
180.29 ± 0.14	180.19 ± 0.14	-0.09 ± 0.19

9.3 Initial and Final State QCD Radiation

Simulated events model initial and final state radiation due to the emission of a gluon in QCD. Uncertainty in this modeling contributes as a systematic uncertainty. Since radiation is a non-leading order effect, this systematic also includes some of the error associated with using a leading order event generator. Simulated samples are generated with a top quark mass of 178 GeV/c^2 and with radiation modeling adjusted to have *less* or *more* radiation, signifying one sigma variation from the nominal modeling. Table 9.4 summarizes the results of measuring m_t in these samples with the one-dimensional likelihood. The largest difference from nominal in ISR and FSR are each taken as a source of systematic uncertainty, 0.76 GeV/c^2 and 0.72 GeV/c^2, respectively.

Table 9.4: Radiation Systematic Uncertainty

Sample	m_t (GeV/c^2)	Δm_t (GeV/c^2)
nominal	180.29 ± 0.14	-
ISR less	180.48 ± 0.16	0.19 ± 0.21
ISR more	181.01 ± 0.16	0.72 ± 0.21
FSR less	180.61 ± 0.16	0.32 ± 0.21
FSR more	181.05 ± 0.23	0.76 ± 0.27

9.4 Secondary Vertex Tag Scale Factor

Modeling of secondary vertex tagging in simulated events has some uncertainty associated with it. This uncertainty is determined in the form of uncertainty in the E_T dependence of a scale factor for the efficiency of secondary vertex tagging between experimental and simulated data [62]:

$$\epsilon^{+} \equiv 0.842 + 0.00118 * E_T \tag{9.2}$$
$$\epsilon^{-} \equiv 0.977 - 0.00118 * E_T,$$

where $\epsilon^{\pm}$ represents one sigma uncertainty. Note the nominal scale factor between experimental and simulated data is about 0.91. A systematic uncertainty is estimated for this effect by weighting events in pseudo-experiments with the appropriate scale factor. An event is weighted for each jet associated with a secondary vertex. No weight greater than unity is allowed. Measurement of m_t in weighted pseudo-experiments fit with the one-dimensional likelihood are shown in Table 9.5. Since $\epsilon^{\pm}$ each represent a one sigma shift, half of this difference is taken as the systematic uncertainty, 0.31 GeV/c^2.

Table 9.5: Secondary Vertex Tag Scale Factor Systematic Uncertainty

ϵ^{+} (GeV/c^2)	ϵ^{-} (GeV/c^2)	Δm_t (GeV/c^2)
179.96 ± 0.10	180.58 ± 0.10	0.62

9.5 Background Composition and Modeling

Systematic error assigned due to background composition and modeling is comprised of three separate effects: uncertainty in the total contribution of background in the event sample, limitations in our understanding of the contribution of individual background processes to the total, and variations in the Q^2 scale at which W+jets simulated events are generated. Uncertainties were estimated using the two-dimensional likelihood and events generated at nominal jet energy scale. Estimations from these three effects are summed in quadrature to produce a total background systematic uncertainty.

Uncertainty in the total contribution of background events includes uncertainty corresponding to scaling the estimation with luminosity of this contribution from a smaller subset of the data, 318 pb^{-1}, to the whole dataset 955 pb^{-1}, see section 5.3. We take the uncertainty on the total background contribution to be a conservative 10%, double the error on the total background given in Table 5.1. Pseudo-experiments using events generated at a top quark mass of 172.5 GeV/c^2 were constructed varying the background contribution by this amount, with m_t measurements listed in Table 9.6. The dependence of m_t on fraction of $t\bar{t}$ events in the sample is also shown in Figure 8.8. Since most of the events are correlated between these samples, we ignore the statistical error on these measurements and take the largest observed difference, 0.09 GeV/c^2, as the contribution for this effect.

Table 9.6: Background Normalization Systematic Uncertainty

Signal fraction	m_t (GeV/c^2)	Δm_t (GeV/c^2)
nominal (83%)	172.68 $\pm$ 0.53	-
70%	172.67 $\pm$ 0.80	-0.01
90%	172.77 $\pm$ 0.59	0.09

Limitations in our understanding of the contribution of individual background processes are estimated by varying the relative contributions of each process by 100%. Pseudo-experiments were constructed using events generated at a top quark mass of 178 GeV/c^2. Results of m_t measurements are listed in Table 9.7. Events are highly correlated between samples, so statistical error is ignored. The largest observed difference from the nominal contribution is taken as the systematic uncertainty, 0.09 GeV/c^2.

Table 9.7: Background Composition Systematic Uncertainty

Sample	m_t (GeV/c^2)	Δm_t (GeV/c^2)
nominal	178.86 ± 2.77	-
non-W	178.80 ± 2.88	-0.06
W+jets	178.79 ± 2.96	-0.09
Wb$\bar{b}$	178.87 ± 2.95	0.01
Wc$\bar{c}$	178.91 ± 2.84	0.05
Wc	178.89 ± 2.84	0.03
Single top	178.82 ± 2.83	-0.04
EWK	178.85 ± 2.86	-0.01

The final background modeling and composition uncertainty component comes from varying the Q^2 scale characteristic of the hard scattering process at which W+jets events are generated. The nominal sample uses $Q^2 = m_W^2$ and is compared to events generated with $Q^2 = \frac{1}{4}m_W^2$, $Q^2 = 4m_W^2$, and $Q^2 = \langle p_{T\,W}^2 \rangle$, fractions of the invariant mass squared and average transverse momentum squared of the W boson. All events were generated with ALPGEN in $W + 4p$ and $Wb\bar{b}$. Table 9.8 lists the results of using these samples in pseudo-experiments minimized with the two dimensional likelihood. The $t\bar{t}$ events used in this test were generated with a top quark mass of 178 GeV/c^2. Although the W+jets events in these pseudo-experiments are uncorrelated, the majority of the events are correlated, so statistical uncertainty is ignored. The contribution to the systematic uncertainty is estimated as the largest shift from nominal, 0.17 GeV/c^2.

Total background composition and modeling systematic uncertainty is taken to be the quadrature sum of estimations from varying the total background contri-

Table 9.8: Background Q^2 Modeling Systematic Uncertainty

Sample	m_t (GeV/c^2)	Δm_t (GeV/c^2)
nominal	178.86 ± 2.77	-
$Q^2 = \frac{1}{4}m_W^2$	179.01 ± 2.90	0.15
$Q^2 = 4m_W^2$	178.91 ± 2.96	0.05
$Q^2 = \langle p_{T\,W}^2 \rangle$	179.03 ± 2.82	0.17

bution, relative contribution of background processes, and the Q^2 used in W+jet event generation. This sum is 0.21 GeV/c^2.

9.6 Parton Distribution Functions

Parton distribution functions (PDFs) are fit to a variety of experimental data by groups such as `CTEQ` [38] and `MRST` [63]. The `CTEQ` group estimates the uncertainty in their parameterization with a set of 20 eigenvector pairs of possible variations. The effect of these variations on the top quark mass measurement is included as a systematic uncertainty. Also included are the differences between using `CTEQ` and `MRST` PDFs and the effect of varying the Λ_{QCD} scale used in the PDFs.

PDF systematic uncertainties are estimated in events generated at a top quark mass of 178 GeV/c^2 and nominal jet energy scale with `CTEQ5L` PDFs. The re-weighting technique is used, minimizing large pseudo-experiments with the two-dimensional likelihood. In these pseudo-experiments, $t\bar{t}$ events are weighted according to the ratio between `CTEQ5L` and the PDF in question. Statistical errors are ignored as the events are almost completely correlated.

Figure 9.1 plots measurements of m_t in these pseudo-experiments as a function of various PDFs and eigenvectors. The uncertainty from the 20 `CTEQ` eigenvec-

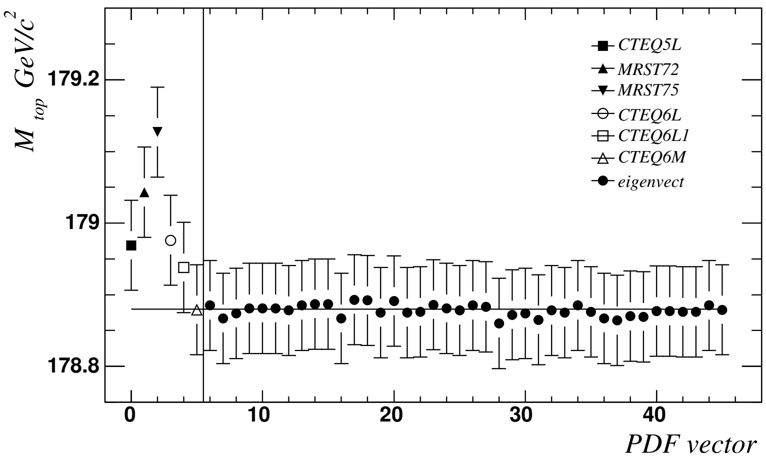

Figure 9.1: Measurements of m_t with 20 CTEQ eigenvector pairs, MRST, and Λ_{QCD} samples.

tor pairs is estimated by adding the differences between each set in quadrature, resulting in 0.05 GeV/c^2. The difference between CTEQ5L and MRST72, both using $\Lambda_{QCD} = 228$ MeV, is 0.07 GeV/c^2. MRST75 uses $\Lambda_{QCD} = 300$ MeV, and the difference between measurements with the two Λ_{QCD} scales is 0.08 GeV/c^2. Summing these three contributions in quadrature results in a total PDF systematic uncertainty of 0.12 GeV/c^2.

As a cross-check, pseudo-experiments are constructed using independent event samples generated at a top quark mass of 178 GeV/c^2 and nominal jet energy scale with MRST72 and MRST75 PDFs and compared to the nominal CTEQ5L sample. Pseudo-experiments are minimized with the one-dimensional likelihood with measurements in m_t listed in Table 9.9. Since event samples are not correlated, statistical error is relevant. Variations due to differing PDF model and Λ_{QCD} are consistent with uncertainties estimated using re-weighted events within statistical error.

Table 9.9: PDF Systematic Uncertainty Cross-Check

Sample	m_t (GeV/c^2)	Δm_t (GeV/c^2)
`CTEQ5L`	180.28 $\pm$ 0.14	-
`MRST72`	180.26 $\pm$ 0.16	-0.02 $\pm$ 0.22
`MRST75`	180.07 $\pm$ 0.17	-0.21 $\pm$ 0.22

9.7 Statistical Limitations

The number of events available in statistical tests of this analysis method are limited by the large amount of CPU time necessary to process events. In some cases, generation of simulated data is also limited. Pseudo-experiments use large amounts of resampling from some background samples. A systematic uncertainty is estimated combining the statistical limitations in tests of the method combined with the effects of heavily resampling in the most statistically limited background, the non-W sample, see section 5.3. Note that resampling used in $t\bar{t}$ events is shown to have no effect in section 9.10.3.

Effects of limited simulated event sample size appear in statistical tests of the method described in section 8.1.2. In terms of the top quark mass, the most important test is the m_t parameter linearity shown in Figure 8.22. The top quark mass estimated in the two-dimensional likelihood is unbiased within the statistical error, 0.26 GeV/c^2, of the residual plot. This error defines the extent to which the assumption of no bias is valid and is included as a systematic uncertainty.

To estimate the effect of heavily resampling the non-W background sample, two separate pseudo-experiments are constructed using two exclusive subsets of the non-W sample. All events except non-W are identical between pseudo-experiments and statistical errors are ignored. Simulated events were generated

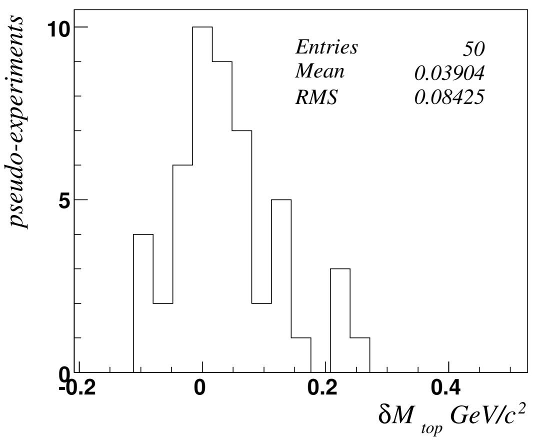

Figure 9.2: Distribution of m_t differences for various divisions of non-W sample

at a top quark mass of 175 GeV/c^2 and nominal jet energy scale. The difference between m_t measurements in pseudo-experiments minimized with the two-dimensional likelihood is histogrammed for 50 randomly selected subset pairs, Figure 9.2. The systematic uncertainty due to this effect is estimated to be $\frac{1}{2}$ the RMS of this distribution, 0.042 GeV/c^2. The factor of $\frac{1}{2}$ arises from using $\frac{1}{2}$ the non-W sample in these pseudo-experiments, contributing $\frac{1}{\sqrt{2}}$, and because the difference of two quantities is used, contributing another factor of $\frac{1}{\sqrt{2}}$.

The total systematic uncertainty due to statistical limitations is the quadrature sum of these two effects. This sum is clearly dominated by limitations in the number of $t\bar{t}$ events. Effects due to heavy resampling in some of the other background samples are assumed to be of the same order as the non-W sample, giving essentially no contribution. The total systematic uncertainty is estimated to be 0.26 GeV/c^2.

9.8 Lepton p_T Uncertainty

Uncertainty in the modeling of charged lepton p_T in simulated data contributes to the systematic uncertainty in the measurement of the top quark mass. The uncertainty of the lepton p_T has been very conservatively estimated to be 1% [64]. To estimate the effects of this uncertainty, pseudo-experiments are constructed using events generated at a top quark mass of 175 GeV/c^2 and nominal jet energy scale and minimized using the two-dimensional likelihood. Table 9.10 lists m_t measurements with nominal reconstructed charged lepton p_T and in samples with p_T shifted by $\pm$ 1%. The events are completely correlated between pseudo-experiments, so statistical error is ignored. The largest shift from the nominal measurement, 0.22 GeV/c^2, is taken as the systematic uncertainty due to uncertainty in charged lepton p_T.

Table 9.10: Lepton p_T systematic uncertainty

Shift (%)	m_t (GeV/c^2)	Δm_t (GeV/c^2)
-1	174.54 $\pm$ 0.57	-0.22
0	174.76 $\pm$ 0.64	-
+1	174.78 $\pm$ 0.52	0.02

9.9 Multiple $p\bar{p}$ Interactions

As discussed in section 5.2, simulated events were generated in a limited range of the full dataset and therefore have lower average instantaneous luminosity. The increase in instantaneous luminosity results in an increase in multiple interactions and can be measured via the number of reconstructed vertices. The dependence of measured m_t on number of vertices was shown to be negligible within the given statistics in Figure 8.17.

A systematic error is assigned for the unmodeled multiple interactions in simulated data according to an estimation made by the top quark mass working group [65]. The effect is estimated by parameterizing jet E_T as a function of number of reconstructed vertices and varying these energies according to the distribution of vertices in the full dataset. The estimate results in 50 MeV/c^2 for analyses directly measuring the jet energy scale systematic uncertainty. This estimation is consistent with the dependence shown in Figure 8.17 and is taken as the systematic uncertainty for this analysis.

9.10 Cross-Checks

This section compares systematic uncertainty estimated using the one-dimensional and two-dimensional likelihoods and discusses some effects not included as systematic uncertainties: the fraction of gluon fusion in $t\bar{t}$ production, resampling of $t\bar{t}$ events in pseudo-experiments, and mis-identified b quarks via secondary vertex tagging.

9.10.1 Likelihood

We show estimations using the two-dimensional likelihood are consistent with those of the one-dimensional likelihood for one of the largest contributions to the systematic uncertainty, final-state radiation. Some systematic uncertainties are estimated from statistically independent simulated event samples. In order for estimations not to be dominated by statistical error, large numbers of events must be processed. Since CPU time was limited, errors were estimated using a fit in the single m_t dimension of the likelihood after minimization for C_s. Pseudo-experiments in the one-dimensional likelihood are drawn from an event pool of about 20,000 events and those in the two-dimensional likelihood are drawn from about 5,000 events. As can be seen in Table 9.11, the two-dimensional likelihood results in smaller offsets from nominal but has large statistical error. Offsets in the one-dimensional likelihood are not statistically limited and are consistent with the two-dimensional results within their error.

Table 9.11: FSR Systematic Uncertainty in 2D and 1D

Sample	2D m_t (GeV/c^2)	2D Δm_t (GeV/c^2)
nominal	178.00 $\pm$ 0.67	-
FSR less	177.78 $\pm$ 0.44	-0.22 $\pm$ 0.80
FSR more	177.92 $\pm$ 0.39	-0.08 $\pm$ 0.80
Sample	1D m_t (GeV/c^2)	1D Δm_t (GeV/c^2)
nominal	180.29 $\pm$ 0.14	-
FSR less	180.61 $\pm$ 0.16	0.32 $\pm$ 0.21
FSR more	181.05 $\pm$ 0.23	0.76 $\pm$ 0.27

9.10.2 Gluon Fusion

The `HERWIG` and `PYTHIA` Monte Carlo generators are leading-order, but some next-to-leading order effects are simulated in parton showering. These parameters are varied in the radiation systematic discussed in section 9.3. Other non-leading order effects include the size of the contribution of gluon fusion to $t\bar{t}$ pair production. Leading order calculations estimate a 5% contribution at the Tevatron, whereas next-to-leading order calculations estimate a 15% contribution. Note that the diagram for gg fusion is not included in the matrix element used in this analysis. We estimate the systematic uncertainty due to varying gg fusion using pseudo-experiments of events constructed with 5% and 15% gg fusion. Events were generated with PYTHIA at a top quark mass of 178 GeV/c^2 and nominal jet energy scale, and pseudo-experiments were minimized with the one-dimensional likelihood. Table 9.12 lists the resulting m_t measurements. The majority of events are correlated, so statistical error is ignored. The resulting shift in m_t, 0.06 GeV/c^2, is negligible compared to approximately 1 GeV/c^2 from radiation.

Table 9.12: Effect of Gluon Fusion on Measurement

gg contribution	m_t (GeV/c^2)	Δm_t (GeV/c^2)
LO (5%)	179.95 ± 0.10	-
NLO (15%)	180.01 ± 0.17	0.06

9.10.3 Event Resampling

Resampling of events in generating pseudo-experiments is widely used throughout this analysis. A systematic error for resampling in background events is discussed in section 9.7. Simulated $t\bar{t}$ data is resampled to a lesser extent and contributes only in the calibration of estimated error, section 8.1.2.2, and to the estimation of systematic uncertainties discussed previously in this chapter. Resampling does not contribute to the statistical tests using a single large pseudo-experiment, so does not affect bias studies. Its contribution to estimation of systematic uncertainty is considered a second-order effect and neglected.

A large simulated event sample (20,000 events) generated at a top quark mass of 178 GeV/c^2 and nominal jet energy scale is used to determine how resampling affects the calibration of estimated error. Pseudo-experiments are minimized using the one-dimensional likelihood. Separate pseudo-experiment tests are done varying the amount of the full sample available for resampling. The amount of resampling is inversely varied with the available sample size in such a way that the total number of pseudo-experiments is held constant to the number of exclusive pseudo-experiments possible with the full sample.

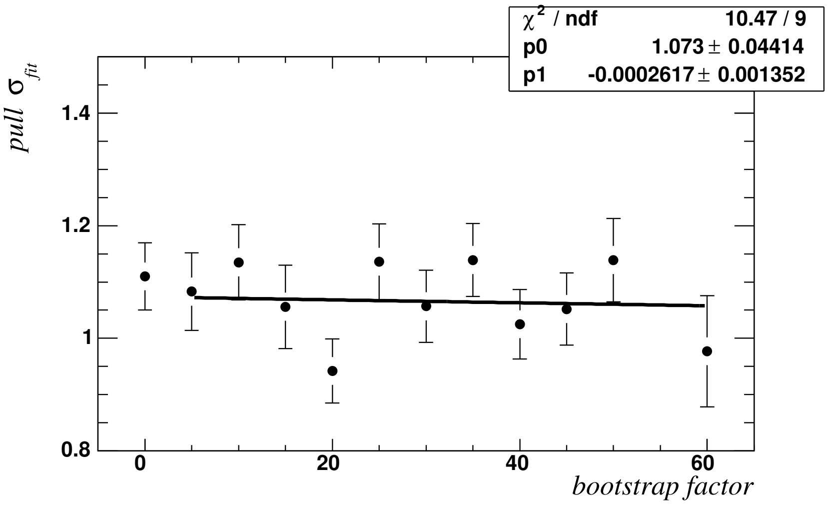

Figure 9.3: Fitted sigma of pull distributions from resampled pseudo-experiments

Figure 9.3 plots σ from a Gaussian fit to the pull distribution against the *bootstrap factor*, defined as the multiplicative factor giving total pseudo-experiments from the number of exclusive pseudo-experiments available from a given event pool. Each point in this figure represents a pseudo-experiment test, with increasing bootstrap factor indicating a smaller subset of events available for pseudo-experiment construction. The point at bootstrap factor of zero is the result using the full event sample and no resampling. Errors are the error on the fit of the pull distribution to the Gaussian σ parameter given by `MINUIT`. The slope of the fit to these points is consistent with zero and the fit is consistent with the result without resampling. Resampling with a bootstrap factor greater than 30 is not used. No additional systematic uncertainty is necessary due to resampling of $t\bar{t}$ events.

9.10.4 Mis-Identified Secondary Vertex Tags

As discussed in section 5.2, the simulated data sample used to test this analysis does not correctly model the instantaneous luminosity of the full dataset. Increasing instantaneous luminosity results in an increasing percentage of mis-identified b quarks due to secondary vertex tagging. Two possible effects on the measurement are considered: contribution to expected background and background composition, and identification of permutations in the $t\bar{t}$ probability.

Effects of mis-identification on the background sample are shown in Figure 9.4. The contribution of the W+4p sample in Table 5.1 is simultaneously increased with total background contribution to the sample. Events are generated at a top quark mass of 175 GeV/c^2 and nominal jet energy scale. Measurements of m_t, JES and C_s are plotted as a function of multiplicative factor increase in mis-identification. The last point in the plots represents an increase of 400% in the W+4p contribution to the background and a decrease in the total $t\bar{t}$ contribution of 5%. The total number of events per pseudo-experiment is held constant. Errors are not shown because most of the events between pseudo-experiments are correlated. Measurements in both m_t and JES fluctuate about zero offset from nominal, but a significant decrease in C_s is observed with increasing mis-identification. This decrease in signal fraction is expected due to the decreasing $t\bar{t}$ content of the pseudo-experiments. The fluctuations in m_t are all within the 0.09 GeV/c^2 systematic uncertainty assigned for uncertainty in background modeling.

Mis-identification of b quarks also affects the permutations used in the $t\bar{t}$ probability, section 6.3.2. This effect is studied by simulating secondary vertex identification using jet-parton matching within an η-ϕ cone of radius 0.4. Matching and secondary-vertex tagging disagree about 3% of the time in the nominal simulated event sample used for this study. Pseudo-experiments are constructed

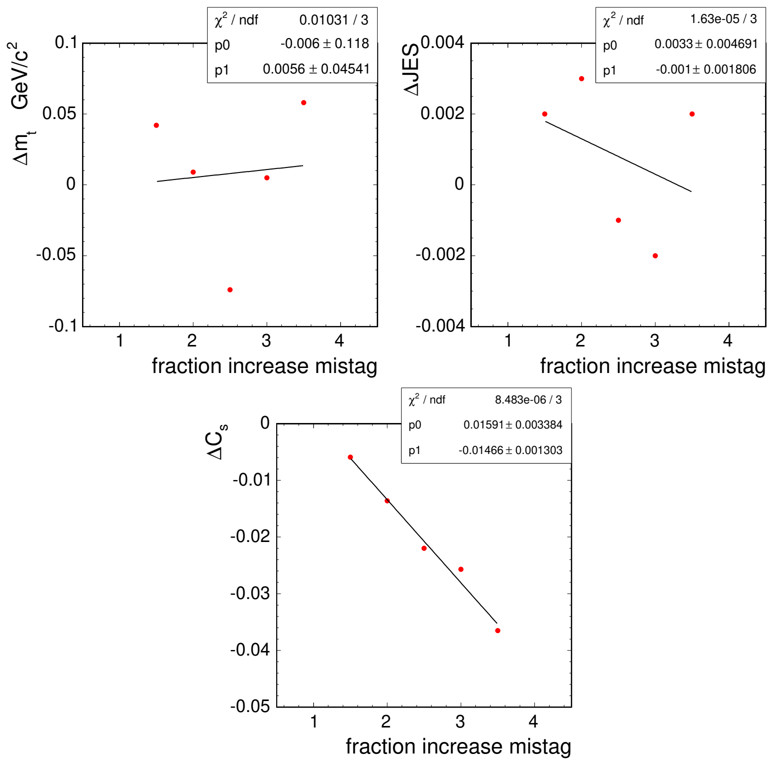

Figure 9.4: Deviation from nominal measurement in measured m_t (upper left), JES (upper right), and C_s (bottom) as a function of increasing W+4p background contribution due to increased b mistag rate in pseudo-experiments.

in which matching information is used to randomly assign secondary vertex identification in a jet. Events were generated at a top quark mass of 178 GeV/c^2 and nominal jet energy scale, and pseudo-experiments were minimized with the two dimensional likelihood. Figure 9.5 shows the results of measurements in m_t, JES and C_s as a percentage of events with randomly assigned secondary-vertex identification. A negative correlation is observed in all variables. The range shown indicates a 500% increase in the number of mis-identified jets and is a considerable over-estimate of the expected effect in data. The shift in m_t is about 500 MeV over this range. We expect this effect to negligibly contribute to systematic uncertainty.

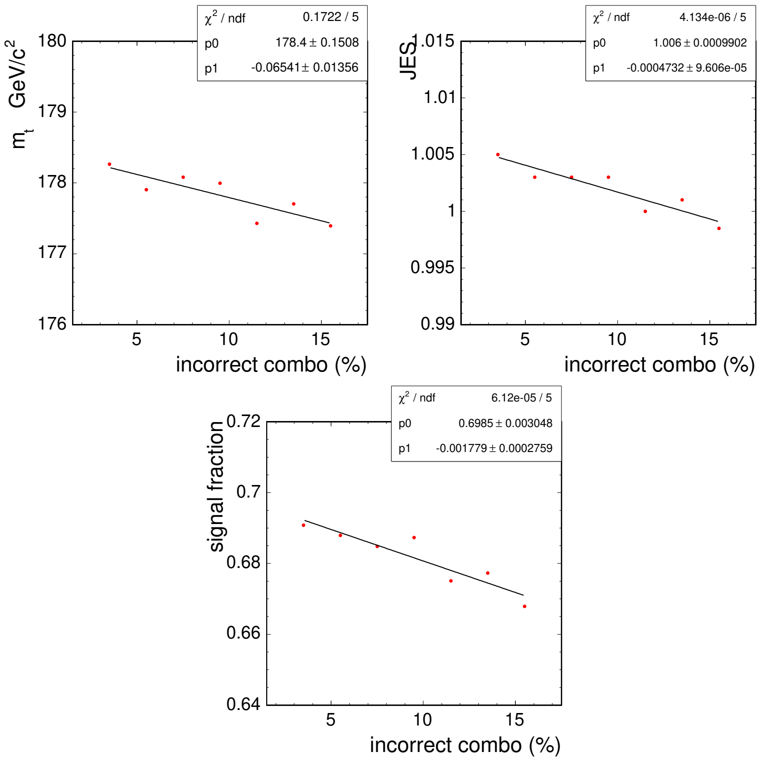

Figure 9.5: Measurements in m_t (upper left), JES (upper right) and C_s (bottom) as a function of percentage of b quark mis-identification.

CHAPTER 10

Conclusions

This analysis selects events from 955 pb^{-1} total integrated luminosity of $p\bar{p}$ collisions at $\sqrt{s} = 1.96$ TeV collected with CDF Run II at FNAL up to February 2006. Events are selected to be consistent with the lepton plus jets decay channel of top quark pair production: 167 such events meet this requirement in data. The mass of the top quark is measured using a matrix element analysis technique with *in situ* measurement of the largest source of systematic uncertainty, the jet energy scale. The analysis also fits for the fraction of events consistent with top quark pair production and is independent from a separate estimate of event sample composition. It does not apply *a priori* information in the likelihood fit to any of the measured parameters. The measured top quark mass is

$$m_t = 170.8 \pm 2.2 \text{ (stat.) } \pm 1.4\text{(syst.)} = 170.8 \pm 2.6 \text{ GeV/c}^2, \tag{10.1}$$

where the statistical error includes uncertainty from the jet energy scale. The measured jet energy scale and signal fraction parameters are consistent with expectations. With a fractional error of 1.5%, this represents the single best measurement to date. It currently dominates the world average top quark mass, contributing with a weight of about 50%. The world average top quark mass using the result of this measurement is [66]

$$m_t = 171.4 \pm 2.1 \text{ GeV/c}^2. \tag{10.2}$$

APPENDIX A

Details of Probability Density Calculations

A.1 Calculation of Top Quark Decay Width

This section describes the calculation of the decay width of the top quark, $t \rightarrow Wb \rightarrow e\nu b$, from the standard expression for a three-body decay, Equation 6.27

$$d\Gamma_t = \frac{1}{2^7(2\pi)^5}\frac{|M|^2}{m_t}(1 - \frac{m_W^2}{m_t^2})\ dm_W^2 d\Omega_W d\Omega_e, \tag{A.1}$$

To be consistent with the assumptions described in Section 6.3.1, we use the narrow-width approximation, Equation 6.26, and the decay part of the Matrix element amplitude from Equation 6.24 expressed as

$$|\mathcal{M}|^2 = \frac{g_w^4}{4}(m_t^2 - m_W^2)\frac{m_t^2(1-c_{eb}^2) + m_{e\nu}^2(1+c_{eb})^2}{(m_{e\nu}^2 - m_W^2)^2 + m_W^2\Gamma_W^2}, \tag{A.2}$$

where g_W is the weak coupling constant, and c_{eb} is defined to be the cosine of the angle between the electron and b quark. Substituting Equation A.2 into Equation A.1 and integrating over the decay phase space results in an expression for the width

$$\Gamma_t = \frac{g_W^4 m_t^3}{2^9(2\pi)^5}\int\left(1 - \frac{m_{e\nu}^2}{m_t^2}\right)^2\left[\frac{1 - c_{eb}^2 + \frac{m_{e\nu}^2}{m_t^2}(1+c_{eb})^2}{(m_{e\nu}^2 - m_W^2)^2 + m_W^2\Gamma_W^2}\right] dm_{e\nu}^2 d^2\Omega_{e\nu} d^2\Omega_e. \tag{A.3}$$

Integration over the angular $d^2\Omega_{e\nu}$ is trivial and results in a factor of 4π. For purposes of integration over $d^2\Omega_e$, we choose a reference frame such that the cosine of the angle between the b quark and lepton, c_{be}, is equivalent to the cosine of the spherical coordinate θ of the lepton, $\cos\theta_e$, where $x \equiv c_{eb} = \cos\theta_e$. In this case, integration over the ϕ component of $d^2\Omega_e$ is trivial and results in a factor of 2π. The remaining expression for the width is

$$\Gamma_t = \frac{g_W^4 m_t^3}{2^8(2\pi)^3} \int \left(1 - \frac{m_{e\nu}^2}{m_t^2}\right)^2 \left[\frac{1 - x^2 + \frac{m_{e\nu}^2}{m_t^2}(1+x)^2}{(m_{e\nu}^2 - m_W^2)^2 + m_W^2\Gamma_W^2}\right] dm_{e\nu}^2\, dx. \qquad (A.4)$$

Defining $\mu \equiv \frac{m_{e\nu}^2}{m_t^2}$, the relevant integral over x is

$$(1-\mu)^2 \int_{-1}^{1} \left[1 - x^2 + \mu(1+x)^2\right]\, dx = \frac{4}{3}(1 - 3\mu^2 + 2\mu^3). \qquad (A.5)$$

We make an approximation and set the event mass $m_{e\nu}$ in Equation A.5 equal to the pole mass m_W and remove this term from the integration. The resulting expression for the width becomes

$$\Gamma_t = \frac{g_W^4 m_t^3}{3\ 2^6(2\pi)^3}(1 - 3\mu^2 + 2\mu^3) \int_0^{(m_t - m_b)^2} \frac{dm_{e\nu}^2}{(m_{e\nu}^2 - m_W^2)^2 + m_W^2\Gamma_W^2}, \qquad (A.6)$$

where $\mu = \frac{m_W^2}{m_t^2}$. Integration over the event mass squared results in

$$\frac{1}{m_W\Gamma_W}\arctan[\frac{(m_t - m_b)^2 - m_W^2}{m_W\Gamma_W}] - \arctan[\frac{-m_W^2}{m_W\Gamma_W}]. \qquad (A.7)$$

The expression for the width is now identical to that of Equation 6.28

$$\begin{aligned} \Gamma_t &= \frac{g_W^4 m_t^3 \Theta}{3\ 2^6(2\pi)^3} \frac{1 - 3(m_W/m_t)^4 + 2(m_W/m_t)^6}{m_W\Gamma_W} \\ \Theta &\equiv \arctan[\frac{(m_t - m_b)^2 - m_W^2}{m_W\Gamma_W}] - \arctan[\frac{-m_W^2}{m_W\Gamma_W}]. \end{aligned} \qquad (A.8)$$

Figure A.1 compares this expression with that of Kuehn [53] after multiplying by an empirical factor of 9.11 in Equation A.8 to make these expressions approximately consistent. This scale factor is applied when using the width in this analysis.

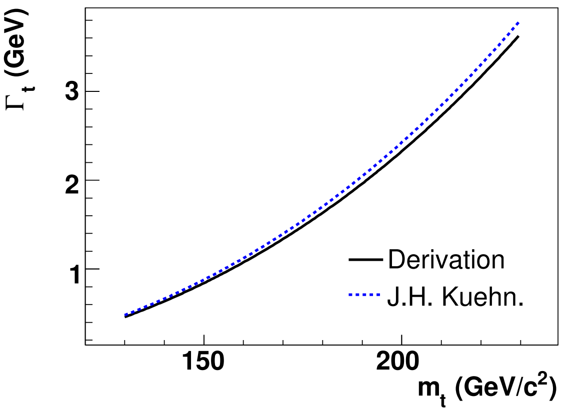

Figure A.1: Comparison of derived expression for top quark decay width, Equation A.8, to Kuehn [53].

A.2 Details of $t\bar{t}$ Variable Change

Section 6.3.2 discusses integration variables in the $t\bar{t}$ probability density. Details of the change of variables follow.

On the hadronic side, variables are changed from (p_{j2}, p_{bh}) to (m^2_{wh}, m^2_{th}). The equations governing this transformation are derived from the standard expression for invariant mass

$$\begin{aligned} m^2_{wh} &= (p_{j1} + p_{j2})^2 \sim 2p_{j1}p_{j2}(1 - \cos\Theta_{12}) && \text{(A.9)} \\ m^2_{th} &= (p_{bh} + p_{j1} + p_{j2})^2 = m^2_b + m^2_{wh} + 2(E_{bh}E_{j1} - p_{bh}p_{j1}\cos\Theta_{b1}) \\ &+ 2(E_{bh}p_{j2} - p_{bh}p_{j2}\cos\Theta_{b2}). && \text{(A.10)} \end{aligned}$$

Equation A.9 immediately results in an expression for the momentum magnitude of the second quark from hadronic W boson decay

$$p_{j2} = \frac{m^2_{wh}}{2p_{j1}(1 - \cos\Theta_{12})}. \qquad \text{(A.11)}$$

Subbing Equation A.11 into Equation A.10 gives solutions for p_{bh}

$$p_{bh} = \frac{-MC \pm P\sqrt{M^2 + m_b^2(C^2 - P^2)}}{C^2 - P^2}. \tag{A.12}$$

The physical solution is given by the negative term, and M, C and P are defined

$$\begin{aligned} M &\equiv \frac{1}{2}(m_{th}^2 - m_{wh}^2 - m_b^2) \\ P &\equiv p_{j1} + p_{j2} \\ C &\equiv p_{j1}\cos\Theta_{b1} + p_{j2}\cos\Theta_{b2}. \end{aligned} \tag{A.13}$$

The solutions for the variable change on the hadronic side are unique.

On the leptonic side, variables are changed from $(p_{bl}, p_{\nu\, z})$ to (m_{wl}^2, m_{tl}^2). Solutions are more complicated because $p_{\nu\, x}$ and $p_{\nu\, y}$ are constrained by integration over four momentum conservation:

$$P_x = p_{bl}\sin\phi_{bl}\, \cos\theta_{bl} + p_\nu \sin\phi_\nu\, \cos\theta_\nu + \sum^4 p_{i\, x} \tag{A.14}$$

$$P_y = p_{bl}\sin\phi_{bl}\, \sin\theta_{bl} + p_\nu \sin\phi_\nu\, \sin\theta_\nu + \sum^4 p_{i\, x}, \tag{A.15}$$

but depend on p_{bl} and $p_{\nu\, z}$. The sum is over the remaining four decay products: the charged lepton, denoted by e; and the hadronic decay products. The momentum P_i are analogous to $p_{t\bar{t}}^i$ used in section 6.3.2. Spherical coordinates are used for convenience. These equations combine with the standard invariant mass expressions for the leptonic top quark and W boson

$$\begin{aligned} \frac{1}{2}m_{wl}^2 &= p_e p_\nu(1 - \sin\phi_e\, \cos\theta_e \sin\phi_\nu\, \cos\theta_\nu \\ &- \sin\phi_e\, \sin\theta_e \sin\phi_\nu\, \sin\theta_\nu - \cos\theta_e \cos\theta_\nu) \end{aligned} \tag{A.16}$$

$$\begin{aligned} \frac{1}{2}(m_{tl}^2 - m_{wl}^2 - m_b^2) &= p_{bl}p_e(1 - \cos\Theta_{be}) + p_{bl}p_\nu(1 - \sin\phi_{bl}\, \cos\theta_{bl}\sin\phi_\nu\, \cos\theta_\nu \\ &- \sin\phi_{bl}\, \sin\theta_{bl}\sin\phi_\nu\, \sin\theta_\nu - \cos\theta_{bl}\cos\theta_\nu). \end{aligned} \tag{A.17}$$

These four equations are reduced to two coupled second order equations and finally a quartic equation, written in terms of $\sin\phi_\nu \cos\theta_\nu$ and $\sin\phi_\nu \sin\theta_\nu$ of the angles of the neutrino. Solving in this manner is simply a convenient choice.

Using equation A.14 and equation A.15, the momentum magnitude of the neutrino and leptonic b quark are

$$\begin{aligned} p_\nu &= \frac{a_1 b_0 - a_0 b_1}{b_1 \sin\phi_\nu \cos\theta_\nu - a_1 \sin\phi_\nu \sin\theta_\nu} && \text{(A.18)} \\ p_{bl} &= \frac{a_0 \sin\phi_\nu \sin\theta_\nu - b_0 \sin\phi_\nu \cos\theta_\nu}{b_1 \sin\phi_\nu \cos\theta_\nu - a_1 \sin\phi_\nu \sin\theta_\nu} && \text{(A.19)} \end{aligned}$$

where

$$\begin{aligned} a_0 &\equiv \sum^4 p_{i\,x} - P_x \\ a_1 &\equiv \sin\phi_{bl} \cos\theta_{bl} \\ b_0 &\equiv \sum^4 p_{i\,x} - P_y \\ b_1 &\equiv \sin\phi_{bl} \cos\theta_{bl}. \end{aligned} \qquad \text{(A.20)}$$

Using these definitions, equation A.16 can be re-written as

$$\cos\theta_e \cos\theta_\nu = 1 - \beta_1 \sin\phi_\nu \cos\theta_\nu - \beta_2 \sin\phi_\nu \sin\theta_\nu, \qquad \text{(A.21)}$$

where

$$\begin{aligned} \alpha_0 &\equiv a_1 b_0 - a_0 b_1 \\ \alpha_1 &\equiv m_{wl}^2 \,/\, 2\, \alpha_0\, p_e \\ \beta_1 &\equiv \sin\phi_e \cos\theta_e + b_1\, \alpha_1 \\ \beta_2 &\equiv \sin\phi_e \sin\theta_e - a_1\, \alpha_1. \end{aligned} \qquad \text{(A.22)}$$

The angular term $\cos\theta_\nu$ is replaced using the trigonometry identity

$$\sin^2\phi_\nu \cos^2\theta_\nu + \sin^2\phi_\nu \sin^2\theta_\nu + \cos^2\theta_\nu = 1, \qquad \text{(A.23)}$$

and the final result is a second order polynomial in $\sin\phi_\nu \cos\theta_\nu$ and $\sin\phi_\nu \sin\theta_\nu$

$$\begin{aligned} 1 - \cos^2\theta_e + \sin^2\phi_\nu \cos^2\theta_\nu(\beta_1^2 + \cos^2\theta_e) + \sin^2\phi_\nu \sin^2\theta_\nu(\beta_2^2 + \cos^2\theta_e) \\ -2\beta_1 \sin\phi_\nu \cos\theta_\nu - 2\beta_2 \sin\phi_\nu \sin\theta_\nu + 2\beta_1\beta_2 \sin\phi_\nu \cos\theta_\nu \sin\phi_\nu \sin\theta_\nu = 0 \end{aligned} \tag{A.24}$$

The other second-order polynomial comes from Equation A.17. Substituting equation A.18 for p_ν results in

$$\frac{M}{p_{bl}} = \frac{\gamma_0 + \gamma_1 \sin\phi_\nu \cos\theta_\nu + \gamma_2 \sin\phi_\nu \sin\theta_\nu}{b_1 \sin\phi_\nu \cos\theta_\nu - a_1 \sin\phi_\nu \sin\theta_\nu} \tag{A.25}$$

where

$$\begin{aligned} d_0 &\equiv p_e(1 - \cos\Theta_{be}) \\ \gamma_0 &\equiv \alpha_0(1 - \frac{\cos\theta_{bl}}{\cos\theta_e}) \\ \gamma_1 &\equiv \alpha_0 \sin\phi_\nu \cos\theta_\nu(\frac{\beta_1 \cos\theta_{bl}}{\cos\theta_e} - \sin\phi_{bl} \cos\theta_{bl}) + d_0 b_1 \\ \gamma_2 &\equiv \alpha_0 \sin\phi_\nu \sin\theta_\nu(\frac{\beta_2 \cos\theta_{bl}}{\cos\theta_e} - \sin\phi_{bl} \sin\theta_{bl}) - d_0 a_1. \end{aligned} \tag{A.26}$$

Substituting equation A.19 results in a second-order equation in $\sin\phi_\nu \cos\theta_\nu$ and $\sin\phi_\nu \sin\theta_\nu$

$$\begin{aligned} & \sin^2\phi_\nu \cos^2\theta_\nu(Mb_1^2 + b_0\gamma_1) + \sin^2\phi_\nu \sin^2\theta_\nu(Ma_1^2 - a_0\gamma_2) \\ + \; & 2\sin\phi_\nu \cos\theta_\nu \sin\phi_\nu \sin\theta_\nu(-Ma_1b_1 - \frac{1}{2}a_0\gamma_1 + \frac{1}{2}b_0\gamma_2) \\ - \; & a_0\gamma_0 \sin\phi_\nu \sin\theta_\nu + b_0\gamma_0 \sin\phi_\nu \cos\theta_\nu = 0. \end{aligned} \tag{A.27}$$

Equation A.24 and equation A.24 represent two coupled second order equations of the form

$$\begin{aligned} ax^2 + 2bxy + cy^2 + 2dx + 2ey + f = 0 \\ Ax^2 + 2Bxy + Cy^2 + 2Dx + 2Ey = 0 \end{aligned} \tag{A.28}$$

this can be written as a quartic equation

$$\begin{aligned}
& x^4(4ab'^2 + 4b\alpha_3 + ca'^2) + x^3(8ab'e' + 4b\alpha_2 + c\gamma_3 + 8db'^2 + 4e\alpha_3) \\
+ \quad & x^2(4ae'^2 + 4b\alpha_1 + c\gamma_2 + 16db'e' + 4e\alpha_2 + 4fb'^2) \\
+ \quad & x(4b\alpha_0 + c\gamma_1 + 8de'^2 + 4e\alpha_1 + 8fb'e') + (cf^2 + 4e\alpha_0 + 4fe'^2) = 0
\end{aligned} \tag{A.29}$$

where

$$\begin{aligned}
a' &\equiv a - \frac{c}{C}A \\
b' &\equiv b - \frac{c}{C}B \\
d' &\equiv d - \frac{c}{C}D \\
e' &\equiv e - \frac{c}{C}E \\
\alpha_0 &\equiv fe' \\
\alpha_1 &\equiv 2d'e' + fb' \\
\alpha_2 &\equiv 2d'b' + a'e' \\
\alpha_3 &\equiv a'b' \\
\gamma_1 &\equiv 4d'f \\
\gamma_2 &\equiv 2a'f + 4d'^2 \\
\gamma_3 &\equiv 4a'd'
\end{aligned} \tag{A.30}$$

Solutions to a quartic equation are described in Appendix B. Due the assumptions of perfect angular resolution and negligible leptonic b quark mass, valid physical solutions could have small imaginary parts. Machine number accuracy also introduces errors in the solutions. A loose requirement $\text{Im}(x) < 10$ is placed on roots. Solutions are further required to be consistent with Equation A.21

$$|1 - (\cos\theta_e \cos\theta_\nu + \beta_1 \sin\phi_\nu \cos\theta_\nu + \beta_2 \sin\phi_\nu \sin\theta_\nu)| < 0.01 \tag{A.31}$$

Physical solutions are also selected by requiring $|p_\nu| < 800$ GeV/c and $0 < q_1 < 980$ GeV/c and $-980 < q_2 < 0$ GeV/c and parton energies less than the transfer function bounds described in section A.4. Note that the approximation of zero mass is used for solving the variable change only. The solution for the leptonic b quark momentum is assumed to be the energy. A a mass of 4.8 GeV/c^2 is assigned to this quark by scaling the magnitude of the momentum appropriately.

A.3 Details of W + Jets Variable Change

Section 6.4.2 discusses integration variables in the W + jets probability density. Details for the calculation of the longitudinal momentum of the neutrino, $p_{\nu\,z}$, from the invariant mass of the W boson squared, m_W^2, follow. Neglecting lepton and neutrino mass compared to momentum, p_e and p_ν, respectively, the invariant mass squared is

$$m_W^2 = 2(p_e p_\nu - \vec{p}_e \cdot \vec{p}_\nu). \tag{A.32}$$

This expression can be written as a quadratic expression in the longitudinal neutrino momentum

$$\frac{1}{2}m_W^2 + p_{e\,x}p_{\nu\,x} + p_{e\,y}p_{\nu\,y} \equiv a = p_e\sqrt{p_{\nu\,T}^2 + p_{\nu\,z}^2} - p_{e\,z}p_{\nu\,z}. \tag{A.33}$$

The solutions of this quadratic are

$$p_{\nu\,z} = \frac{a p_{e\,z} \pm p_e\sqrt{(a + p_{e\,T}p_{\nu\,T})(a - p_{e\,T}p_{\nu\,T})}}{p_{e\,T}^2}. \tag{A.34}$$

Either of the two solutions could be the correct momentum. To be physical, the transverse mass of the combined lepton and neutrino must be less than the invariant mass of the W boson. This constraint is applied during integration.

A.4 Parton Energy Integration Limits

The jet energy transfer functions are parameterized with two Gaussian functions, see Equation 7.4 in section 7.1. Few simulated events populate the tails of distributions such as the δ_E distribution, see Figure 7.2. Generally, the transfer function parameterization of the tails extends far beyond the limit of the simulated events and is not considered to be physical. Both the $t\bar{t}$ and W + jets probability densities set integration limits on parton energies. In the case of the $t\bar{t}$ probability density, only the upper limit is used.

The lower and upper bounds are a function of jet energy and are parameterized with a third-order polynomial describing the parton energy at which the value of the transfer function is one thousandth the maximum possible value of the transfer function at a given jet energy. The lower bound is forced to be physical and not allowed to be less than zero energy. The maximum transfer function value as a function of jet energy is parameterized with a ninth-order polynomial. Generally good agreement in fits are shown for light quarks in Figure A.2 and for b quarks in Figure A.3. Table A.1 lists the parameters describing the lower bound, Table A.2 lists the parameters describing the upper bound, and Table A.3 lists the parameters describing the maximum transfer function value.

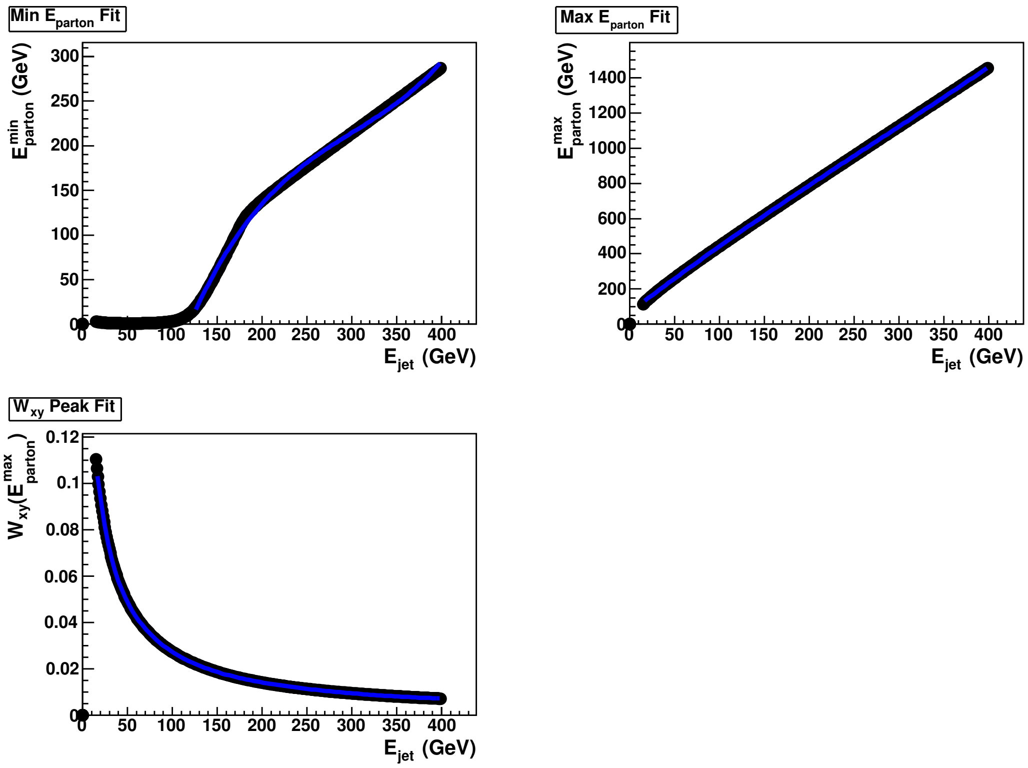

Figure A.2: Minimum parton energy (right), maximum parton energy (left), and maximum value of transfer function (bottom) as a function of jet energy in light quark transfer function parameters.

Table A.1: Parameters describing minimum parton energy in the jet energy transfer Function

	light quark jets	b quark jets
p_0	-334.386	-46.4269
p_1	4.03926	0.784917
p_2	-0.0108404	0.000961648
p_3	1.1617e-05	-1.76734e-06

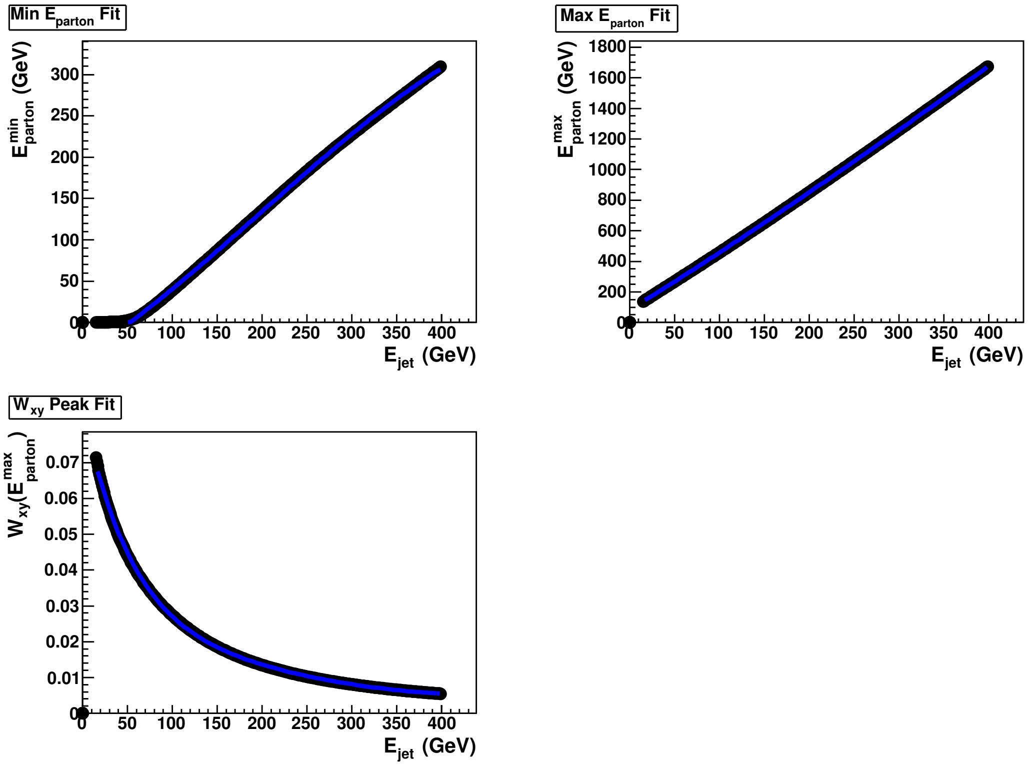

Figure A.3: Minimum parton energy (right), maximum parton energy (left), and maximum value of transfer function (bottom) as a function of jet energy in b quark transfer function parameters.

Table A.2: Parameters describing maximum parton energy in the jet energy transfer function

	light quark jets	b quark jets
p_0	66.4827	83.2186
p_1	3.94928	3.62891
p_2	-0.00224589	0.00123535
p_3	2.70608e-06	-8.72611e-07

Table A.3: Parameters describing maximum value of jet energy transfer function

	light quark jets	b quark jets
p_0	0.0579384	0.024763
p_1	0.0750545	0.018406
p_2	-0.663452	-0.255494
p_3	0.0420245	0.024763
p_4	0.0191666	0.0184059
p_5	-0.503761	-0.255494
p_6	0.0222408	0.0214873
p_7	-5.4025e-05	-4.15971e-05
p_8	2.0287e-08	-6.25139e-08
p_9	5.2199e-11	1.65854e-10

APPENDIX B

Solutions to Quartic Equation

Solutions to a general quartic equation are based on discussion in [67]. The salient points are repeated here. A general quartic equation is given by

$$x^4 + a_3\, x^3 + a_2\, x^2 + a_1\, x + a_0 = 0. \tag{B.1}$$

Solutions begin by finding one real root from the resolvent cubic equation, defined by

$$y^3 - a_2 y^2 + y(a_1 a_3 - 4a_0) + (4a_2 a_0 - a_1^2 - a_3^2 a_0) = 0. \tag{B.2}$$

This analysis uses `GSL`, *poly_solve_cubic*, returning at least one real root, y_1. We then define some useful constants in the complex plane

$$\begin{aligned} R &\equiv \sqrt{\frac{1}{4}a_3^2 - a_2 + y_1} \\ D &\equiv \sqrt{c_1 + c_2} \\ E &\equiv \sqrt{c_1 - c_2}, \end{aligned} \tag{B.3}$$

where

$$\begin{aligned} c_1 &\equiv \left\{ \begin{array}{ll} \frac{3}{4}a_3^2 - R^2 - 2a_2 & , \mathrm{Re}(R) \neq 0 \\ \frac{3}{4}a_3^2 - 2a_2 & , \mathrm{Re}(R) = 0 \end{array} \right\} \\ c_2 &\equiv \left\{ \begin{array}{ll} \frac{1}{4}(4a_3 a_2 - 8a_1 - a_3^3)R^{-1} & , \mathrm{Re}(R) \neq 0 \\ 2\sqrt{y_1^2 - 4a_0} & , \mathrm{Re}(R) = 0 \end{array} \right\}. \end{aligned} \tag{B.4}$$

Solutions to the quartic are then given by

$$\begin{aligned}
x_0 &= -\frac{1}{4}a_3 + \frac{1}{2}R + \frac{1}{2}D \\
x_1 &= -\frac{1}{4}a_3 + \frac{1}{2}R - \frac{1}{2}D \\
x_2 &= -\frac{1}{4}a_3 - \frac{1}{2}R + \frac{1}{2}E \\
x_3 &= -\frac{1}{4}a_3 - \frac{1}{2}R - \frac{1}{2}E.
\end{aligned} \tag{B.5}$$

APPENDIX C

Likelihood Minimum and Errors

The minimum and errors from the two-dimensional m_t-JES minus log likelihood after minimization of C_s are estimated from a fit with a two-dimensional second-order polynomial of the form

$$a_0x^2 + a_1xy + a_2y^2 + a_3x + a_4y + a_5. \tag{C.1}$$

Setting the partial derivatives in x and y to zero

$$\begin{aligned} 2a_0x + a_1y + a_3 &= 0 \\ 2a_2y + a_1x + a_4 &= 0 \end{aligned} \tag{C.2}$$

determines the minimum (x_0, y_0) of this function

$$\begin{aligned} x_0 &= \frac{a_1a_4 - 2a_2a_3}{4a_0a_2 - a_1^2} \\ y_0 &= \frac{2a_0a_4 - a_1a_3}{a_1^2 - 4a_0a_2}. \end{aligned} \tag{C.3}$$

Measured m_t and JES correspond to x_0 and y_0, respectively.

To estimate errors, we translate coordinates to the minimum given in equation C.3. The relevant equation in terms of translated coordinates is

$$a_0x^2 + a_1xy + a_2y^2 = \frac{S}{2} \tag{C.4}$$

where $\frac{S}{2}$ gives the distance from the minimum of the likelihood, and the a_0, a_1 and a_2 parameters are not affected by coordinate translation. This equation describes confidence interval ellipses based on S. The estimated error in this analysis before scaling corresponds to $S = 1$ and is determined by a line tangent to this ellipse. A line in x is given by $x = \delta_x$. Substituting this value into equation C.4 results in

$$a_0\delta_x^2 + a_1\delta_x y + a_2 y^2 - \frac{S}{2} = 0. \tag{C.5}$$

Equation C.5 has a single real root when the line is tangent to the ellipse, or when

$$a_1^2\delta_x^2 - 4a_2\left(a_0\delta_x^2 - \frac{S}{2}\right) = 0. \tag{C.6}$$

The errors are thus given by

$$\begin{aligned} \delta_x &= \sqrt{\frac{2a_2 S}{4a_0a_2 - a_1^2}} \\ \delta_y &= \sqrt{\frac{2a_0 S}{4a_0a_2 - a_1^2}}, \end{aligned} \tag{C.7}$$

where δ_y is derived similarly.

Errors without correlation from the other dimension are obtained by taking one-half the width of the ellipse along the desired axis. This is accomplished by setting $x = 0$ or $y = 0$ in equation C.4 and results in

$$\begin{aligned} \delta_x &= \sqrt{\frac{S}{2a_0}} \\ \delta_y &= \sqrt{\frac{S}{2a_2}}. \end{aligned} \tag{C.8}$$

Note that these definitions are consistent with the standard σ_x and σ_y of a two-dimensional Gaussian function. The correlation between m_t and JES is estimated from the Gaussian correlation constant ρ given by

$$\rho = -\frac{1}{2}\frac{a_1}{\sqrt{a_0a_2}} \tag{C.9}$$

APPENDIX D

Selected Event Likelihoods

The section shows selected event likelihoods calculated from experimental data. Figures D.1 to D.4 show the two-dimensional likelihood for events after maximization of the C_s parameter. Events are sorted according to the calculated value of the W + jets probability density evaluated at nominal JES (denoted P_{bkg} in the plots), and those with lower values are expected to be more signal like. Also listed are the number of secondary vertex tags in each event.

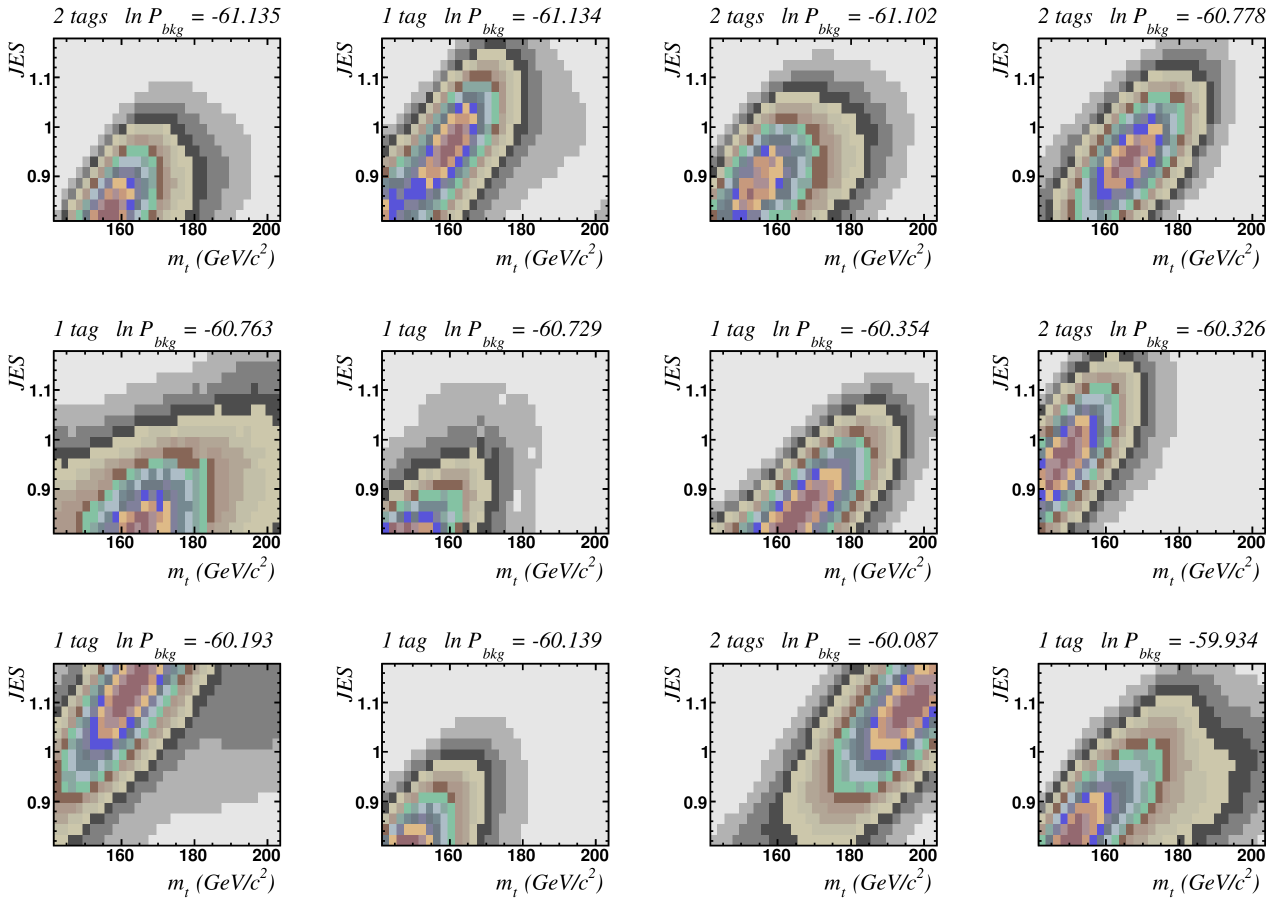

Figure D.1: Two-dimensional likelihood for selected experimental data events.

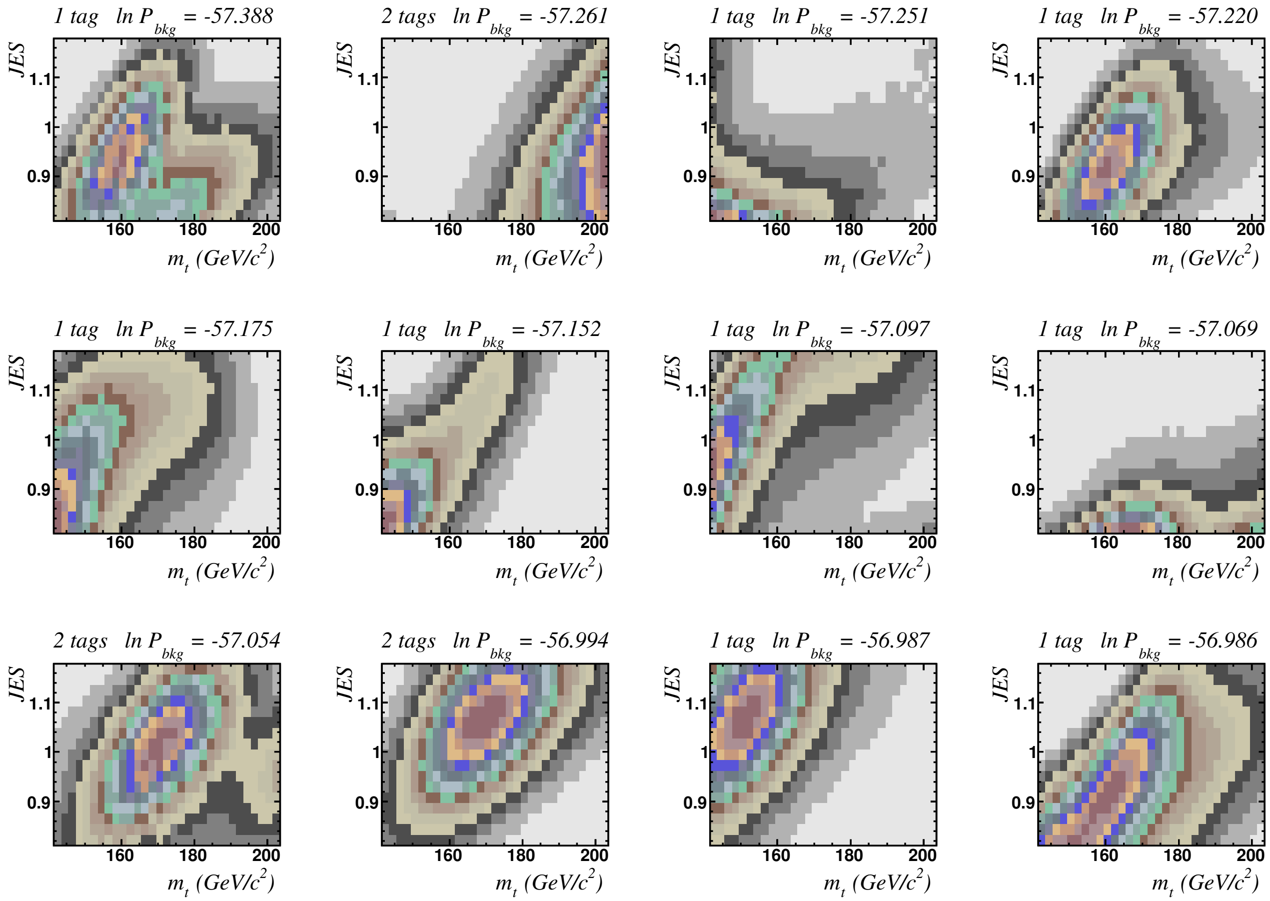

Figure D.2: Two-dimensional likelihood for selected experimental data events.

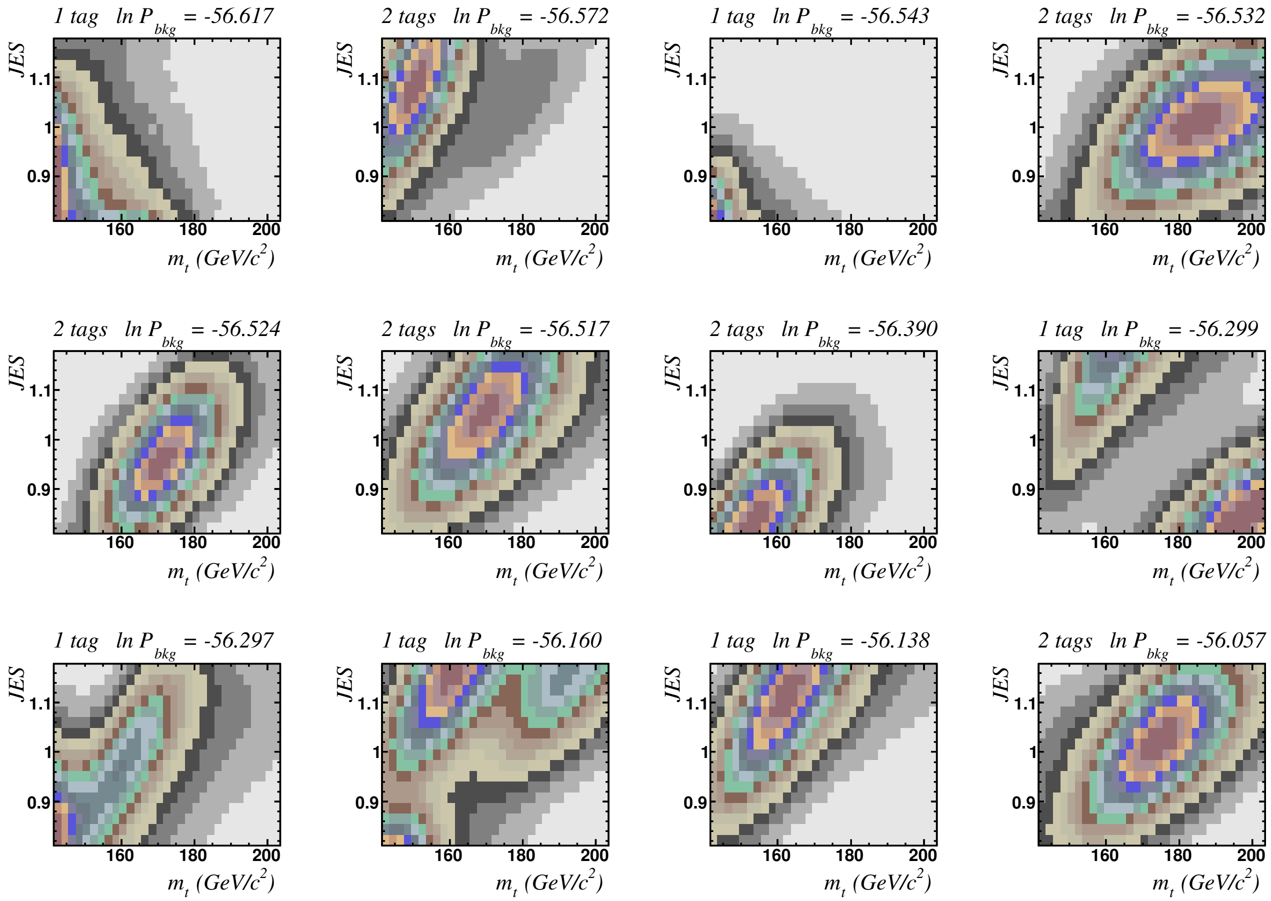

Figure D.3: Two-dimensional likelihood for selected experimental data events.

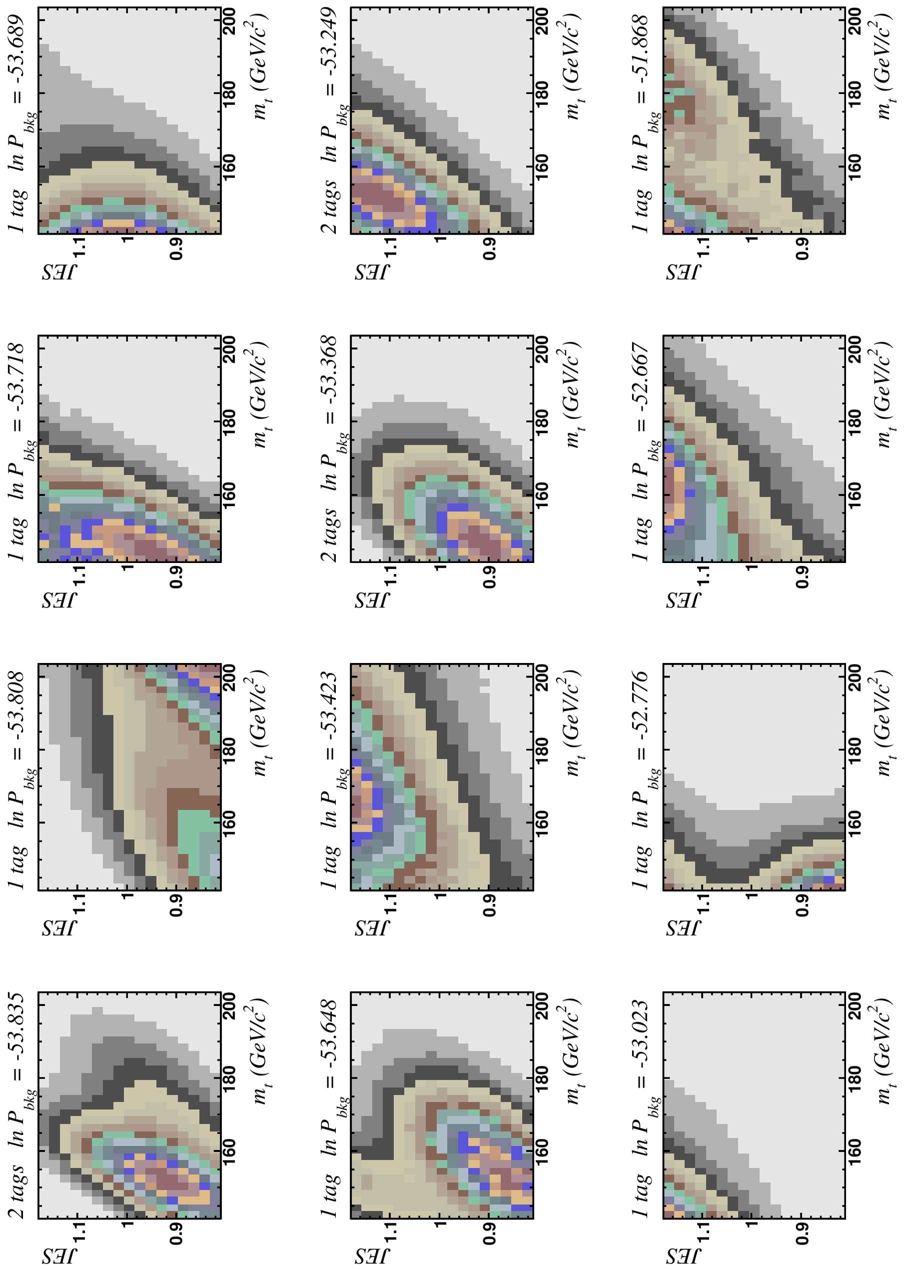

Figure D.4: Two-dimensional likelihood for selected experimental data events.

References

[1] S. L. Glashow, Nucl. Phys. **22**:579, (1961); S. Weinberg, Phys. Rev. Lett. **19**:1264, (1967); A. Salam, Weak and Electromagnetic Interactions, Proceedings of the Nobel Symposium held at Lerum, Sweden, (1968).

[2] P.W. Higgs, Phys. Rev. Lett. **13**:508, (1964).

[3] P.W. Higgs, Phys. Rev. **145**:1156, (1966).

[4] W.-M. Yao *et al.* (Particle Data Group), J. Phys. **G 33**:1, (2006).

[5] F. Abe *et al.*, Phys. Rev. Lett. **74**:2626-2632, (1995). hep-ex/9503002.

[6] S. Abachi *et al.*, Phys. Rev. Lett. **74**:2632-2637, (1995). hep-ex/9503003.

[7] A. Abulencia, *et al.* (CDF Collaboration), Phys. Rev. Lett. **96**:022004, (2006), Phys. Rev. **D 73**:092002, (2006), Phys. Rev. **D 72**:032003, (2006); V. M. Abazov, *et al.* (DØCollaboration), Phys. Rev. **D 74**:092005, (2006).

[8] J. Erler and P. Langacker, Phys. Lett. **B 592**:1, (2004).

[9] LEP Electroweak Working Group, hep-ex/0612034 (2006).

[10] The ALEPH, DELPHI, L3, OPAL, SLD Collaborations, the LEP Electroweak Working Group, the SLD Electroweak and Heavy Flavour Groups, Phys. Rept. **427**:257 (2006).

[11] Tevatron Electroweak Working Group, Fermilab-TM-2355-E, hep-ex/0608032, (2006).

[12] S. Pokorski, hep-ph/0502132, (2005).

[13] S.P. Martin, hep-ph/9709356, (1999).

[14] D. Cronin-Hennessy, A. Beretvas, P.F. Derwent, Nucl. Instrum. Meth. **A 443**:37-50, (2000).

[15] S. Van Der Meer, *et al.*, Phys. Rep. **58**:73, (1980).

[16] R. Blair *et al.* (CDF Collaboration), Fermilab Report No. FERMILAB-Pub-96-390-E, Section 12, (1996).

[17] D. Acosta, *et al.* (CDF Collaboration), Phys. Rev. **D 71**:032001, (2005).

[18] D. Acosta *et al.*, Nucl. Instrum. Meth. **A 461**:540-544, (2001).

[19] D. Acosta *et al.*, Nucl. Instrum. Meth. **A 494**:57-62, (2002).

[20] C. S. Hill, *et al.*, Nucl. Instrum. Meth. **A 530**:1, (2004).

[21] A. Sill, Nucl. Instrum. Meth. **A 447**:1-8, (2000).

[22] A. Affolder, *et al.*, Nucl. Instrum. Meth. **A 453**:84, (2000).

[23] T. Affolder *et al.*, Nucl. Instrum. Meth. **A 526**:249-299, (2004).

[24] L. Balka *et al.*, Nucl. Instrum. Meth. **A 267**:272-279, (1998).

[25] S. Bertolucci *et al.*, Nucl. Instrum. Meth. **A 267**:301-314, (1998).

[26] M. Albrow *et al.*, Nucl. Instrum. Meth. **A 480**:524-545, (2002).

[27] R. Blair *et al.* (CDF Collaboration), Fermilab Report No. FERMILAB-Pub-96-390-E, Section 9, (1996).

[28] G. Apollinari *et al.*, Nucl. Instrum. Meth. **A 412**:515-526, (1998).

[29] A. Artikov *et al.*, Nucl. Instrum. Meth. **A 538**:358-371, (2005).

[30] P. Gatti, Fermilab-Thesis-2001-23.

[31] P. Billoir, R. Fruhwirth, M. Regler, Nucl. Instrum. Meth. **A 241**:115-131, (1985).

[32] D. Acosta, *et al.* (CDF Collaboration), Phys. Rev. **D 71**:052003, (2005).

[33] A. Bhatti *et al.*, Nucl. Instrum. Meth. **A 566**:375, (2006).

[34] A.A. Affolder, *et al.* (CDF Collaboration), Phys. Rev. **D 64**:032002, (2001).

[35] D. Goldstein *et al.*, CDF Note 6588, (2003). CDF Note 6830, (2004).

[36] G. Corcella, I. G. Knowles, G. Marchesini, S. Moretti, K. Odagiri, P. Richardson, M. H. Seymour, and B. R. Webber. JHEP **01**:010, (2001); G. Marchesini *et al.*, Comp. Phys. Commun. **67**:465, (1992).

[37] T. Sjostrand, L. Lonnblad, and S. Mrenna, TP 01-21, LU (2001); T. Sjostrand *et al.*, Comp. Phys. Commun. **135**:238, (2001).

[38] J. Pumplin *et al.*, Nucl. Instrum. Meth. **A 447**:1, (2002).

[39] P. Avery, K. Read, and G. Trahern. CLEO Report CSN-212 (1985). (unpublished)

[40] M. L. Mangano, M. Moretti, F. Piccinini, R. Pittau, and A. D. Polosa, JHEP **07**:001, (2003).

[41] S. Agostinelli *et al.*, Nucl. Instrum. Meth. **A 506**:250-303, (2003).

[42] T. Affolder *et al.*, Nucl. Instrum. Meth. **526**:249, (2004).

[43] G. Grindhammer, M. Rudowicz, and S. Peters, Nucl. Instrum. Meth. **A 290**:469, (1990).

[44] A. Abulencia *et al.*, Phys. Rev. Lett. **97**:082004, (2006).

[45] G. Cowan, *Statistical Data Analysis*, Oxford Science Publications, (2002).

[46] K. Kondo, J. Phys. Soc. Jpn. **57**:4126, (1988), J. Phys. Soc. Jpn. **57**:4126, (1998), J. Phys. Sox. Jpn. **57**:4126, (1998).

[47] R. H. Dalitz and G. R. Goldstein, Phys. Rev. **D 45**:1531, (1992).

[48] V. M. Abazov, *et al.* (DØCollaboration), Nature **429**:02589, (2004); V. M. Abazov, *et al.* Phys. Lett. **B 617**, (2005); F. Canelli, Ph.D. thesis, University of Rochester, (2003).

[49] R. Barlow, Nucl. Instrum. Meth. **A 297**:496-506, (1990).

[50] L. Lyons, W. Allison, and J. Comellas, Nucl. Instrum. Meth. **A 245**:530-534, (1986).

[51] F. James, CERN Program Library Long Writeup **D 506**.

[52] G. Mahlon and S. Parke, Phys. Rev. **D 53**:4886-4896, (1996).

[53] J.H. Kuehn. SLAC-R-494 CONF-9507258-UC-414, pg.1, (1995); hep-ph/9707321.

[54] M. Galassi, *et al.*, *GNU Scientific Library Reference Manual (2*$^{\text{nd}}$ *Ed.*, Network Theory Ltd., (2004).

[55] G. P. Lepage, J. Comp. Phys. **27**:192, (1998).

[56] F.A. Berends, H. Kuijf, B. Tausk and W.T. Giele, Nucl. Phys. **B 357**:32-64, (1991).

[57] W. A. Rolke, A. M. Lopez and J. Conrad, Nucl. Instrum. Meth. **A 551**:493-503, (2005).

[58] D. Glenzinski, private communication.

[59] Charles Plager, private communication.

[60] J.-F. Arguin, P. Sinervo and S. Xie, CDF Note 7252, (2004).

[61] J.-F. Arguin, P. Sinervo and S. Xie, CDF Note 7505, (2005).

[62] F. Garberson, *et al.*, CDF Note 8025, (2006); F. Garberson, J.R. Incandela, CDF Note 8223, (2006).

[63] A.D. Martin, R.G. Roberts, and W.J. Stirling, Phys. Rev. **D 50**:6734-6752, (1994); http://durpdg.dur.ac.uk/hepdata/mrs.html.

[64] B. Heinemann, CDF Note 8312, (2006).

[65] U.K. Yang, private communication.

[66] Tevatron Electroweak Working Group, hep-ex/0608032.

[67] http://mathworld.wolfram.com/QuarticEquation.html